THE
SHOCK AND VIBRATION
BULLETIN

Part 2
Structural Analysis, Design Techniques

JUNE 1973

A Publication of
THE SHOCK AND VIBRATION
INFORMATION CENTER
Naval Research Laboratory, Washington, D.C.

Office of
The Director of Defense
Research and Engineering

82 02 26 069

SYMPOSIUM MANAGEMENT

THE SHOCK AND VIBRATION INFORMATION CENTER

Robert O. Belsheim, Director
Henry C. Pusey, Coordinator
Edward H. Schell, Coordinator
Rudolph H. Volin, Coordinator

Bulletin Production

Graphic Arts Branch, Technical Information Division,
Naval Research Laboratory

THE
SHOCK AND VIBRATION
BULLETIN

JUNE 1973

A Publication of
**THE SHOCK AND VIBRATION
INFORMATION CENTER**
Naval Research Laboratory, Washington, D.C.

The 43rd Symposium on Shock and Vibration was
held at the Asilomar Conference Grounds, Pacific
Grove, California, on 5-7 December, 1972. The U.S.
Army, Fort Ord, was host.

Office of
The Director of Defense
Research and Engineering

CONTENTS

PART 2

Structural Analysis

Design Techniques

PAPERS APPEARING IN PART 1

REMARKS
Dr. Elias Klein, Ret., Sarasota, Florida

Invited Papers

A QUARTER CENTURY OF PROGRESS
Mr. Dwight C. Kennard, Consultant, Traverse City, Michigan

FORMER SHOCK
Dr. Donald E. Marlowe, Vice President for Administration, Catholic University,
Washington, D. C.

THE ARMY'S BIG FIVE AND RDTE PROGRAM THRUSTS
Major General John R. Guthrie, Deputy Commanding General for Materiel
Acquisition, Army Materiel Command Headquarters, Washington, D. C.

Submarine Shock Testing

UNDERWATER EXPLOSION TESTS WITH THE SWEDISH FULL-SCALE TEST SECTION
"STÅLMYGGAN". Part I: TEST SECTION WITH OBJECTS AND MEASURING POINTS,
ARRANGEMENTS AND DIMENSIONAL MEASUREMENTS
H. Nilsson, Kockums Mekaniska Verkstads AB, Naval Department, Malmö, Sweden

UNDERWATER EXPLOSION TESTS WITH THE SWEDISH FULL-SCALE SUBMARINE TEST
SECTION "STÅLMYGGAN": RECORDING AND DATA REDUCTION SYSTEM
L. Westin and A. Henningson, Military Electronics Laboratory, Stockholm, Sweden

UNDERWATER EXPLOSION TEST WITH THE SWEDISH FULL SCALE SUBMARINE TEST SECTION
"STÅLMYGGAN": PART III. INTERPRETATION OF RESULTS OF SHOCK MEASUREMENTS
K. Spång, IFM-AKUSTIKBYRÅN AB, Stockholm, Sweden

Shock Analysis

SHOCK ANALYSIS ERRORS IN THE PRESENCE OF VIBRATION
C. T. Morrow, Advanced Technology Center, Inc., Dallas, Texas

APPROXIMATE RESPONSE SPECTRA OF DECAYING SINUSOIDS
A. E. Galef, TRW Systems, Inc., Redondo Beach, California

STEADY-STATE MOTIONS OF ORBITAL CABLE PLOWS
M. Senator and L. J. Scerbo, Bell Laboratories, Whippany, New Jersey

TRANSIENT MOTIONS OF ORBITAL CABLE PLOWS
L. J. Scerbo and M. Senator, Bell Laboratories, Whippany, New Jersey

SHOCK WAVE INDUCED TRANSIENT PRESSURE ENVIRONMENT ABOUT THE SPRINT II
MISSILE CAUSED BY LAUNCH CELL EJECTION
A. J. Culotta, Martin Marietta Aerospace Corporation, Orlando, Florida

Shock Testing

DIGITAL CONTROL TECHNIQUE FOR SEISMIC SIMULATION
G. C. Kao, K. Y. Chang, and W. W. Holbrook, Wyle Laboratories, Huntsville, Alabama

PYROTECHNIC SHOCK SIMULATION USING THE RESPONSE PLATE APPROACH
C. L. Thomas, Honeywell Inc., Aerospace Division, St. Petersburg, Florida

TEST METHOD TO QUALIFY ELECTRONIC COMPONENTS IN SHOCK AND SUSTAINED
ACCELERATIONS
R. K. Melzer, Sperry Univac, St. Paul, Minnesota

THE USE OF SHAKER-OPTIMIZED PERIODIC TRANSIENTS IN MATCHING FIELD SHOCK
SPECTRA
D. O. Smallwood, Sandia Laboratories, Albuquerque, New Mexico and A. F. Witte,
Kaman Sciences, Colorado Springs, Colorado

A TRANSIENT VIBRATION TEST TECHNIQUE USING LEAST FAVORABLE RESPONSES
D. O. Smallwood, Sandia Laboratories, Albuquerque, New Mexico

PAPERS APPEARING IN PART 3

Skylab

SKYLAB VIBROACOUSTIC TESTING — AN OVERVIEW
G. M. Mosely, Teledyne-Brown Engineering, Huntsville, Alabama

SKYLAB VIBRATION AND ACOUSTIC STRUCTURAL TEST SYSTEMS
J. D. Johnston, Jr., NASA, Manned Spacecraft Center, Houston, Texas and D. L. Knittle,
Northrop Services Inc., Houston, Texas

ORBITAL WORKSHOP VIBROACOUSTIC TEST PROGRAM
W. H. Keller and E. Yoshida, McDonnell Douglas Astronautics Co., Huntington Beach, Calif.

v

OPTIMUM PASSIVE SHOCK ISOLATION FOR UNDERGROUND PROTECTIVE STRUCTURES
   D. L. Platus, Mechanics Research Inc., Los Angeles, California

INFLUENCE OF AN ABSORBER ON MACHINE TOOL VIBRATION
   O. Susolik, The Timken Company, Canton, Ohio

STRUCTURAL ANALYSIS

APPROXIMATE METHOD FOR CALCULATING THE RESPONSE

OF EMPLACEMENT STRUCTURES SUBJECTED TO GROUND SHOCK

FROM UNDERGROUND NUCLEAR DETONATIONS*

Mark Hartzman

University of California, Lawrence Livermore Laboratory
Livermore, California 94550

A method for calculating dynamic response of emplacement structures is described in this paper. It consists in replacing the structural system by an idealized lumped mass/finite element model. The equations of motion for each mass, expressed as functions of the internal and external forces, are solved in a step-by-step manner by a numerical algorithm. A running frictional pressure pulse applied to the external surface of the structure simulates the ground shock environment. Comparison of calculated response values with limited experimental data indicates reasonable agreement.

INTRODUCTION

A problem of considerable practical interest at Lawrence Livermore Laboratory is the calculation of the dynamic response of buried emplacement structures. Such structures are used for emplacement and support of nuclear devices and associated instrumentation. They usually include a diagnostic section that contains instrumentation systems and an emplacement pipe used for supporting the rest of the structure. Since these structures are buried in soil, the soil-structure interaction plays an important role in the response calculations.

The complexity of the problem means that responses can usually be obtained by numerical techniques only. A number of finite element and difference continuum programs exist that could be used for obtaining solutions. However, these programs are time-consuming because a very small mesh must be chosen to represent the pipe wall thickness. This paper is a description of an approximate method that circumvents this difficulty and at the same time gives reasonable results, adequate for practical design.

The method consists in replacing the continuous structure by a lumped mass/one-dimensional finite element system. For each lumped mass, the equation of motion is expressed in terms of the instantaneous internal forces caused by deformation of the

structure and the external force that the soil is assumed to exert on the structure. We obtain the displacement histories by applying a step-by-step algorithm to integrate the system of equations, taking into account the initial conditions and the material properties of the structure.

METHOD OF ANALYSIS

Equations of Motion

Figure 1 shows an idealized structure and the corresponding lumped mass/finite element system. We assume that each mass has one degree of freedom, motion along the axial direction. The equations of motion for the mass system may be expressed in matrix form as

$$[\ulcorner M \lrcorner] \{\ddot{u}\} + [K]\{u\} + [D]\{\dot{u}\} = \{F\}, \qquad (1)$$

where

$[\ulcorner M \lrcorner]$ = diagonal mass matrix, assumed constant

$\{u\}$ = total displacement to time t

$[K]$ = instantaneous structure stiffness matrix, which depends on the displacements, stresses, and material properties

$[D]$ = damping matrix

$\{F\}$ = external load vector.

1
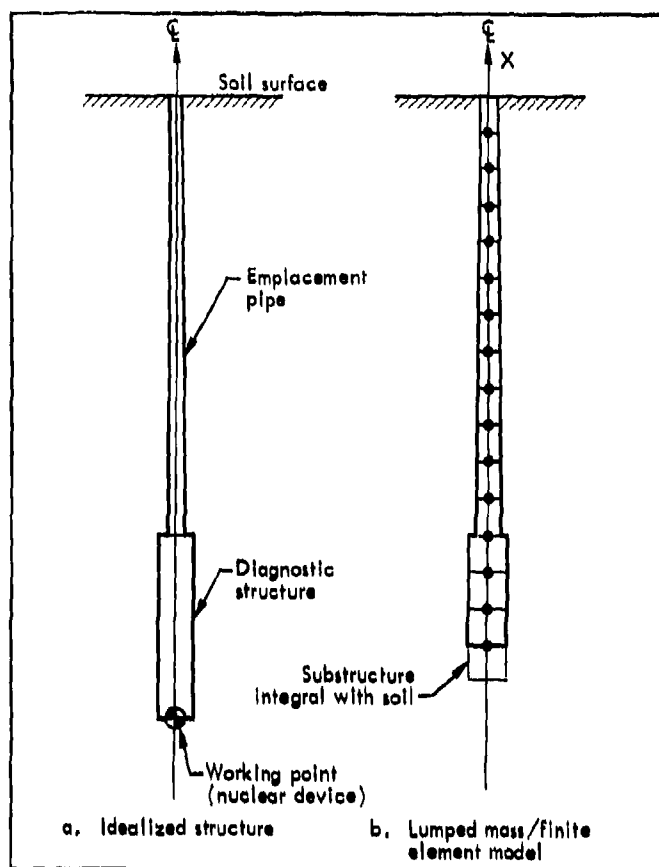
Fig. 1. Buried emplacement structure and lumped mass/finite element model.

Equations (1) are set of nonlinear second-order differential equations that can be solved by numerical methods only. In this analysis, we will use an explicit method of numerical integration. Assuming a diagonal mass matrix, we can rewrite Eqs. (1) in the form

$$[\neg M \neg]\ \{\ddot{U}\} = \{F\} - \{U^E\} - \{U^D\},\qquad(2)$$

where the vectors $\{U^E\}$ and $\{U^D\}$ can be interpreted as resultants of internal deformational and damping forces from the elements connected to the ith lumped mass. Thus, any equation of the above system of equations can be expressed as

$$m_i \ddot{u}_i = F_i - \sum_j U^E_{ij} - \sum_j U^D_{ij},\qquad(3)$$

where

$m_i = i$th lumped mass

$\ddot{u}_i =$ acceleration of the ith mass

$F_i =$ external force resultant acting on the ith mass

$\sum_j U^E_{ij} =$ internal forces caused by elastic-plastic deformation in the elements adjacent to the ith mass

$\sum_j U^D_{ij} =$ internal forces caused by damping.

The forces acting on this mass are shown in Fig. 2. By adopting an explicit scheme of step-by-step integration, we can calculate the complete internal force system at any time without first solving for the unknown incremental displacements. We thus eliminate the need to assemble stiffness and damping

2
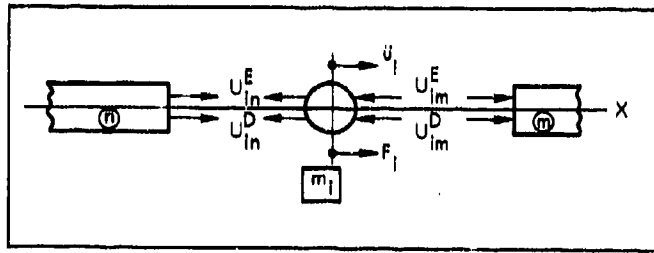
Fig. 2. Lumped mass and force system.

matrices since we can determine the acceleration vector completely as long as we know the external force system.

An explicit algorithm for the numerical integration of second-order differential equations is described in Ref. 1. At the sth instant, the incremental displacements and the velocities are given as

$$\{\dot{u}\}^s = \{\dot{u}\}^{s-1} + \frac{\Delta t}{12} [5\{\ddot{u}\}^s + 8\{\ddot{u}\}^{s-1} - \{\ddot{u}\}^{s-2}] \quad (4)$$

and

$$\{\Delta u\}^{s+1} = \{\dot{u}\}^s \Delta t + \frac{(\Delta t)^2}{6} [4\{\ddot{u}\}^s - \{\ddot{u}\}^{s-1}]. \quad (5)$$

The total displacements at the $(s+1)$th instant are then obtained from

$$\{u\}^{s+1} = \{u\}^s + \{\Delta u\}^{s+1}. \quad (6)$$

Assuming the initial velocities and accelerations are given, the first displacement increments are

$$\{\Delta u\}^1 = \{u\}^1 - \{u\}^0 = \Delta t\{\dot{u}\}^0 + \frac{(\Delta t)^2}{2} \{\ddot{u}\}^0. \quad (7)$$

The acceleration at any instant t^s are obtained from Eq. (3) and are rewritten as

$$\{\ddot{u}\}^s = [M]^{-1} \left\{ \{F\} - \{U^E\} - \{U^D\} \right\}^s. \quad (9)$$

Calculation of Internal Forces

The internal force resultants acting at any instant can be calculated directly if we know (1) stress and strain states at the beginning of a time increment, (2) incremental displacements and strains, (3) incremental uniaxial stress-strain relations, and (4) instantaneous velocities.

Consider a generic massless element n and the two connected masses at its ends, as shown in Fig. 3. At a given instant t^s, we assume that the internal forces act as shown. Over the time increment $\Delta t = t^s - t^{s-1}$, the ends of the element are assumed to have experienced incremental displacements Δu_i, Δu_j.
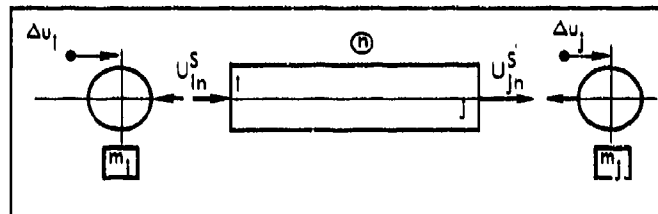
Fig. 3. Finite element and internal forces.

The velocity at t^1 is then $\qquad\qquad (8)$

$$\{\dot{u}\}^1 = \{\dot{u}\}^0 + \Delta t\{\ddot{u}\}^1.$$

From equilibrium we have

$$U^E_{in}{}^s = -U^E_{jn}{}^s \quad (10)$$

3

and by definition

$$U_{jn}^{s} = \sigma_n^{s} A_n,$$ (11)

where

σ_n^{S} = element axial stress at t^{S}

A_n = initial cross-sectional area.

The incremental strain $\Delta\varepsilon_n$ experienced over Δt is defined as

$$\Delta\varepsilon_n = \frac{\Delta u_j - \Delta u_i}{L_n},$$ (12)

where L_n = initial element length at time $t = 0$.

The total strain t^S is obtained as

$$\varepsilon_n^{s} = \varepsilon_n^{s-1} + \Delta\varepsilon_n$$ (13)

We can thus evaluate immediately the incremental strains over a time interval and the total current strains. We can also evaluate the current stresses if we know the stresses at $t = t^{s-1}$ and the incremental stresses and if we postulate suitable stress-strain relations.

The stress-strain relation for the materials considered here is replaced by a piece-wise linear approximation and is based on the assumption that (1) no buckling or collapse is considered, (2) Poisson, thermal, and strain rate effects are ignored, and (3) nonisotropic hardening (i.e. yield strengths in tension and compression may be different) is postulated.

Figures 4 and 5 show the postulated behavior of the material. The main objective of this material description is to model the large deformation that presumably might occur because of compression. However, it is also possible that large tensile deformation, unloading and reloading, or cyclic loading may occur. The present formulation could also describe these phenomena.

We can describe deformation in the compressive range as follows: The material is initially assumed to deform elastically until the yield limit σ_y (<0) is reached. Deformation then continues plastically until the strain $\bar{\varepsilon}_c$ (<0) is reached. This region is supposed to represent very approximately both yielding of the material and axisymmetric collapse of the structure. If loading is further increased, the deformation proceeds elastically again, reflecting the assumptions of circumferential
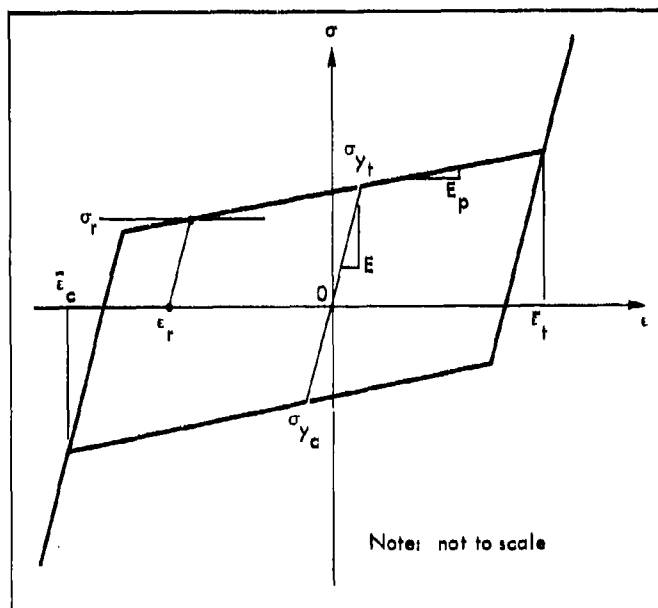
Fig. 4. Assumed stress-strain relation.

4

(1) $\quad \sigma^s = E\Delta\epsilon + \sigma^{s-1}$

(2) $\quad \sigma^s = E_p\Delta\epsilon + \sigma_m^b(1-r) + r\,\sigma^{s-1}$

(3) $\quad \sigma^{s'} = E_p\Delta\epsilon + \sigma^{s-1}$

(4) $\quad \sigma^s = E_p\Delta\epsilon + \sigma_m(1-r) + r\sigma^{s-1} + (1-r)\,E(\epsilon^s - \bar{\bar{\epsilon}})$

(5) $\quad \sigma^s = E_p\Delta\epsilon + \sigma^{s-1} + (1-r)\,E(\epsilon^s - \bar{\epsilon})$

(6) $\quad \sigma^s = 0$

(7) $\quad \sigma^s = E\Delta\epsilon + E(\epsilon^{s-1} - \epsilon_r)$

Legend

σ^s = current stress

σ^{s-1} = stress of the beginning of a time increment

$\Delta\epsilon$ = strain increment

σ_m^s = current yield strength
(varies as work-hardening progresses)

ϵ^s = current strain

E = elastic modulus

E_p = plastic modulus

r = ratio (E_p/E)

$\bar{\epsilon}$ = inelastic strain limit

ϵ_r = residual strain

σ_r = rupture stress
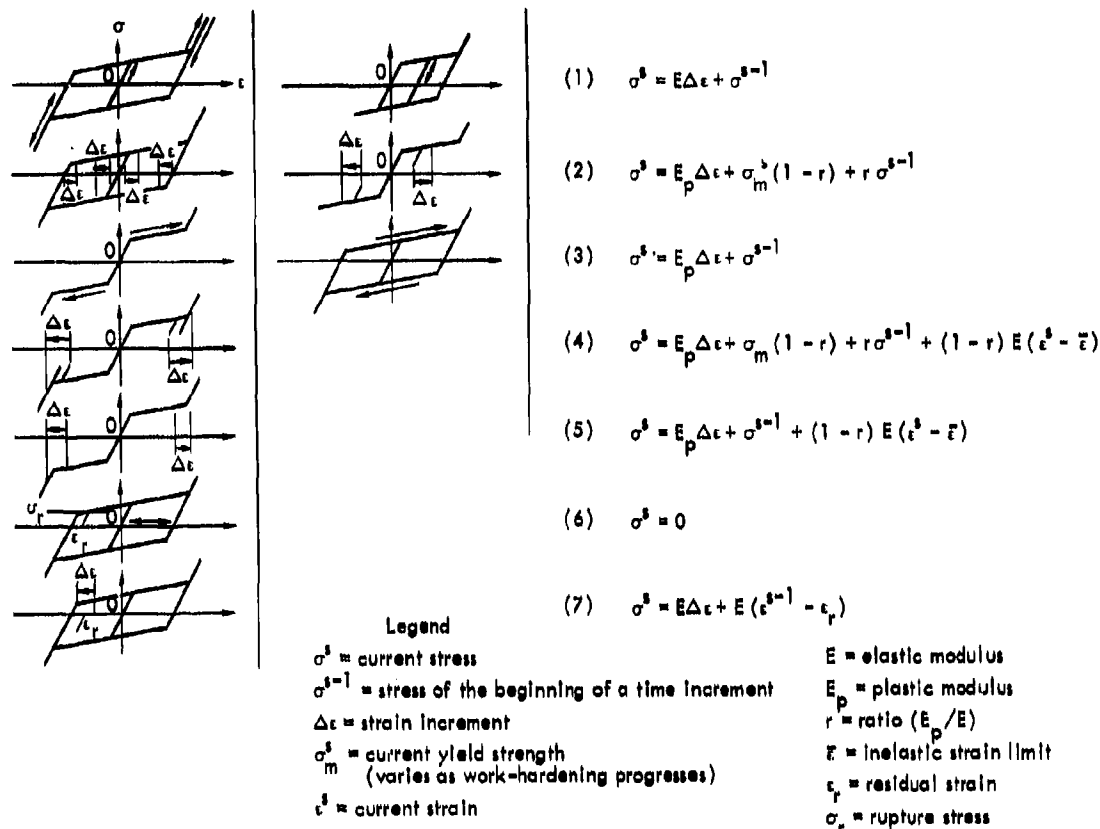
Fig. 5. Deformation patterns and corresponding stress-strain relations.

collapse and radial soil constraint, effects that tend to stiffen the structure against further deformation. Unloading occurs elastically at any point until reverse plastic (tensile) loading is experienced. If the stress σ_r is reached, the material is assumed to fail and the stress vanishes. However, a compressive residual strain ϵ_r, indicating permanent shortening of the element, remains. As long as $\epsilon > \epsilon_r$, the stress remains zero and separation occurs. If the motion is such that $\epsilon < \epsilon_r$, compressive loading is experienced; tensile loading cannot occur again.

Figure 5 shows several possible modes of deformation, together with the corresponding stress-strain relations.

Once the stresses due to deformation are obtained, we can get the corresponding internal forces from Eqs. (10) and (11). We obtain the internal viscous forces by assuming a simple

Kelvin solid whose stress-strain relation has the general form

$$\sigma = \sigma^E + \sigma^D,\qquad (14)$$

where

$$\sigma^D = \eta\,\dot{\epsilon}.$$

Since $\dot{\epsilon}_n = \dfrac{1}{L_n}\left(\dot{u}_j^s - \dot{u}_i^s\right)$, the viscous forces take the form

$$U_{jn}^D = \alpha_n\left(\dot{u}_j^s - \dot{u}_i^s\right),$$

where

$$\alpha_n = \left(\frac{\eta A}{L}\right)_n,\qquad (15)$$

5

and

$$U_{in}^{D_s} = - U_{jn}^{D_s} . \tag{16}$$

The viscosity coefficient n_p is generally difficult to determine. A typical value for steel is 1×10^6 psf-sec.^{2}

the working point. We also assume the existence of a static component due to overburden. We can transform this lateral pulse into axial forces acting on the masses by using prescribed Coulomb friction factors. The sense of these forces is determined by the relative velocities of the masses and the corresponding points in the soil. We assume that these loads act only on that portion of the structure that remains underground. The choice of these mechanisms is
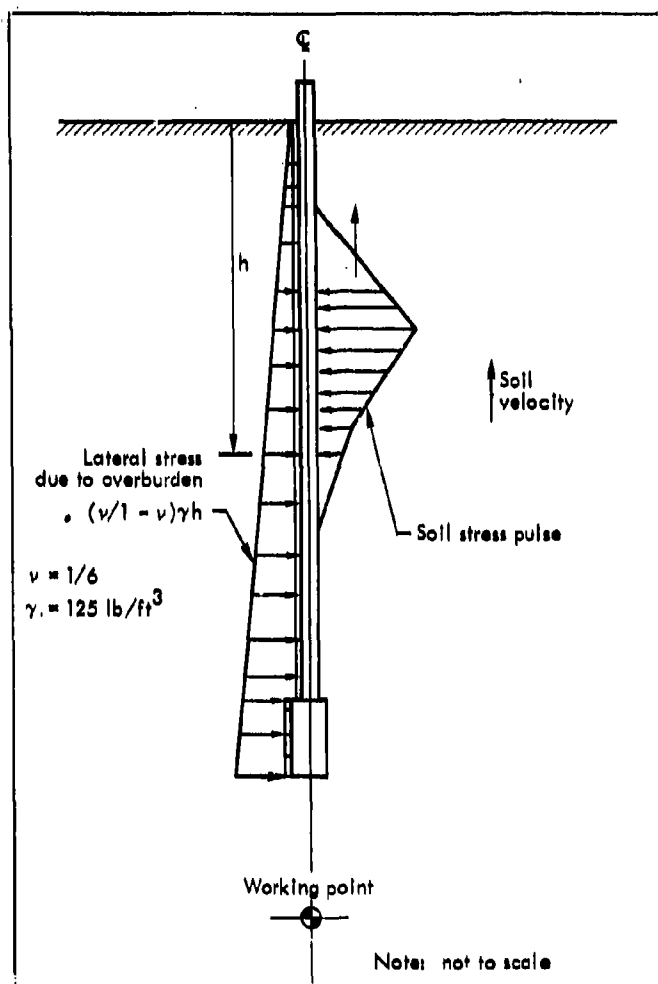
Fig. 6. Assumed axisymmetric lateral loading at a given instant.

Calculation of External Forces

We assume that the forces acting on the structure are caused by an axisymmetric lateral stress pulse propagating through the soil from

based on limited numerical experimentation and is not unique. The weight is also included and acts over the entire structure.

Figure 6 shows the shapes of the assumed

6

lateral loading. We obtain the magnitude of the lateral stress at each mass point from the soil stress history at each mass point. This history is obtained from calculations, based on empirical results, of peak stress and arrival times as functions of axial distance from the working point. Figure 7 shows the postulated shock stress history at a generic mass point. In these calculations, t_a represents the arrival time of the plastic front. The elastic precursor in the soil is assumed negligible. The rarefaction wave due to reflection from the surface is also neglected.

The particle velocity pulse is related to the stress pulse and is assumed to have the same history.

Once we know the lateral stress history for a given instant, we can transform it into a set of lateral forces distributed around the structure acting on the lumped masses. These calculations are performed at the element level.

Figure 8 shows three masses connected by two elements, and the instantaneous lateral stress distribution. From considerations of
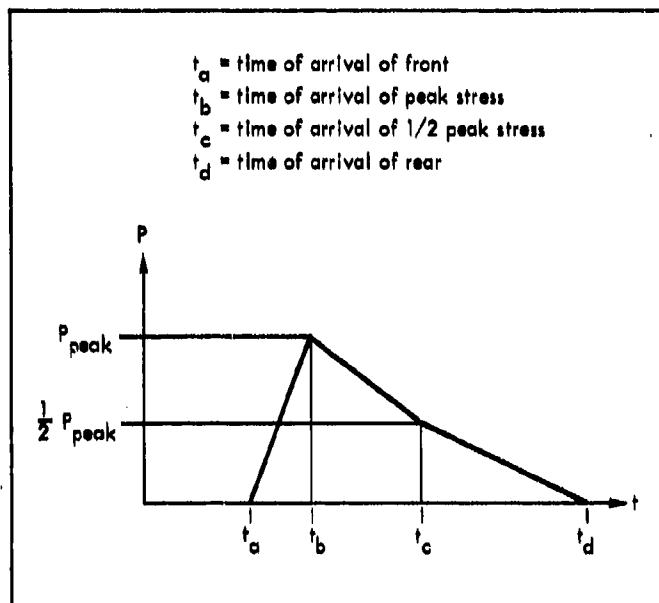
Fig. 7. Lateral stress pulse history at a generic mass point.
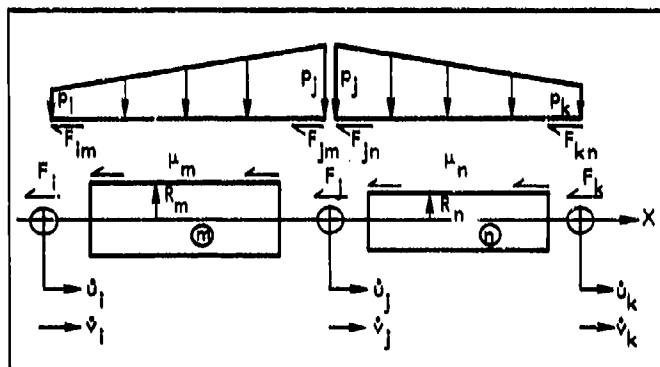
Fig. 8. Axial forces due to lateral stress distribution.

7

virtual work, the equivalent axial forces caused by lateral stress acting at the ends of the elements are

Element m:

$$F_{im} = -\frac{L_m}{6} (2p_i + p_j) \, 2\pi R_m \mu_m \left(\frac{\dot{u}_i - \dot{v}_i}{|\dot{u}_i - \dot{v}_i|}\right) \quad (17)$$

$$F_{jm} = -\frac{L_m}{6} (p_i + 2p_j) \, 2\pi R_m \mu_m \left(\frac{\dot{u}_j - \dot{v}_j}{|\dot{u}_j - \dot{v}_j|}\right), \quad (18)$$

Element n:

$$F_{jn} = -\frac{L_n}{6} (2p_j + p_k) \, 2\pi R_n \mu_n \left(\frac{\dot{u}_j - \dot{v}_j}{|\dot{u}_j - \dot{v}_j|}\right) \quad (19)$$

$$F_{kn} = -\frac{L_n}{6} (p_j + 2p_k) \, 2\pi R_n \mu_n \left(\frac{\dot{u}_k - \dot{v}_k}{|\dot{u}_k - \dot{v}_k|}\right), \quad (20)$$

where $\dot{v}$ = soil velocity.

We can therefore obtain the external forces acting on the masses by summing the components due to the associated elements, i.e.,

$$F_j = F_{jn} + F_{jm} . \quad (21)$$

Prescribed Boundary and Initial Conditions

We assume that the external forces described in the last section are applied to all masses except the bottommost; we further assume that the bottommost mass experiences the soil displacement history obtained by integrating the soil velocity history at this mass point. We can integrate the soil velocity history if we assume that a portion of the structure at and just below the bottommost mass collapses and remains rigidly attached to the soil.

Initially we consider all velocities, displacements, and accelerations to be zero. However, the stresses and strains caused by the static weight of the structure are calculated.

Numerical Procedure

Assume we have calculated the incremental displacements over a period of time. The calculational algorithm for the displacement history consists of the following steps:

1. For each element calculate incremental strains. Calculate the stresses and internal forces as described in the section on internal forces.

2. Calculate external lateral stresses and axial forces. Check for signs based on the relative velocity between soil and structure, as described in the section on external forces.

3. Calculate the total force resultant acting on each mass.

4. Calculate accelerations of masses from Eq. (9).

5. Calculate velocities and incremental displacements from Eqs. (4) and (5).

6. Introduce prescribed displacements.

7. Calculate total displacements from Eq.(6)

8. Return to step 1.

See Fig. 9 for a graphic presentation of the algorithm. The algorithm gives the displacement histories of the masses and the internal force histories; the element stress histories are obtained implicitly in the process.

COMPARISON WITH EXPERIMENTAL RESULTS

To check the validity of the method, we calculated the response of an already-tested emplacement structure and compared the results with the empirical data.[3] The response was characterized by the displacement of the top of the emplacement pipe. Figure 10 shows both a diagram of the analyzed structure and the finite element model of the structure. We set the bottommost point of the structure at 90 ft above the working point, assuming that the structure below this point displaced with the soil. No structural damping was included.

To calculate the response we varied a number of factors until we got approximate agreement between the calculated and experimental results. The comparison is shown in Fig. 11. The varied parameters were the friction factor, the maximum tensile stress σ_r, and the minimum strain $\bar{\epsilon}_c$. We found that the most critical and least known parameter is the friction factor. In this case, we chose the friction factors as shown in Fig. 10b.

Figure 12 shows displacement and velocity histories at three selected points. The displacement of node 12 was considerably larger than that of node 1 because of tensile failure in the diagnostic structure. Once this failure occurred, the structure above the failure was in free flight, retarded only by the ground friction and the weight. The average permanent compression was ~4%, but near the base it was ~14%, indicating considerable damage.

8

```
┌──────────────────────────────────────────────────────┐
│  ┌─────────────────────┐                              │
│  │ Incremental          │      Known                  │
│  │ displacements        │                             │
│  │ Previous stress and  │                             │
│  │ strain states        │                             │
│  └─────────────────────┘                              │
│            │                                           │
│            ▼                                           │
│  ┌─────────────────────┐      ┌──────────────────┐   │
│  │ Incremental and total│◄─────│ Strain-displacement│  │
│  │ strains              │      │ relation          │   │
│  └─────────────────────┘      └──────────────────┘   │
│            │                                           │
│            ▼                                           │
│  ┌─────────────────────┐      ┌──────────────────┐   │
│  │ Total stresses       │◄─────│ Stress-strain     │   │
│  │                      │      │ relation          │   │
│  └─────────────────────┘      └──────────────────┘   │
│            │                                           │
│            ▼                                           │
│  ┌─────────────────────┐                              │
│  │ Internal forces      │                             │
│  └─────────────────────┘                              │
│            │                                           │
│            ▼                                           │
│  ┌─────────────────────┐      ┌──────────────────┐   │
│  │ Acceleration of      │◄─────│ External load     │   │
│  │ masses               │      │ history; external │   │
│  └─────────────────────┘      │ forces            │   │
│            │                  └──────────────────┘   │
│            ▼                                           │
│  ┌─────────────────────┐      ┌──────────────────┐   │
│  │ New incremental      │◄─────│ Boundary conditions│  │
│  │ displacements        │      │ Prescribed displ. │   │
│  └─────────────────────┘      └──────────────────┘   │
│            │                        ▲                  │
│            │                  ┌──────────────────┐   │
│            │                  │ Numerical         │   │
│            │                  │ integration       │   │
│            │                  └──────────────────┘   │
│            ▼                                           │
│  ┌─────────────────────┐                              │
│  │ Total displacements  │                             │
│  └─────────────────────┘                              │
└──────────────────────────────────────────────────────┘
```

Fig. 9.   Numerical algorithm for calculation of response over
a generic time increment.

COMMENTS AND CONCLUSIONS

This method of dynamic analysis of
emplacement structures appears to give reason-
able results when compared to limited experi-
mental data. It incorporates a friction
mechanism that couples the structure to the
surrounding soil. We found that the
coefficient of friction is the most critical
factor in determining the response; it
apparently varies considerably over the
structure (from 0.300 at the canister to 0.140

over the emplacement pipe). This indicates
that the actual friction mechanism needs to be
examined in greater detail.[4]

Additional investigation of the
deformation characteristics of the finite
elements is needed. At present, these do not
include an explicit collapse mechanism, and
attempts to include this in the calculation
were not successful. However, the comparison
with the experimental results indicates that
the present description of the deformation is
adequate for practical purposes.

9
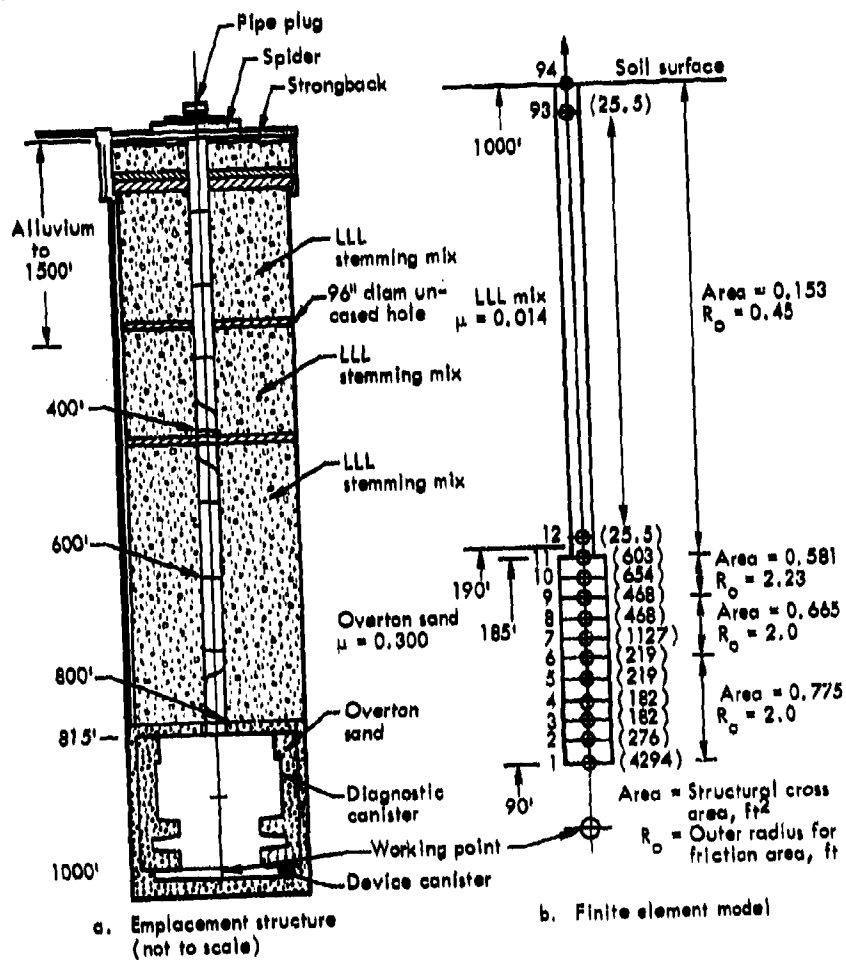
Fig. 10. Emplacement structure and finite element model. Numbers in parentheses indicate additional external nodal masses.
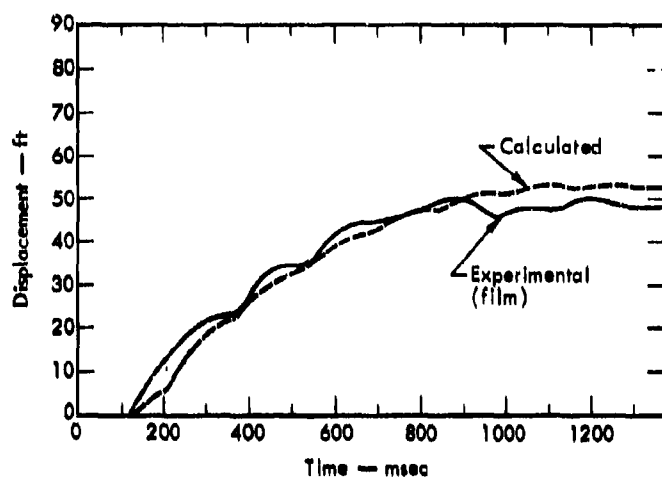
Fig. 11. Comparison of calculated and experimental results.
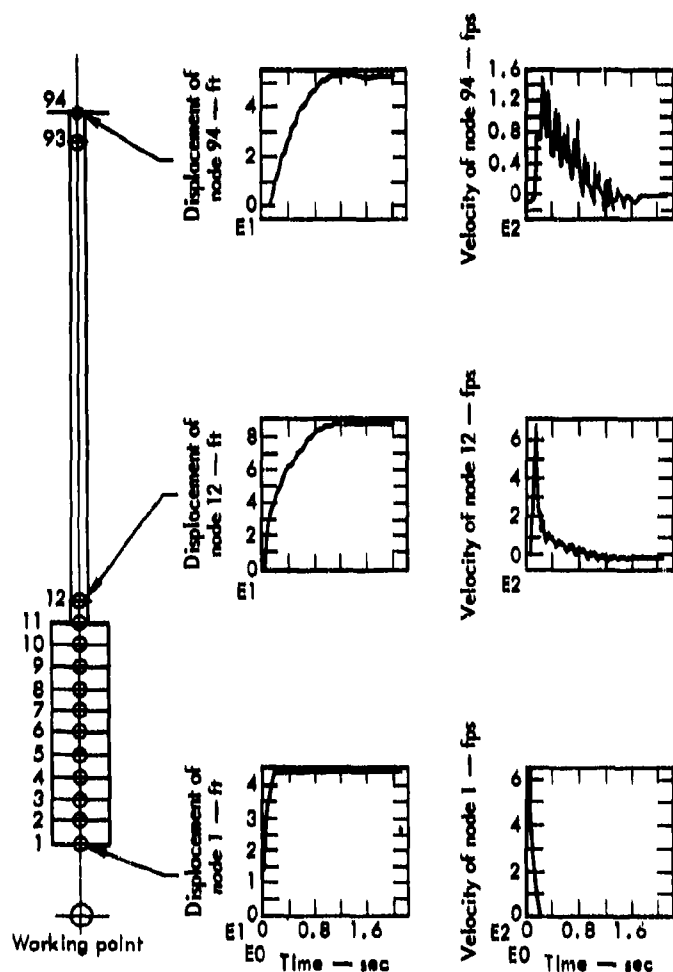
Fig. 12. Displacement and velocity histories at three points in the structure.

11

REFERENCES

Cited

1. M. Hartzman, <u>Comput. Struct.</u> <u>1/2</u>, 47 (1972).

2. E. Voltera, <u>Dynamics of Vibrations</u> (Charles E. Merril Books, Inc., Columbus, O., (1965), p. 86.

3. J. R. Smith, Lawrence Livermore Laboratory, personal communication.

4. A. Blake and M. Zaslawsky, <u>Behavior of Stemming Material Under Stress</u>, Lawrence Livermore Laboratory, Rept. UCRL-51034 (1971).

Uncited

1. J. Biggs, <u>Introduction to Structural Dynamics</u> (McGraw Hill Co., New York, 1964).

2. E. Witmer, H. Balmer, J. Leech, and T. Pian, <u>AIAA J.</u> <u>1</u> (8), 1848 (1963).

DISCUSSION

<u>Mr. Thomson (University of California)</u>: You have to assume some kind of soil velocity to take account of the spacing between the various masses as well as the time in your finite difference calculation. Is that right?

<u>Mr. Hartzman</u>: The soil velocity is given as input and is proportional to the stress while it's propagating through the soil.

VIBRATION ANALYSIS OF STRUCTURAL SYSTEMS

USING VIRTUAL SUBSTRUCTURES

Alex Berman

Kaman Aerospace Corporation
Bloomfield, Connecticut

A method is described in which substructure components of a structural system may be exactly represented within the equations of motion of the main structure. The method may be used to obtain forced responses or natural frequencies of the complete system.

INTRODUCTION

In many structural dynamics analyses, the most important results are the natural frequencies and normal modes of the structure because these indicate the frequencies and distribution of the maximum amplitude responses under operational conditions. This is not the case when the structure analyzed is a component of a structural system. When a system is vibrating at its natural frequency, the components are responding off-resonance to multiple exciting forces. There is no unique relationship between the response of a component as a part of a system and the modes of the component as an independent structure. The approach to component synthesis which is described in this paper avoids the common technique of using modes of the components as generalized coordinates of the system. The method presented here makes use of substructure response to forces at the interface coordinates and performs an exact reduction of this substructure to these coordinates. This results in a representation of the entire system where the influence of the substructures or components are exactly present, in effect, without a corresponding increase in the number of degrees of freedom. Thus, the designation "virtual substructures".

Detailed discussions of the reasons for component synthesis and descriptions of the characteristics of all the important contributions to the field have been very well covered by Hou[1] and Benfield, et al[2]. The major motivations for subsystem analysis are: (1) computer storage limitations or excessive execution times which prevent the analysis of the complete system; (2) separate components are analyzed at different sites or at different times; (3) it is desired to study variations in only portions of the structural system with considerations of efficiency preventing repeated analyses of the complete system.

The modal approach to component synthesis uses modes of the components as generalized coordinates of the system. Hurty[3] developed an excellent and a generally applicable technique using modes of the independent substructures. In addition to normal modes of the components, this method uses redundant interface constraint modes. Various simplified but related methods (see References 1 and 2) use different modes and somewhat different techniques. All the simpler methods which use modes of the independent components are subject to the same deficiency. The practical success of these methods must depend on how well a small number of the chosen modes can represent the response of the structural system. Since the actual response of each component may have little resemblance to the modes used as generalized coordinates, there can be significant errors in the derived characteristics of the system. Comparisons of various methods using various numbers of modes have been presented in Reference 2.

An improvement was made by Benfield and Hruda[4] when they added approximate interface loading (mass and stiffness) to each component before obtaining its modes, which are then more representative of the actual displacements of the system. Significant improvements of this technique over the simplified methods are reported in Reference 2 where accuracies approaching Hurty's method[1] are achieved.

The method of this paper might, at first, be considered to be an extension of the previously mentioned method. Instead of adding approximate interface loadings, exact quantities are used. The major difference is that, now, rather than solving for generalized coordinates to be used in an analysis of the structural system, any solution is a solution of the complete system since the characteristics of the other subsystems are exactly represented in the model. Because of the nature of the model, the quantities which are directly obtained are responses rather than natural frequencies and modes. The subsystems are linearly represented and include damping. The virtual representation of the subsystems is frequency dependent and this analysis leads to some general observations regarding the reduction of linear models.

This method is presented here primarily as an analytic tool, however, it appears that test or combined test and analysis applications may be developed.

NOMENCLATURE

C	Damping Matrix
K	Stiffness Matrix
M	Mass Matrix
Y	Mobility Matrix (= Z^{-1})
Z	Impedance Matrix (= $-\omega^2 M + (1 + ig)K$)
f	Force Vector
y	Displacement Vector
g	Structural Damping Coefficient
ω	Frequency of Excitation
Re( )	Real Part of
Im( )	Imaginary Part of

Subscripts

a,b,c	Refers to Substructure a,b,c
s	Refers to System
v	Refers to Virtual or Reduced System

Superscripts

-	Refers to Interface Coordinates
^	Refers to Non-Interface Coordinates
⌂	Refers to Coupling Between Interface and Non-Interface Coordinates
T	Transpose of Matrix
-1	Inverse of Matrix

BASIC CONSIDERATIONS

A structural system is a structure composed of discrete interconnected structural units. These units are called components or substructures. The entire system and each component are assumed here to be represented by discrete element linear mathematical models consisting of a stiffness matrix, K, a mass matrix, M, and a damping matrix. In this presentation, for sinusoidal motion, the damping is represented in the form igK where g is the commonly used structural damping coefficient. The procedures apply to any linear form of the equation of motion, however.

The response of the system or any component at one steady-state frequency may be written in the form:

$$Zy = f \qquad (1)$$

where y and f are complex vectors representing the displacement and applied force amplitudes at each coordinate of the structure. Z is the complex "impedance" matrix of the structure and is of the form

$$Z = -\omega^2 M + (1 + ig)K \qquad (2)$$

where ω is the frequency of the motion. The impedance matrix can be called the model of the system. The inverse of Z will be called the "mobility" matrix, Y, resulting in the relationship

$$y = Yf \qquad (3)$$

14

The matrices Z, Y, M, K are all symmetric. There are no restrictions on whether the structures are constrained or free, except that for the free condition at $\omega = 0$, the mobility matrix, Y, is not defined since K is singular.

The forces, displacements, and coordinates may be considered to be generalized quantities with no loss in applicability of the equations. In the applications considered here, however, the "forces" are either ordinary forces or moments and the displacements are either translational or rotational motions of physical points on the structure. There is no necessary ordering of the elements of the matrices and they may be rearranged as desired providing that the corresponding rows and columns and the elements of y and f are also consistently rearranged.

The impedance and mobility matrices, while inverses of each other, have surprisingly different physical significances. The impedance matrix is wholly dependent on the specific model formulation. Changes in the number and location of coordinates will change the elements of this matrix. This matrix can be more-or-less intuitively derived from the physical characteristics of the structure and has been called an "intuitive" quantity (See Reference 4 for a discussion of these concepts.). The elements of the inverse, however, cannot physically depend on the locations of the other coordinates in the model. This matrix is a "measurable" quantity and the elements represent the deflection at a point due to a force at a point. These are quantities which all valid models of the same structure must yield.

The contributions of physical quantities to the impedance matrix are simply additive. That is, if all necessary coordinates are represented in the matrices, the addition of spring, inertial or damping characteristics simply requires that the values of these parameters be added to the appropriate elements of the matrix.

These concepts will be applied in the following paragraphs to the analysis of structural systems.

THE PARTITIONS OF THE IMPEDANCE MATRIX

Consider two structures a, b, which are parts of a structural system as illustrated schematically in Figure 1.
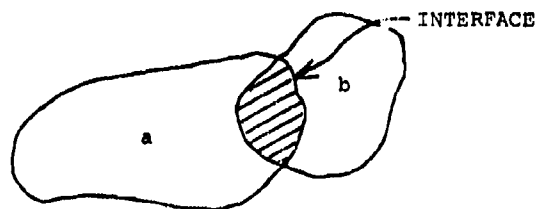
Figure 1. Structural System Composed of Two Substructures

The coordinates of the structures are established or transformed so that the common points (or interface coordinates) are compatible. Each structure has an independent equation of the form

$$z_a y_a = f_a \qquad (4a)$$

$$z_b y_b = f_b \qquad (4b)$$

It is convenient to rearrange and partition the elements of the impedance matrices in the following fashion:

$$z_a = \begin{vmatrix} \hat{z}_a & \hat{\bar{z}}_a \\ \hat{\bar{z}}_a^T & \bar{z}_a \end{vmatrix} \qquad (5a)$$

$$z_b = \begin{vmatrix} \bar{z}_b & \hat{\bar{z}}_b \\ \hat{\bar{z}}_b^T & \hat{z}_b \end{vmatrix} \qquad (5b)$$

where $\bar{z}_a$ and $\bar{z}_b$ are the partitions of the corresponding independent structures at the common system interface. The impedance of the system, then, may be exactly formed by superimposing these matrices as follows:

$$z_\omega = \begin{vmatrix} \hat{z}_a & \hat{\bar{z}}_a & 0 \\ \hat{\bar{z}}_a^T & \bar{z}_a + \bar{z}_b & \hat{\bar{z}}_b \\ 0 & \hat{\bar{z}}_b^T & \hat{z}_b \end{vmatrix} \qquad (6)$$

These relationships have been written as though the substructures are rigidly

15

attached, however, there is no loss in generality here for elastically coupled substructures. The elastic members may either be considered to be part of one of the substructures, or divided between them, or they may be treated as a separate component of the system.

It is the objective here to form the matrix Z_s so that it is no larger in order than that of the main component, a. If a valid model of substructure b could be formed using only the interface coordinates, the impedance of the system could be written:

$$Z_s = \begin{vmatrix} \hat{Z}_a & \hat{\hat{Z}}_a \\ \hat{\hat{Z}}_a^T & \bar{Z}_a + Z_v \end{vmatrix} \quad (7)$$

where Z_v is called the virtual impedance or virtual model of the substructure. This matrix then would represent the system with no more matrix elements than is required to represent one component. The only portion of the matrix which is changed is that portion representing the interface coordinates.

This concept readily extends to a structural system of several components (as in Figure 2, for example).
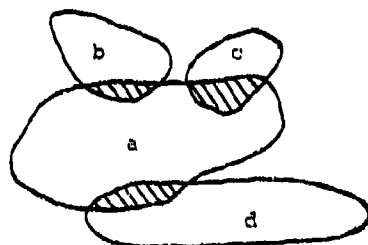
Figure 2. A Structural System of Several Subsystems

The impedance matrix of substructure a may be partitioned as follows:

$$Z_a = \begin{vmatrix} \hat{Z}_a & \cdot & \cdot & \cdot \\ \cdot & \bar{Z}_{ab} & \cdot & \cdot \\ \cdot & \cdot & \bar{Z}_{ac} & \cdot \\ \cdot & \cdot & \cdot & \bar{Z}_{ad} \end{vmatrix} \quad (8)$$

Where the off-diagonal submatrices represent the transfer impedances between the non-interface coordinates and the interface coordinates and between the various interfaces themselves. This matrix is formed simply by rearranging the elements of the impedance of component a. If each of the components b, c, d may be represented by impedance matrices only at their respective interfaces, then the entire system may be written as:

$$Z_s = \begin{vmatrix} \hat{Z}_a & \cdot & \cdot & \cdot \\ \cdot & \bar{Z}_{ab} + Z_{vb} & \cdot & \cdot \\ \cdot & \cdot & \bar{Z}_{ac} + Z_{vc} & \cdot \\ \cdot & \cdot & \cdot & \bar{Z}_{ad} + Z_{vd} \end{vmatrix} \quad (9)$$

where the off-diagonal and the non-interface submatrices of Z_a do not change. This approach is quite readily extended to cover more complex arrangements with no loss in generality.

The question of determining the virtual impedance Z_v is investigated in the next section.

REDUCED IMPEDANCE

The reduction of the static stiffness matrix to any set of coordinates has been performed in an exact manner by Turner, et al[6]. When the stiffness matrix is partitioned as above:

$$K = \begin{vmatrix} \bar{K} & \hat{K} \\ \hat{K}^T & \hat{K} \end{vmatrix} \quad (10)$$

the apparent stiffness matrix seen at the interface is

$$K_v = \bar{K} - \hat{K} \hat{K}^{-1} \hat{K}^T \quad (11)$$

A similar, but not exact, reduction of the mass matrix has been derived by Guyan[7]:

$$M_v = \bar{M} + \hat{K} \hat{K}^{-1} \hat{M} \hat{K}^{-1} \hat{K}^T \quad (12)$$

These reduced quantities are used in Reference 4 to obtain the interface-loaded component modes as discussed above.

16

When considered from the point of view of a reduction which must be a good approximation over a relatively wide frequency range, there are several apparent deficiencies in this process: (1) the resulting linear model can have only as many natural frequencies as there are interface coordinates (unless additional degrees of freedom are added) thus, if the number of interface coordinates is relatively small, one would not expect adequate frequency response characteristics of the reduced model; (2) the Guyan reduction can be expected to be most valid when the chosen coordinates are physically representative of the structure and since interface coordinates are usually inappropriately distributed, this reduction can be expected to be of limited applicability; (3) the type and distribution of the appropriate damping parameter is not obvious.

A more general approach to the reduction will now be presented. A requirement for a valid analytical model is that it correctly predict the responses of the structure to applied forces. Thus, a reduced model must predict the same responses to forces at the retained coordinates as the full model, that is to say, the retained elements of the mobility matrix must remain invariant with respect to the model changes.

Consider the impedance matrix of a substructure and its inverse, partitioned so the coordinates to be retained (the interface coordinates) are in the upper left-hand corner.

$$Z = \begin{vmatrix} \overline{Z} & \hat{Z} \\ \hat{Z}^T & \hat{z} \end{vmatrix} \tag{13}$$

$$Y = Z^{-1} = \begin{vmatrix} \overline{Y} & \hat{Y} \\ \hat{Y}^T & \hat{y} \end{vmatrix} \tag{14}$$

If Z_v is the virtual (or reduced) impedance, then, using the usual expression for a partitioned inverse:

$$Z_v \equiv \overline{Y}^{-1} = \overline{Z} - \hat{Z} \hat{z}^{-1} \hat{Z}^T \tag{15}$$

which is an exact representation of the full size model at the reduced coordinates. This equation is identical in form to Equation (11) which may be derived in the same way, except that here the dynamic response rather than

only the static response is preserved. Each Z in Equation (15) is made up of mass, stiffness, and damping matrices, e.g., $-\omega^2 M + (1 + ig)K$.

In order to better illustrate the significance of this reduction, consider the simple case of a full size model having a diagonal mass matrix and no damping. Equation (15) then becomes (this equation has also been obtained in Reference 8):

$$Z_v = \overline{K} - \omega^2 \overline{M} - \hat{K}(\hat{K} - \omega^2 \hat{M})^{-1} \hat{K}^T \tag{16}$$

Note that for $\omega = 0$, $Z_v = K_v$ (as in Equation 11). If Z_v is itself assumed to be of the form $K_v - \omega^2 M_v$ and K_v is taken from Equation (11), Equation (16) becomes

$$M_v = -\frac{1}{\omega^2} (Z_v - K_v) = \overline{M} + \hat{K} \hat{K}^{-1} \hat{M}(I$$
$$- \omega^2 \hat{K}^{-1} \hat{M})^{-1} \hat{K}^{-1} \hat{K}^T \tag{17}$$

This reduced mass matrix will vary with ω. At $\omega = 0$, Equation (17) becomes the Guyan mass reduction. It is not immediately apparent how important this frequency dependence will be. When the constant mass matrix is used, the reduced system will have only as many natural frequencies it has coordinates. When the frequency range of, say, the first half of these natural frequencies is less than the range of interest, it is apparent that such a model is inadequate. When the reduction is made to a relatively small number of interface coordinates which are typically distributed on a portion of the periphery of the structure, the situation can be expected to be much worse.

The mass given by Equation (17) is exact under the simplifying assumptions made there. It is not suggested that this formulation necessarily be used in practice, but was presented to point out the frequency dependence of the reduced mass matrix.

The next section shows how the model may be obtained numerically using a more general large model and including damping.

NUMERICAL SUBSTRUCTURE REDUCTION

At first thought, one might consider writing the more general form of the impedance of the full size model of the substructure and then substituting into Equation (15) and attempting to identify the matrices of the reduced

model. This procedure would be quite laborious and also unnecessary unless one were searching for an analytical approximation. There is no need to obtain separately identified mass, stiffness, and damping matrices since what is required is the reduced impedance.

The most direct way to obtain this quantity at each frequency is as follows: (1) Form the substructure impedance matrix; (2) Obtain its inverse; (3) Form a matrix of the elements corresponding to the interface coordinates; (4) Invert this matrix to obtain the virtual impedance matrix. These operations simply implement the identity, $Z_v = Y^{-1}$ as in Equation (15). When the number of degrees of freedom of the substructure is large and the inversion in Step (2) above, is not economical, then a modal representation of the full substructure may be the most efficient means of obtaining the mobility matrix of the interface coordinates at each frequency. This matrix, when inverted would be the virtual impedance of the substructure. In using the modal approach at this point, one must be careful that sufficient modes are used to obtain the mobility accurately at each frequency over the range of interest.

While it is true that there is no need to interpret the virtual impedance in terms of mass, stiffness and damping matrices, such an interpretation can shed some light on the general study of reduced models of linear systems. If the complete model of the substructure is written as

$$Z_b = -\omega^2 M_b + (1 + ig)K_b \qquad (18)$$

and if one assumes a reduced model of corresponding form

$$Z_v = -\omega^2 M_v + K_v + iC_v \qquad (19)$$

then M_v and C_v may be obtained from:

$$M_v = -\frac{1}{\omega^2} [Re(Z_v) - K_v] \qquad (20)$$

and

$$C_v = Im(Z_v) \qquad (21)$$

where Z_v has been computed as above and K_v has been obtained from Equation (11). It should be noted that no assumption is made that $C_v = gK_v$ as in the full size model. Such an assumption would, in general, be contradictory to Equation (21). This interpretation in terms of intuitive physical quantities is more-or-less arbitrary. A logical argument could be made for a constant mass matrix and a frequency dependent stiffness matrix or any other combination. However, if the form of Equation (19) is assumed and if K_v is assumed to be independent of ω, then Equations (20) and (21) follow.

From previous discussions, it is expected that M_v (from Equation 20) will vary with frequency. It is further to be expected that C_v will not be always proportional to K_v. These presumptions are borne out in the numerical illustration presented.

APPLICATION CONSIDERATIONS

The following procedure is suggested to determine the frequency response of a system. (1) Choose one of the components to be the main structure (as "a" in Figure 2). (2) Arrange the coordinates of the impedance matrix associated with this structure so that all the interface coordinates are grouped as in Equation (8). (3) At each frequency of interest, determine the virtual impedance of the substructures (see previous section) and add as in Equation (9). (4) Solve this system for its response.

It is not necessary to have any one substructure as the main structure, as in (1) in the previous paragraph, but all structures may be reduced to models at the interfaces only. This would remove the first row and column of submatrices in Equation (9). This variant would be useful when actual responses are not required but natural frequencies of the system are the objective.

If it is desired to obtain natural frequencies of the system, this can be obtained from the frequency response characteristics just as would be done with test data, for example, by observing frequencies of maximum response or by applying the method of Kennedy and Pancu[9].

When the number of degrees of freedom of the system, Equation (9), is relatively small, the direct inversion of this matrix would be the most economical means of determining the response of the system. If many degrees of freedom make this approach impractical then such techniques as a modal analysis at each frequency or a correction method for the inverse of a modified matrix should be considered. The details of these considerations are outside the scope of this paper.

18

The obvious situation for direct applicability of these procedures is where several medium size components are interfaced at a relatively small number of coordinates. The virtual models of each substructure would be obtained independently over the frequency range of interest and then the responses of the system could be obtained with relative ease and with confidence.

ILLUSTRATIVE COMPUTATIONS

As an illustration of the techniques discussed, a simple 10-degree-of-freedom lumped parameter longitudinal model was analyzed as a substructure. Figure 3 shows the model and indicates the masses and stiffnesses. The structure was considered to be unconstrained with a structural damping coefficient of 2%. The structure was assumed to interface another component at masses 3 and 4. Thus, a 2x2 virtual impedance matrix was calculated versus frequency. The reduced stiffness matrix is:

$$K_v = \begin{vmatrix} .4635 & -.4635 \\ -.4635 & .4635 \end{vmatrix}$$

and the reduced mass matrix at $\omega = 0$ is

$$M_v(\omega = 0) = \begin{vmatrix} .4226 & 0 \\ 0 & .3763 \end{vmatrix}$$
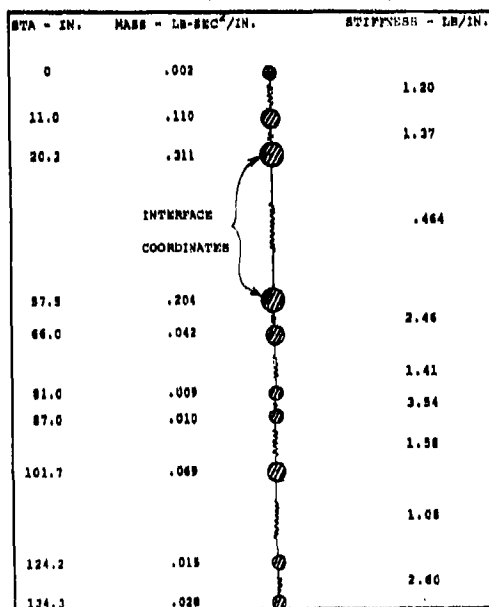
Figure 3. Longitudinal Model

The reduced stiffness is considered to be constant, as discussed above, to be compatible with the static solution. Because the interface coordinates are adjacent to each other, the reduced mass matrix remains diagonal, which fact makes the interpretation of the results intuitively more understandable.

Figure 4 illustrates the response of mass 3 to a force at mass 3 versus frequency, up through the 3^d non-zero resonance. The dashed line on this figure shows the response of the system which is predicted using the model of K_v, $M_v(\omega = 0)$, and $g = .02$ as would be determined by the usual reduction methods. Notice that, in this case, the usual method is completely inadequate for predicting response except at very low frequencies.

Figure 5 illustrates the elements of the virtual mass matrix as a function of frequency. This data was obtained by the method suggested above for obtaining Z_v and then using Equation (20). At $\omega = 0$, these values agree with the Guyan reduction. The damping matrix was obtained using Equation (21), i.e., using the imaginary part of the virtual impedance. At frequencies up to the vicinity of the first non-zero resonance the C matrix was nearly proportional to the K_v matrix with the factor of .02 which was the original form of the damping. However, at higher frequencies this proportionality does not exist. On Figure 6 is shown a plot of $(C_v)_{11}/(K_v)_{11}$ and $(C_v)_{22}/(K_v)_{22}$. It is seen that these quantities vary widely and above the lowest frequencies do not anywhere approach the nominal value of .02.

The model represented by K_v (above), M_v (Figure 5), C_v (Figure 6) exactly represents the correct response of the substructure as represented by the 10-degree-of-freedom model and illustrated in Figure 4. This, of course, must be true since the correct response is used to compute the virtual impedance.

This impedance may now be directly added to any other substructure interfaced at masses 3 and 4 as previously discussed to obtain the exact frequency response of the structural system.
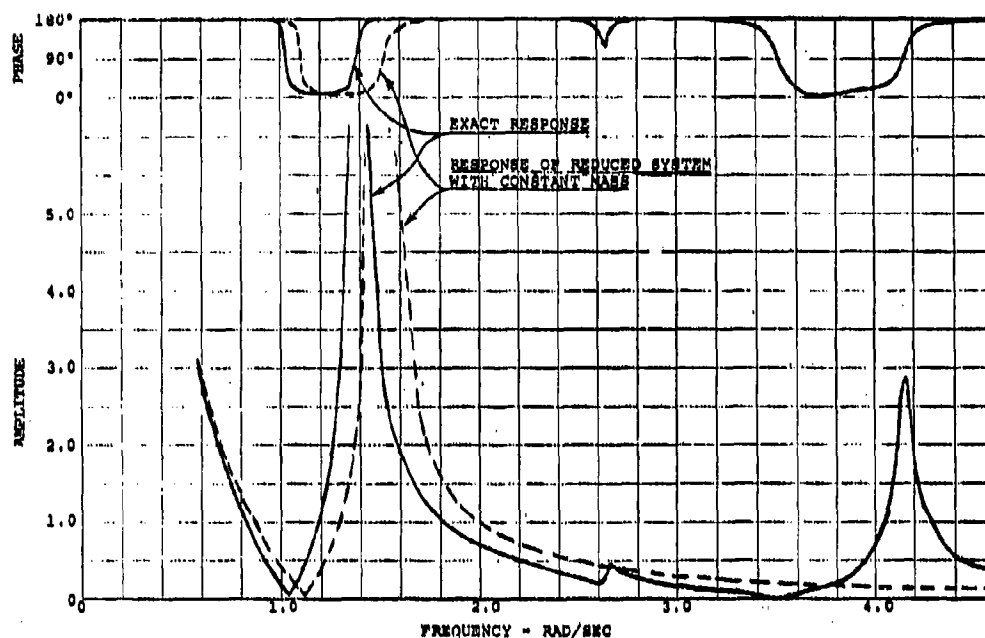
Figure 4. Response of Mass 3 to Force at Mass 3
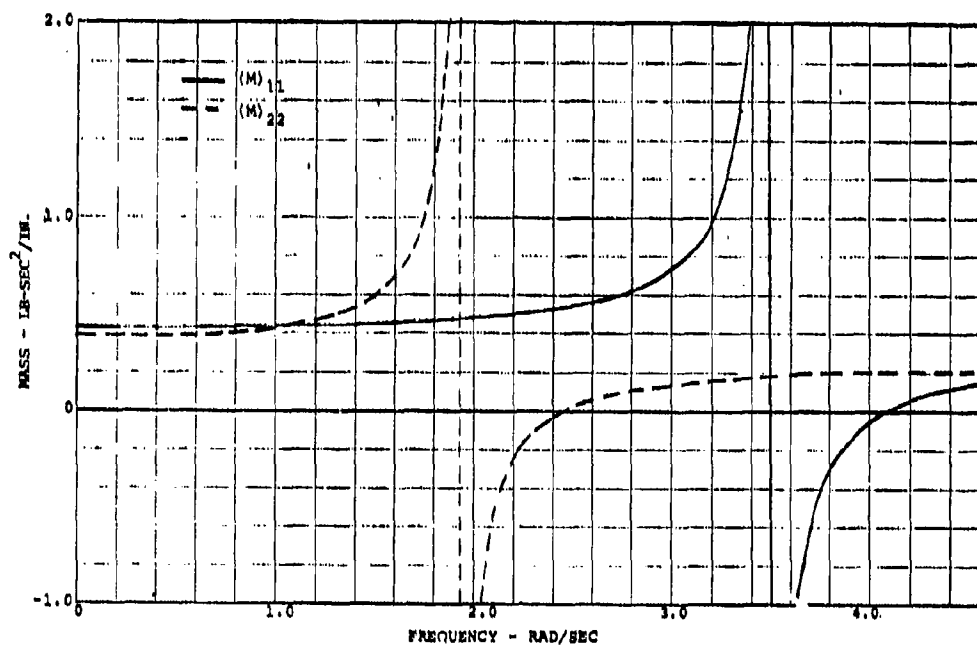
Figure 5. Virtual Mass Variation With Frequency

20
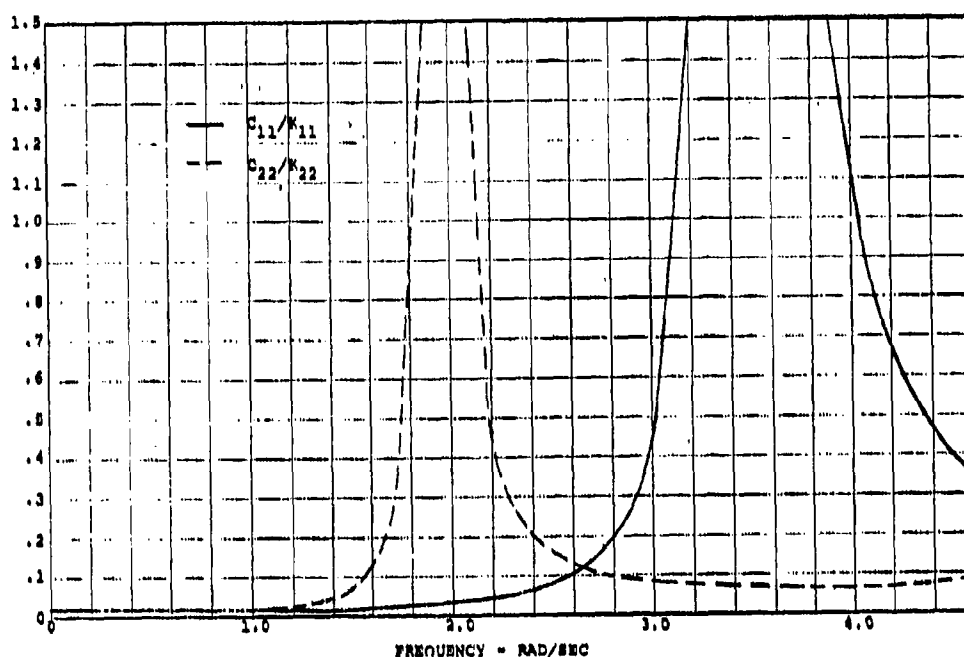
Figure 6. Damping Coefficients Versus Frequency

CONCLUDING REMARKS

An analytical technique has been described which allows an exact representation of substructures within the model of the main structure.

The method is directly applicable where the frequency response at the interface coordinates of each of the substructures may be obtained independently and where the total number of interface coordinates is relatively small. For other situations, variants of this procedure should be considered.

This method can be an efficient means of studying the effects of alternate substructures or variations in substructures on the response of a structural system.

It has been discussed and illustrated that any constant mass reduction technique is inadequate when the number of reduced coordinates is small and when these coordinates are not physically representative of the structure.

The virtual impedance of a structure at its interface (or any reduced set of coordinates) may be interpreted in terms of a constant stiffness matrix and mass and damping matrices which vary with frequency.

REFERENCES

1. Shou-nien Hou, "Review of Modal Synthesis Techniques and a New Approach", Shock and Vibration Bulletin #40, Dec. 1969.

2. W.A. Benfield, C.S. Bodley, and G. Morosow, "Modal Synthesis Methods", Presented at the Space Shuttle Dynamics and Aeroelasticity Working Group Symposium on Substructuring, Marshall Space Flight Center, Alabama, Aug. 30-31, 1972.

3. W.C. Hurty, "Dynamic Analysis of Structural Systems by Component Mode Synthesis", Jet Propulsion Lab. Technical Report 32-530, Jan. 15, 1964.

4. W.A. Benfield and R.F. Hruda, "Vibration Analysis of Structures by Component Mode Substitution", AIAA Journal, Vol. 9, No. 7, July 1971.

5. W.G. Flannelly and A. Berman, "The State of the Art of System Identification of Aerospace Structures", Presented at ASME 93rd Winter Annual Meeting, New York, New York, Nov. 26-30, 1972, Published in Symposium Volume: "System Identification of Vibrating Structures: Mathematical Models From Test Data".

21

6. M.J. Turner, et al, "Stiffness and Deflection Analysis of Complex Structures", J.A.S., Vol. 23, 805-823 (1956).

7. R.J. Guyan, "Reduction of Mass and Stiffness Matrices", AIAA Journal, Vol. 3, No. 2, 380 (1965).

8. R.M. Mains, "Results of Comparative Studies on Reduction of Size Problem", Shock and Vibration Bulletin #42 (Part 5), 135-141, Jan. 1972.

9. C.C. Kennedy and C.D.P. Pancu, "Use of Vectors in Vibration Measurement and Analysis", Journal of the Aeronautical Sciences, Vol. 14, No. 11, Nov. 1947.

DISCUSSION

Mr. Thomson (University of California): Am I correct in assuming that this method of yours is one in which an equivalent impedance is calculated for the interface points?

Mr. Berman: Yes, In effect an entire structure is modeled only at the interface points. We do this when we are not interested in specifically getting the response of that particular component. The force is at other points if we do a modal analysis, for example.

22

MULTIDEGREE-OF-FREEDOM ELASTIC SYSTEMS HAVING
MULTIPLE CLEARANCES

by

Richard C. Winfrey
Project Engineer
Burroughs Corporation
Westlake Village, California 91360*

A computer program has been written to aid in the design and analysis of multidegree-of-freedom elastic systems with clearances. The use of finite element methods has permitted the program to be applied to a variety of problems. A simple algorithm is described for monitoring and directing the computations as the elastic system changes due to the clearances. A cam-driven valve train and an impact damper are shown as examples.

INTRODUCTION

The investigation into the dynamic behavior of machinery in general and mechanisms in particular has recently led to the inclusion of elastic deformations in the modeling of mechanisms. These deformations are caused by both inertial and externally applied forces. The mechanism is typically modeled using finite element methods,[1-3] and the resulting equations of motion are numerically integrated. More recently, the effect of clearances and impact in mechanisms has been studied in an effort to obtain a more realistic mathematical model of a piece of machinery. Dubowsky[4] reported on the affect of clearances, but he was more concerned with the modeling of a single joint rather than a complete mechanism.

The modeling and analysis of a complete mechanism has been described previously by this author; however, the method was limited to the case where one member of each impact pair had its motion completely specified as a function of time. The cam-driven valve train, shown in Figure 1, was used as an example; the effect of a clearance at the cam and at the valve seat was discussed. The computer program described by Reference 5 has been modified to eliminate the previous limitation, and it is now possible to model the impact between any two machine members undergoing arbitrary motion. The method for improving the computer program consisted of using conservation of momentum just before and just after initial contact of an impact pair. The primary intention here is to demonstrate this more general method of solution by investigating the same cam-driven valve train, using four clearances instead of the previous two, and then by studying the behavior of an impact damper.

Figure 1. Cam-Driven Valve Train With Harmonic Cam.

* Formerly, Mechanical Engineer, Naval Civil Engineering Laboratory, Port Hueneme, California.
** One is arbitrarily added because it is not convenient to have a configuration number of 0.
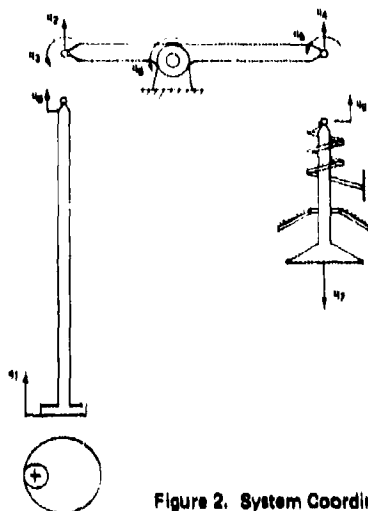
Figure 2. System Coordinates.
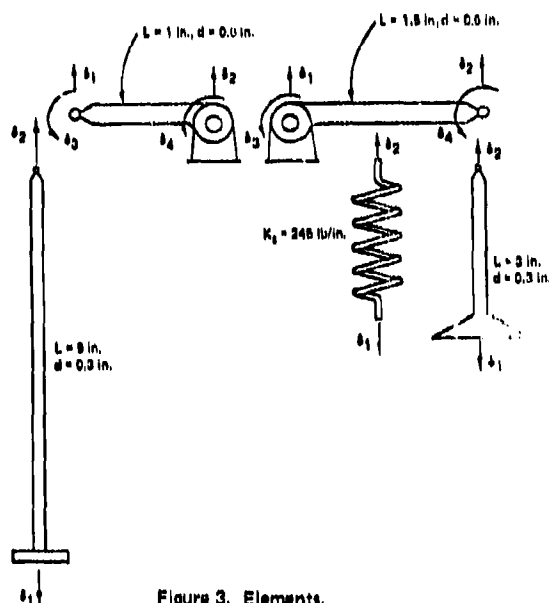
Figure 3. Elements.

CAM-DRIVEN VALVE TRAIN

The cam-driven valve train, which contains nine degrees of freedom and four clearances (Figure 1), will be used as the first example. The finite element model is shown in Figure 2, and the elements are shown in Figure 3. A cam profile that causes sinusoidal motion was arbitrarily chosen for simplicity, and, similarly, the cam was arbitrarily chosen to turn at a constant angular velocity. Both the cam and valve seat were assumed to have infinite mass and stiffness. This is not a requirement of the present program, but it was required in Reference 5; thus, the assumption was retained so as to provide continuity between results.

Control of the program is accomplished by continuously monitoring displacements and forces at each of the clearances—i.e., cam—push rod, push rod—rocker arm, rocker arm—valve stem, and valve—valve seat. The system exists as a unique structural configuration, depending on which member of the system is in contact and which is not. The total number of possible configurations is given by

$$C = 2^n$$

where C = number of configurations

n = number of clearances (four for this case)

A systematic method of keeping track of the various configurations can be obtained by using the table of binary numbers shown in Table 1. Note that the number of the configuration is equal to one plus the decimal equivalent of the column of binary numbers below it. A zero in the table means that there is no contact at the corresponding clearance. Hence, the displacement of each member of the impact pair must be monitored after each numerical integration time step to check for possible interference (i.e., contact). Similarly, a one in the table indicates contact at a clearance, and, hence, the force between members must be monitored to see if separation has occurred (the sign convention requires that forces at a clearance be positive to maintain contact). For example, if

Table 1. Configuration Matrix

Clearances	Configuration Number															
	1	2	3	4	5	6	7	8	9	10	11	12	13	14	15	16
Cam–pushrod	0	1	0	1	0	1	0	1	0	1	0	1	0	1	0	1
Push rod—rocker arm	0	0	1	1	0	0	1	1	0	0	1	1	0	0	1	1
Rocker arm—valve stem	0	0	0	0	1	1	1	1	0	0	0	0	1	1	1	1
Valve—valve seat	0	0	0	0	0	0	0	0	1	1	1	1	1	1	1	1

24
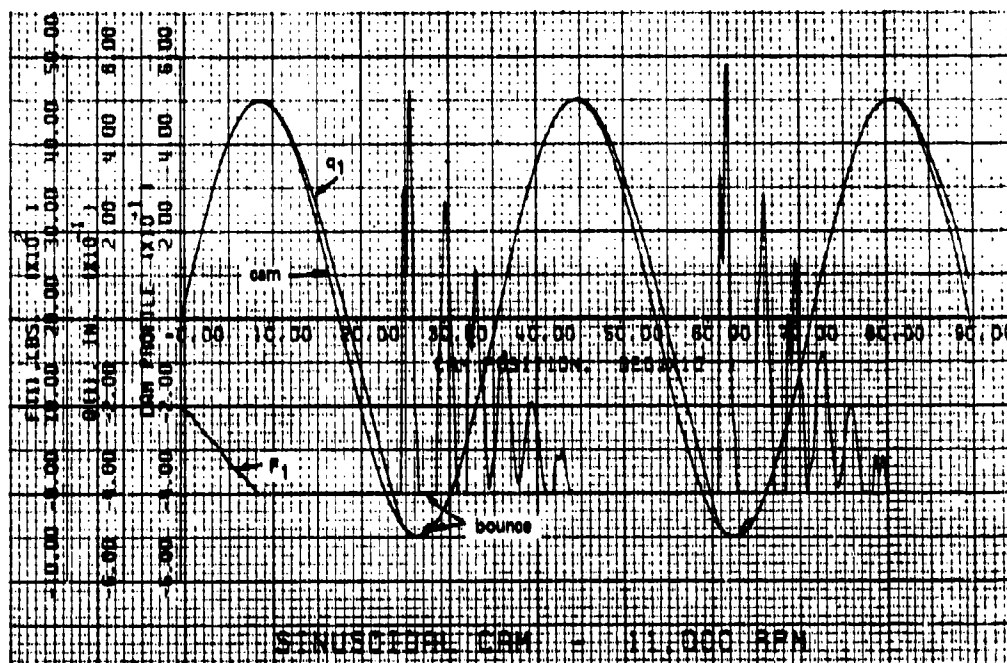
Figure 4. One Clearance.

the system is in contact at the cam and at both ends of the rocker arm, but is not in contact at the valve seat, then the binary column is

1
1
1
0

The decimal equivalent of this column is 7; after adding 1, the system is in configuration number 8, and the program is told to monitor the force at clearances 1, 2, and 3 and to monitor the displacements at clearance 4. Now, assume that the force at the cam becomes negative, and that separation occurs. The one in the first row changes to a zero, making the equivalent decimal number 6. Thus, the program jumps to configuration 7 and begins to monitor forces and displacements according to the seventh column. The computer algorithm to perform this process is quite simple and general. Also, the program generates the binary table at the beginning of execution on the basis of the number of clearances specified by the programmer.

Figure 4, which is based on the computer program of Reference 5, shows the force and displacement of the push rod with q_2 and q_6 pinned together, q_4 and q_0 pinned together, and the valve seat removed. It can be seen that the push rod bounces several times before remaining on the cam, and that it actually bounces once more because of residual high frequency oscillations just before the major separation.

Separation is permitted at each end of the rocket arm in Figure 5, and in Figure 6 the valve seat is also included. In an attempt to clarify the results, the displacement curves were offset by a constant distance of 1 inch, 2 inches, and 3 inches. Also, the forces were plotted as $-F_1$, $+F_2$, $-F_7$ plus a constant, and $+F_4$ plus the same constant. It is obvious that a great deal is going on at once even in this relatively simple system. The idea in interpreting the results shown is to follow a displacement curve of interest. However, because of the resolution of the plotter, it is not always possible to detect a separation. Thus, one needs to also keep an eye on the force curves since they go to zero when separation occurs. In each set of displacement curves, the cam profile is superimposed as a reference for the displacement curves.

IMPACT DAMPER

A second example that can be used to demonstrate the program is the impact damper, which contains only two clearances. However, each of these clearances involves a fixed off-set. This interesting device is at least 28 years old,[5] and more recently has been the subject of a number of publications.[7-10] The most common approach to analyzing the impact damper has been to use the concept of coefficient of restitution and to assume two impacts occurring symmetrically during each cycle of the forcing frequency. The question of stability has been examined at least in part on the validity of this last assumption.

25
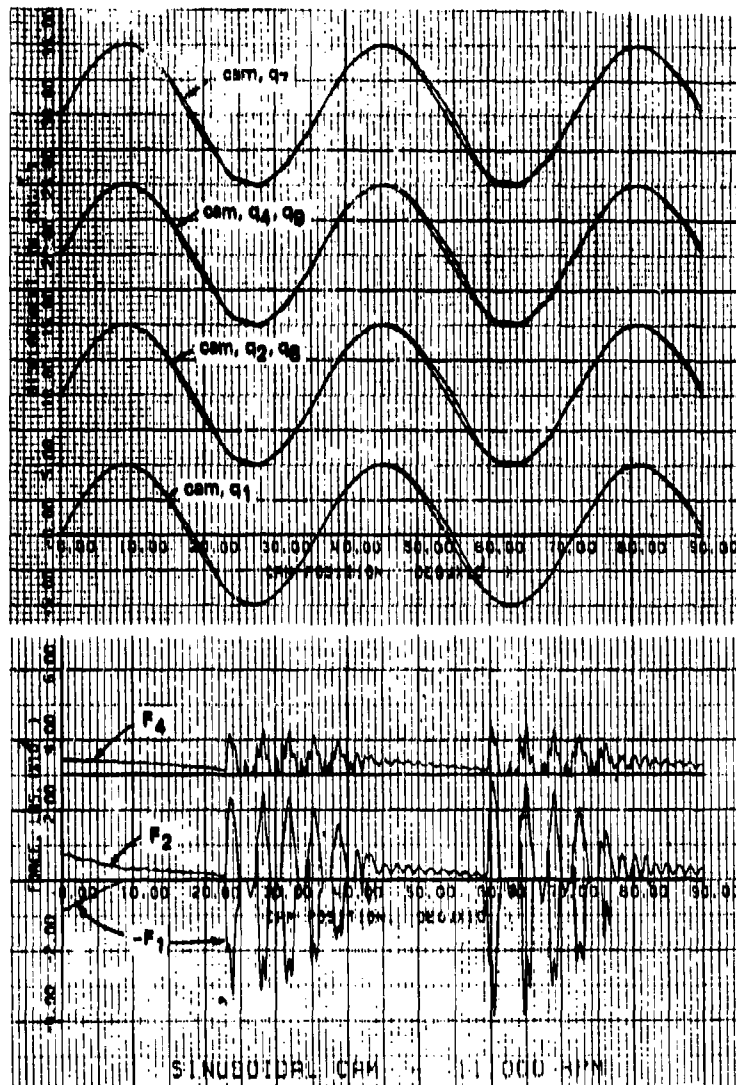
Figure 5. Three Clearances.
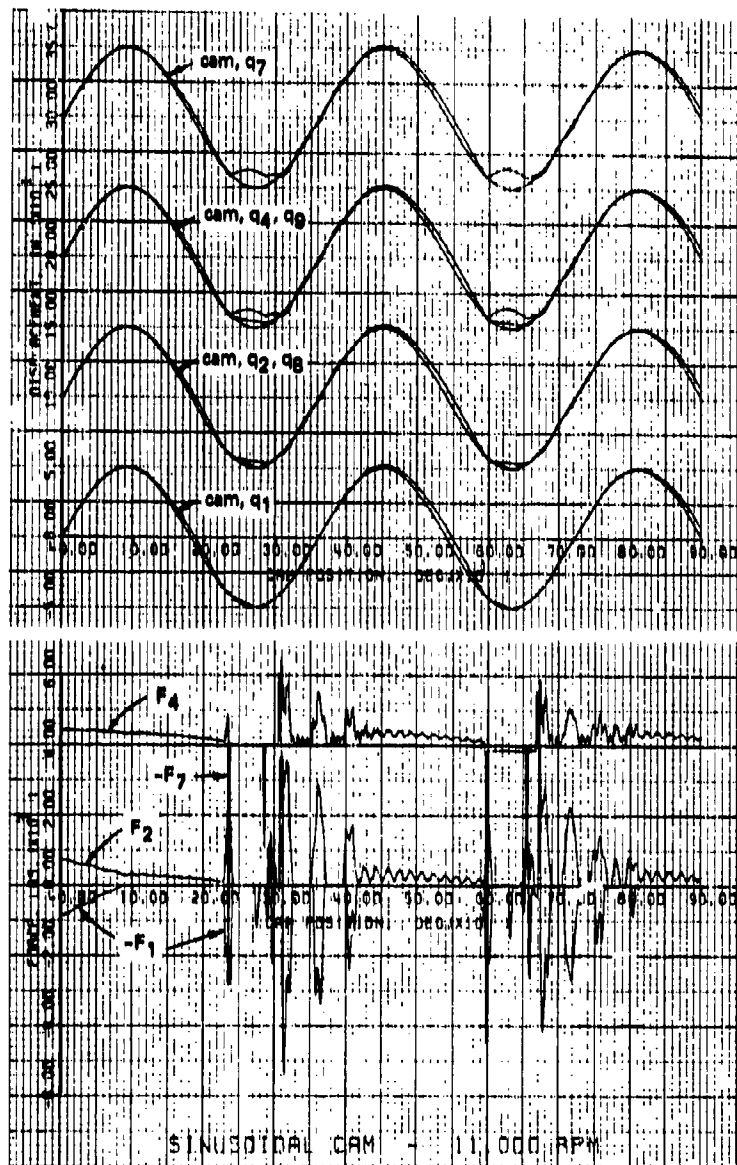
Figure 6. Four Clearances.

27
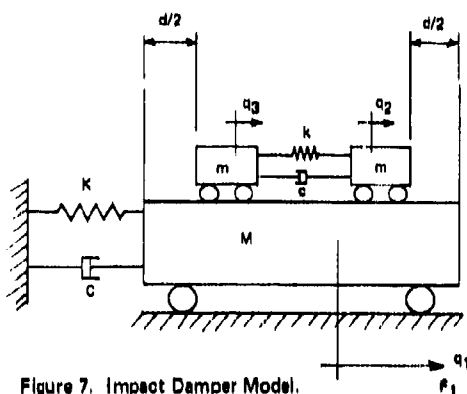
Figure 7. Impact Damper Model.

Figure 8. Damped Response for d/2 = 5 inches.

The system to be analyzed is shown in Figure 7, where the conventional ball has been replaced by a two degree-of-freedom spring-mass-damper system. It has been found experimentally[3] that the friction between the ball and the container has negligible effect on the total motion, and, thus, it is assumed that the "ball" in Figure 7 rolls without friction on the larger mass, M.

The coefficient of restitution is defined in terms of the relative velocity of two bodies just before impact and just after impact; thus, one is permitted to ignore what happens *during* impact. However, as the total gap, d, is decreased, the time during impact becomes a larger percentage of the total time, and, thus, the concept of coefficient of restitution becomes less valid. It was decided to investigate the effect of impact time by using a "ball" which was relatively soft. In this way, impact times of up to 15% of the total time would be obtained for smaller values of d.

The values for the constants used in Figure 7 are as follows:

$$M = \frac{100}{g} \text{ (lb-sec}^2/\text{in.)}$$

$$C = 2\xi_1 \sqrt{KM} \text{ (lb-sec/in.)}; \xi_1 = 0.05$$

$K = 10.0$ (lb/in.)

$$m = \frac{5}{g} \text{ (lb-sec}^2/\text{in.)}$$

$k = 50$ (lb/in.)

$$c = \xi_2 \sqrt{k(2m)} \text{ (lb-sec/in.)}; \xi_2 = 0.19$$

$$F_1 = K \sin \omega t \text{ (lb)}; \omega = \sqrt{\frac{K}{M}} \text{ (rad/sec)}$$

A value for c was determined through modal damping. As previously stated, zero damping was assumed for the rigid body mode shape ($q_2 = q_3 = 1$), and $\xi_2 = 0.19$ was used for the elastic mode shape ($q_2 = -q_3 = 1$) so as to give a coefficient of restitution of approximately 0.35.

For $\xi_1 = 0.05$, the maximum amplitude of oscillation is ± 10.0 inches. Figure 8 shows the system behavior when started from rest with d/2 = 5 inches. The amplitude built up until the damper was contacted. There was a slight overshoot before the system settled into a constant, steady motion with a peak amplitude of about ± 3.2 inches. (It should be pointed out that only the peak values from the computer run were plotted in Figures 8 through 10; the lines in between were drawn as either being straight or approximately sinusoidal.) Next, d/2 was
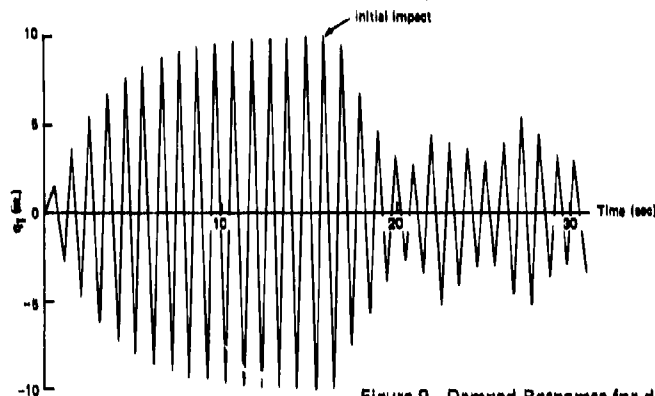
Figure 9. Damped Response for d/2 = 9.9 inches.

28

set at 9.9 inches, with the result shown in Figure 9. Again, the amplitude was quickly reduced once the impact damper was contacted, but this time, a constant, steady-state amplitude was not obtained. The reason for this fluctuating amplitude is easily seen by examining Figure 10. The upper and lower curves are identical and represent the motion of the left and right bumpers of the mass, M, while the middle curve represents the ball bouncing back and forth. It can be seen that when the ball impacts near the center of a bumper curve where the velocity of M is maximum, the amplitude of the displacement of M decreases. However, due to the time required for the ball to traverse the gap, the period of the ball is not the same as that of the mass, M. Thus, after several bounces, the ball impacts at a peak displacement (zero velocity of M) and rebounds relatively slowly, missing one complete cycle of M. The amplitude of M then builds up, but the ball now impacts at a point near maximum velocity, and, thus, the cycle is repeated.
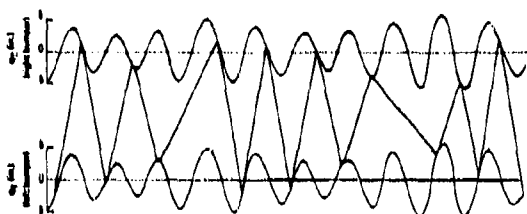
Figure 10. Motion of Ball and Bumpers.

Because the ball is assumed to roll without friction, the large mass, M, cannot make contact with the ball if d/2 is greater than 10.0 inches. Therefore, the results shown in Figure 11 were obtained by giving the ball an initial velocity of 0.5 in./sec so as to insure eventual contact regardless of gap size. For all values of d less than about 15 inches, the response showed a constant, steady-state motion similar to that of Figure 8. However, for larger values of d, a fluctuating response similar to Figure 9 was obtained. These larger values, plotted in Figure 11, represent an average of the peak values obtained. Also, for the largest values of d, the motion of M was fairly repeatable, but not completely settled into a true steady-state motion.

SUMMARY

A computer program has been written for the dynamic analysis of mechanisms and machinery, and two examples have been discussed. The cam-driven valve train has been the subject of analysis (in various forms) for the past few years. However, once the program became operational, the second example—that of the impact damper—was completed within a few weeks. It must be emphasized that the purpose here has not been to design a better cam profile or damper mechanism, but rather to describe a method which will lead to a better understanding of elastic systems with multiple clearances.
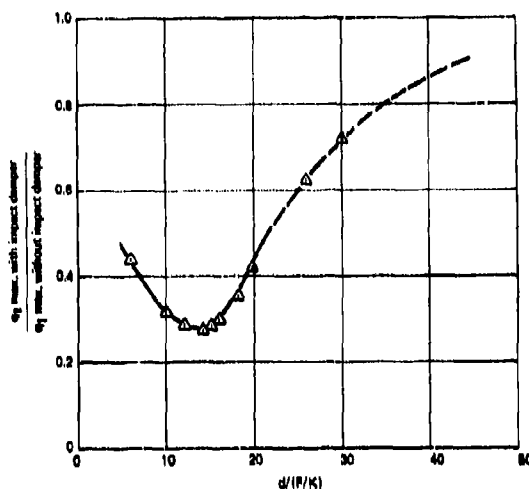
Figure 11. System Response for Varying Gap, d.

REFERENCES

1. Winfrey, R. C., "Elastic Link Mechanism Dynamics," Journal of Engineering for Industry, Trans. ASME, Series B, Vol. 93, No. 1, Feb 1971, pp. 268-272.

2. Erdman, A. G., Sandor, G. N., and Oakberg, R. G., "A General Method for Kineto-Elastodynamic Analysis and Synthesis of Mechanisms," ASME Paper No. 71-WA/DE-8. (To be published in the Journal of Engineering for Industry, Trans. ASME.)

3. Imam, I., Sandor, G. N., and Kramer, S. N., "Deflection and Stress Analysis in High Speed Planar Mechanisms With Elastic Links," ASME Paper No. 72-MECH-44. (To be published in the Journal of Engineering Industry, Trans. ASME.)

4. Dubowsky, S., and Freudenstein, F., "Dynamic Analysis of Mechanical Systems with Clearances, Part 1: Formation of Dynamic Model," and "Part 2: Dynamic Response," Journal of Engineering for Industry, Trans. ASME, Series B, Vol. 93, No. 1, Feb. 1971, pp. 305-316.

5. Winfrey, R. C., Andersen, R. V., and Gnilka, C. W., "Analysis of Elastic Machinery with Clearances," ASME Paper No. 72-MECH-37. (To be published in the Journal of Engineering for Industry, Trans. ASME.)

6. Lieber, P., and Jensen, D. P., "An Acceleration Damper: Development, Design, and Some Applications," Trans. ASME, Vol. 67, 1945, pp. 523-530.

7. Masri, S. F., and Caughey, T. K., "On the Stability of the Impact Damper," Journal of Applied Mechanics, Trans. ASME, Vol. 88, Series E, 1966, pp. 586-592.

8. Egle, D. M., "An Investigation of the Impact Vibration Absorber," Journal of Engineering for Industry, Trans. ASME, Series B, Vol. 89, No. 4, Nov. 1967, pp. 653-657.

9. Masri, S. F., and Ibrahim, A. M., "A Hybrid Electromechanical Analog Computer Technique for Optimizing Vibration Systems," Journal of Engineering for Industry, Trans. ASME, Series B, Vol. 94, No. 2, May 1972, pp. 381-387.

10. Masri, S. F., "Steady-State Response of a Multidegree System with an Impact Damper," ASME Paper 72-APM-39. (To be published in the Journal of Applied Mechanics.)

DISCUSSION

Mr. Zanoni (Westinghouse): What numerical integration was used?

Mr. Winfrey: This was a Newmark method. It was a straight line on the acceleration between time intervals.

Mr. Zanoni: When you have a large number of degrees-of-freedom, isn't this going to reduce the time step size?

Mr. Winfrey: This would be a function of the maximum natural frequency. So, presumeably if you have a large number of degrees-of-freedom you have high natural frequencies. The time step for the numerical integration was approximately one fourth of the highest natural period.

Mr. Zanoni: The title of the paper indicates multiple clearances and a large number of degrees-of-freedom. My experience with this kind of program is this problem of having a lot of degrees-of-freedom and having the thing blow up.

Mr. Winfrey: Well, it is not going to blow up if you are above the natural frequency.

Mr. Zanoni: When you have a large number of degrees-of-freedom you are talking about a very very small ---

Mr. Winfrey: You can say about a number of programs that there are no theoretical limits but there are certainly practical limits in the size and speed of the computer that you have. Ten-degrees-of-freedom was the largest system that I did run. To give you a ball park number this was on an IBM 370, Model 165. The problem I showed with nine-degrees-of-freedom took about 20 seconds to run out through 2½ revolutions. This was about 100,000 iterations, so the program works fairly rapidly.

RESPONSE BOUNDS FOR STRUCTURES WITH

INCOMPLETELY PRESCRIBED LOADING

W. D. Pilkey
Department of Aerospace Engineering and
Engineering Physics
University of Virginia
Charlottesville, Virginia, 22901

A. J. Kalinowski
Division of Engineering Mechanics
ITT Research Institute
Chicago, Illinois, 60616

Problems concerned with finding upper and lower bounds on the response of elastic and plastic structures subjected to incompletely prescribed loading are treated. The solutions are formulated as mathematical programming problems. The particular members of the class of loadings that lead to the bounding values of the response are determined in addition to the extreme responses. Both transient and steady state problems are considered. The loading can be characterized by amplitude bounds or properties such as total energy or impulse.

INTRODUCTION

The important problem of determining information on the dynamic response of structures when the loading is not fully prescribed has been given limited attention. This is especially true when the loading is to be characterized deterministically rather than statistically. This paper is devoted to the deterministic case.

References 1-18 are representative of past efforts in this area. The work presented in these documents along with references contained therein constitute a reasonably complete state of the art. Generally the problem is treated in terms of determining the upper and lower bounds on the response that can be achieved for the prescribed class of loadings. References 2, 4, 5, 6, 7, 8, 9, 10, 11, 12, 17 and 18 contain a fascinating array of analytical solutions. These range from graphical solutions to the use of Pontryagin's maximum principle and Liapunov's direct method. The analytical efforts are restricted to either simple dynamic systems or simple characterization of the loading, e.g. a load defined by a constant upper bound.

Computational techniques are proposed in References 1, 13, 14, 15, and 16 for transient problems. The problem is cast in terms of mathematical programming. For linear systems and a linear loading characterization the linear programming approach applies and a

multi-degree of freedom dynamic system can be treated. Also, the loading characterization is flexible, e.g. a load can be defined by a time-varying band.

Several interesting mechanical system transient problems are to be found in these references. Reference 10 discusses the peak response of a beam subject to a load, which is defined in terms of upper and lower bounds, moving along the beam. The maximum response of a structural system for which the energy of the input excitations is bounded for a given time duration is handled in Reference 5. In Reference 4 a beam column is presented for which only upper bounds are known on the transverse and axial transient loads. Reference 18 deals with structural systems for which the loading can be defined with inequalities, e.g. a band in time within which the forcing function must lie. References 16 and 17 determine peak responses for single degree of freedom systems loaded by a forcing function of specified duration and total impulse. Several transient structural systems with various loading characterizations are considered in References 13 and 15.

In the present work, computational formulations are given for a steady state vibration problem. Also, an extension of the formulation to apply to inelastic structures is proposed.

31

CHARACTERIZATION OF LOADING

Consider a structure that is subject to a loading for which only limited local and/or global characteristics are known. Typically, a time-varying bandwidth, within which the magnitude and/or rise times of the loading must lie, may constitute the class of admissable loads, with nothing being said about the probabilities of occurrence within the band. Thus for a loading, $f(x,t)$, where x is the spatial coordinate (vector) and t is time, with discrete representation $f_{ij} = f(x_i, t_j)$, it could be prescribed for a given position x_i on the structure that

$$f_j^L \leq f_{ij} \leq f_j^U \qquad\qquad j = 1, 2, \ldots, J \qquad (1)$$

where the boundary values f_j^L, f_j^U are specified. Similar descriptions can be formed for the rate or slope of loading. Also, upper and lower limits to the total force distributed over a portion of the structure might be known as functions of time, or perhaps the total impulse and duration might be prescribed for a given position. In the latter case, it is required for x_i that

$$\sum_{j=1}^{J} f_{ij}\, \Delta t_j = I_T, \qquad I_T \text{ and } J \text{ specified} \quad (2)$$

Any combination of these requirements also could serve to define the class of admissible loads. In the case of steady state systems perhaps the amplitudes of various loadings are defined by upper and lower bounds.

THE PROBLEM

The problem posed is that of finding for such a prescribed class of loadings:

1. the peak response (stress or displacement) of the structure that cannot be exceeded, i.e. the worst case,

2. the peak response that at least must occur, i.e. the best case,

3. the corresponding loadings that generate these extremal responses.

More precisely, these problem situations may be stated for a response function $u(x_m,t)$ as:

Best Disturbance -- For prescribed constraints on f_{ij} find

$$\underset{f_{ij}}{\text{Min}}\ \underset{t_j}{\text{Max}}\ u(x_m,t_j) \quad \begin{array}{l} j = 1, 2, \ldots, J \\ i = 1, 2, \ldots, I \end{array} \quad (3)$$

and the corresponding f_{ij}. Here, the time interval of interest is assumed to be $0 \leq t \leq t_J$

Worst Disturbance -- For prescribed constraints on f_{ij} find

$$\underset{f_{ij}}{\text{Max}}\ \underset{t_j}{\text{Max}}\ u(x_m,t_j) \quad \begin{array}{l} j = 1, 2, \ldots, J \\ i = 1, 2, \ldots, I \end{array} \quad (4)$$

These problems can be restated in terms of mathematical programming making them suitable for solution using computational techniques.

TRANSIENT RESPONSE OF ELASTIC STRUCTURES

Consider first the best disturbance problem of Eq. (3). Set

$$\phi = \underset{0 \leq t \leq t_j}{\text{max}}\, u(x_m,t) = \underset{t_j}{\text{max}}\, u(x_m,t_j) = \underset{j}{\text{max}}\, u_{mj} \qquad (5)$$
$$j = 1, 2, \ldots, J$$

or, equivalently,

$$u_{mj} \leq \phi \qquad\qquad j = 1, 2, \ldots, J \qquad (6)$$

The mathematical programming statement of the problem becomes:

Find the f_{ij}, subject to prescribed constraints, such that

$$\phi \text{ is minimized and } u_{mj} \leq \phi,\ j = 1, 2, \ldots, J$$

In the case of linear elastic structures u_{mj} can be computed as a linear function of the loading parameters f_{ij}. If the constraints can also be expressed as linear functions of f_{ij}, e.g. Eqs. (1), (2), then the problem is one of linear programming. Large-scale linear programming computer programs are standard items in the software library of computer centers.

The worst disturbance mathematical programming formulation is simpler still. The particular set of f_{ij} that is generated for the class of admissible loadings, the maximum possible u_{mj}, and the corresponding worst disturbance can be found by maximizing u_{mj}, at several time intervals in $0 \leq t \leq T$, where T may be greater than t_j. The maximum of these peak u_{mj} is then the maximum possible u_{mj}. The relative simplicity of the worst-disturbance problem, resulting from the fact that the loading class definitions constitute the only constraints for this formulation, is significant from a computational standpoint. For linear structures, the objective function is linear in the loading f_{ij}. If the disturbance constraints are linear in f_{ij} the problem is again one of linear programming.

Structures modeled by nonlinear elastic theories are also suitable for extremal disturbance analysis, although the computational burden of nonlinear programming solutions can be great. Limited degree of freedom models can be solved with dynamic programming. In

the case of linear structural models, the extremal disturbance analysis approach represents a powerful, versatile technique. Not only can a wide range of realistic classes of disturbances be treated, but numerical results are readily obtained with standard linear programming codes. No repetitive analyses of the structure are required, as a single response analysis is sufficient input to the linear programming formulation. This input is wholly independent of the complexity of the structural model because it does not vary with the degrees of freedom of the structural representation. For transient systems any available dynamic analysis, e.g. a structural analysis computer program, that can provide the response of the structure to unit impulses can be coupled to the linear programming formulation.

Several computational formulations of the transient problem for elastic structures, including the above, are described in References 13 and 15. Typical worst and best disturbance results for simple systems are sketched in Figs. 1 and 2. These were found using linear programming.
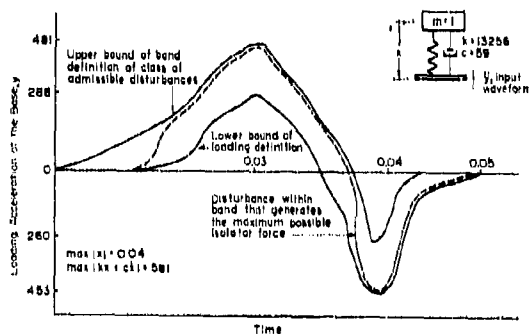
Fig. 1 – Worst Disturbance Analysis
of Spring-Dashpot Isolator

Best Disturbance Quantities
Are Starred.
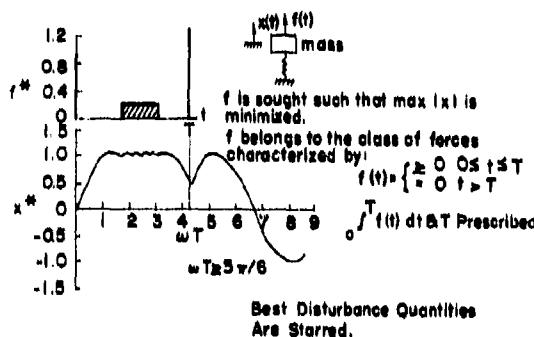
Fig. 2 – Best Disturbance Analysis
of Spring Mass System

STEADY STATE RESPONSE OF ELASTIC STRUCTURES

We choose to treat a specific steady state vibration problem rather than a generic formulation. It will become clear that this work can be extended to a variety of vibration problems. Consider the problem of balancing rotating shafts. Many techniques have been developed for identifying the unbalance force (moment) distribution along a shaft and for removal of this unbalance using balancing weights. However, there is often some uncertainty involved in placing the balancing weights, especially in the case of at-speed balancing. It is of interest to study the rotor's sensitivity to misplaced weights. For example, how much runout can be generated by a prescribed percent possible error in magnitude or phase angle placement of the weights. For a complex shaft model it is useful to cast this problem in the worst disturbance format.

Let $\{f\}$ be a vector of known balance moments or weights that are to be applied to a shaft. They are related to vibration displacements $\{u\}$, so-called runouts, at various speeds and locations along the axis of the shaft by the matrix equation

$$\{u\} = [A] \{f\} \qquad (7)$$

where $[A]$ is a matrix of experimentally or analytically determined influence coefficients. Equation (7) is formed using a linear rotor model. Because of the two-dimensional nature of the deflections and unbalance moments, the elements in Eq. (7) are complex numbers. It is usually desirable to expand Eq. (7) making the elements real numbers.

Suppose the components of the elements of $\{f\}$ are incompletely prescribed in accordance with Eq. (1) due to the uncertainties involved in placing the balancing weights. Then the problem of determining the sensitivity of the rotor due to these uncertainties can be stated as: Find maximum $|u_m|$, where u_m is an element of $\{u\}$ of Eq. (7), and $\{f\}$ of Eq. (7) is subject to constraints of the form of Eq. (1). The quantity $|u_m|$ is a vibration amplitude involving a quadratic equation in $\{f\}$, i.e.

$$u_m^2 = \sum_i \sum_j a_{ij} f_i f_j \qquad (8)$$

Thus, the objective function is quadratic while the constraints (Eq. (1)) are linear. This becomes a quadratic programming problem. Computer programs of reasonable dimension are available for quadratic programming problems.

Representative results for the rotor of Fig. 3 are shown in Table 1. This rotor was modeled by 25 lumped masses with several unbalance masses. The rotor is to be balanced using weights at five locations. The balance weights are identified with a least square

33

fit on runout observations through the first
three criticals. The $|u_m|$ of the final
column of Table 1 are located close to the
antinodes.

Station	Speed (RPM)	Unbal- anced Runout (Mils)	Runout (Mils) with Balance Weights	Runout $|u_m|$ (Mils) Resulting from 10% Error in Magnitude and $10°$ Error in Phase Angle
13	590	5990	7	2538
7	2310	648	3	1085
5	5060	193	5	296

Table 1 Typical Worst Balance Results

a. Rotor Model

591 RPM

2312 RPM

5010 RPM

1 3 5 7 9 11 13 15 17 19 21 23 25
rotor station
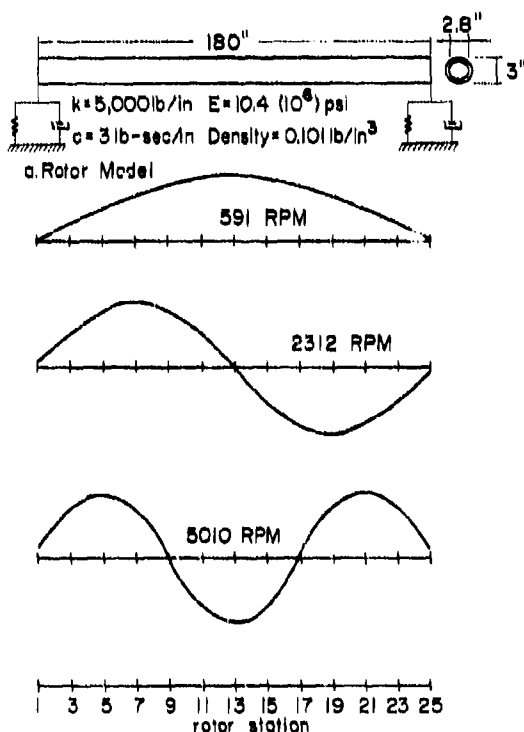
b. Three Critical Speeds and Mode Shapes

Fig. 3 – Test Rotor and Its
Characteristics

TRANSIENT RESPONSE OF INELASTIC STRUCTURES

Over the past several years, mathematical
programming methods have been applied to the
solution of certain plasticity problems, partic-
ularly in the area of determining upper and
lower bounds to limit loads for rigid-perfectly
plastic structures [21,23,25,26,27,29]. There
is a related area in plasticity to which these
same mathematical programming techniques can
be applied. Specifically, the problem of deter-
mining response bounds of continua composed of
a plastic material subject to a suddenly

applied initial velocity distribution. Although
general bounding theorems have been developed
for determining the displacement bounds for a
three dimensional continuum [19,22], applica-
tions appear to be restricted to problems no
more complicated than beams or symmetrically
loaded circular plates. Furthermore, the solu-
tions have been applied to problems where the
initial velocity field was completely speci-
fied. We propose to show that with the aid of
modern mathematical programming techniques and
the method of finite elements, efficient
numerical solution techniques for finding the
response bounds of complex impulsively loaded
structures can be formulated. Unlike the
previous applications of the bounding theorems,
we also consider a class of problems having un-
certainty in the initial velocity field wherein
this field is specified only to within a para-
metric family. Bounds on the maximum in time
value of the displacement for the worst possi-
ble initial velocity field are to be determined.
The worst velocity field will also be estab-
lished as a product of the solution. For the
case of a single deterministic initial
velocity field, the mathematical programming
formulation reduces to the usual problem types
considered previously, except that even in
this case it appears that the mathematical pro-
gramming approach combined with finite elements
has not yet been studied.

We choose the plane stress problem as a
representative situation for which to formu-
late the solution. The mathematical pro-
gramming solution to the displacement bound
problem could be formulated more generally in
terms of generalized stress and displacement
variables (e.g. moments and curvatures for
plates) so that it would be applicable to a
wider class of problems. However, this is
set aside because the practical details needed
to fully describe the procedure differ sub-
stantially from beam problems to plate problems
to plane stress problems, etc. The main
ingredient common to all of these problem
types is that a parametric family to kinemat-
ically admissable displacement fields or a
parametric family of statically admissable
equilibrium fields is needed to implement the
solution techniques. The mathematical form of
fields generated and the restrictions imposed
on them differ considerably for the different
problem types. References will be identified
which explain how these admissable fields may
be constructed for problem types other than
the plane stress case considered here.

In the development to follow it is con-
venient to apply first the combined mathemati-
cal programming-finite element approach to the
case where the initial velocity field is com-
pletely prescribed. Following this, the
additional complication of incompletely
prescribed initial velocity fields will be
taken into account.

Problem Description

Consider a two dimensional continuum com-
posed of a rigid-plastic strain rate insen-
sitive material subjected to an initial

34

velocity distribution. Suppose that at time $t = 0$ the body particle velocities are completely prescribed at all points in the body V and that thereafter $(t > 0)$ either the displacement rates on the surface are zero (e.g. at a rigid boundary) or the tractions are zero on the surface S. Assume that no body forces (other than inertia forces) are present for the time duration of the problem. Also assume that the yield function for the material is convex and the plastic flow is governed by mathematical programming, we will apply the theorems to a simple example problem. Since all the plane stress examples are too complicated to arrive at simple solutions, consider the simply supported beam subject to a sine shape initial velocity distribution $\dot{v}(x,0) = V_0 \sin(\pi x/L)$ as shown in Figure 4. We seek the bound at, say, $x = L/2$.
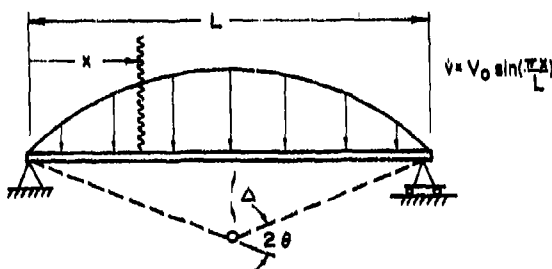
Fig. 4 - Simple Beam Model

First apply the upper bound theorem wherein the limit load due to a concentrated force applied at the mid-span is needed. Applying the methods of limit analysis [20], the limit load is easily found to be $R^L = 4M_0/L$ where M_0 is the yield moment of the cross section of the beam. Then by directly applying the inequality of Eq. (10) we obtain

$$\delta^f \le \frac{\int_0^{x=L} \bar{m}V_0^2 \sin\left(\frac{\pi x}{L}\right)^2 dx}{R^L} = .0625\bar{m}V_0^2L^2/M_0 \qquad (14)$$

where $\bar{m} = A\rho$ (mass/unit length) and $A =$ section area.

To obtain a corresponding lower bound with the lower bound theorem, Eq. (13), we need to first assume a kinematically admissable velocity field (or more specifically, we assume the spatial function $U^*(x)$). Select the simple piecewise symmetrical linear function shown by the dotted line in Figure 4.

Thus

$$U^*(x) = \begin{cases} 2x\Delta/L & 0 \le x \le L/2 \\ 2\Delta(1-x/L) & L/2 \le x \le L \end{cases} \qquad (15)$$

where $\Delta = \theta L/2$.

Upon substituting $\dot{v}(x,0) = V_0\sin(\pi x/L)$ and the kinematically admissable field, Eq. (15), into the beam formulation equivalent of Eq. (13) (note the dissapation for the beam at the hinge is simply $2\theta M_0$), we arrive at

$$\Delta^f \ge \frac{\frac{1}{2} \cdot 2\int_0^{L/2} \bar{m} \theta x \left[V_0 \sin\left(\frac{\pi x}{L}\right)\right]^2 dx}{2\theta M_0} = 0.04418\bar{m}V_0^2L^2/M_0 \qquad (16)$$

Thus we have bounded the mid-span deflection, $v(L/2)$, within the limits

$$0.04418\frac{mV_0^2 L^2}{M_0} \le v(L/2) \le 0.0625\frac{mV_0^2 L^2}{M_0} \qquad (17)$$

An elastic plastic analysis of this same beam problem [28] shows that (neglecting the elastic portion of the Reference 28 solution) it falls within the bounds given by Eq. (17).

Computation of the Displacement Upper Bounds by Mathematical Programming

Upon examining the upper bound theorem Eq. (10), we note that in order to evaluate the bound it is necessary to know the limit load due to a concentrated force $\hat{n}_i R^L$. If we know a lower bound, R^{-L}, to the true limit load, then we can still obtain an upper bound to the displacements, δ^f, by simply replacing R^L in Eq. (10) with R^{-L}. Hence the problem of finding the upper displacement bound is reduced to finding a lower bound, R^{-L}, to the true limit load.

Belytschko and Hodge [23] have formulated the solution to finding the lower bound, R^{-L}, by applying nonlinear mathematical programming techniques. Briefly, the method consists of subdividing the plane stress region into a finite number of triangles as shown in the model of Fig. 5. An n-parameter family of
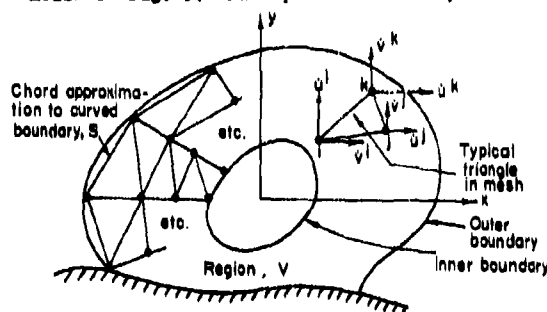
Fig. 5 - Plane Stress Model

statically admissable stress fields is derivable from a general fourth-order polynominal Airy stress function and identically satisfies the equation of equilibrium within the triangular element. These stress distributions are linear

35

an associated flow rule. Because plastic deformation is an essentially dissipative process and no energy can be stored in a rigid-plastic continuum, the velocities in the continuum will, in general, vanish after some time t_f. We will consider the problem of finding bounds of the displacement vector, δ_f, and bounds on the associated response time t_f.

Upper Displacement Bound Theorem

For the two dimensional continuum described above the mass density per unit volume is denoted by ρ, the displacement response by the displacement vector $u_i(x,y,t) = (u(x,y,t), v(x,y,t),0)^T$, the stress tensor by σ_{ij}, and the strain tensor by ε_{ij}. The indicial notation σ_{11} corresponds to stress components σ_{xx}, σ_{12} to σ_{xy}, etc., and a similar subscript notation correspondence holds for strain. For the plain stress problem $\sigma_{zz} = \sigma_{xz} = \sigma_{yz} = 0$ and $\varepsilon_{xz} = \varepsilon_{yz} = 0$, $\varepsilon_{zz} = -(\varepsilon_{xx} + \varepsilon_{yy})$. In view of the above notational agreement, the given information is the initial velocity field $\dot{u}_i(x,y,0)$. Let u_i^f denote the final displacement vector function defined over the surface S of the body and let T_i^S be, in the terminology of limit analysis theorems, a set of safe surface tractions applied quasistatically to the continuum under examination. For these flow will <u>not</u> occur, (i.e. the state of stress nowhere violates the yield criteria). Then the bound on the surface displacements must satisfy [22].

$$\int_S T_i^S u_i^f \, dA \le \frac{1}{2} \int_V \rho \dot{u}_i(x,y,0) \, \dot{u}_i(x,y,0) \, dV \quad (9)$$

To obtain more explicit information, let $T_i^S \, dA$ correspond to the limiting case of a concentrated force of magnitude R acting in the direction $\bar{n}_i$. Furthermore, let R^L be the largest value of R for which the yield criterion is not violated in the body (i.e. R^L is the limit load for the concentrated force). Then a bound, δ^f, on the projection of deformation vector u_i^f in the direction $\bar{n}_i$ is given by

$$||u_i^f|| \cos\theta = \delta^f \le \frac{\frac{1}{2} \int_V \rho \dot{u}_i(x,y,0)\dot{u}_i(x,y,0)dV}{R^L} \quad (10)$$

where θ is the angle between the $\bar{n}_i R^L$ vector and u_i^f, and $||u_i^f||$ is the magnitude of the vector u_i^f at the point where the concentrated load is applied.

A bound on the magnitude $||u_i^f||$ can be achieved by obtaining a bound on two orthogonal components of u_i^f. This can be accomplished by employing an inequality twice for two orthogonal point loads $\bar{n}_i R^L$ and $\bar{n}_i^0 R^L$ from which we obtain the bounds on two orthogonal components of u_i^f, δ_0^f and δ_{q0}^f. Thus

$$||u_i^f|| \le \sqrt{(\delta_0^f)^2 + (\delta_{q0}^f)^2} \quad (11)$$

Lower Time Response Bound Theorem

For the two dimensional problem statement, let t_f be the response time measured from the initial instant t=0, for the structure to reach its final displacement state u_i^f. Then if u_i^* is any postulated time independent kinematically admissible velocity field, the response time can be bounded from below by the relation

$$t_f \ge \frac{\int_V \rho\dot{u}_i(x,y,0)\dot{u}_i^*(x,y)dV}{\int_V \sigma_{ij}^* \dot{\varepsilon}_{ij}^* \, dV} \quad (12)$$

where the denominator represents the power of dissipation associated with the assumed velocity field and is computed from the strain rates, $\dot{\varepsilon}_{ij}^*$, associated with the assumed velocity field, u_i^*, and from the stresses,σ_{ij}^*, (not necessarily unique) associated with $\dot{\varepsilon}_{ij}^*$ through the plasticity associated flow rule.

Lower Displacement Bound Theorem

For the two dimensional problem statement, let Δ^f denote the spatial maximum value of the magnitude of the displacement vector $||u_i^f||$ (i.e. $\Delta^f = \max_{x_i \in V} ||u_i^f||$).

Then according to Reference 18, the displacement quantity Δ^f can be bounded from below by the inequality

$$\Delta^f \ge \frac{\int_V \rho U_n^* ||\dot{u}_i(x,y,0)||^2 \, dV}{2 \int_V \sigma_{ij}^* E_{ij}^* \, dV} \quad (13)$$

where u_i^* is a kinematically admissible velocity field (assumed separable in the form $\dot{u}_i^*(x,y,t) = U_i^*(x,y) \, \dot{T}(t)$), E_{ij}^* is a strain rate field corresponding to the spatial variation $U_i^*(x,y)$ (i.e. $E_{ij}^* = \frac{1}{2}(U_{i,j}^* + U_{j,i}^*)$), and stresses σ_{ij}^* are associated with E_{ij}^* through the plasticity associated flow rule. Two further constraints on the application of the bound given by Eq. (13) are that the rate of dissipation (the denominator of inequality (13)) be non-negative and the rather restrictive assumption that the direction cosines, $n_i(x,y)$, of the acceleration field are known a priori and remain constant in time during the entire deformation process. A consequence of this last assumption is that the velocity field will also have these same constant-in-time direction cosines. Although this constant n_i assumption creates no particular problem for plate or beam type structures (in these cases there is only one non-zero displacement component, namely the normal displacement along with its associated velocity and acceleration) it does limit the range of problems for rigorously applying the lower bound theorem.

Example Problem

Before proceeding to the formulation of the solution to the displacement bound by

36

in the unknown field parameter, A_i, and quadratic functions of the space variables x,y. Further, continuity requirements in the normal and tangential stresses are enforced along each interface between adjacent elements. Finally, it is required that the parametric stress field satisfy the yield criterion for all points x,y, within the region V. The lower bound is obtained by finding the A_i quantities that result in the largest lower bound and satisfies all constraints. The manner in which this last constraint is handled determines the type of mathematical programming problem we have to employ in order to maximize R^{-L}. In Reference 23 the authors employed the Mises yield criterion (a nonlinear expression in the stress variables). Thus, even though all the stress equations are linear in the unknown parameters, the yield criterion inequality destroys the prospect of applying the more powerful linear programming methods to obtain a bound. A further nonlinearity in their approach is introduced when they force the yield criteria to be satisfied at all points in the triangle. This is accomplished by finding the relative maximum points of the yield function over x,y and enforcing the yield criteria at least at these points. The formulae that define the positions of the relative maximum are nonlinear functions of the field parameters, A_i. Because of the two types of nonlinearities discussed, the authors were forced to use nonlinear mathematical programming techniques, in particular, the "Sequential Unconstrained Minimization Technique" developed by Fiacco and McCormick. The computer program referred to in Reference 23 is limited to only 20 elements.

By making some sacrifices on the accuracy of the bound, R^{-L}, the formulation discussed in Reference 23 can be converted to one of linear programming. First, the Mises yield criterion (a closed convex surface in a three dimensional space consisting of σ_{xx}, σ_{yy}, σ_{xy} as the coordinates) can be approximated by a set of bounding planes tht inscribe the original yield criterion. The expressions describing these planes will be a set of inequalities that are linear in the field parameter A_i. The consequence of this approximation will be that the bound, R^{-L}, will be lower than if we had used the Mises criterion, all other things being equal. Next, we will enforce the yield criteria only at a finite, fixed set of points within a typical triangle. The step of computing the positions where the relative maxima appear will be omitted. There is of course always the danger of the yield criteria being violated at points between the designated points. This problem can most likely be overcome by selecting a high density of check points within the triangle. Also, the distribution of the check points could be changed on successive solutions of the same problem to insure the stability of the results. Finally, once a solution is obtained, the satisfaction of the yield criterion at the relative maximum points can be checked to insure that no drastic violations of the yield criterion have been experienced. Slight violations of the yield should not result in any drastic consequences on the final solution for R^{-L}, however, strictly speaking, unless the yield criterion is satisfied at all points x,y within the triangle, the bound theorem is not guaranteed to hold.

Computation of the Lower Time Response by Mathematical Programming

Analogous to the upper displacement bound problem, we begin by representing the continuum with a set of triangular finite elements as shown in Fig. 5. The integrals in the bounding inequality of Eq. (12) are volume integrals, therefore we concentrate on evaluating the integrals over a triangular region (of thickness h) and simply sum the results over all triangles to obtain the total volume integral.

Consider a typical triangular element, e, having nodes i,j,k as shown in Fig. 5. The component velocities of the three nodes are $\dot{u}^i$, $\dot{u}^j$, $\dot{u}^k$ and $\dot{v}^i$, $\dot{v}^j$, $\dot{v}^k$. Next we construct a parameter kinematically admissible field (e.g. see Reference 21) of the form

$$\dot{u}^* = C_1 x + C_2 y + C_3$$
$$\dot{v}^* = D_1 x + D_2 y + D_3 \tag{18}$$

where $\dot{u}_2^* = (\dot{u}^*, \dot{v}^*, 0)^T$

The $C_1, C_2, \ldots D_3$ parameters are related to the nodal velocities by the relation

$$
\begin{bmatrix} C_1 & D_1 \\ C_2 & D_2 \\ C_3 & D_3 \end{bmatrix}
=
\begin{bmatrix} x_i & y_i & 1 \\ x_j & y_j & 1 \\ x_k & y_k & 1 \end{bmatrix}^{-1}
\begin{bmatrix} \dot{u}^i & \dot{v}^i \\ \dot{u}^j & \dot{v}^j \\ \dot{u}^k & \dot{v}^k \end{bmatrix}
\tag{19}
$$

where $x_i, x_j, \ldots y_k$ are coordinates of the element nodal points, and $\dot{u}^i = \dot{u}^*(x_i,y_i)$, $\dot{u}^j = \dot{u}^*(x_j,y_j)$, etc.

The strain rates within the element are given by

$$\dot{\epsilon}_{xx} = \frac{\partial \dot{u}^*}{\partial x} = C_1$$
$$\dot{\epsilon}_{yy} = \frac{\partial \dot{v}^*}{\partial x} = D_2 \tag{20}$$
$$\dot{\epsilon}_{xy} = \frac{\partial \dot{u}^*}{\partial y} + \frac{\partial \dot{v}^*}{\partial x} = C_2 + D_1$$

which are constant throughout the element. The

dissipation rate for plane stress in conjunction with the Mises yield criterion is

$$[\sigma^*_{ij} \dot{\epsilon}^*_{ij}]_e = \frac{2\sigma_0}{\sqrt{3}} \left[\dot{\epsilon}^2_{xx} + \dot{\epsilon}^2_{yy} + \dot{\epsilon}_{xx}\dot{\epsilon}_{yy} + (\frac{\dot{\epsilon}_{xy}}{2})^2 \right]^{\frac{1}{2}}$$

or in terms of the C_i, D_i quantities by

$$[\sigma^*_{ij} \dot{\epsilon}^*_{ij}]_e = \frac{2\sigma_0}{\sqrt{3}} \left[C_1^2 + D_2^2 + C_1 D_2 + \left(\frac{C_2 + D_1}{2}\right)^2 \right]^{\frac{1}{2}} \quad (21)$$

Finally, substituting Eqs. (19) into (21) and summing over all elements, we can express the denominator of Eq. (12) as a nonlinear function of the nodal displacement parameters $u^1, u^j, u^k, \ldots v^k$. Thus

$$\int_V [\sigma^*_{ij} \dot{\epsilon}^*_{ij}] \, dV = V \sum_{e=1}^{e=NE} [\sigma^*_{ij} \dot{\epsilon}^*_{ij}]_e = f(\dot{u}^1, \dot{u}^2, \ldots \dot{v}^{NN}) \quad (22)$$

where NE is the number of elements and NN is the number of nodes in the finite element model, V is the volume of the body, and f is a nonlinear function of the kinematically admissable field parameters, $\dot{u}^1, \dot{u}^2, \ldots \dot{v}^{NN}$. Similarly, the numerator of Eq. (12) can be calculated for each triangle by substituting Eqs. (18) and (19) into the numerator and explicitly integrating over the triangular region and adding up each element's contribution.

Therefore we have

$$\rho \int_V \dot{u}_i(x,y,0) \, \dot{u}^*_i(x,y) \, dV$$

$$= \rho \sum_{e=1}^{e=NE} h \int_{V_e} (\dot{u}(x,y,0) [C_1 x + C_2 y + C_3]$$

$$+ \dot{v}(x,y,0) [D_1 x + D_2 y + D_3]) \, dx \, dy = g(\dot{u}^1, \dot{u}^2, \ldots \dot{v}^{NN})$$

where V_e is the volume region of the eth element and g is a linear function of the kinematically admissable field parameters, $\dot{u}^1, \dot{u}^2, \ldots \dot{v}^{NN}$. The $C_1, \ldots D_3$ coefficients in Eq. (22) are related to the $\dot{u}^1, \dot{u}^2, \ldots \dot{v}^{NN}$ parameters through Eq. (19).

Finally the lower bound inequality on the response time may be written

$$t_f \geq \frac{g(\dot{u}^1, \dot{u}^2, \ldots \dot{v}^{NN})}{f(\dot{u}^1, \dot{u}^2, \ldots \dot{v}^{NN})} \equiv t_f^- \quad (24)$$

for any set of nodal parameters $\dot{u}^1, \dot{u}^2, \ldots \dot{v}^{NN}$ satisfying the constraint

that the dissapation, f, be non negative (i.e. $f(\dot{u}^1, \dot{u}^2, \ldots \dot{v}^{NN}) > 0$). The most useful bound will be the largest lower bound t_f^-. Thus stated as a mathematical programming problem we wish to

$$\text{maximize} [t_f^- = \frac{g(\dot{u}^1, \dot{u}^2, \ldots \dot{v}^{NN})}{f(\dot{u}^1, \dot{u}^2, \ldots \dot{v}^{NN})}] \quad (25)$$

over the 2·NN variables $\dot{u}^1, \dot{u}^2, \ldots \dot{v}^{NN}$

subject to the constraint $f(\dot{u}^1, \dot{u}^2, \ldots \dot{v}^{NN}) > 0$

If we divide the numerator and denominator of g/f by any one of the nonzero nodal velocities, say, $\dot{u}^1$, it can be shown that for the particular functional forms of g and f, t_f^- can be rewritten as

$$t_f^- = \frac{g(1, \dot{u}^2/\dot{u}^1, \ldots \dot{v}^{NN}/\dot{u}^1)}{f(1, \dot{u}^2/\dot{u}^1, \ldots \dot{v}^{NN}/\dot{u}^1)} \quad (26)$$

and the constraint as $f(1, \dot{u}^2/\dot{u}^1, \ldots \dot{v}^{NN}) > 0$, where there are now 2·NN-1 independent variables namely the ratios $\dot{u}^2/\dot{u}^1, \dot{u}^3/\dot{u}^1, \ldots \dot{v}^{NN}/\dot{u}^1$. This means that only the ratios above determine the maximum t_f^-, not the actual values of $\dot{u}^1, \dot{u}^2, \ldots \dot{v}^{NN}$. Thus we can specify any additional equation relating the $\dot{u}^1, \dot{u}^2, \ldots \dot{v}^{NN}$ quantities and still arrive at the same max t_f^- solution to the problem stated in the form of Eq. (25). The most convenient additional equation would be to set $f(\dot{u}^1, \dot{u}^2, \ldots \dot{v}^{NN}) = C$ where C is any positive constant we choose. By enforcing this equality constraint, we also automatically satisfy the non-negative dissapation requirement, f>0. Thus the new problem is to

$$\text{maximize} [t_f^- = g(\dot{u}^1, \dot{u}^2, \ldots \dot{v}^{NN}) \div C]$$

over the 2·NN variables $\dot{u}^1, \dot{u}^2, \ldots \dot{v}^{NN}$

subject to the equality constraint

$f(\dot{u}^1, \dot{u}^2, \ldots \dot{v}^{NN}) = C$ where C is any

positive constant.

The expression for t_f^- given by Eq. (27) can be maximized by applying large scale nonlinear mathematical programming computer codes. The bases for such codes can be found in Reference 24. We note that even though the g function is linear in the parameters $\dot{u}^1, \dot{u}^2, \ldots \dot{v}^{NN}$, the equality constraint is nonlinear. Consequently, linear programming methods cannot be applied.

Computation of the Displacement Lower Bound
by Mathematical Programming.

Here our goal is to compute lower displacement bounds, Δ^L, by applying the inequality defined by Eq. (13). Again we appeal to the finite element model shown in Fig. 5. A direct comparison between Eq. (13) and the previously formulated problem based on Eq. (12) will show there is a great similarity between the two inequalities of Eqs. (12) and (13). The construction of the dissipation volume integral from linear kinematically admissable fields follows the same procedure of the previous demonstration, as long as we let the velocity field shape function vector U_i^*, take the place of the $\dot{u}_i^*$ variable in the previous development leading up to Eq. (22). Thus in place of Eq. (22) we have from a parallel development

$$\int_V \sigma_{ij}^* E_{ij}^* \, dV = V \sum_{e=1}^{a=NE} \left[\sigma_{ij}^* E_{ij}^*\right]_e = \hat{f}(u^1, u^2 \ldots v^{NN})$$

where the parameters $u^1, u^2, \ldots, v^{NN}$ now represent the values of shape function U_i^* at the nodal points rather than the actual displacement components as in the prior development. Otherwise the functional form of $\hat{f}$ is exactly the same as f. The construction of the numerator follows closely where

$$\frac{1}{2}\int \rho U_i^* \, n_i \, ||u_i(x,y,0)||^2 \, dV =$$

$$\frac{1}{2} \rho \sum_{e=1}^{a=NE} h \iint \{[C_1 x + C_2 y + C_3]n_x +$$

$$[D_1 x + D_2 y + D_3]n_y\}\{\dot{u}(x,y,0)^2 + \tag{28}$$

$$\dot{v}(x,y,0)^2\} \, dx \, dy$$

$$= \hat{g}(u^1, u^2, \ldots, v^{NN})$$

in which h is the element thickness, V_e is the volume region of the eth triangle and $\hat{g}$ is a linear function of the kinematically admissable field parameters $u^1, u^2, \ldots, v^{NN}$. As in the development of Eq. (23), Eq. (19) is used to eliminate the $C_1, \ldots, D_3$ coefficients in terms of the field parameters $u^1, u^2, \ldots, v^{NN}$. Analogous to the previous Eq. (27) the final bound determination is reduced to the problem of

Maximize $\left[\Delta^L = g(u^1, u^2, \ldots v^{NN}) \div \hat{C}\right]$

over the $2 \cdot NN$ variables $u^1, u^2, \ldots v^{NN}$

subject to the equality constraint

$\hat{f}(u^1, u^2, \ldots v^{NN}) = \hat{C}$ where $\hat{C}$ is any

positive constant.

The nonlinearity of the equality constraint requires the use of nonlinear programming to solve for Δ^{L-}.

Computation of Upper and Lower Displacement Bounds For Worst Disturbance

The previous development is based on a completely prescribed initial velocity field. Consider now the same problem statement except let the initial velocity field be any distribution within the uncertainty bounding surfaces $\dot{U}_+(x,y)$, $\dot{U}_-(x,y)$, $\dot{V}_-(x,y)$, $\dot{V}_+(x,y)$. That is, a possible initial velocity field is one that satisfies the bounding constraints

$$\dot{U}_-(x,y) \leq \dot{u}(x,y,0) \leq \dot{U}_+(x,y)$$
$$\dot{V}_-(x,y) \leq \dot{v}(x,y,0) \leq \dot{V}_+(x,y) \tag{30}$$

for all x, y∈V. The new problem statement is as follows:

Find the worst maximum in time value of the displacement, δ_{wd}, at some desired point P on the plate boundary, S, subject to any initial velocity field that satisfies inequalities of Eq. (30) (where "worst" refers to the initial velocity field that gives the largest time maximum displacement).

An upper bound to δ_{wd} can be achieved by maximizing the right side inequality (10) over all possible velocity fields within the bounds prescribed by constraint inequalities (30). Since the denominator of inequality (10) is independant of the initial velocity field and the numerator is independent of the statically admissable parameters used to maximize R^{-L}, we can obtain the worse disturbance bound, δ_{wd}, by separately maximizing the numerator,

$$e = \frac{1}{2}\int_V \rho \dot{u}_i(x,y,0)\dot{u}_i(x,y,0) \, dV$$

subject to inequalities (30).

39

We approach the problem in a similar fashion to determine the time response bound. Approximate the initial velocity fields in a typical triangle by a linear velocity field of form

$$\dot{u}_i(x,y,0) \equiv \begin{bmatrix} \dot{u}(x,y,0) \\ \dot{v}(x,y,0) \end{bmatrix} = \begin{bmatrix} E_1 x + E_2 y + E_3 \\ F_1 x + F_2 y + F_3 \end{bmatrix} \quad (31)$$

where the coefficients E_1, E_2, . . . F_3 are related to the nodal initial velocities $(\dot{u}_0^i, \dot{u}_0^j, \ldots \dot{v}_0^k)$ by

$$\begin{bmatrix} E_1 & F_1 \\ E_2 & F_2 \\ E_3 & F_3 \end{bmatrix} = \begin{bmatrix} x_i & y_i & 1 \\ x_j & y_j & 1 \\ x_k & y_k & 1 \end{bmatrix}^{-1} \begin{bmatrix} \dot{u}_0^i & \dot{v}_0^i \\ \dot{u}_0^j & \dot{v}_0^j \\ \dot{u}_0^k & \dot{v}_0^k \end{bmatrix} \quad (32)$$

where x_i, x_k, . . . y_k are the nodal coordinates.

Upon substituting Eq. (32) and Eq. (31) into the relation for ϕ and integrating over the element and summing over all elements, we find the quadratic form

$$\phi = \sum_{p=1,q=1}^{2 \cdot NN, 2 \cdot NN} A_{pq} W_p W_q$$

where A_{pq} are known coefficients and W_p is a column vector of the NN unknown nodal initial velocities (i.e. $W_p = (\dot{u}_0^1, \dot{u}_0^2, \ldots \dot{v}_0^{NN})^T$). The constraints (30) can be linearized by representing the curved bounding surfaces with approximating planes and forcing the constraints only at the nodal points instead of for all x, $y \ni V$. Then Eq. (3) becomes

$$\dot{U}_-(x_p,y_p) \le W_p \le \dot{U}_+(x_p,y_p) \quad p = 1, 2, \ldots NN$$

$$\quad (33)$$

$$\dot{V}_-(x_p,y_p) \le W_p \le \dot{V}_+(x_p,y_p) \quad p = NN+1, NN+2, \ldots 2 \cdot NN$$

Thus the problem of finding a bound, δ_{wd}^+, on the time worst disturbance δ_{wd} can be reduced to

$$R^{L} \cdot \delta_{wd}^+ = \max \sum_{p=1,q=1}^{2 \cdot NN, 2 \cdot NN} A_{pq} W_p W_q \text{ over } W_1, W_2 \ldots W_{2 \cdot NN}$$

subject to linear constraints (33). The above problem is the dual form of the standard quadratic programming problem for which there exist standard computer programs. Information on a lower bound on the worst disturbance, δ_{wd}, can be obtained by using the worst disturbance initial velocity field, found as a byproduct of the above solution, in the lower bound relation (29) discussed earlier.

Discussion of Formulations

Although the plasticity formulations presented here have dealt directly with the plane stress problem, the procedures are applicable to other structures such as beams, plates, shells, and arches.

The main differences from problem type to problem type are in the parametric representation for the kinematically and statically admissable fields. For example, such admissable fields are considered for beams in Reference 25, plates in Reference 27, shells in Reference 29, and arches in Reference 26.

The usefulness of lower bound inequality (13) appears quite restricted by the requirement that a priori knowledge of the kinematic velocity field direction cosines, n_i, be known. The practical usefulness of this bound appears to be limited to beams and flat plates where only one displacement component is considered. In these cases the direction of the kinematic velocity field is known as required. Another drawback to applying (13) to multicomponent displacement problems is that Eq. (13) bounds the maximum value of the displacement over the volume whereas the corresponding upper bound (10) or (11) bounds the displacement at a point on the surface. Thus, knowing the largest value of the displacement on the surface does not imply knowledge of the largest value of the displacement within the volume. Therefore it is not clear whether we are bounding the same quantity with the two displacement bounding theorems. In the case of plates in bending or beams, however, both bounds will refer to the same middle surface displacements.

SUMMARY

Several response bound problems for structures with incompletely prescribed loading have been presented. The loading can be characterized by amplitude bands or in terms of a global property such as total energy or impulse and time duration. Both elastic and inelastic structures subjected to transient or steady state loading are considered. Computational solution formulations are established. A number of practical problem situations can be treated as linear programming problems. Because of the availability of powerful computer software, large-scale structures can be handled with ease.

40

REFERENCES

1. W. A. Glasser, K. D. Graham, C. A. Harvey, "Minimax Studies," NASA CR-547, 1966.

2. J. E. Gibson, Z. V. Rekasius, D. R. Howard, R. Mukundan, "Analysis of Worst Case Behavior in Forced Control Systems," AD460750, 1963.

3. W. D. Ashcroft, W. Hochwald, "Design by Worst-Case Analysis: A Systematic Method to Approach Specified Reliability Requirements," IRE Transactions on Reliability and Quality Control, Vol. 10, pp. 15-21, 1961.

4. R. H. Plaut, "Displacement Bounds for Beam-Columns with Initial Curvature Subjected to Transient Loads," Int. J. Solids Structures, Vol. 7, pp. 1229-1235, 1971.

5. J. N. Yang, E. Heer, "Maximum Dynamic Response and Proof Testing," J. Eng. Mech. Div., ASCE, Vol. 97, pp. 1307-1313, 1971.

6. D. R. Howard, Z. V. Rekasius, "Error Analysis with the Maximum Principle," IEEE Transactions on Automatic Control, July, pp. 223-229, 1964.

7. A. J. Koivo, "Performance Sensitivity of Dynamical Systems," Purdue University, Indiana.

8. R. K. Cavin, C. L. Phillips, D. L. Chenoweth, "The Computation of an Output Bound for a Discrete System with a Bounded Input," Auburn University, Alabama.

9. A. J. Koivuniemi, "Parameter Optimization in Systems Subject to Worst (Bounded) Disturbance," IEEE Transactions on Automatic Control, Vol. 11, pp. 427-433, 1966.

10. V. A. Svetlitskii, "Determining the Maximum Possible Reactions in Dynamic Systems Acted on by Perturbations of Bounded Absolute Value," Mekhanika Tverdogo Tela, Vol. 2, pp. 161-165, 1967.

11. I. M. Horowitz, "Analysis and Synthesis of Linear Systems with Inputs Satisfying Certain Bounding Conditions," J. Electronics Control, Vol. 12, pp. 195-208, 1962.

12. B. J. Birch, R. Jackson, "The Behavior of Linear Systems with Inputs Satisfying Certain Bounding Conditions," J. Electronics Control, Vol. 6, pp. 366-375, 1959.

13. E. Sevin, W. D. Pilkey, A. J. Kalinowski, "Optimum Performance Bounds and Synthesis of Dynamic Systems," in Computer Applications in Applied Mechanics, pp. 107-132, ASME, NY, NY, 1969.

14. E. Sevin, W. D. Pilkey, Optimum Shock and Vibration Isolation, Shock and Vibration Information Center, Wash. D. C., 1971.

15. E. Sevin, W. D. Pilkey, "Min-Max Response Problems of Dynamic Systems and computational Solution Techniques," Shock and Vibration Bulletin, Vol. 36, pp. 69-76, 1967.

16. E. Sevin, W. D. Pilkey, "Computational Approaches to the Min-Max Response of Dynamic Systems with Incompletely Prescribed Input Functions," J. Appl. Mech., Vol. 34, pp. 8/-90, 1967.

17. E. Sevin, "Min-Max Solutions for the Linear Mass-Spring System," J. Appl. Mech., Vol. 24, pp. 131-136, 1957.

18. C. D. Michalopoulos, T. A. Riley, "Response of Discrete Linear Systems to Forcing Functions with Inequality Constraints," AIAA J., Vol. 10, pp. 1016-1019, 1972.

19. T. Wierzbicki, "Improved Lower Bound Theorem for Impulsively Loaded Continua," Archiuum Mechaniki Stosowarej, Brief Note #23, pp. 423-425, 1971.

20. W. Prager, An Introduction to Plasticity, Addison-Wesley, Reading, Massachusetts.

21. D. Hayss, D. V. Marcal, "Determination of Upper Bounds for Problem in Plane Stress Using Finite Element Techniques," Intern. J. Mech. Sci. 1967.

22. J. B. Martin, "Impulsive Loading Theorems for Rigid-Plastic Continua," ASCE J. Mech. Div., 1964.

23. T. Belytschko, P. G. Hodge, "Lower Bound Limit Analysis of Plane Stress Problems by a Finite Element Method," DOMIIT Report 1-42, IIT 1970.

24. G. Hadley, Nonlinear and Dynamic Programming, Addison-Wesley, Reading, Massachusetts, 1964.

25. D. E. Grierson, M. L. Gladwell, "Collapse Load Analysis Using Linear Programming," ASCE, J. Struct. Div., 1971.

26. T. Belytschko, P. G. Hodge, "An Automatic Program for Calculating the Yield-Point

41

Load of Arches," DOMIIT Report No. 3-6A,
IIT 1967.

27. P. G. Hodge, T. Belytschko, "Numerical
Methods for the Limit Analysis of Plates,"
J. of App. Mech., Paper No. 68-WA/APM-21,
1968.

28. J. A. Seiler, B. A. Cotter, R. S. Symonds,
"Impulsive Loading of Elastic-Plastic
Beams," J. of Appl. Mech., Vol. 23, Trans.
ASME, Vol. 78, 1956.

29. A. Biron, P. G. Hodge, "Limit Analysis of
Rotationally Symmetric Shells Under
Central Loadings by A Numerical Method,"
J. of Appl. Mech. Vol. 34, 1967.

DISCUSSION

Mr. Arthur (Aerojet): Does the load
vector on the elastic structure have to have
the same proportion as for the unknown one?
Is there a proportionality constant?

Mr. Pilkey: No, there is none.

Mr. Thomson (University of California):
It seems that many people are now interested
in parameter identification problems, where
you start out with the known response and work
back to the parameters of the system. I notice
that your paper is somewhat similar except that
the unknowns are the loadings which you are
optimizing to get the type of response. Is
that correct?

Mr. Pilkey: It is the same problem and
the approaches are the same. The inverse of
the problem I talk about today is to say,
given the response of the structure, go back
and identify the loadings. Here, if you are
given something about the loadings, you are to
find the peak responses. The formulations are
the same.

Mr. Fritz (General Electric Co.): I have
a question about the class of problems that you
showed us. I didn't get a full understanding
of those problems. For instance, was the one
with the rotating shaft a practical problem
taken from an application or was it made up
to show the method?

Mr. Pilkey: The technique was developed
for practical problems. The particular
problem for which the numerical results were
given was just a simulated rotor. It has been
applied to real rotors at much higher speeds
than the third critical.

Mr. Fritz: You mean they had rotors
running at 3000 RPM at 0.3 inches unbalanced?

Mr. Pilkey: There is no attempt to make a
practical problem out of the one that I gave
results on, but it has been applied in practical
cases. That was a rather arbitrarily chosen
rotor that had no particular characteristics of
interest to anyone.

Mr. Scavuzzo (Rensselaer Polytechnic
Institute): The question I have concerns
uniqueness. Have you run into uniqueness
problems in trying to define the input giving
the response?

Mr. Pilkey: The input or particular
forcing function giving the peak response is
not unique. What is of interest is that the
response itself is unique, otherwise we would
not have solved the problem. If you find the
absolute upper bound on the response, the worse
disturbance that is, it is unique, but the
forcing function generating it is not unique.
There is no particular reason for it to be.

NONLINEAR VIBRATIONS OF
MULTILAYER SANDWICH PLATES

Riad M. Shahin

Gibbs & Hill, Inc.

393 Seventh Avenue, New York, New York 10001

A system of differential equations for the large amplitude free and forced vibrations of a multilayer sandwich plate is derived by variational principles. The plate consists of n isotropic faces and (n-1) orthotropic cores having different thicknesses and elastic properties. When the faces are assumed to possess equal Poisson's ratio, the system of equations is reduced to two equations involving the transverse deflection w, and a membrane stress function ϕ. Assuming the existence of harmonic vibrations, the time variable is eliminated by employing a technique analogous to that used by Van der Pol. Using double trigonometric series, solutions for a simply supported rectangular plate are presented. Newton's generalized method is used in solving the resulting nonlinear algebraic equations, and convergence proved to be quite rapid. The dynamic response curves of the plate are presented. A behavior similar to that of Duffing's hard spring is evident, and it is found that the stress resultants are nonlinear functions of the relative amplitude at the center of the plate. The influence of the nondimensional parameters is studied and illustrated.

INTRODUCTION

Lightweight structures which have high strength and stiffness properties fulfill the requirements of many structural design problems. Therefore, sandwich constructions, which are characteristically lightweight and comparatively rigid, are being given increasing consideration for varied applications, such as in the primary structure for ballistic missiles and space vehicles, secondary structures for airplanes, and wall panels in building construction.

In the design of sandwich plates that vibrate under lateral and edge loading, formulas based on the Kirchhoff theory which neglects stretching and shearing in the middle surface are quite satisfactory provided that the amplitudes are small compared with the thickness. If the amplitudes of motion are of the same order of magnitude as the thickness, the Kirchhoff theory may yield results that are considerably in error. A more rigorous theory that takes into account the effects of the deformations in the middle surface and the transverse shear should be applied.

The small amplitude vibrations of the single-sandwich plates have been extensively studied by many investigators [1-17]. The large amplitude vibrations of a single-sandwich plate have received limited attention. Yu [18] derived a set of nonlinear equations, describing the vibrations of sandwich plates, from the variational equation of motion of the nonlinear theory of elasticity. Ebcioglu [19] extended the variational procedure used by Yu to derive the equations of motion and the boundary conditions of sandwich panels subjected to large displacements and large angles of rotation.

The aforementioned investigations have been restricted to single-sandwich plates. For multilayer rectangular sandwich plates only static problems have been considered. Among the investigators of static problems are Liaw and Little [20] who investigated the bending of multilayer sandwich plates with isotropic faces and orthotropic cores. Wong and Salama [21] considered the static stability of sandwich plates with isotropic faces and orthotropic cores. Azar [22] extended Liaw's problem to a plate with orthotropic faces.

Recently, multilayer sandwich plates have been used extensively in the aeronautical industries and building construction. For proper design it is important to study the dynamic behavior of multilayer sandwich construction. Thus, the present paper studies the free and forced vibrations of a rectangular multilayer sandwich plate at finite amplitude. Using the principle of complementary energy, a set of governing equations is obtained for multilayer sandwich plate consisting of n faces and (n-1) cores having different thicknesses and elastic moduli. If the faces of the plate are assumed to have equal Poisson's ratio, the set of equations is reduced to a pair of equations of sixth order and fourth order involving the transverse deflection and the membrane stress function. Harmonic vibrations are assumed and the time variable is eliminated. For a simply supported plate a double trigonometric series is used to reduce the remaining nonlinear eigen-value problem to a set of cubic equations. Figures are presented which show the effects of core orthotropicity, core shear modulus, and aspect ratio, on the free resonance frequency. The influence of large amplitude on the stress resultants

is established. The accuracy of the method is assessed by comparison of solutions obtained by using three and six deflection coefficients.

GENERAL ANALYSIS

Consider a rectangular plate consisting of n faces of thickness $t_1, t_2, \ldots, t_n$, and $(n-1)$ cores of thicknesses $h_1, h_2, \ldots, h_{n-1}$ as shown in Fig. 1. The xy reference plane is assumed to be parallel to the underformed surface of the plate, and its position is chosen so that the first moment of the transformed area is equal to zero, i.e.

$$z = \sum_{i=1}^{n} \frac{E_i t_i z_i}{1 - \nu_i^2} = 0 \tag{1}$$

where E_i and ν_i are Young's modulus and Poisson's ratio of the ith face, respectively, and z_i is the distance measured from the middle plane of the ith face to the xy plane.
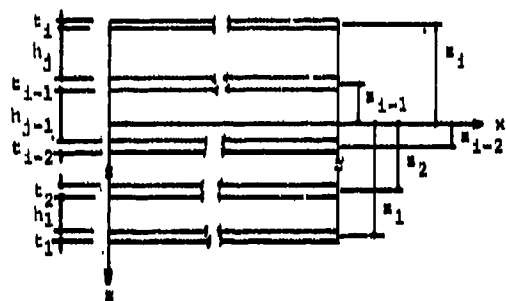
Fig. 1   A Cross Section of the Plate

The assumptions used in this analysis are:
i) The faces are homogeneous, isotropic, and elastic thin plates of different thicknesses and/or materials, and they resist normal and in-plane shearing stresses only.
ii) The cores are orthotropic, elastic media, and carry only the transverse shear which is uniformly distributed over the thickness.
iii) The total thickness of the plate is small in comparison to the other dimensions.
iv) The effect of the rotatory and in-plane inertias on the natural frequencies are neglected.
v) All the bonds between layers are strong enough that under loadings no bond failure will occur and the stresses can be transmitted without discontinuity.
vi) The magnitude of the deflection w is of the same order as the thickness of the plate, but small compared with the in-plane dimensions.
vii) The in-plane displacements, u and v are infinitesimal. In the strain-displacement relations only those nonlinear terms which depend on $w_{,x}$ and $w_{,y}$ are retained. All other nonlinear terms are neglected.
Consider the differential plate element shown in Fig. 2. The equations defining the stress resultants are:

$$\left[M_x , M_y , M_{xy} \right] - \sum_{i=1}^{n} t_i z_i \left[\sigma_{ix} , \sigma_{iy} , \sigma_{ixy} \right] = 0 \tag{2}$$

$$\left[Q_x , Q_y \right] - \sum_{j=1}^{n} h_j \left[\tau_{jxz} , \tau_{jyz} \right] = 0 \tag{3}$$

$$\left[N_x , N_y , N_{xy} \right] - \sum_{i=1}^{n} t_i \left[\sigma_{ix} , \sigma_{iy} , \sigma_{ixy} \right] = 0 \tag{4}$$

Equilibrium of forces and moments on a differential plate element leads to

$$N_{x',x} + N_{xy',y} = 0 \tag{5}$$

$$N_{y',y} + N_{xy',x} = 0 \tag{6}$$

$$(N_x w_{,x} + N_{xy} w_{,y})_{,x} + (N_y w_{,y} + N_{xy} w_{,x})_{,y}$$
$$- \mu w_{,tt} + Q + Q_{x',x} + Q_{y',y} = 0 \tag{7}$$

$$M_{y',y} + M_{xy',x} - Q_y = 0 \tag{8}$$

$$M_{x',x} + M_{xy',y} - Q_x = 0 \tag{9}$$

where a comma designates a partial derivative, and μ is the mass per unit area of the plate.
Combining Equations (5), (6) and (7) results in

$$Q_{x',x} + Q_{y,y} + P = 0 \tag{10}$$

where

$$P = Q - \mu w_{,tt} + N_x w_{,xx} + 2 N_{xy} w_{,xy} + N_y w_{,yy} \tag{11}$$

The complementary energy of the plate is

$$V = \frac{1}{2} \int_0^a \int_0^b \left\{ \sum_{i=1}^{n} t_i \left[\frac{1}{E_i} (\sigma_{ix}^2 + \sigma_{iy}^2 - 2\nu_i \sigma_{ix}\sigma_{iy}) + \frac{\sigma_{ixy}^2}{G_{ixy}} \right] \right.$$

$$\left. + \sum_{j=1}^{n-1} h_j \left[\frac{\tau_{jxz}^2}{G_{jxz}} + \frac{\tau_{jyz}^2}{G_{jyz}} \right] \right\} dx\,dy +$$

$$+ \frac{1}{2} \int \int \left\{ N_x (w_{,x})^2 + 2 N_{xy} w_{,x} w_{,y} + N_y (w_{,y})^2 \right\} dx\,dy$$

$$- \int_{0_d} \left\{ \overline{X} u + \overline{Y} v + (\overline{X} w_{,x} + \overline{Y} w_{,y} + \overline{Z}) w + \overline{M}_x \alpha \right.$$

$$\left. + \overline{M}_y \beta \right\} ds \tag{12}$$

where the first integral represents the complementary energy inside the domain; the second integral designates the work done by the membrane stress resultants due to large deflection; and the third integral is the work done by the stress resultants on the part of the boundary o_d where the displacements are specified. G_{jxz} and G_{jyz} are the shear moduli of the jth core, G_{ixy} is the shear modulus of the ith face, a and b are the plate dimensions. The capital bar letters indicate the total resultants in a specific
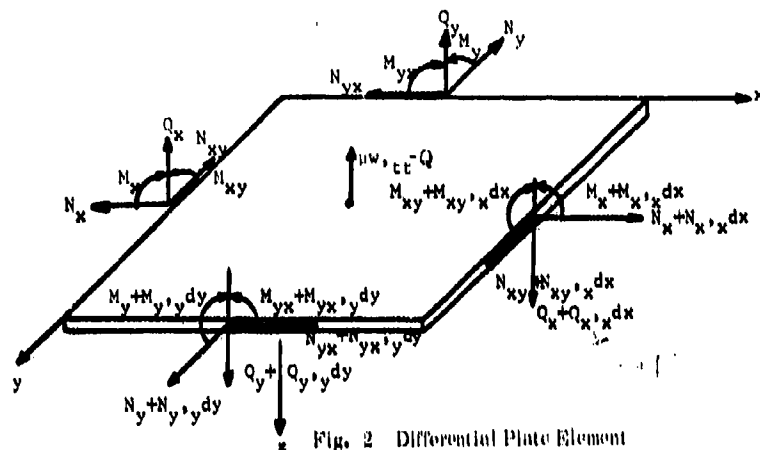
Fig. 2 Differential Plate Element

direction along the boundary. For example, $\bar{X}$ represents N_x on $x = 0$ and $x = a$, while it represents N_{yx} on $y = 0$ and $y = b$. u, v, w, α and β are the generalized displacements.

Thus, the problem becomes one of finding the conditions which extremalize the function V of Equation (12) subject to the constraints of Equations (2-9). Introducing thirteen Lagrangian multipliers λ_k the auxiliary functional can be written as

$$I = V + \int_0^b \int_0^a \sum_{k=1}^{13} \lambda_k g_k \, dx \, dy \tag{13}$$

where g_k denotes the functions defined by Equations (2-9), respectively. The first variation of the auxiliary functional vanishes; i.e. $\delta I = 0$. Carrying out the first variation of I and integrating by parts, one obtains

$$\delta I = \int_0^b \int_0^a \left\{ \sum_{i=1}^n \left[\frac{t_i}{E_i}(\sigma_{ix} - \nu_i \sigma_{iy}) - \lambda_1 t_i z_i - \lambda_4 t_i \right] \delta\sigma_{ix} \right.$$

$$+ \sum_{i=1}^n \left[\frac{t_i}{E_i}(\sigma_{iy} - \nu_i \sigma_{ix}) - \lambda_2 t_i z_i - \lambda_5 t_i \right] \delta\sigma_{iy}$$

$$+ \sum_{i=1}^n \left(-\frac{t_i}{G_{ixy}} \sigma_{ixy} - \lambda_3 t_i z_i - \lambda_6 t_i \right) \delta\sigma_{ixy} +$$

$$\sum_{j=1}^{n-1} \left(\frac{h_j}{G_{jxz}} \tau_{jxz} - \lambda_7 h_j \right) \delta\tau_{jxz} + \sum_{j=1}^{n-1} \left(\frac{h_j}{G_{jyz}} \tau_{jyz} - \lambda_8 h_j \right) \delta\tau_{jyz}$$

$$+ (\lambda_1 - \lambda_{12',x}) \delta M_x + (\lambda_2 - \lambda_{13',y}) \delta M_y + (\lambda_3 - \lambda_{12',y} - \lambda_{13',x}) \delta M_{xy} + \left[\lambda_4 - \lambda_{9',x} - \lambda_{11',x} w_{,x} + \frac{1}{2}(w_{,x})^2 \right] \delta N_x +$$

$$\left[\lambda_5 - \lambda_{10',y} - \lambda_{11',y} w_{,y} + \frac{1}{2}(w_{,y})^2 \right] \delta N_y + \left[\lambda_6 - \lambda_{11',x} w_{,y} - \right.$$

$$\left. \lambda_{11',y} w_{,x} - \lambda_{9',y} - \lambda_{10',x} + w_x w_y \right] \delta N_{xy} + (\lambda_7 - \lambda_{11',x} - \lambda_{12}) \delta Q_x$$

$$+ (\lambda_8 - \lambda_{11',y} - \lambda_{13}) \delta Q_y \bigg\} \, dx \, dy +$$

$$\int_{S_d} \left\{ \lambda_9 \delta\bar{X} + \lambda_{10} \delta\bar{Y} + \lambda_{11}(w_{,x} \delta\bar{X} + w_{,y} \delta\bar{Y} + \delta\bar{Z}) \right.$$

$$+ \lambda_{12} \delta\bar{M}_x + \lambda_{13} \delta\bar{M}_y \bigg\} \, ds - \int_{S_d} \bigg\{ u\,\delta\bar{X} + v\,\delta\bar{Y} +$$

$$w(w_{,x} \delta\bar{X} + w_{,y} \delta\bar{Y} + \delta\bar{Z}) + \alpha\,\delta\bar{M}_x + \beta\,\delta\bar{M}_y \bigg\} ds = 0 \tag{14}$$

The vanishing of the surface integral yields thirteen Euler's equations:

$$\frac{t_i}{E_i}(\sigma_{ix} - \nu_i \sigma_{iy}) - \lambda_1 z_i - \lambda_4 = 0 \tag{15}$$

$$\frac{t_i}{E_i}(\sigma_{iy} - \nu_i \sigma_{ix}) - \lambda_2 z_i - \lambda_5 = 0 \tag{16}$$

$$\frac{\sigma_{ixy}}{G_{ixz}} - \lambda_3 z_i - \lambda_6 = 0 \tag{17}$$

$$\frac{\tau_{jxz}}{G_{jxz}} - \lambda_7 = 0 \tag{18}$$

$$\frac{\tau_{jyz}}{G_{jyz}} - \lambda_8 = 0 \tag{19}$$

$$\lambda_1 - \lambda_{12',x} = 0 \tag{20}$$

$$\lambda_2 - \lambda_{13',y} = 0 \tag{21}$$

$$\lambda_3 - \lambda_{12',y} - \lambda_{13',x} = 0 \tag{22}$$

45

$$\lambda_4 - \lambda_{9,x} - \lambda_{11,x} w_{,x} + \frac{1}{2}(w_{,x})^2 = 0 \qquad (23)$$

$$\lambda_5 - \lambda_{10,y} - \lambda_{11,y} w_{,y} + \frac{1}{2}(w_{,y})^2 = 0 \qquad (24)$$

$$\lambda_6 - \lambda_{11,x} w_{,y} - \lambda_{11,y} w_{,x} - \lambda_{9,y} - \lambda_{10,x} + w_{,x} w_{,y} = 0 \qquad (25)$$

$$\lambda_7 - \lambda_{11,x} - \lambda_{12} = 0 \qquad (26)$$

$$\lambda_8 - \lambda_{11,y} - \lambda_{13} = 0 \qquad (27)$$

Since the line integrals must be zero, one obtains the following boundary conditions on the boundary

$$\lambda_9 = u \qquad (28)$$

$$\lambda_{10} = v \qquad (29)$$

$$\lambda_{11} = w \qquad (30)$$

$$\lambda_{12} = \alpha \qquad (31)$$

$$\lambda_{13} = \beta \qquad (32)$$

Combining Eqs. (15 - 19), (20 - 32) and Eqs. (2 - 4), results in the following equations for the generalized forces:

$$M_x = A\left[C\beta_{,y} + \alpha_{,x}\right] + D\left[v_{,y} + \frac{1}{2}(w_{,y})^2\right] \qquad (33)$$

$$M_y = A\left[C\alpha_{,x} + \beta_{,y}\right] + D\left[u_{,x} + \frac{1}{2}(w_{,x})^2\right] \qquad (34)$$

$$M_{xy} = H_x\left[\alpha_{,y} + \beta_{,x}\right] + H_y\left[v_{,x} + u_{,y} + w_{,x} w_{,y}\right] \qquad (35)$$

$$N_x = B\left\{F\left[v_{,y} + \frac{1}{2}(w_{,y})^2\right] + \left[u_{,x} + \frac{1}{2}(w_{,x})^2\right]\right\} +$$

$$D\beta_{,y} \qquad (36)$$

$$N_y = B\left\{F\left[u_{,x} + \frac{1}{2}(w_{,x})^2\right] + \left[v_{,y} + \frac{1}{2}(w_{,y})^2\right]\right\} + D\alpha_{,x} \qquad (37)$$

$$N_{xy} = H_y\left[\alpha_{,y} + \beta_{,x}\right] + H_z\left[v_{,x} + u_{,y} + w_{,x} w_{,y}\right] \qquad (38)$$

$$Q_x = G_x(w_{,x} + \alpha) \qquad (39)$$

$$Q_y = G_y(w_{,y} + \beta) \qquad (40)$$

where

$$\left[A, B, D\right] = \sum_{i=1}^{R} \frac{t_i E_i}{1 - \nu_i^2}\left[z_i^2, 1, z_i \nu_i\right]$$

$$\left[C, F\right] = \frac{1}{\left[A, B\right]} \sum_{i=1}^{R} \frac{t_i E_i \nu_i}{1 - \nu_i^2}\left[z_i^2, 1\right] \qquad (41)$$

$$\left[H_x, H_y, H_z\right] = \sum_{i=1}^{R} t_i G_{ixy}\left[z_i^2, z_i, 1\right]$$

$$\left[G_x, G_y\right] = \sum_{i=1}^{R} h_i\left[G_{ixz}, G_{iyz}\right]$$

Substitution of Eqs. (33 - 40) into Eqs. (5 - 9) results in five nonlinear differential equations which govern the vibration of the problem under consideration.

$$Bu_{,xx} + H_z \alpha_{,yy} + H_y \alpha_{,yy} + (H_x + BF)v_{,xy} +$$
$$(D + H_y)\beta_{,xy} + Bw_{,x} w_{,xx} + H_z w_{,x} w_{,yy} +$$
$$(H_z + BF)w_{,y} w_{,xy} = 0 \qquad (42)$$

$$Bv_{,yy} + H_z v_{,xx} + H_y \beta_{,xx} + (H_z + BF)u_{,xy} +$$
$$(D + H_y)\alpha_{,xy} + Bw_{,y} w_{,yy} + H_z w_{,y} w_{,xx} +$$
$$(H_z + BF)w_{,x} w_{,xy} = 0 \qquad (43)$$

$$G_x(w_{,xx} + \alpha_{,x}) + G_y(w_{,yy} + \beta_{,y}) + Q - \mu w_{,tt} +$$
$$D(w_{,xx}\beta_{,y} + w_{,yy}\alpha_{,x}) + B\left\{F\left[v_{,y} + \frac{1}{2}(w_{,y})^2\right]\right.$$
$$\left. + \left[u_{,x} + \frac{1}{2}(w_{,x})^2\right]\right\}w_{,xx} +$$
$$2w_{,xy}\left\{H_y(\alpha_{,y} + \beta_{,x}) + H_z(v_{,x} + u_{,y} +\right.$$

46

$$w_{,x}w_{,y})\} + B\left\{F\left[u_{,x} + \frac{1}{2}(w_{,x})^2\right] + \left[v_{,y} + \frac{1}{2}(w_{,y})^2\right]\right\}w_{,yy} = 0 \qquad (44)$$

$$H_x \beta_{,xx} + A\beta_{,yy} + (H_x + AC)\alpha_{,xy} + H_y v_{,xx}$$
$$+ (H_y + D)u_{,xy} + (H_y + D)w_{,x}w_{,xy} + H_y w_{,y}w_{,xx}$$
$$- G_y(\beta + w_{,y}) = 0 \qquad (45)$$

$$H_x \alpha_{,yy} + A\alpha_{,xx} + (H_x + AC)\beta_{,xy} + H_y u_{,yy}$$
$$+ (H_y + D)v_{,xy} + (H_y + D)w_{,y}w_{,xy} + H_y w_{,x}w_{,yy}$$
$$- G_x(\alpha + w_{,x}) = 0 \qquad (46)$$

In the static sense, Eqns. (42 - 46) agree with the governing equations obtained by Wong and Salama [21] using linear theory.

REDUCTION OF THE PROBLEM FOR A SPECIAL CASE

For simplicity, the faces of a plate are assumed to have equal Poisson's ratios, $\nu_1 = \nu_2 = \nu_0 = \nu$. Thus, Eqns. (33 - 40) can be reduced to the following form:

$$M_x = A(\alpha_{,x} + \nu\beta_{,y}) \qquad (47)$$

$$M_y = A(\beta_{,y} + \nu\alpha_{,x}) \qquad (48)$$

$$M_{xy} = \frac{A(1-\nu)}{2}(\alpha_{,y} + \beta_{,x}) \qquad (49)$$

$$N_x = B\left\{\left[u_{,x} + \frac{1}{2}(w_{,x})^2\right] + \nu\left[v_{,y} + \frac{1}{2}(w_{,y})^2\right]\right\} \qquad (50)$$

$$N_y = B\left\{\left[v_{,y} + \frac{1}{2}(w_{,y})^2\right] + \nu\left[u_{,x} + \frac{1}{2}(w_{,x})^2\right]\right\} \qquad (51)$$

$$N_{xy} = \frac{B(1-\nu)}{2}(v_{,x} + u_{,y} + w_{,x}w_{,y}) \qquad (52)$$

$$Q_x = G_x(w_{,x} + \alpha) \qquad (53)$$

$$Q_y = G_y(w_{,y} + \beta) \qquad (54)$$

Introducing a stress function ϕ, i.e., $N_x = \phi_{,yy}$, $N_y = \phi_{,xx}$, $N_{xy} = -\phi_{,xy}$, and by eliminating u and v from Eqns. (50 - 52) one obtains

$$\nabla^4\phi + \frac{B(1-\nu^2)}{2}L(w,w) = 0 \qquad (55)$$

where

$$L(w,w) = 2\left[w_{,xx}w_{,yy} - (w_{,xy})^2\right] \qquad (56)$$

Employment of the method used by Cheng [23] for eliminating the transverse shear resultants yields

$$A\left[1 - K_y\frac{\partial^2}{\partial x^2} - K_x\frac{\partial^2}{\partial y^2}\right]\nabla^4 w = \left[1 - (K_y + \frac{2K_x}{1-\nu})\frac{\partial^2}{\partial x^2} - (K_x + \frac{2K_y}{1-\nu})\frac{\partial^2}{\partial y^2} + \frac{2K_x K_y}{1-\nu}\nabla^4\right]\left[-\mu w_{,tt} + Q + L(\phi,w)\right] \qquad (57)$$

where

$$\left.\begin{array}{l} [K_x, K_y] = \frac{A(1-\nu)}{2}\left[\frac{1}{G_x}, \frac{1}{G_y}\right] \\ L(\phi,w) = \phi_{,yy}w_{,xx} - 2\phi_{,xy}w_{,xy} + \phi_{,xx}w_{yy} \end{array}\right\} \qquad (58)$$

Equations (55) and (57) are the dynamic analogs of Von Karman equations for homogeneous isotropic plates. In the static sense, Eqns. (55) and (57) agree with the equations derived by Ueng [24] for a single - sandwich plate. By deleting the nonlinear operator L, Eq. (57) is reduced to the one obtained by Jacobson [9] for a single sandwich plate.

SOME EXAMPLES

Vibration of a Multilayer Sandwich Plate

Consider the vibration of a simply supported multilayer sandwich plate whose faces have equal Poisson's ratios. Taking coordinate axes x and y along the edges of the plate, the boundary conditions are

$$\left.\begin{array}{l} w = \beta = M_x = 0 \text{ at } x = 0 \text{ and } x = a \\ w = \alpha = M_y = 0 \text{ at } y = 0 \text{ and } y = b \end{array}\right\} (59)$$

These conditions are satisfied if w, α, and β are taken in the form,

$$w = a\sum_m^\infty\sum_n^\infty W_{mn}\sin\frac{m\pi x}{a}\sin\frac{n\pi y}{b}\sin\omega t \qquad (60)$$

$$\alpha = \sum_m^\infty\sum_n^\infty A_{mn}\cos\frac{m\pi x}{a}\sin\frac{n\pi y}{b}\sin\omega t \qquad (61)$$

$$\beta = \sum_m^\infty\sum_n^\infty B_{mn}\sin\frac{m\pi x}{a}\cos\frac{n\pi y}{b}\sin\omega t \qquad (62)$$

47

By substitution of Eq. (60) into Eq. (55), it is found that the latter equation is satisfied if the expression for the stress function is taken as

$$\phi = \frac{a^2 B (1-\nu^2)}{2} \sum_m^\infty \sum_n^\infty \phi_{mn} \cos \frac{m\pi x}{a} \cos \frac{n\pi y}{b} \sin^2 \omega t$$

(63)

For a uniform load q the forcing function may be expressed in the form of a double Fourier series as

$$Q = \frac{16q}{\pi^2} \sum_m^\infty \sum_n^\infty \frac{1}{mn} \sin \frac{m\pi x}{a} \sin \frac{n\pi y}{b} \sin \omega t$$

(64)

Substitution of Eqs. (60) and (63) into Eq. (55) results in

$$\sum_m \sum_n \phi_{mn}^* \left(\frac{m^2}{\rho} + n^2 \rho \right)^2 \cos \frac{m\pi x}{a} \cos \frac{n\pi y}{b} =$$
$$\frac{1}{4} \sum_r \sum_s \sum_p \sum_q W_{rs} W_{pq} \left\{ (rq+sp)^2 \left[\cos(r-p) \frac{\pi x}{a} \cos(s+q) \frac{\pi y}{b} \right. \right.$$
$$\left. + \cos(r+p) \frac{\pi x}{a} \cos(s-q) \frac{\pi y}{b} \right] -$$
$$(rq-sp)^2 \left[\cos(r-p) \frac{\pi x}{a} \cos(s-q) \frac{\pi y}{b} + \right.$$
$$\left. \left. \cos(r+p) \frac{\pi x}{a} \cos(s+q) \frac{\pi y}{b} \right] \right\}$$

(65)

where

$$\phi_{mn}^* = \frac{a^2}{d^2} \phi_{mn} \;, \qquad W_{rs} = \frac{d}{d} w_{rs} \;,$$
$$d = z_1 + z_1$$

(66)

$$m, n = 0, 2, 4, \ldots$$
$$r, s, p, q = 1, 2, 3, \ldots$$

Substitution of Eqs. (60) and (63 - 64) into Eq. (57), use of the identity $\sin^3 \theta = 3/4 \sin\theta - 1/4 \sin 3\theta$, and equation of the coefficients of $\sin \omega t$ leads to

$$\sum_m \sum_n W_{mn} \left\{ (T_1 + \gamma m^2 + \rho^2 n^2)(m^2 + \rho^2 n^2)^2 - (\Omega^2 + \frac{Q^*}{mn W_{mn}}) \left[T_1 + m^2(\gamma + \frac{2}{1-\nu}) + n^2 \rho^2 (1 + \frac{2\gamma}{1-\nu}) + \frac{2\gamma}{(1-\nu)T_1} (m^2 + \rho^2 n^2)^2 \right] \right\} \sin \frac{m\pi x}{a} \sin \frac{n\pi y}{b} =$$
$$\frac{3(1-\nu^2) \rho^2 H}{32} \sum_r \sum_s \sum_p \sum_q \phi_{rs}^* W_{pq} \left((qr-sp)^2 \left\{ T_1 \right. \right.$$
$$+ (\gamma + \frac{2}{1-\nu})(p+r)^2 + \rho^2 (1 + \frac{2\gamma}{1-\nu})(q+s)^2 +$$
$$\frac{2\gamma}{(1-\nu)T_1} \left[(p+r)^2 + \rho^2(q+s)^2 \right]^2 \right\} \sin(p+r) \frac{\pi x}{a} \sin(q+s) \frac{\pi y}{b}$$
$$+ (qr+sp)^2 \left\{ T_1 + (\gamma + \frac{2}{1-\nu})(p+r)^2 + \rho^2 (1 + \frac{2\gamma}{1-\nu})(q-s)^2 \right.$$
$$+ \frac{2\gamma}{(1-\nu)T_1} \left[(p+r)^2 + \rho^2(q-s)^2 \right]^2 \right\} \sin(p+r) \frac{\pi x}{a} \sin(q-s) \frac{\pi y}{b}$$

$$+ (qr+sp)^2 \left\{ T_1 + (\gamma + \frac{2}{1-\nu})(p-r)^2 + \right.$$
$$\rho^2 (1 + \frac{2\gamma}{1-\nu})(q+s)^2 + \frac{2\gamma}{(1-\nu)T_1} \left[(p-r)^2 + \right.$$
$$\left. \rho^2 (q+s)^2 \right]^2 \right\} \sin(p-r) \frac{\pi x}{a} \sin(q+s) \frac{\pi y}{b} +$$
$$(qr-sp)^2 \left\{ T_1 + (\gamma + \frac{2}{1-\nu})(p-r)^2 + \rho^2 (1 + \frac{2\gamma}{1-\nu})(q-s)^2 \right.$$
$$\left. + \frac{2\gamma}{(1-\nu)T_1} \left[(p-r)^2 + \rho^2(q-s)^2 \right]^2 \right\} \sin(p-r) \frac{\pi x}{a} \sin(q-s) \frac{\pi y}{b} \right)$$

(67)

where

$$H = \frac{d^2 B}{A} \;, \qquad \gamma = \frac{G_1}{G_y} \;, \quad T_1 = \frac{2a^2 G_1}{\pi^2 (1-\nu) A} \;,$$
$$\Omega = \omega (\frac{\mu}{A})^{1/4} (\frac{a}{\pi})^2 \;, \qquad Q^* = \frac{16 a^4 q}{\pi^6 A d} \;,$$
$$m, n, p, q = 1, 2, 3, \ldots ; r, s = 0, 2, 4, \ldots$$

(68)

Equation (67) represents a doubly infinite family of equations. In each of the equations of the family the stress coefficients may be replaced by their values as given by Eq. (65). The resulting equations involve the known normal pressure coefficients, the cubes of the deflection coefficients, and the frequency. The number of these equations is equal to the number of unknown deflection coefficients. If the first six deflection coefficients are considered one obtains six cubic equations. The six cubic equations are solved using Newton's generalized method.

Initially, the problem of free vibrations is considered ($Q^* = 0$). Small values are assigned to W_{11}, W_{13}, W_{31}, W_{33}, W_{15}, and W_{51} while the initial value for Ω is extracted from linear theory. Holding W_{11} constant, the values of W_{13}, W_{31}, W_{33}, W_{15}, W_{51}, and Ω are corrected until the components of the error vector are within a range of allowable error. The correction vector is equal to the inverse of the Jacobian matrix times the error vector. The corresponding solution is recorded. By continually incrementing W_{11} and starting iteration for each increment from the previously obtained values, the resonance curve and accompanying solutions are found. Having obtained the resonance curve, the response due to forced oscillation can be obtained by a perturbation technique. By setting $W_{11} = 1.5$ and applying a small load Q^*, the response can be easily determined. $Q^*(x,y) < 0$ if the response is 180 degrees out of phase with the load, and $Q^*(x,y) > 0$ if the response is in phase with the load. With $Q^*(x,y)$ held constant, W_{11} is decremented as iteration yields subsequent solutions to the forced vibration problem.

Having obtained the deflection coefficients, the membrane stress resultants evaluated at $t = \frac{\pi}{2\omega}$ are

$$N_x^* = -\sum_{m=0,2} \sum_{n=0,2} n^2 \phi_{mn}^* \cos \frac{m\pi x}{a} \cos \frac{n\pi y}{b}$$
$$N_y^* = -\sum_{m=0,2} \sum_{n=0,2} \frac{m^2}{\rho^2} \phi_{mn}^* \cos \frac{m\pi x}{a} \cos \frac{n\pi y}{b}$$

$$N_{xy}^{\#} = -\sum_{m=0,2}^{\infty} \sum_{n=0,2}^{\infty} \frac{mn}{\rho^2} \phi_{mn}^{*} \sin \frac{m\pi x}{a} \sin \frac{n\pi y}{b}$$

(69)

where

$$N_x^{*} = \frac{2a^2 N_x}{\rho^2 \pi^2 d^2 B(1-\nu^2)}, \qquad N_y^{*} = \frac{2a^2 N_y}{\rho^2 \pi^2 d^2 B(1-\nu^2)},$$

$$N_{xy}^{*} = \frac{2a^2 N_{xy}}{\rho^3 \pi^2 d^2 B(1-\nu^2)},$$

(70)

Introduction of Eq. (60) into Eqs. (A-3) and (A-4) yields

$$A_{mn} = -m\pi \frac{R_1}{R_3} w_{mn}, \quad B_{mn} = -\rho n\pi \frac{R_2}{R_3} w_{mn},$$

(71)

where

$$R_1 = \left\{ \frac{(1-1/\gamma)}{(1-\nu)} (n^2\rho^2) + \frac{(m^2+n^2\rho^2)}{(1+\nu)} + \frac{T_1}{\gamma(1+\nu)} \right\}$$

$$R_2 = \left\{ \frac{(1/\gamma-1)}{(1-\nu)} m^2 + \frac{(m^2+n^2\rho^2)}{\gamma(1+\nu)} + \frac{T_1}{\gamma(1+\nu)} \right\}$$

$$R_3 = \left\{ \frac{2(m^2+n^2\rho^2)^2}{1(1-\nu^2)} + \frac{(1+1/\gamma)}{(1+\nu)} (m^2+n^2\rho^2) + \frac{(m^2\gamma+n^2\rho^2)}{(1-\nu)} \right.$$

$$\left. + \frac{T_1}{\gamma(1+\nu)} \right\}$$

(72)

Having determined A_{mn} and B_{mn}, the expressions for M_x, M_y, M_{xy}, Q_x, and Q_y at $t = \frac{\pi}{2\omega}$ are

$$M_x^{\#} = \sum_{m=1,3}^{\infty} \sum_{n=1,3}^{\infty} \frac{(m^2 R_1 + \nu n^2 \rho^2 R_2)}{R_3} W_{mn} \sin\frac{m\pi x}{a} \sin\frac{n\pi y}{b}$$

$$M_y^{\#} = \sum_{m=1,3}^{\infty} \sum_{n=1,3}^{\infty} \frac{(m^2\nu R_1 + n^2\rho^2 R_2)}{R_3} W_{mn} \sin\frac{m\pi x}{a} \sin\frac{n\pi y}{b}$$

$$M_{xy}^{\#} = -\sum_{m=1,3}^{\infty} \sum_{n=1,3}^{\infty} \frac{mn(R_1+R_2)}{R_3} W_{mn} \cos\frac{m\pi x}{a} \cos\frac{n\pi y}{b}$$

$$Q_x^{*} = \sum_{m=1,3}^{\infty} \sum_{n=1,3}^{\infty} m\left(1-\frac{R_1}{R_3}\right) W_{mn} \cos\frac{m\pi x}{a} \sin\frac{n\pi y}{b}$$

$$Q_y^{*} = \sum_{m=1,3}^{\infty} \sum_{n=1,3}^{\infty} n\left(1-\frac{R_2}{R_3}\right) W_{mn} \sin\frac{m\pi x}{a} \cos\frac{n\pi y}{b}$$

(73)

where

$$M_x^{\#} = \frac{a^2 M_x}{\pi^2 dA}, \qquad M_y^{\#} = \frac{a^2 M_y}{\pi^2 dA},$$

$$Q_x^{*} = \frac{a Q_x}{\pi d G_x}, \qquad Q_y^{*} = \frac{a Q_y}{\pi d\rho G_y},$$

$$M_{xy}^{\#} = \frac{2a^2 M_{xy}}{A\pi^2 \rho d(1-\nu)}$$

(74)

NUMERICAL RESULTS AND DISCUSSION

The solution of the two nonlinear differential equations governing the motion of a multilayer sandwich plate with isotropic faces and orthotropic cores was accomplished by means of trigonometric series. The resulting cubic equations were solved by means of Newton's generalized method using the IBM 360-50 digital computer and convergence proved to be quite rapid.

Figure (3) shows the nonlinear response as is commonly found for the forced oscillation of a single degree of freedom Duffing [25] system. The points of vertical tangency (J_1, J_2) are points which give rise to a jump phenomenon commonly found in nonlinear vibratory systems.
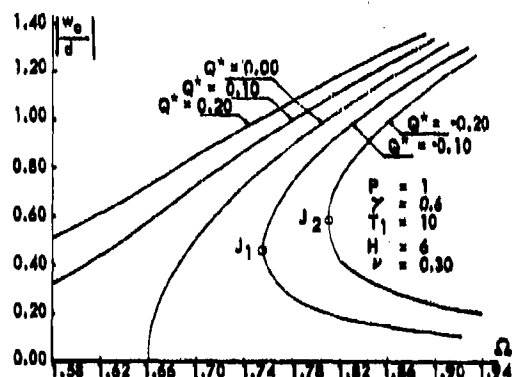
Fig. 3. Response curves for a multilayer sandwich plate with isotropic faces and equal Poisson's ratios.

Figure (4) depicts the increased nonlinearity in the response curves as the aspect ratio is increased. From this one concludes that the membrane influence is more significant in a rectangular plate than in a square plate.

From Figure (4) it is apparent that the nonlinearity is greater for smaller values of the core shear modulus T_1. Large values of T_1 indicate a relatively rigid core. Likewise, small values of T_1 correspond to a relatively less rigid core. A reduction in the core rigidity places increased emphasis upon the support of the plate by membrane influence. Thus the nonlinearity decreases with an increase of T_1.

Figure (4) shows the effect of the orthotropicity, γ, of the core on the resonance frequency for a fixed value of T_1. If T_1 is fixed then G_x is fixed. Hence, a decrease in γ corresponds to an increase in G_y. This leads to the conclusion that the shear influence is more important, and the nonlinearity is reduced. $\gamma = 0.60$ is a typical value for aluminum and stainless steel honeycomb cores, $\gamma = 0.20$ is typical for a material with high orthotropicity, and $\gamma = \ldots$ is the value for an isotropic core.

Figures (5-8) show the rapid increase of the stress resultants with amplitude. The membrane stress resultants are nonlinear functions of the transverse deflection

coefficients W_{ij}, whereas the bending and transverse shear resultants are linear functions of the W_{ij}. However, all the stress resultants are nonlinear functions of the relative amplitude at the center of the plate.
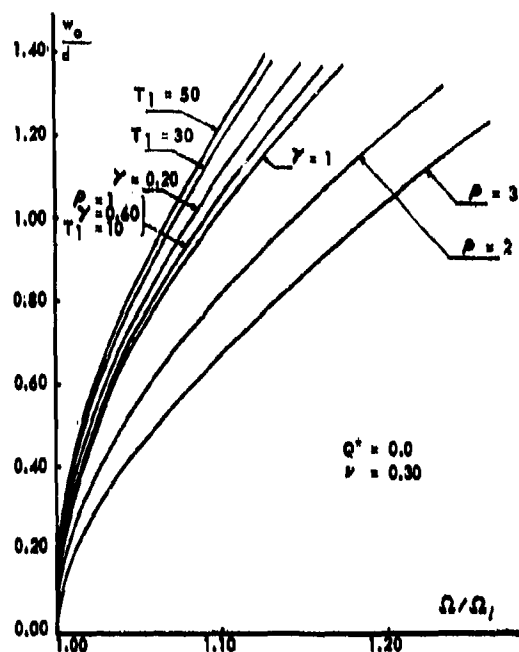
Fig. 4. Effects of aspect ratio, core orthotropicity, and core shear modulus.
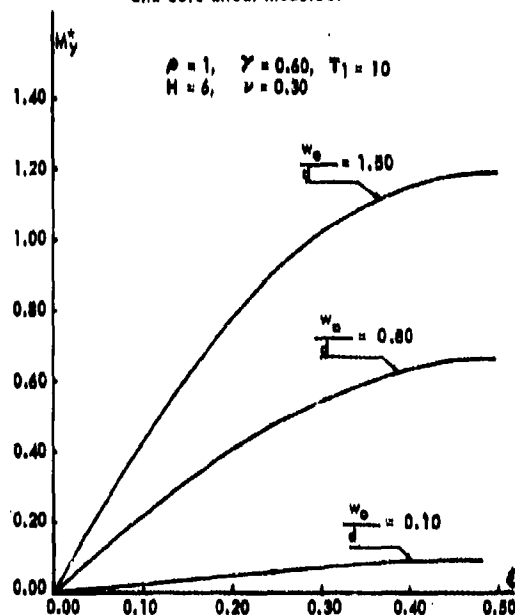
Fig. 5. Bending stress resultant across the section y = b/2
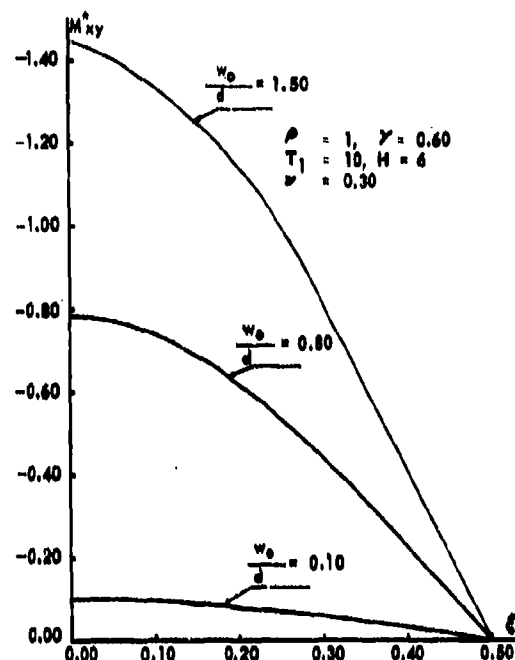
Fig. 6. Twisting moment stress resultant M_{xy}^* across the section y = b/4

CONCLUSION

The assumption of a finite number of coefficients in the solution of the example problems introduces an error into the solution. As a measure of the error resulting from the use of only six of the equations in the foregoing solution, the results obtained by using three, and six equations of the family are given in Tables 1 and 2. It is evident that for a square plate the results obtained by the first three of six deflection coefficients are in good agreement. However, use of the first three deflection coefficients for a rectangular plate yields results that are more in error than for a square plate. From a study of the order of magnitude of the first six deflection coefficients as obtained from the six terms solutions, one observes that the first three coefficients are not necessarily the largest three. For a rectangular plate whose dimension in x - direction is greater than in the y - direction, the dominant terms are W_{11}, W_{31}, and W_{51}. Use of these three terms for a rectangular plate yields results that are in good agreement with six terms solutions. However, all the solutions presented in this paper were based on six terms.

As a check on the validity of the present approach, the six cubic equations are used to solve the free vibration problem of a homogeneous isotropic plate. The results obtained by the present method and by Yamaki [26] are shown in Table 3, and they appear to be in good agreement.

TABLE 1

COMPARISON OF SIX AND THREE TERMS SOLUTIONS FOR A SQUARE PLATE

$T_1 = 10.0$, $Q^* = 0.0$, $\gamma = 0.60$, $H = 6.0$, $\nu = 0.30$

No. of Terms	W_{11}	W_{13}	W_{31}	W_{33}	W_{15}	W_{51}	$\dfrac{w_0}{a}$	Ω
3	0.1000	0.0000	0.0000				0.1000	1.6606
	0.4000	0.0005	0.0007				0.3988	1.6835
	0.7000	0.0025	0.0033				0.6942	1.7321
	1.0000	0.0068	0.0089				0.9843	1.8026
	1.3000	0.0137	0.0177				1.2686	1.8944
	1.5000	0.0198	0.0253				1.4549	1.9641
6	0.1000	0.0000	0.0000	0.0000	0.0000	0.0000	0.1000	1.6606
	0.4000	0.0005	0.0007	0.0000	0.0000	0.0000	0.3988	1.6835
	0.7000	0.0025	0.0033	0.0001	0.0000	0.0000	0.6943	1.7321
	1.0000	0.0067	0.0090	0.0006	0.0000	0.0000	0.9849	1.8036
	1.3000	0.0138	0.0180	0.0019	0.0001	0.0002	1.2704	1.8943
	1.5000	0.0201	0.0258	0.0035	0.0002	0.0004	1.4582	1.9637

TABLE 2

COMPARISON OF SIX AND THREE TERMS SOLUTION FOR A RECTANGULAR PLATE

$T_1 = 10.0$, $Q^* = 0.0$, $\gamma = 0.60$, $H = 6.0$, $\nu = 0.30$, $\rho = 3.0$

No. of Terms	W_{11}	W_{13}	W_{31}	W_{33}	W_{15}	W_{51}	$\dfrac{w_0}{a}$	Ω
1	0.1000		0.0007			0.0000	0.0993	5.9853
	0.5000		0.0554			0.0070	0.4516	6.2748
	1.0000		0.2048			0.0528	0.8480	6.8311
	1.5000		0.3581			0.1146	1.2565	7.5935
6	0.1000	0.0000	0.0007	0.0000	0.0000	0.0000	0.0993	5.9853
	0.5000	0.0000	0.0554	0.0000	0.0000	0.0070	0.4515	6.2748
	1.0000	0.0005	0.2050	0.0019	0.0000	0.0529	0.8493	6.8306
	1.5000	0.0027	0.3589	0.0081	0.0001	0.1150	1.2616	7.5902
3	0.1000	0.0000	0.0007				0.0993	5.9853
	0.5000	0.0000	0.0539				0.4461	6.2807
	1.0000	0.0006	0.1927				0.8067	6.9219
	1.5000	0.0024	0.3365				1.1611	7.8413

TABLE 3

COMPARISON OF PRESENT AND YAMAKI SOLUTION FOR A HOMOGENEOUS ISOTROPIC PLATE

$\nu = 0.30, \quad \rho = 1.0, \quad Q^* = 0.0$

$\dfrac{w_0}{d}$	Ω/Ω	
	YAMAKI	PRESENT
0.0	1.00	1.00
0.4	0.98	0.98
0.8	0.93	0.93
1.2	0.85	0.85
1.6	0.78	0.78
2.0	0.71	0.70

APPENDIX

DEPENDENCE OF α AND β ON w

Substitution of Eqs. (47 - 49) and Eqs (53-54) into Eqs. (8 - 9), respectively, yields

$$\frac{A}{(1+\nu)}\nabla^2\alpha + \frac{A}{(1-\nu)}(\alpha_{,xx}+\beta_{,xy}) - \frac{2G_x}{(1-\nu^2)}(w_{,x}+\alpha) = 0 \tag{A-1}$$

$$\frac{A}{(1+\nu)}\nabla^2\beta + \frac{A}{(1-\nu)}(\beta_{,yy}+\alpha_{,xy}) - \frac{2G_y}{(1-\nu^2)}(w_{,y}+\beta) = 0 \tag{A-2}$$

Equations (A - 1) and (A - 2) are two simultaneous differential equations in α and β. Upon eliminating β one obtains the dependence of α on w as

$$\frac{A}{(1+\nu)^2}\nabla^4\alpha - \frac{(G_x+G_y)}{(1+\nu)^2}\nabla^2\alpha - \frac{(G_x\alpha_{,yy}+G_y\alpha_{,xx})}{(1-\nu^2)}$$

$$- \frac{(G_y-G_x)}{(1-\nu^2)}w_{,xyy} - \frac{G_x}{(1+\nu)^2}\nabla^2 w_{,x} +$$

$$\frac{2G_xG_y}{A(1+\nu)^2(1-\nu)}(w_{,x}+\alpha) = 0 \tag{A-3}$$

In a similar manner, one obtains the functional relationship between β and w which is

$$\frac{A}{(1+\nu)^2}\nabla^4\beta - \frac{(G_x+G_y)}{(1+\nu)^2}\nabla^2\beta - \frac{(G_y\beta_{,xx}+G_x\beta_{,yy})}{(1-\nu^2)}$$

$$- \frac{(G_y-G_x)}{(1-\nu^2)}w_{,xxy} - \frac{G_y}{(1+\nu)^2}\nabla^2 w_{,y} +$$

$$\frac{2G_xG_y}{A(1+\nu)^2(1-\nu)}(w_{,y}+\beta) = 0 \tag{A-4}$$

For a single-sandwich plate with isotropic faces and cores Eqs. (A-3) and (A-4) reduce to the equations obtained by Jacobson [9].

REFERENCES

1. Y. Y. Yu, "A New Theory of Elastic Sandwich Plates - One Dimensional Case", J. Appl. Mech., Vol. 26, 415-421, 1959.

2. Y. Y. Yu, "Simple Thickness - Shear Modes of Vibrations of Infinite Sandwich Plates", J. Appl. Mech., Vol. 26, pp. 679-681, 1959.

3. Y. Y. Yu, "Flexural Vibrations of Elastic Sandwich Plates", J. Aerospace Sci., Vol. 27, pp. 272-283, 1960.

4. Y. Y. Yu, "Simplified Vibration Analysis of Elastic Sandwich Plates", J. Aerospace Sci., Vol. 27, pp.

5. Y. Y. Yu, "Forced Flexural Vibrations of Sandwich Plates in Plain Strain", J. Appl. Mech., Vol. 27, pp. 535-540, 1960.

6. R. D. Mindlin, "Flexural Vibrations of Elastic Sandwich Plates", ONR TR. No. 35, 1959.

7. C. C. Chang and B. T. Fang, "Transient and Periodic Response of a Loaded Sandwich Panel", J. Aerospace Sci., Vol. 28, pp. 382-396, 1961.

8. H. N. Chu, "High - Frequency Vibrations of Sandwich Plates", J. Acoustl Soc. Am., Vol. 34, pp. 1184-1190, 1962.

9. M. J. Jacobson, "Effects of Orthotropic Cores on the Free Vibrations of Sandwich Plates", Shock and Vibration Bull., Vol. 35, pp. 9-14, 1966.

10. Abdulhadi and L. P. Supetta "Vibrations of Sandwich Plates with Orthotropic Faces and Cores", Shock and Vibration Bull., Vol. 39, pp. 73-80, 1969.

11. T. E. Falgout, "A Differential Equation of Free Transverse Vibrations of Isotropic Sandwich Plates", Proc. 7th Midwestern Mech. Conf., Vol. 1, pp. 223-227, 1961.

12. M. P. Bieniek and A. M. Freudenthal, "Frequency Response Functions of Orthotropic Sandwich Plates", J. Aerospace Sci., Vol. 28, pp. 732-735, 1961.

13. J. E. Greenspon, "Vibrations of Cross - Stiffened and Sandwich Plates with Application to Underwater Sound

Radiators", J. Acoust. Soc. Am., Vol. 33, pp. 1485-1497, 1961.

14. D. J. Mead and A. J. Pretlove, "On the Vibrations of Cylindrically Curved Elastic Sandwich Plates", R. & M., No. 3363, 1964.

15. V. Kovarik and P. Slapak, "Natural Transverse Vibrations of Sandwich Plates", Acta Technica, CSAV 12, pp. 187-219, 1967.

16. M.E. Raville and C.E.S. Ueng, "Determination of Natural Frequencies of Vibration of Sandwich Plates", Experimental Mech., Vol. 7, pp. 490-493, 1967.

17. R.M. Shahin, "Free Vibration of Multilayer Sandwich Plates in the Presence of In-Plane Load", J. of the Astronautical Sciences, Vol. XIX, No. 6, pp. 433-447, May-June 1972.

18. Y. Y. Yu, "Nonlinear Flexural Vibrations of Sandwich Plates", J. Acoust. Soc. Am., Vol. 34, pp. 1176-1183, 1962.

19. I.K. Ebeloglu, "On the Theory of Sandwich Panels in the Reference State", Int. J. Eng. Sci., Vol. 12, pp. 544-564, 1965.

20. B. D. Liaw and R. W. Little, "Bending of Multilayer Sandwich Plates", AIAA J., Vol. 5, pp. 301-304, 1967.

21. J. P. Wong and A. E. Salama, "Stability of Multilayer Sandwich Plates, J. Engr. Mech. Div., ASCE, Vol. 93, pp. 19-31, 1967.

22. J. J. Azar, "Bending Theory of Multilayer Orthotropic Sandwich Plates", AIAA J., Vol. 6, pp. 2166-2169, 1968.

23. S. Cheng, "On the Theory of Bending of Sandwich Plates", Proc. of the 4th U.S. Nat. Congr. of Appl. Mech., Vol. 1, pp. 511-518, 1962.

24. C. E.S. Ueng and Y. J. Lin, "A Note on a Nonlinear Theory on bending of Orthotropic Sandwich Plates", Aeronautical Quarterly, Vol. XIX, pp. 127-134, 1968.

25. J. J. Stocker, "Nonlinear Vibrations in Mechanical and Electrical Systems", 2nd Ed., pp. 81-86 Interscience publishers, 1950.

26. N. Yamaki, "Influence of Large Amplitudes on Flexural Vibrations of Elastic Plates", ZAMM, Vol. 41, pp. 1951-1953, 1961.

A DIGITAL COMPUTER PROGRAM FOR AIRCRAFT RUNWAY ROUGHNESS STUDIES

Tony G. Gerardi and Adolph K. Lohwasser
Air Force Flight Dynamics Laboratory
Wright-Patterson Air Force Base, Ohio

(U) The Air Force Flight Dynamics Laboratory has developed a method for determining the dynamic response of an aircraft to runway roughness during take-off and constant speed taxi. The mathematical model has been programmed for a CDC 6600 digital computer and several comparisons have been made between experimental data and analytical results. Results of the comparison were very good and they substantiate that model simulations can be substituted for costly taxi tests with instrumented airplanes.

INTRODUCTION

A major problem which can occur during take-off and taxiing operations of aircraft is abnormally high acceleration levels caused by the interaction between the aircraft landing gear and an excessively rough runway. Due to these accelerations, runways are evaluated with respect to roughness in order to insure timely pavement maintenance to control aircraft structural loads and fatigue. Also, rough runways affect crew member abilities by reducing instrument readability and crew comfort. The objective of these evaluations is to locate the rough areas of a runway and reduce the aircraft's response to them by either grinding the rough areas down or resurfacing them. Specific examples of this problem were the excessive dynamic response during ground operations of two heavy aircraft at two different overseas locations. In both cases pilot reports indicated excessive crew member discomfort. As a result of these pilot reports, both airplanes were instrumented with low frequency servo accelerometers and tested at these two locations. In each test, acceleration levels greater than .4g peak at the pilot's station were measured. These levels exceed the acceptable criterion as shown in Figure 1, which is a comparison between the human tolerance criterion and the levels measured [1]. It should be noted that the peak acceleration for the first and second test aircraft were .54g at 2Hz and .62g at 4Hz respectively. Employing these tests results, the rough sections of the runway for both cases were identified and recommendations of repair were made. This demonstrates that tests of this type are effective in locating the rough areas of a runway. However, they require large expenditures of both time and manpower. Thus, another less costly technique to meet this requirement was needed.
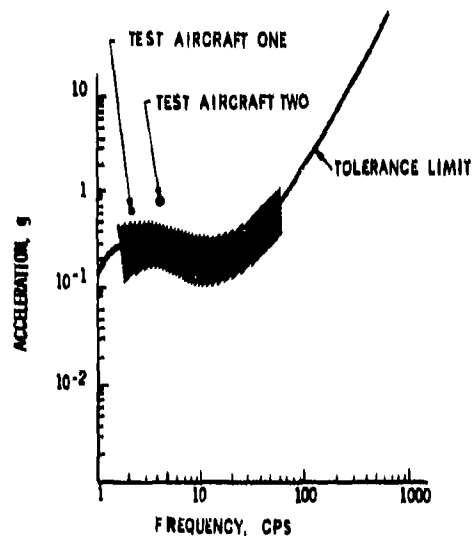

Figure 1. Human Tolerance Vibration Criteria

One such technique involves the use of a mathematical model to simulate the aircraft and runway interaction. The feasibility of this technique for specific aircraft was proven by the Boeing Company [2] in 1967 with a simulation of a heavy aircraft. This technique

55

gave good results but required hours of computer time as well as large amounts of highly detailed airplane data. In 1970 the Lockheed-Georgia Company [3] developed a technique for simulating another heavy aircraft during ground operations. This technique required less than one hour of computer time, less airplane data than the previous program, but still could simulate only one aircraft. These techniques did, however, prove the feasibility of the simulation of the aircraft and runway interaction.

The principle purpose of this analytical investigation, "A Digital Computer Program for Aircraft Runway Roughness Studies", was to develop a general airplane/runway model capable of simulating any aircraft traversing a runway profile*. The major advantages of this model over previous techniques are that it is simple to use, requires less than two minutes on a CDC 6600 to simulate a typical aircraft in a take-off, and, of upmost importance, compares very well with experimental data.

GENERAL AIRPLANE/RUNWAY MODEL

The general model consists of a flexible aircraft, landing gear struts and tires, and the runway profile. This general model is shown in Figure 2.
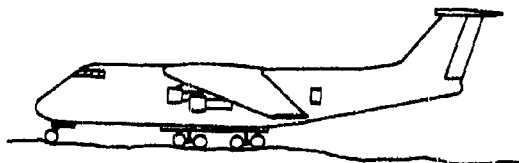

Figure 2. General Airplane

Each separate component of the model will now be described in the following order; structure, landing gear struts, tires, and runway profile representation.

Flexible Structure:

The flexible structure as shown in Figure 3 is modeled as an elastic structure whose motion is a superposition of its free vibration modes, weighted by time-dependent generalized coordinates. These vibration modes are calculated mode shapes and frequencies of the aircraft being modeled. In addition, the aircraft has three rigid body degrees of freedom; pitch, plunge and horizontal translation. The elastic
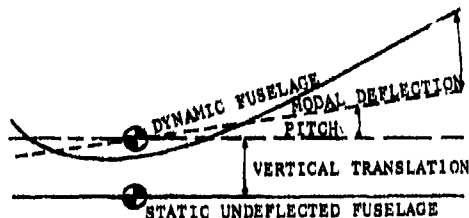
Figure 3. Elastic Structure

* This work is being done for the Air Force Weapons Laboratory

model is excited by forces at the landing gear attachment points. The data required to represent this elastic structure is the generalized mass and frequency for each mode, the modal deflections at the gear attachment points, the center of gravity, a tail location and the pilot's station.

Landing Gear Strut:

A schematic of a typical landing gear strut is shown in Figure 4. The total force in a landing gear strut is comprised of three forces. These are the air spring (pneumatic force) [4], the viscous damping (hydraulic force) [4] and an internal strut friction force [4]. When an airplane is static, sitting on a ramp, the only force in the strut is the pneumatic force. This force can be expressed as follows:

$$F_A = \frac{P_{ao} V_o{}^n A_a}{(V_o - S A_a)^n} \qquad \text{(isothermal process)} \quad (1)$$
$$(n=1)$$

where P_{ao} = the fully extended strut pressure

V_o = the fully extended strut volume

A_a = the pneumatic piston area

S = Strut stroke
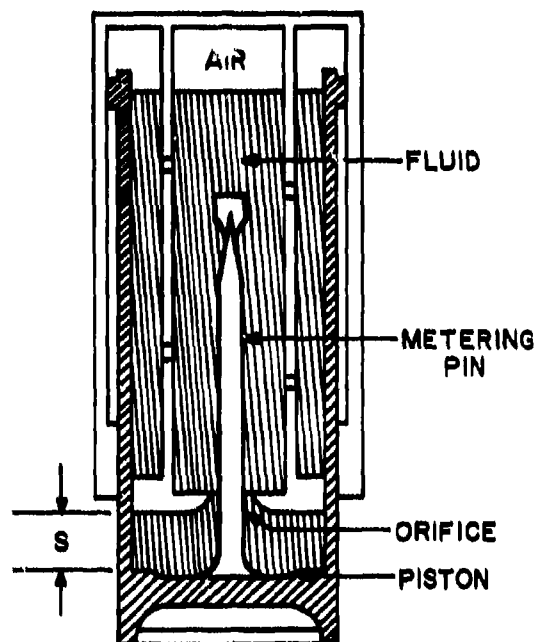
Figure 4. Landing Gear Strut Schematic

During a taxi or take-off condition, the pneumatic force is the largest of the strut forces. A plot of a typical load vs. stroke curve showing the magnitude of the pneumatic

force as a function of stroke is shown in Figure 5. As can be seen, the pneumatic spring force increases exponentially as the piston or lower portion of the strut moves up and compresses the air.

Figure 5. Strut Static Load Stroke Curve

The second of the three strut forces is the hydraulic force. This force can be expressed as:

$$F_h = \frac{\rho h\, A_h^3\, \dot{s}|\dot{s}|}{2\,(C_d\, A_o)^2} \tag{2}$$

where: ρ_h = density of the Hydraulic fluid

A_h = hydraulic piston area

A_o = effective orifice area (constant orifice minus metering pin area)

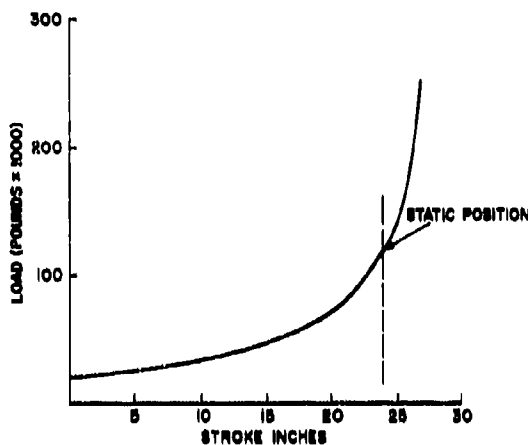C_d = orifice coefficient (use .9)

$\dot{s}$ = strut piston velocity

From equation (2) it can be seen that the hydraulic force is proportional to the strut piston velocity squared. Thus, if the strut piston is not moving the hydraulic force is zero. Figure 6 illustrates that as the strut piston moves up or down the effective orifice area (total orifice are minus metering pin area) changes. Therefore, the hydualic force is a function of both the strut piston velocity and strut position. During taxi equation (2) is representative of the hydraulic force during strut compression and extension.

The metering device which is used to vary the effective orifice area with stroke, can be a conventional metering pin, a fluted metering pin or a metering tube. The change of the effective orifice area with strut stroke for each

device is accounted for in this model.

The third and final strut force is a frictional force. From a previous in-house study, a typical strut friction force during taxi and take-off was less than .6 percent of the total strut force. Thus, since the frictional force is very small it is neglected.
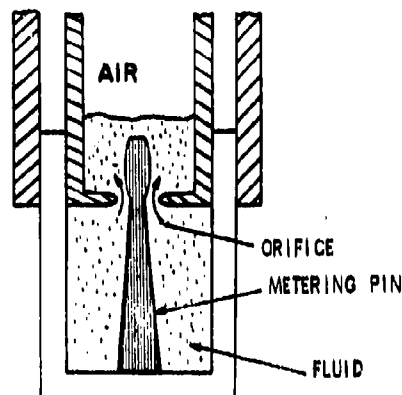
Figure 6. Typical Metering Device

Tire:

The next component of the model is the tire. The analytical representation of the tire force is as follows:

$$F_T = K_T\, T_D \tag{3}$$

where T_D = tire deflection

K_T = linear tire spring constant

Figure 7 shows a typical tire load deflection curve. Generally, a tire is inflated to a pressure such that the static deflection will be approximately 35 percent of its section height. This deflection is used in the analysis to determine the tire spring constant. It should be noted in Figure 7 that the load-deflection curve is very nearly linear in and around the static deflection area. During taxi and take-off the tire deflection is in the linear portion of the curve. Therefore, a linear spring constant (K_T) which is the slope of the load-deflection curve, can be used for the taxi analysis.

The tire deflection is defined as the sum of the deflection of the unsprung mass (strut piston, tire and wheel assembly) and the runway profile elevation.

57
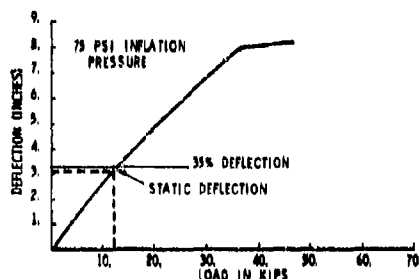
Figure 7. Tire Load Deflection Curve

(a) TYPICAL RUNWAY (NOT TO SCALE)

(b) TYPICAL RUNWAY ELEVATION PROFILE

Figure 8. Runway Profile

Runway Profile:

The final component in the general model is the runway profile. The runway profile data is normally measured as the height above some datum line as illustrated in Figure 8. The runway elevation profile (y_1) is then tabulated for each successive increment of measurement. The increment of horizontal distance, (x), is usually two (2) feet, but a one-half (1/2) foot incremental distance is also common. This model uses data taken on two (2) foot intervals.

To properly interface with the other components of the model it is necessary to express the runway profile as a function of time. This can be done by first determining the runway elevation profile as a function of distance. One approach [5] is to use a polynomial equation for fitting a curve to a selected number of points on the runway, that is:

$$Y(x) = a_1 + a_2 x + a_3 x^2 + a_4 x^3 \ldots \ldots a_n s^{n-1}, \quad n=1,2,3 \tag{4}$$

This method uses the slope and three runway elevation points to solve for the coefficients a_1, a_2, a_3, and a_4.

$$
\begin{Bmatrix} y'(x_1) \\ y(x_1) \\ y(x_2) \\ y(x_3) \end{Bmatrix} = \begin{Bmatrix} q_1 \\ q_2 \\ q_3 \\ q_4 \end{Bmatrix} = \begin{bmatrix} 0 & 1 & 2x_1 & 3x_1^2 \\ 1 & x_1 & x_1^2 & x_1^3 \\ 1 & x_2 & x_2^2 & x_2^3 \\ 1 & x_3 & x_3^2 & x_3^3 \end{bmatrix} \begin{Bmatrix} a_1 \\ a_2 \\ a_3 \\ a_4 \end{Bmatrix} \tag{5}
$$

The slope at the beginning of a runway segment is made to equal the slope at the end of the previous segment, thus maintaining a continuous slope from one segment to another.

This technique provides a method for obtaining the analytical function $y(x)$ for the runway elevation profile for a selected segment of the runway. The process is repeated as many times as necessary to cover the total horizontal distance required for a specified problem.
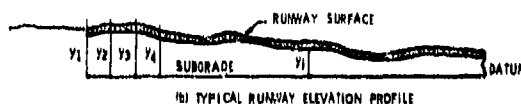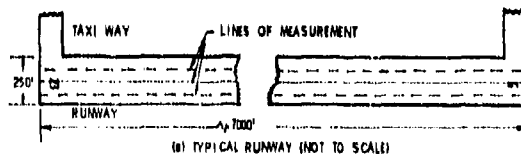
Mathematical Model:

All of the above components of the general model can now be combined to form the detailed mathematical model shown in Figure 9. The detailed model incorporates a flexible fuselage with one nose gear and multiple main landing gear. The landing gear struts can be conventional, articulated and or the double acting type. Also, this model includes lift, thrust, aerodynamic and rolling drag. The degrees of freedom of the model are pitch, plunge, horizontal translation and up to 15 flexible modes of vibration.

Equation of Motion:

The differential equations of motion for the mathematical model were derived by application of Hamilton's principle of minimum energy. The general form of these equations is shown below and correspond to the notation shown in Figure 9.

Rigid Body Equations of Motion

$$\ddot{Z} = (F_{s1} + F_{s2} + F_{s3} + L - W)/M_{cg} \tag{6}$$
[c.g. vertical acceleration]

$$\ddot{Z}_1 = (F_{t1} - F_{s1} - W_1)/M_1 \tag{7}$$

$$\ddot{Z}_2 = (F_{t2} - F_{s2} - W_2)/M_2 \tag{8}$$

$$\ddot{Z}_3 = (F_{t3} - F_{s3} - W_3)/M_3 \tag{9}$$
[landing gear unsprung mass acceleration

$$\ddot{\Theta} = (F_{s1}A + F_{s2}B + F_{TD}C_1 - F_{s3}C)/I_{yy} \tag{10}$$
[pitching acceleration]

$$\ddot{X} = (F_T - F_{TD} - F_{AD})/(M_{cg} + M_1 + M_2 + M_3) \tag{11}$$
[horizontal translation acceleration]

where:

F_{s1}, F_{s2}, F_{s3} = total landing gear strut forces

58
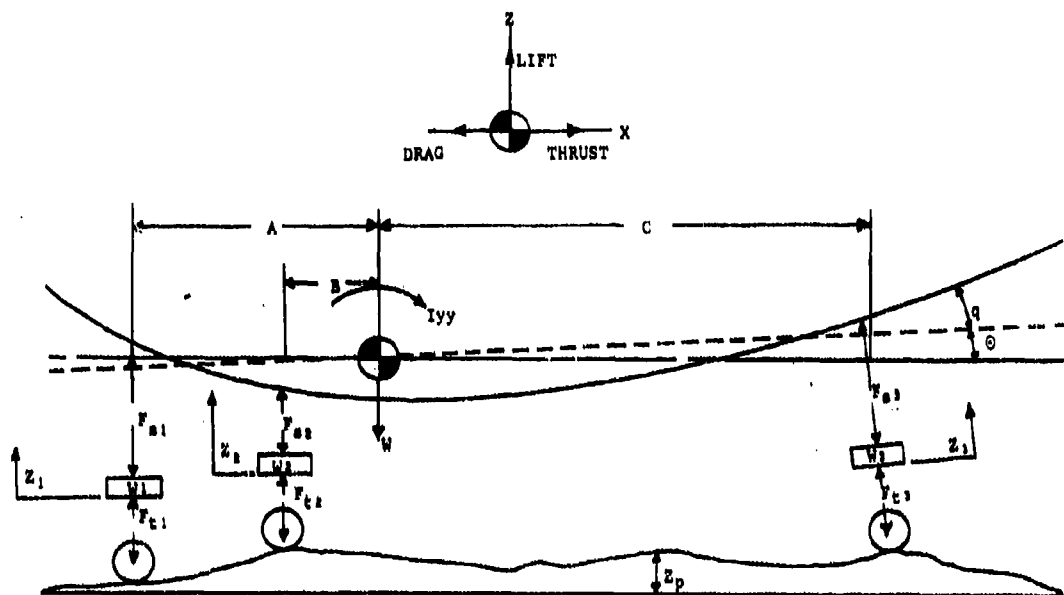
Figure 9. Mathematical Model

F_{t1}, F_{t2}, F_{t3} = tire forces

M_{cg}, W, I_{yy} = aircraft mass, weight and pitching inertia

W_1, W_2, W_3 = unsprung landing gear weights

A, B, z_1 = moment arms

L, F_T, F_{TD}, F_{AD} = lift, thrust and tire and aerodynamic drag forces; [L,F_T and F_{AD} act through the center of gravity]

Flexibility Equations of Motion

$$M_i \ddot{q}_i = \xi_{i1}F_{s1} + \xi_{i2}F_{s2} + \xi_{i3}F_{s3} - 2\zeta_i\omega_i M_i \dot{q}_i$$

$$-\omega_i^2 M_i q_i \text{ for the ith mode} \qquad (12)$$

where:

M_i = the generalized mass

ξ_{i1}, ξ_{i2}, ξ_{i3} = modal deflections at gear location 1, 2 and 3

ω_i = modal frequency

ζ_i = damping factor

q_i, $\dot{q}_i$, $\ddot{q}_i$ = generalized coordinate and time derivatives

The generalized force due to lift is not included in the flexibility equation of motion because the time rate of change of lift is small compared to the rate of change of the landing gear forces.

Solution Algorithm:

The technique used for solving the coupled non-linear differential equations of motion that describe the simulated aircraft is a three term Taylor Series. For example, the equation:

$$\ddot{x} = c\dot{x} + kx \qquad (13)$$

The three term Taylor Series representation can be written as:

$$x_{(I+1)} = x_{(I)} + \dot{x}_{(I)}\Delta t + \ddot{x}_{(I)}\frac{\Delta t^2}{2} \qquad (14)$$

Where $I = 1 \rightarrow N$

The values for $\ddot{x}$, $\dot{x}$ and x from the previous step are substituted into equation (14) and a new value for x is obtained. Differentiating equation (14) we obtain for the velocity $\dot{x}$, the expression

$$\dot{x}_{(I+1)} = \dot{x}_{(I)} + \ddot{x}_{(I)}(\Delta t) \qquad (15)$$

The values for $\dot{x}$ and $\ddot{x}$ are then substituted into equation (15) and a new value of x is found. This entire process is repeated with the new values of x and $\dot{x}$ to obtain the next point in the solution. When compared to a general Runga-Kutta solution, which was used on one of the previous taxi simulation programs, this three term Taylor series yielded the same accuracy.

59

Output Format:

The results of the model are provided as both a printed output and a time history plot. The printed output lists ten important parameters every one hundredth of a second.

Figure 10 shows a photographic reduction of a typical Calcomp plotted time history. This figure depicts a simulated fighter aircraft taking off from the runway at test location one. The plotted output includes titles showing the airplane simulated, its gross weight, the runway number and its location. The ordinate is the time axis annotated every second. At every time annotation the current value of aircraft speed, in feet per second, and the current aircraft position on the runway, in feet, are printed out. Runway markers (1000 foot markers) are plotted on the time scale to aid in aircraft positioning. The plot titled "Nose Gear Track" is a time history of the runway profile as it is encountered by the aircraft's nose gear. There are two aircraft acceleration time histories. One is the vertical acceleration at the aircraft's center of gravity (CGA). Each time history is banded by the human tolerance criteria of ± .4g. In order to minimize the amount of core required to store the acceleration time histories, the higher frequency components were effectively filtered out by limiting the sample interval. All of the acceleration peaks, however, are shown on the plot. It should be noted that the pilot station and center of gravity acceleration time histories are not always within the band of accepted human tolerance criteria. Thus, the plot is very useful in that it provides a graphical record of the level

of acceleration and it shows which bumps in the runway profile caused the high acceleration responses.

Results:

Results of this analytical investigation have been compared to recorded experimental data of two heavy airplanes at two overseas locations. Figure 11 is a plot of pilot station acceleration versus distance down the runway for test aircraft one taking off from test location one at 273,000 pounds with the center of gravity at 23.1 percent of the mean aerodynamic chord (MAC). The solid line shows the analytical results and the dashed line shows the measured results. The test and analysis results indicate that one area of the runway consistently produces aircraft accelerations greater than the .4g criterion. The location of this rough area measured from the northeast end of the runway is between 3700 and 4700 feet as shown on Figure 11. Both curves show that for most of the runway the acceleration levels are less than .2g which is typical of the levels for an acceptable runway.

The results of the computer program "TAXI" were also compared to experimental data measured on a heavy bomber (test aircraft two) operating out of test location two. Figure 12 shows the acceleration time histories of simulated (top three lines) and measured (bottom three lines) data for the pilot station, cg at a location in the tail FS 1655 respectively for a 400,000 pound airplane during a constant speed 40 knot taxi. The location of the rough section of this runway is clearly identified at runway
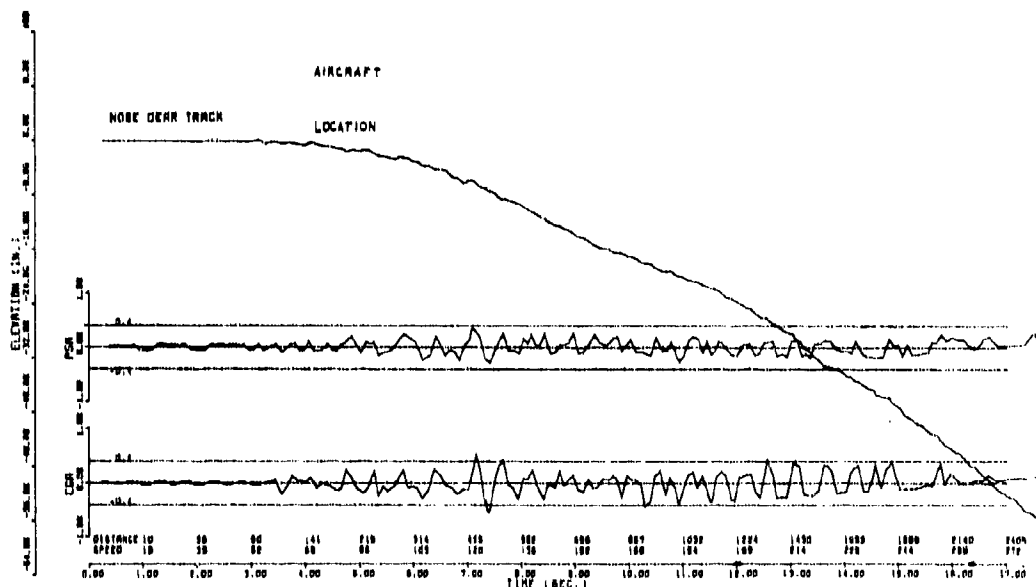
Figure 10. Typical Plot of Simulated Output

marker number three. The simulated acceleration levels were within six percent of the measured levels where the peaks occurred.

A comparison of simulated results to measured data was also made on a fighter aircraft. Figure 13 shows the plotted results of simulated (top two lines) and measured (bottom two lines) data on the 37,500 pound fighter during a constant speed 29 knot taxi over a built up ramp. The ramp was a bump 15.5 feet long with a maximum amplitude of 1.5 inches. The simulated acceleration level at the aircraft center of gravity was within nine percent of the measured level at the peak.

Figures 11, 12, and 13 demonstrate that the computer program "TAXI" will work satis-

factorily on cargo, bomber and fighter type aircraft respectively.
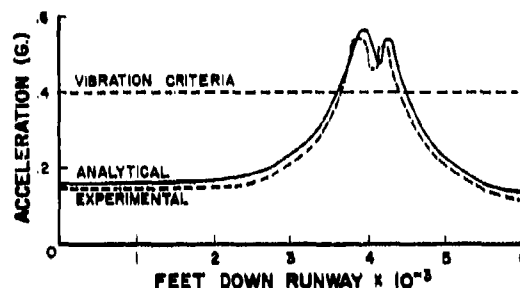
Figure 11. Comparison of Mean Values of Experimental and Analytical Results of Test Aircraft Number 1
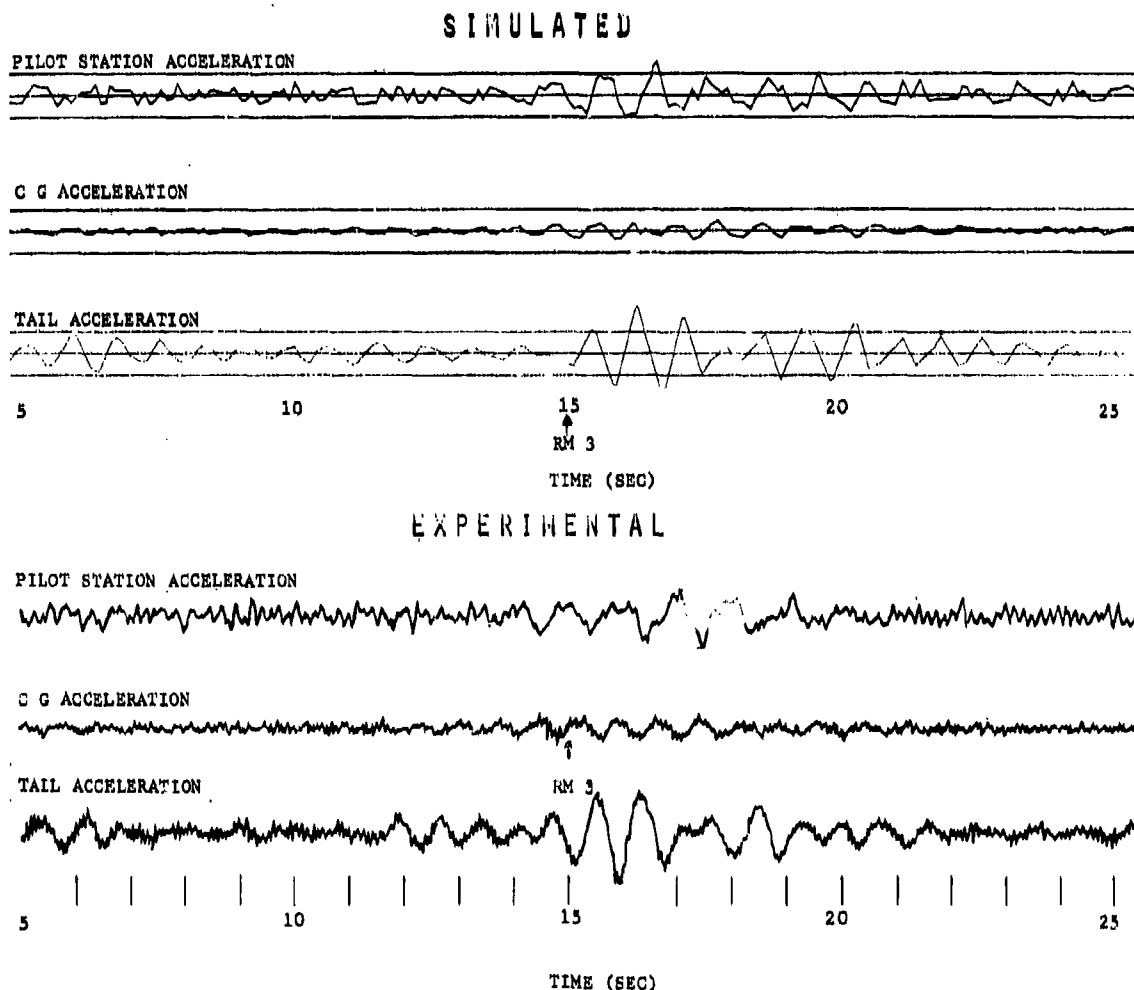
Figure 12. Comparison of Simulated and Measured Acceleration Time Histories of Test Aircraft 2 During a 40 Knot Taxi at Test Location 2.

61

TIME (SEC)
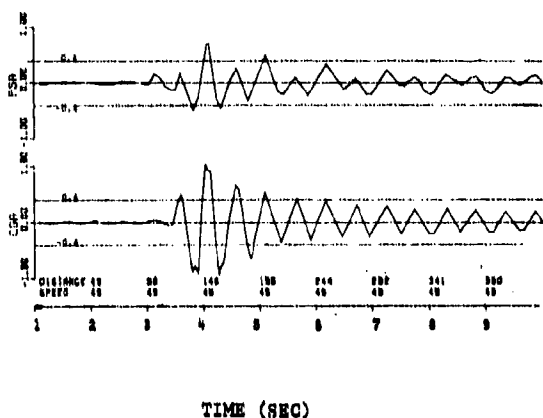
Figure 13. Comparison of Simulated and
Measured Acceleration Time
Histories of a Fighter Aircraft
Traversing a Ramp

Conclusion:

In conclusion, the goals of generating
a general airplane/runway model capable of
accurately simulating practically any airplane
traversing a runway profile with a minimum of
input data and in a reasonable amount of com-
puter time were fulfilled. Three aircraft have
successfully been simulated with the model and
the results compare favorably with available
experimental data. The amount of airplane data
required by the program has been kept to a mini-
mum. The computer time required to simulate a
typical airplane taking off is less than two
hundred seconds and less than 77700 storage
locations on a CDC 6600 computer.

The model simulation compares very
well with experimental data in that the rough
areas of the runway were located and peak pilot
station accelerations were closely matched.

A model of this type has many possible
applications. Runway repairs can be simulated
to determine if the repair will be effective in
reducing airplane response. Another application
would be to determine the response of new
systems to runway roughness in order to expose
a potential roughness problem in the design

stage. Still another application would be the
evaluation of new pavement techniques and
designs. A typical example is the recently
used "Slip-Form" method of paving runways. This
model, with minor modifications should lend
itself very readily to these and other future
applications.

The present objective of formulating
a general model has been met and now that it
has successfully been demonstrated, runways can
be evaluated for roughness characteristics with-
out a costly taxi test.

References

1. Cyril M. Harris and Charles E. Crede, ed.,
"Shock and Vibration Handbook" Vol. 3, McGraw-
Hill, 1961.

2. Delmar A. Quade, The Boeing Company, Wichita
Division, "Location of Rough Areas of Runways
For B-52 Aircraft" AFFDL-TR-67-175, March 1968.

3. C.K. Butterworth and D.E. Boozer Jr.,
"C-141A Computer Code For Runway Roughness
Studies" AFWL-TR-70-71, August 1970.

4. Chance Vought Corporation, "A Rational
Method for Predicting Alighting Gear Dynamic
Loads", ASD-TDR-62-555, December 1963.

5. Robert F. Cook, Air Force Flight Dynamics
Laboratory, "Use of Discrete Runway Profile
Elevation Data in Determining the Dynamic Res-
ponse of Vehicles" TM-68-3-FDDS, May 1968.

6. George, N. Miles, "Construction Procedure
of Slip-Form Pavement", Highway Research Board
Bulletin 29S, Concrete Mixing and Paving,
Presented at the 40th annual meeting, Jan 9-13
1961.

Mr. O'Leary (Boeing Vertol Division):
Did I understand you to say that you needed the
input to be defined for the runway roughness?
In other words, what is the input to the
program?

Mr. Gerardi: The input is actual profile
data taken on two foot intervals. The profile
is measured.

Mr. O'Leary: Do you have any wing or
airplane aerodynamics in there. I noticed for
instance that the oleo spring and the tire
springs are nonlinear. To represent the
dynamics of that structure you almost need the
time history of a takeoff.

Mr. Gerardi: We do have aerodynamics
in it both drag and lift. It is a function of
speed as it should be. We have located the
lift force at the center of gravity to off-set
the problem of moments that would have to be
pilot input.

Mr. O'Leary: You say it is a general
model. Do you generally have bottoming
springs in the oleos: I didn't see that
represented on your oleo spring.

Mr. Gerardi: No, we don't. We have
never run into a problem where we have
bottomed a strut in simulation.

Mr. Lamoree (Lockheed, California Co.):
It would seem to me that there should be some
application of Dr. Pilkey's work to your work
in defining classes of runway roughness which
would fall within the scope of keeping the
response levels below the required 4 g's.

Mr. Gerardi: I think the areas are
probably related.

Mr. Srinivas (NASA Langley): Does the
peak acceleration occur at the same point as
the peak roughness?

Mr. Gerardi: Generally, there is a slight
time lag and it depends on the vertical
translation or the pitching frequency of the
airplane.

Mr. Thomson (University of California):
How do you make these profile measurements at
two foot intervals? What kind of instrument
do you use?

Mr. Gerardi: We started out with a rod
and level, but the Air Force now has a machine
that will take runway elevation points at five
miles per hour. It takes elevation points
every six inches, digitizes them and puts them
on magnetic tape.

63

AN ALGORITHM FOR

SEMI-INVERSE ANALYSIS OF NONLINEAR DYNAMIC SYSTEMS

R. L. Eshleman
Senior Research Engineer

T. M. Scopelite
Manager

Engineering Mechanics Division
IIT Research Institute
10 West 35th Street
Chicago, Illinois 60616

This paper describes an algorithm for determing the transient response and control functions of nonlinear dynamic systems subjected to prescribed time dependent constraints. The directional handling behavior of a tractor semi-trailer performing a prescribed maneuvor is computed using this technique.

INTRODUCTION

Modern development of the digital computer has rendered the simulation of the dynamic behavior of nonlinear systems a reality. Using mathematical models and computer soft-ware, the conceptual design of a system can be evolved; prototype hardware can be developed; and production product can be evaluated for function through digital simulation. Therefore, through the design, development and production stages of an evolving product, a digital simulation model of a system's performance and structural integrity can be a vital asset.

Often the transient response of nonlinear systems is required to determine performance and structural integrity. Present technology calls for the direct integration of the system equations of motion using a numerical integration technique such as Runge-Kutta or predictor-corrector implemented on the digital computer. Direct integration of the system's equations of motion is usually a costly procedure. Many small time steps over several periods or duration of phenomena are required. If the formulated problem has many interrelated state variables, then the integration time may become prohibitive, especially if multi-runs are required for design or diagnosis. For a class of problems involving time dependent open loop controls to achieve a prescribed system performance, a semi-inverse algorithm combining parameter perturbation and numerical integration has been shown to have functional and economical advantages over direct integration. Specifically, this technique has been successfully implemented in tractor semi-trailer handling studies [1].

This paper is devoted to the description of the semi-inverse computational technique, to its implementation on the digital computer, and to its application to tractor semitrailer directional handling.

TECHNIQUE DESCRIPTION

The semi-inverse technique is applicable to a class of open loop controlled dynamic systems which can be mathematically modeled by the following set of equations:

$$c_{ij} \ddot{x}_j = f_i (\dot{x}_j, x_j, t, \beta_k) \qquad (1)$$

65

where,

X_j = system dependent variables (response),

t = time,

C_{ij} = constants,

β_k = system control parameters (input disturbance),

f_i = nonlinear functions of system variables and control parameters

i, j = 1, 2, ..., N

k = 1, 2, ..., M

The basic strategy of the semi-inverse techniques is to find the system control parameters, β_k (t), that impose a prescribed response on a finite number M of the system variables, X_j. The number of prescribed dependent variables, X_M, must equal the number of system control parameters, β_M. Figure 1 schematically shows this computational model. The computational technique involves the use of the D'Alembert principle followed by integration of the unknown response variables at discrete time instants. The steps involved in the development of a semi-inverse computational model are now described in detail.

Prescribed Response X_M

Mathematical Model

Control variables β_M System response variables $X_{M+1}....X_N$
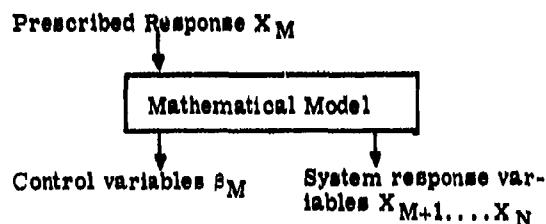
Figure 1 - Semi-Inverse Computational Model

The system dependent variables, X_k, are prescribed as a function of time. This description can be in a functional or numerical form. For example, the path of a vehicle center of gravity can be expressed in the form of a polynomial. The velocities, $\dot{X}_k$, and accelerations, $\ddot{X}_k$, are derived from the dependent variables, X_k, through differentiation. If the accelerations, $\ddot{X}_k$, are given as basic data, then integration must be performed on the problem input data provided the physics of the problem requires it. A set of perturbed equations are

established by replacing the control variables β_k (t) by their perturbed values β_k (t + Δt) at time, t + Δt, in the system equations of motion, equation (1). At time step, t + Δt, the control variables are written in the following form:

$$\beta_k \ (t + \Delta t) = \beta_k(t) + \Delta\beta_k \qquad (2)$$

Equation (2) is substituted into the system equations of motion, equation (1), to obtain the following set of simultaneous differential equations:

$$C_{ij} \ \ddot{X}_j = f \ (\ddot{X}_j, \dot{X}_j, t + \Delta t, \ \beta_k + \Delta\beta_k) \qquad (3)$$

The equations of motion given in the form of equation (3) are rearranged to obtain a set of linear simultaneous equations with variables X (those not prescribed) and $\Delta\beta_k$. The form of this set of equations is shown schematically by equation (4):

$$[A] |y| = |B| \qquad (4)$$

where:

[A] is a constant coefficient matrix evaluated at discrete time instants in the computation;

$$y = \begin{vmatrix} \Delta\beta_1 \\ \cdot \\ \cdot \\ \Delta\beta_M \\ \cdot\cdot \\ X_{M+1} \\ \cdot \\ \cdot \\ X_N \end{vmatrix}$$ is an unknown vector composed of accelerations and control variable increments to be determined at discrete time intervals

$$B = f(\ddot{X}_1, \ldots, \ddot{X}_M, \dot{X}_j, X_j, t + \Delta t, \beta_1, \beta_2, \ldots, \beta_M)$$

is a constant vector evaluated at discrete time instants.

Equation (4) is used to determine the values of the increments in control variables, $\Delta\beta_k$, and the unknown response variables, $X_{M+1}, \ldots, X_N$. Essentially this procedure is an application of D'Alemberts principle at discrete time points in the system transient response. The response accelerations are

constants, equation (5):

$$X_j = D_j \quad M+1 < j \leq N \quad (5)$$

for the given discrete time point, and, are intergrated using a Taylor series expansion. System quantitites dependent on $\ddot{X}_{M+1}, \ldots, \ddot{X}_N$ and $\dot{X}_{M+1}, \ldots, \dot{X}_N$ are obtained after integration of equations (5).

COMPUTATIONAL PROCEDURE

The computational procedure consists of a series of numerical evaluations at discrete time instants during the elapsed time of the system motion. It is almost mandatory that this technique be implemented on the digital computer. Therefore a brief description of its use on the digital computer is given.

The input trajectory values, $\ddot{X}_k$, $\dot{X}_k$, X_k, are determined as a function of time. Experience has shown that where the trajectory displacement, X_k, is used to obtain $\dot{X}_k$, and $\ddot{X}_k$, a mathematical function should be used. If experimental data is available, a curve fitting scheme should be utilized to form the function. Normally it is a good procedure to print out the generated values of $\dot{X}_k$ and $\ddot{X}_k$, to assure authenticity prior to using them in the equations of motion. The system is sensitive to the values of X_k since it is the fundamental input to the set of linear simultaneous equations.

The computation is initiated at time t = 0 using the initial values of the system and the computation proceeds in a step-by-step manner at time intervals, Δt. To minimize computer time it is advantageous to select the largest value of Δt possible which will maintain numerical stability. The value of Δt is dependent on the dynamic characteristics of the system. In a low frequency system such as a tractor semitrailer, a time step of 0.05 sec. was used with a requirement of about 60 computational points for a complete maneuver. In this example it was found that decreasing the size of the time step had no effect on the accuracy of the results.

Variable values, $(X_j(t), \dot{X}_j(t), \beta_k(t))$ from the previous time step, t, are used to form the constants in the simultaneous equations, equation (4), at time step, $t - \Delta t$. This set of simultaneous equations is solved using a linear equation solver for the control variable increments, $\Delta \beta_k$, and the unprescribed accelerations, $\ddot{X}_j$. The values of $\ddot{X}_j$ are integrated

to find $\dot{X}_j$ and X_j at that time step. The required control parameters are formed by letting $\beta_k = \beta_k + \Delta \beta_k$. The unprescribed variables, X_j and $\dot{X}_j$, the control parameters β_k, and the prescribed trajectories are used to establish the simultaneous equations for the next time step. Figure 2 is a schematic representation of the computational procedure used for the semi-inverse analysis of nonlinear dynamic systems.

AN EXAMPLE: TRACTOR SEMITRAILER HANDLING

The semi-inverse technique has been applied successfully to the simulation of directional handling of tractor semitrailer vehicles. Due to the kinematics of the vehicle and the tire side force-slip angle (ratio of the wheel side velocity to its forward velocity) relationships, a set of ordinary nonlinear differential equations result. The criterion for good vehicle handling is the ability of the vehicle to negotiate prescribed maneuvers such as lane changes and cornering in a stable manner within the constraints of the road boundary. Therefore, the forward and lateral motions of the vehicle are prescribed. The semi-inverse method is used to find the required driver controls (steering and braking) that will yield the prescribed tractor motions on a given road surface with specified environmental conditions. During the maneuver the unprescribed responses, tractor and semitrailer yaw angles, are also found as a function of time.

The equations of motion are similar to equation (1) except that the position coordinates, X_j do not enter into the formulation.

$$C_{ij}\ddot{X}_j = f_i(\dot{X}_j, \delta, D) \quad i,j = 1,2,\ldots, \quad (6)$$

where

C_{ij} is a function of the vehicle masses and moments of inertia,

$\ddot{X}_j$ vehicle accelerations,

$\dot{X}_j$ vehicle velocities,

δ steering angle,

D braking force

The problem is formulated as a set of four linear simultaneous equations after perturbing the control variables (steering and

```
            ┌─────────────────────────┐
            │         READ:           │
            │   SYSTEM DESCRIPTION     │
            │          AND            │
            │  PRESCRIBED TRAJECTORIES │
            └─────────────────────────┘
```
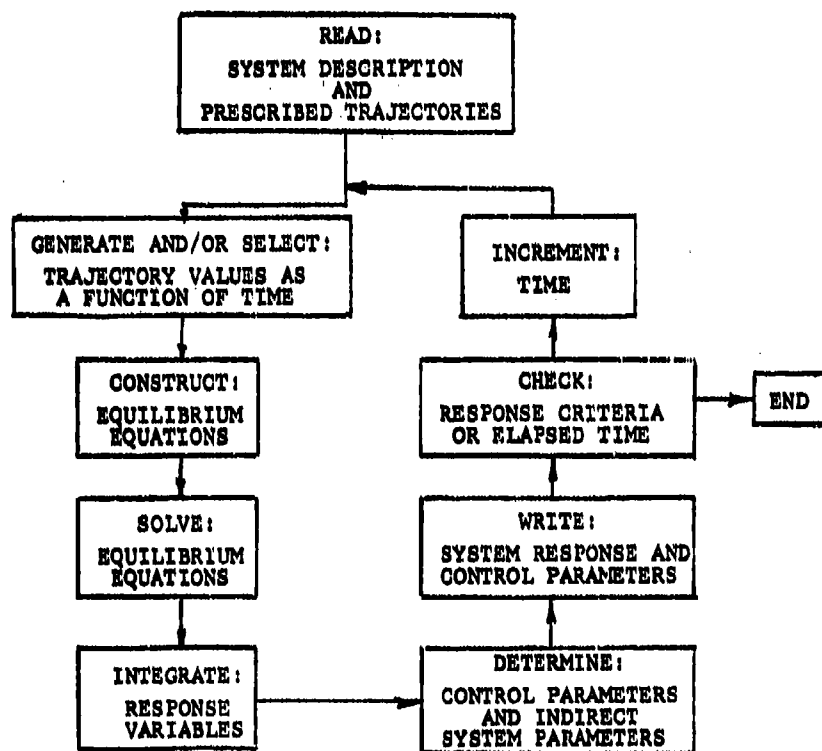
Figure 2 - Computational procedure for semi-inverse
analysis of nonlinear dynamic systems

braking). From this set of simultaneous equations the vehicle yaw angular accelerations, the steering angle and the braking force are found as a function of time. Figure 3 shows an example of the results obtained from this method as applied to the tractor semitrailer simulation. The prescribed motions (12 ft lane change in 275 ft at 50 mph) is shown initially followed by the steering angles required to pursue that trajectory. Succeeding portions of the figure shown the resulting yaw angle responses and rear tractor tire slip angles. From this information, the driver control requirements can be examined along with the vehicle response resulting from the prescribed trajectory in given environmental conditions. The experimental verification of this method as applied to the tractor semitrailer directional handling problem is also shown in Figure 3.

DISCUSSION

The semi-inverse method has been employed successfully in all variable regimes of the tractor semitrailer directional handling problem. In fact, it has been used to establish physical stability limits for cornering and lane-changing vehicles. It was found that the computer costs were less than those incurred when running a comparable conventional control-response digital computer program.

In the use of the semi-inverse technique, certain factors such as error estimates, determinant singularity and control limits have not been investigated in general. In fact it appears that these factors may have to be considered on a problem to problem basis because of the wide disparity in the nonlinear differential equations encountered.

The algorithm is dependent on the solution of a set of linear simultaneous equations. Therefore the solution could become inaccurate if the determinant of the matricies becomes singular or near singular. In the example problem noted here, this never presented itself as a problem. As a precaution it seems advisable that the determinant of the coefficient matrix of the set of linear equations be examined as part of the computation process.

Error estimates that relate to the chosen time increment would be useful in setting up a problem for computer analysis. To date the trial and error process employing additional computer runs has been utilized to obtain the optimum time step size. A good initial value for the time step size can be obtained from an estimate of the maximum rate and period of the control parameter.

In all physical problems, there are limits on the control parameter-ranges resulting in physical limits on the ability to control the dynamic variables. Since this algorithm determines the controls required for specified system responses, the problem of physical limits of the controls must be addressed. If the algorithm is being used for design, the control parameter requirements can be determined. When the algorithm is being used for analysis of an existing system, the physical limits on the control parameters must be programmed into the computational logic to constrain the range of controls and responses of the system during operation.

REFERENCE

1. R. L. Eshleman and S. Desai, "Articulated Vehicle Handling", Department of Transportation, NHTSA contract DOT-HS-105-1-151, IITRI project J6255, HS800674, April, 1972.
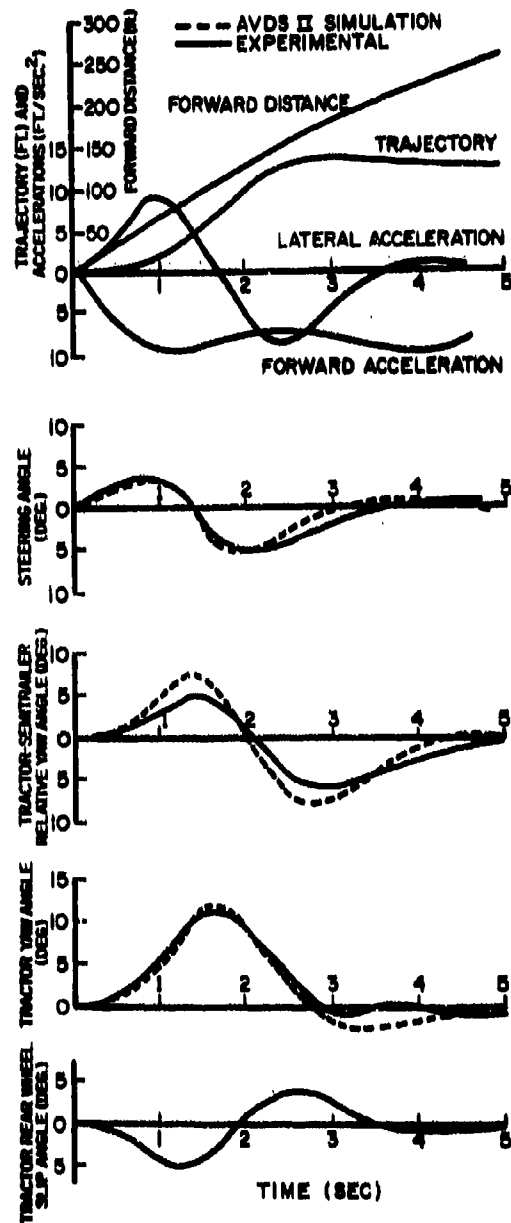
Figure 3 - Analytical-experimental comparison of the
articulated vehicle response for a 12 ft x 275 ft
lane change maneuver at 50 mph with hard
braking. [1]

GUNFIRE-INDUCED VIBRATION ON
THE A-7E AIRPLANE

T. W. Elliott
Naval Missile Center
Point Mugu, California

During the period 29 September 1969 through 6 March 1970 the U.S. Naval Missile Center participated in the Board of Inspection and Survey (BIS) service acceptance trials of the A-7E airplane. During the BIS trials measurements were taken of vibration induced in avionics and airborne stores. These measurements were taken during various flight conditions of steady captive flight, maneuvers, and firing of the M61A1 gun, a 20-millimeter cannon. The objective of these measurements was to investigate the nature of the vibrations induced in avionics and airborne stores as functions of flight parameters and the firing of the M61A1 gun.

Examination of the vibration response data during gunfire revealed that three distinct types of response occurred: (1) a discrete sinewave vibration response at the gun-firing frequency and at several higher harmonics of this frequency; (2) a repetitive narrowband random vibration, approximately 80 Hz wide, repeating at multiples of 170 Hz; and (3) a shaped random vibration.

It was found that although firing of the M61A1 gun significantly increased the vibrational response of various units, the overall level of response was not significantly different for the different gunfire rates. It was also found that the peak values and frequency of occurrence of the discrete responses of types 1 and 2 behavior tended to exhibit an exponential decrease with harmonic number.

INTRODUCTION

During the period 29 September 1969 through 6 March 1970 the U.S. Naval Missile Center participated in the Board of Inspection and Survey (BIS) service acceptance trials of the A-7E airplane. During the BIS trials measurements were taken of vibration induced in avionics and airborne stores. These measurements were taken during various flight conditions of steady captive flight, maneuvers, and firing of the M61A1 gun, a 20-millimeter cannon. The objectives of these measurements were (1) to determine vibration levels that exceed specification or that might be potentially damaging to avionic equipment and missiles, and (2) to investigate the nature of the vibrations induced in avionics and airborne stores as a function of flight parameters and firing of the M61A1 gun. This paper is concerned with the results of the investigation focused on objective (2).

DESCRIPTION OF MEASUREMENTS

The A-7E airplane (Fig. 1) is a single-place, carrier- or land-based light attack airplane with limited all-weather attack capability. The A-7E has an airframe structurally equivalent to the A-7A and A-7B airplanes but incorporates advanced radar, navigation, and weapon systems. A-7E BU No. 156739 was the prime test airplane for the guided missile trials and the only airplane used for the vibration measurements. A-7E BU No. 156739 was representative of production airplanes except for details of airplane wiring. It was manufactured for use in contractor development testing; therefore production wiring techniques were not used in its manufacture although major systems were representative of production airplanes.

Vibration data were acquired before and during firing of the M61A1 gun at high and low airspeed at altitudes of 5,000 feet and 20,000 feet MSL. The gun was fired at both the high fire rate (6,000 rounds/minute) and the low fire rate (4,000 rounds/minute). Vibration data were also obtained while the gun was fired during a full-power dive and high-speed pullout. Table I lists the flight conditions obtained during these tests.

Vibration response levels were measured on the following equipment:

1. AN/APQ-126(U) forward-looking radar transmitter, in the nose (isolated)

2. AN/AVQ-7(U) head-up display (HUD) unit, in the cockpit

3. Air data computer (ADC), in the weapons bay (isolated)

4. AN/APQ-126(U) forward-looking radar command computer, in the weapons bay
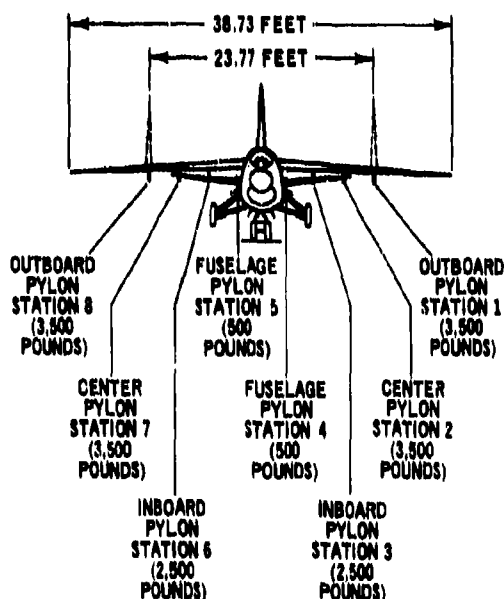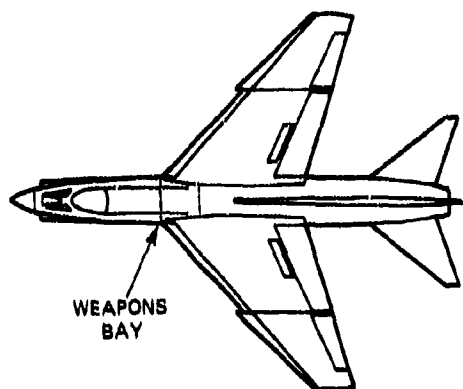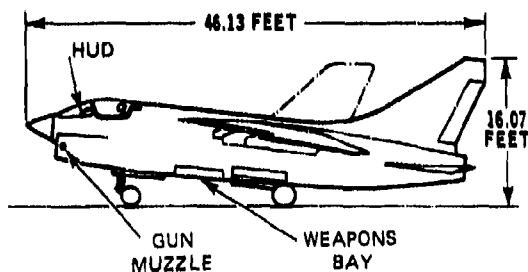
(WEIGHT SHOWN IS MAXIMUM LOAD FOR INDIVIDUAL PYLON)

Fig. 1 – Three-view drawing of A-7E aircraft

TABLE 1
Flight Parameters of Vibration-Response Measurements
on A-7E Airplane

Required Flight Parameters		Flight Conditions Attained	
Gunfire Rate	Speed/Altitude	Altitude (Feet)	Mach No.
4,000 Rounds/Minute	Low/low	5,000	0.34
	Low/high	20,000	0.45
	High/low	5,000	0.76
	High/high	20,000	0.74
	Dive	20,000 (initial)	300 KIAS
	Pullout	8,000 (final)	0.84
6,000 Rounds/Minute	Low/low	5,000	0.34
	Low/high	20,000	0.48
	High/low	5,000	0.75
	High/high	20,000	0.75

5. AN/ASN-91(V) tactical computer set, in the weapons bay

6. AN/AVQ-7(V) head-up display signal data processor, in the weapons bay (isolated)

7. Armament station control unit (ASCU), in the weapons bay

8. WALLEYE weapon, on pylon station 2

9. SHRIKE weapon, on pylon station 3

10. SIDEWINDER weapon, on pylon station 4.

The data were recorded on a 14-track magnetic tape recorder carried in an instrumentation pod on pylon station 1. Table 2 is a list of the equipment, locating the accelerometers.

For ease of describing vibration response, the accelerometers were separated into various groups as defined in Table 3. Salient variables were axes of accelerometers, locations in the aircraft, and gunfire rates.

Also listed in Table 3 are the number of available data points for each group. Other groupings are possible, but, it is believed, the grouping in Table 3 provides the most useful information that can be obtained without reducing the number of data points to a level where statistical confidence is lost.

RESULTS

General

Five separate flights were made to obtain the data required. Two flights were made to obtain data during the four conditions of straight and level flight before and during 4,000 rounds/minute gunfire rate. Two flights were made to obtain data during the four conditions of straight and level flight before and during 6,000 rounds/minute gunfire

TABLE 2
Accelerometer Locations for Measurements

Accelerometer No.	Measurement Direction	Aircraft Subsystem (Unit)
1 2 3	Longitudinal Vertical Lateral	Command computer unit (forward-looking radar assembly)
4 5 6	Longitudinal Vertical Lateral	Radar transmitter unit (forward-looking radar assembly)
7 8 9	Longitudinal Vertical Lateral	Weapons delivery system computer
10 11 12	Longitudinal Vertical Lateral	Air data computer
13 14 15	Longitudinal Vertical Lateral	Head-up display
16 17 18	Longitudinal Vertical Lateral	Signal data processor (head-up display unit)
19 20 21	Longitudinal Vertical Lateral	Armament station control
22 23 24	Longitudinal Vertical Lateral	SIDEWINDER weapon (at missile station 3B)
25 26 27	Longitudinal Vertical Lateral	WALLEYE weapon (at missile station 25)
28 29 30	Longitudinal Vertical Lateral	SHRIKE weapon (at missile station 14.5)

TABLE 3
Accelerometer Groupings and Number of Data Points

Group		Data Points
No.	Accelerometers Description (Nos.)	
1	All (1 to 30)	264
2	All Vertical (2, 5, 8, 11, 14, 17, 20, 23, 26, 29)	88
3	All Longitudinal (1, 4, 7, 10, 13, 16, 19, 22, 25, 28)	88
4	All Lateral (3, 6, 9, 12, 15, 18, 21, 24, 27, 30)	88
5	All at 4,000 Rounds/Minute Gunfire Rate (1 to 30)	156
6	All at 6,000 Rounds/Minute Gunfire Rate (1 to 30)	108
7	All Nose (4, 5, 6)	30
8	All Bay (1, 2, 3, 7 to 12, 16 to 21)	130
9	All Cockpit (13, 14, 15)	20
10	All Stores (22 to 30)	84

rate. One flight was made to obtain data during the maneuvers at each gunfire rate. Unfortunately, because of pilot error, data were not obtained during maneuvers for 6,000 rounds/minute gunfire rate. Table 4 is a summary of the rms g-levels measured by all accelerometers under all flight conditions during this program, and indicates the increase in vibration response level due to firing the gun.

Table 4 was examined to determine whether one of the straight and level flight parameters seemed to be dominant in inducing the highest level of response. As a result of the examination, data are presented in Table 5 to show, for each group, the number of accelerometers that had the highest vibration response in each of the four conditions of straight and level flight before and during gunfire. The vibration levels at the two different gunfire rates are not distinguished in Table 5 since, in general, the response was highest at the same flight condition for each gunfire rate. From Table 5 it can be seen that, in general, the condition of high speed–low altitude induced the highest vibration response level during normal captive flight (before gunfire). During gunfire, however, no such trend existed. This implies, in essence, that there is no generalized dependency of vibration response level during gunfire on the flight condition of the airplane.

Gunfire

Examination of the vibration response data recorded during gunfire revealed three distinct types. The first, and most predominant type, which shall be called type 1 behavior, consisted of a discrete sine-wave vibration response at the gun-firing frequency and at several higher harmonics of this frequency. This spectrum was superimposed upon the low-level broadband random vibration of normal captive flight. Fig. 2 is an example of the type 1 behavior.

The second type of response, which shall be called type 2 behavior, was characterized by a repetitive narrowband random vibration with an upper band limit of 170 Hz, repeating at multiples of this upper frequency superimposed on the low-level broadband vibration. The intensity of the narrowband tended to increase from the lower band limit to a peak at the upper band limit. Fig. 3 is an example of this behavior.

The third type of response, which shall be called type 3 behavior and may be considered a special case of type 2 behavior, was a random vibration characterized by a low level from 20 to 80 Hz, and an approximately flat very high level from 80 to 160 to 170 Hz, followed by a tail-off of approximately 3 db per octave to about 1,000 Hz, where it leveled off below 20 to 80 Hz. Some of the highest vibrational response levels were characterized by type 3 behavior. Fig. 4 is an example of the type 3 behavior. Table 6 shows where these different types of behavior occurred.

The data were examined, counted to determine the frequency of occurrence of each type of response in each group, and summarized in Table 7. Table 7 also contains a column labeled "%" where this number represents the contribution of the frequency of occurrence of a response

type to the total number of data points from Table 3 (i.e., 175/264 = 66.4%).

It can be seen from Table 7 that the type 1 behavior was the dominant response. Type 1 behavior also showed a slight affinity for the longitudinal direction, showed a large tendency to occur during gunfire at the 4,000 rounds/minute rate, and always occurred in the nose and cockpit. It can be seen that type 2 behavior occurred only in the weapons bay and stores, showing a large tendency for the stores. It can also be seen that the type 3 behavior occurred only during gunfire at the 6,000 rounds/minute rate and, as with type 2 behavior, only in the stores and weapons bay.

A further examination of the data not evident in Table 7 revealed

1. That type 2 behavior in the stores occurred only on the SIDEWINDER and SHRIKE missiles (never on the WALLEYE)

2. That type 2 behavior occurred only during gunfire at the 6,000 rounds/minute rate except during maneuvers

3. That type 2 behavior always occurred on these two stores during maneuvers, and

4. That the flight condition of low speed–high altitude induced the highest number of harmonics.

This examination also revealed that the air data computer in the weapons bay was the only other unit to exhibit this type of response. Finally it was noticed that type 2 behavior occurred only at high altitude, and that type 3 behavior occurred only at low altitude.

ANALYSIS AND DISCUSSION

General

The data was subjected to two different types of analyses, an analysis of variance and a statistical behavior analysis. The rms g-levels measured on each accelerometer during each gunfire rate were subjected to an analysis of variance. The independent variables used were low and high levels of speed and altitude and the dependent variable was rms g-level. Thus a 2 x 2 analysis of variance table was used in each instance to determine which, if any, of the primary parameters, speed and altitude, most significantly affected the rms g-level of vibrational response. The data for each accelerometer were also subjected to an analysis of variance by using the parameters of normal captive flight and one gunfire rate in each analysis. Thus a 4 x 2, or in some cases a 3 x 2, analysis of variance table was constructed whereby the data in one column were the measured rms g-levels for all runs during normal captive flight and the data in the second column were the measured rms g-levels for all the runs at one gunfire rate. Thus a determination could be made of how significantly firing of the gun affected the rms g-level of the vibrational response during the straight and level conditions of flight.

74

TABLE 4
Vibration Response Values Measured (rms g-Levels) (20 to 2,000 Hz)

Accel. No.	4,000 Rounds/Minute Gunfire Rate								6,000 Rounds/Minute Gunfire Rate								4,000 Rounds/Minute	
	Low Speed Low Altitude		High Speed Low Altitude		Low Speed High Altitude		High Speed High Altitude		Low Speed Low Altitude		High Speed Low Altitude		Low Speed High Altitude		High Speed High Altitude		Dive	Pullout
	Before	During	Before	During	Before	During	Before	During	Before	During	Before	During	Before	During	Before	During	During	During
1	0.90	3.20	0.99	2.55	1.38	2.60	1.42	2.49	0.90	3.90	0.99	2.75	1.38	3.00	1.42	2.60	2.52	2.30
2	No Data								No Data									
3	0.95	1.60	1.00	1.74	0.98	1.98	0.95	1.54	0.95	1.87	1.00	1.78	0.98	1.45	0.95	1.53	1.60	1.63
4	0.32	0.56	0.31	0.64	0.46	0.61	0.39	0.58	0.32	0.67	0.31	0.71	0.46	0.60	0.39	0.61	0.86	0.55
5	0.29	0.66	0.27	0.98	0.33	0.64	0.41	0.99	0.29	0.62	0.27	0.57	0.33	0.57	0.41	0.49	0.54	0.53
6	0.47	0.51	0.45	0.61	0.46	0.99	0.41	0.65	0.47	0.55	0.46	0.55	0.46	0.53	0.41	0.53	0.56	0.58
7	0.96	2.50	1.05	2.20	1.00	2.00	1.00	2.00	0.96	1.58	1.05	1.74	1.00	1.85	1.00	1.73	2.10	2.10
8	0.54	0.86	0.63	0.88	0.59	0.87	0.54	0.88	0.54	0.86	0.63	1.10	0.59	1.42	0.54	1.32	0.82	1.00
9	0.74	0.93	0.86	0.94	0.83	0.86	0.73	0.94	0.74	0.95	0.86	1.05	0.83	1.08	0.73	1.03	1.00	1.07
10	No Data								No Data									
11	0.73	0.79	0.95	1.98	0.80	1.86	0.89	6.20	0.73	5.30	0.95	6.70	0.80	6.70	0.89	6.30	6.60	6.40
12	0.83	0.96	1.12	2.24	1.02	2.30	1.00	7.00	0.83	6.30	1.12	7.70	1.02	7.80	1.00	7.30	7.80	7.40
13	0.27	4.00	0.44	6.70	0.32	4.80	0.39	4.90	0.27	4.10	0.44	8.40	0.32	4.65	0.39	5.40	4.75	6.80
14	0.23	3.80	0.30	4.55	0.25	4.20	0.33	4.40	0.23	4.90	0.30	9.20	0.25	4.50	0.33	6.30	4.38	4.95
15	No Data								No Data									
16	0.56	0.82	0.67	0.77	0.60	0.70	0.56	0.66	0.56	0.83	0.67	0.83	0.60	0.81	0.56	0.68	0.61	0.66
17	0.80	2.15	0.67	1.00	1.10	0.87	1.05	0.92	0.80	0.94	0.67	1.00	1.10	0.89	1.05	0.79	0.67	0.67
18	1.05	1.10	1.00	1.24	1.60	0.98	1.42	1.00	1.05	1.15	1.00	1.18	1.60	1.00	1.42	0.90	0.67	0.71
19	0.32	1.30	0.93	1.03	0.32	1.25	0.52	1.18	0.32	2.05	0.93	1.78	0.32	2.32	0.52	1.75	1.65	1.10
20	0.62	5.90	1.15	4.65	0.81	4.85	0.90	3.60	0.62	3.20	1.15	3.00	0.81	3.10	0.90	2.40	1.60	1.43
21	0.62	1.20	0.75	1.04	0.68	1.05	0.66	1.08	0.62	1.60	0.75	1.75	0.68	1.73	0.66	1.67	1.55	1.90
22	0.66	0.97	0.88	1.84	0.66	1.72	No Data		0.66	1.45	0.88	1.62	0.66	1.28	0.74	1.48	1.45	1.58
23	0.59	0.89	0.91	1.65	0.59	1.58	No Data		0.59	1.14	0.91	1.47	0.59	1.15	0.73	1.25	1.43	1.55
24	0.70	1.10	1.25	1.78	0.69	1.76	No Data		0.70	1.40	1.25	1.83	0.69	1.39	0.87	1.45	1.54	2.00
25	0.31	0.46	0.44	0.45	0.34	0.53	0.37	0.55	0.31	0.59	0.44	0.58	0.34	0.73	0.37	0.63	0.45	0.53
26	0.28	0.42	0.37	0.41	0.28	0.45	0.38	0.50	0.28	0.50	0.37	0.65	0.28	0.66	0.38	0.59	0.39	0.65
27	0.44	0.65	0.63	0.65	0.44	0.73	0.43	0.64	0.44	0.77	0.63	0.80	0.44	1.02	0.43	0.72	0.59	0.72
28	0.54	1.15	1.00	1.70	0.62	1.76	No Data		0.54	3.35	1.00	3.70	0.62	4.72	0.69	3.65	3.90	3.90
29	0.43	0.89	0.88	1.33	0.51	1.46	No Data		0.43	2.70	0.88	3.00	0.51	3.60	0.59	2.90	3.10	3.00
30	0.61	0.87	0.87	1.39	0.68	1.52	No Data		0.61	2.90	0.87	3.20	0.68	4.10	0.64	3.10	3.25	3.15

75

TABLE 5
Density of Most Severe Flight Condition Affecting Vibration Response

Group No.	Number of Accelerometers With Highest Vibration Response							
	Before Gunfire				During Gunfire			
	Low Speed Low Altitude	Low Speed High Altitude	High Speed Low Altitude	High Speed High Altitude	Low Speed Low Altitude	Low Speed High Altitude	High Speed Low Altitude	High Speed High Altitude
1	1	3	19	4	12	18	22	7
2	0	1	5	3	4	6	7	3
3	0	1	7	1	5	6	7	1
4	1	1	7	0	3	6	8	3
5	--	--	--	--	6	6	10	7
6	--	--	--	--	6	12	12	0
7	1	1	0	1	2	1	4	1
8	0	2	10	1	10	7	9	4
9	0	0	1	1	0	0	4	0
10	0	0	8	1	0	10	6	2

ACCELERATOR LOCATION: HEAD-UP DISPLAY
DIRECTION OF MEASUREMENT: VERTICAL
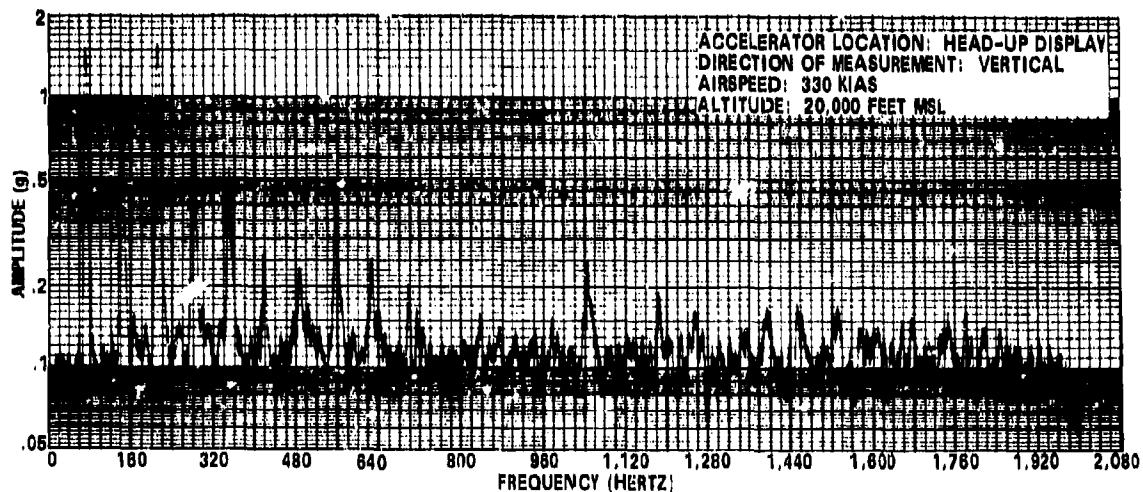AIRSPEED: 330 KIAS
ALTITUDE: 20,000 FEET MSL

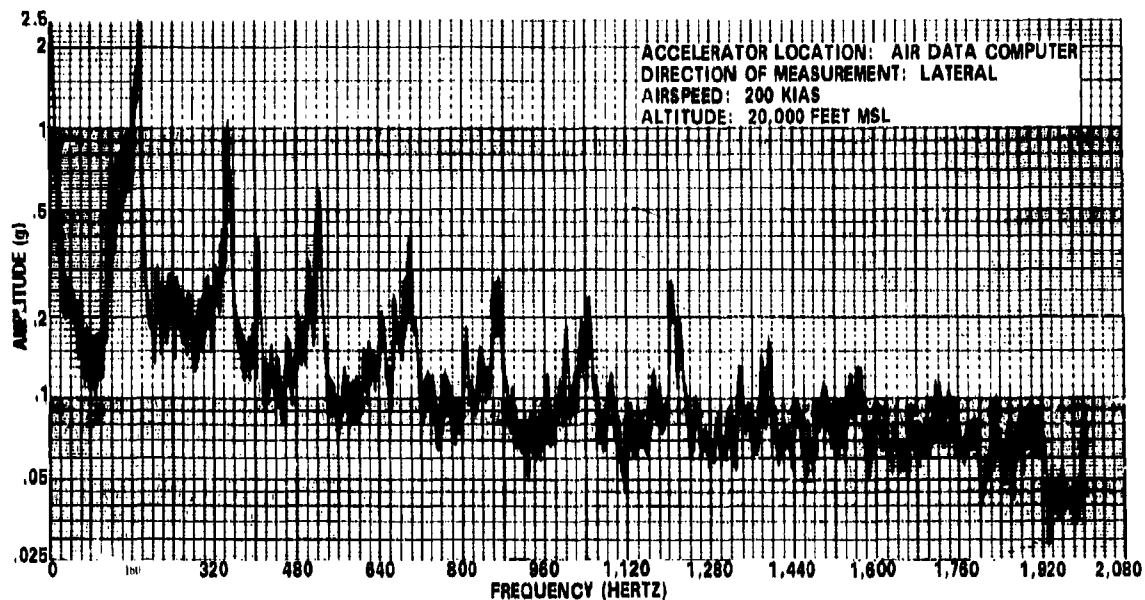Fig. 2 – Typical vibration spectrum of type 1 behavior

76

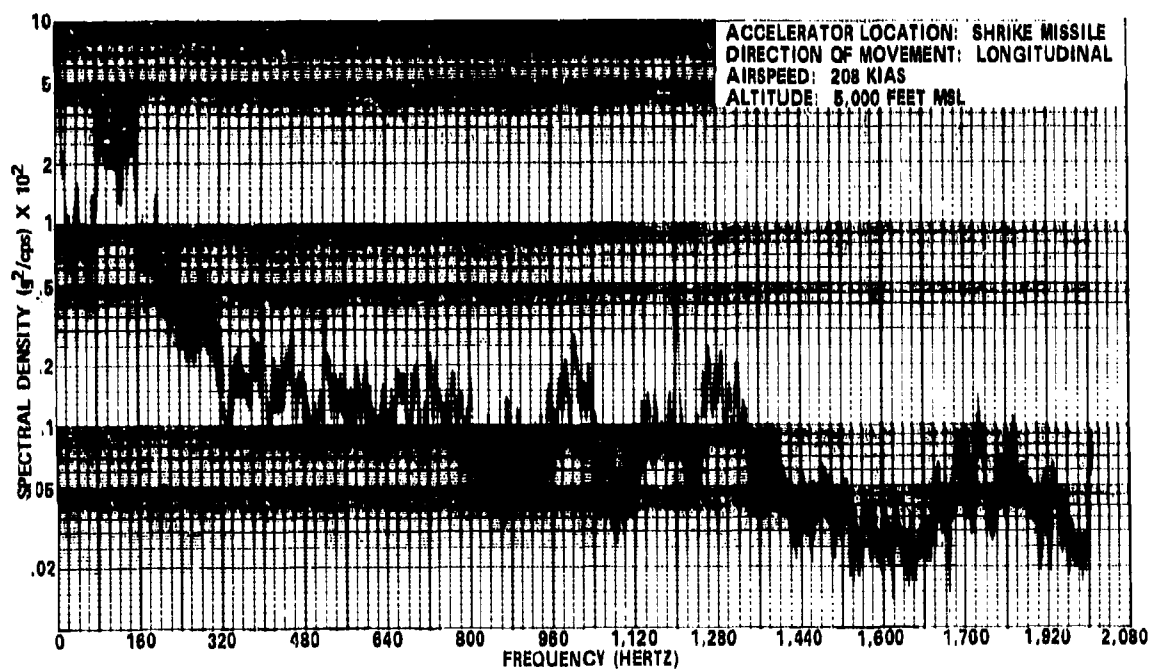Fig. 3 – Typical vibration spectrum of type 2 behavior

Fig. 4 – Typical vibration spectrum of type 3 behavior

77

TABLE 6
Occurrence of Type of Behavior in Vibration Response in Accelerometers.

Acceler-ometer No.	Gunfire (4,000 Rounds Per Minute)				Gunfire (6,000 Rounds Per Minute)			
	Low Speed/ Low Altitude	Low Speed/ High Altitude	High Speed/ Low Altitude	High Speed/ High Altitude	Low Speed/ Low Altitude	Low Speed/ High Altitude	High Speed/ Low Altitude	High Speed/ High Altitude
1	1	1	1	1	1	1	1	1
2				1				
3	1	1	1	1	1	1	1	1
4	1	1	1	1	1	1	1	1
5	1	1	1	1	1	1	1	1
6	1	1	1	1	1	1	1	1
7	1	1	1	1	1	1		
8	1	1	1	1				
9	1	1	1					
10		1	1					
11		1	1		3	2	3	1 and 2
12		1	1		3	2	3	1 and 2
13	1	1	1	1	1	1	1	1
14	1	1	1	1	1	1	1	1
15								
16	1	1	1	1	1			1
17	1	1	1	1	1		1	1
18	1	1	1	1	1			
19	1	1	1	1	1	1	1	1
20	1	1	1	1	1		1	1
21	1	1	1	1	1	1	1	1
22	1	1	1		1	1 and 2	1	1 and 2
23	1	1	1			2		1 and 2
24	1	1				2		
25								
26	1				1			
27								
28		1	1		3	2	3	2
29					3	2	3	2
30		1	1		3	2	3	2

TABLE 7
Frequency of the Three Different Types of Response

Group No.	Type 1 Frequency	Type 1 %	Type 2 Frequency	Type 2 %	Type 3 Frequency	Type 3 %
1	175	66.4	31	11.7	10	3.8
2	57	65.0	12	13.6	4	4.5
3	69	78.5	8	9.1	2	2.3
4	49	55.6	11	12.5	4	4.5
5	123	78.9	16	10.3	0	0.0
6	52	48.1	15	13.9	10	9.3
7	30	100.0	0	0.0	0	0.0
8	93	71.5	8	6.2	4	3.1
9	20	100.0	0	0.0	0	0.0
10	32	38.1	23	27.4	6	7.2

The statistical behavior analysis of types 1 and 2 behavior was a counting and averaging procedure. From the reduced data the peak g-values of the discrete sine-wave vibration and narrowband vibration were determined. These data were analyzed to determine the average value and standard deviation of the value of the first spike (a normal distribution was assumed). Then the average value was assigned a value of 1.0 and the average value of all the harmonics determined and normalized to the average value of the first spike. This presented a qualitative analysis of the general behavior of each group of accelerometers, providing a quick comparison in the difference in behavior. The frequency of occurrence of each fundamental spike and harmonic was determined and presented in a pictorial form to determine the general nature of the probability of occurrence of each spike. These data are presented in terms of the percentage of possible occurrences (frequency of occurrence/total number of data points) for each spike to show probability of occurrence.

Analysis of Variance

During Gunfire: The results of the analysis of variance of the data recorded during gunfire are given in Table 8. The numbers in the blocks of Table 8 represent the number of accelerometers in each group the data from which passed some level-of-significance test but would not pass a higher test. The data was slightly more affected by altitude than speed. Fewer than half of the accelerometer data would, however, pass any level-of-significance test, and of those that did most would pass only a 70% test. This indicates that the level of vibrational response is not largely affected by changes in speed or altitude in the regions covered in this measurement program.

TABLE 8
Results of Analysis of Variance of Data Recorded During Gunfire

Group No.	Speed 70%	Speed 90%	Speed 95%	Speed Total	Altitude 70%	Altitude 90%	Altitude 95%	Altitude Total	Total Data Points
1	10	2	1	13	11	2	3	16	48
2	4	0	1	5	3	0	1	4	16
3	5	2	0	7	4	2	1	7	16
4	1	0	0	1	4	0	1	5	16
5	5	1	1	7	5	1	2	8	21
6	5	1	0	6	6	1	1	8	27
7	3	0	0	3	3	0	1	4	6
8	4	1	1	6	6	0	2	8	26
9	2	0	0	2	0	0	0	0	4
10	1	1	0	2	2	2	0	4	12

TABLE 9
Results of Analysis of Variance to Determine Effect of Gunfire

Group No.	Guns				Runs				Total Data Points
	70%	90%	95%	Total	70%	90%	95%	Total	
1	12	6	30	48	30	4	7	41	54
2	2	2	11	15	13	0	3	16	18
3	4	4	10	18	9	1	1	11	18
4	6	0	9	15	8	3	3	14	18
5	11	1	11	23	18	1	2	21	27
6	1	5	19	25	12	3	5	20	27
7	1	2	3	6	2	1	0	3	6
8	3	2	15	20	13	3	2	18	26
9	0	0	4	4	4	0	0	4	4
10	8	2	8	18	11	0	5	16	18

Effect of Gunfire: The results of the analysis of variance to determine the effect of gunfire, given in Table 9, are distinctly different from the previous data. Here almost all the accelerometer data passed some level-of-significance test (48 out of 54) and, more importantly, more than one half (30 out of 54) of the data passed the 95% level-of-significance test. In only 2 out of the 10 groups did less than one half of the data pass the 95% level, and in all groups more than one half of the data passed the 90% level of significance. Thus, in general, firing of the gun significantly increases the level-of-vibration response over that of normal captive flight. The data of Table 4 provide an indication of how much the level is increased for each accelerometer because of firing of the gun.

Statistical Behavior Analysis

Type 1: Discrete sine-wave vibrations at the gun-firing frequency (fundamental) and at several harmonics above (up to the 15th harmonic in some cases) constituted type 1 behavior, the discrete sine waves being superimposed upon a broadband random vibration due to normal flight. In this section the broadband random aspect will be ignored and attention directed to the discrete sine-wave portion of type 1 behavior.

From the reduced records, the peak g-values of the sine-wave vibration at the fundamental were investigated. On the assumption of a normal distribution, the average value and standard deviation of the fundamental were calculated for each group (Table 10). The 90% and 95% values were also calculated (Table 10). These values and the normalized behavior patterns provide a complete description of the discrete sine-wave portion of the type 1 behavior.

It can be seen from Table 10 that the vertical direction had the highest response of the three directions. The longitudinal direction was noticeably lower in response indicating that gun recoil is not a significant exciting force. The lateral direction had the lowest response. Table 10 also indi-

TABLE 10
Definition of Fundamental Response of Type 1 Behavior

Group No.	Average Magnitude $\bar{X}$ (g-Peak)	Standard Deviation σ (g-Peak)	$\bar{X} + 1.65\sigma$ (g-Peak)	$\bar{X} + 2.33\sigma$ (g-Peak)
1	0.5235	0.6347	1.574	2.007
2	0.6943	0.8887	2.161	2.765
3	0.5470	0.5014	1.374	1.715
4	0.3014	0.4636	1.066	1.382
5	0.5097	0.6216	1.535	1.958
6	0.5753	0.6681	1.678	2.132
7	0.1826	0.0778	0.311	0.364
8	0.5724	0.6516	1.648	2.091
9	1.4205	0.6404	2.477	2.913
10	0.1899	0.0919	0.342	0.404

cates that the response at 6,000 rounds/minute firing rate is slightly higher than that at 4,000 rounds/minute; however, the difference is small and probably not significant.

One other unanticipated result found in Table 10 was that, of the four aircraft mounting areas investigated, the nose equipment had the lowest response of all. This was not expected since this equipment is located next to and closest to the gun muzzle and would normally be expected to have the highest response. The cockpit, which is located behind the nose and further from the gun muzzle, had the highest response of all groups investigated. This indicates that cockpit equipment is the most affected by firing of the gun. Hutchinson and Musson (reference 1) analyzed vibrations induced by gunfire and concluded that vibration response is highest nearest the gun muzzle. This was not the case here and may indicate that gun recoil forces are significant in the cockpit equipment. However, the data did not

80

lend itself to an investigation of this hypothesis. The response of the stores was also very low, about the same as the nose equipment, indicating that airborne stores are not very susceptible to type 1 behavior during firing of the gun.

The average peak value of the sine-wave vibration for all data (group 1) at the fundamental, or gun-firing, frequency was assigned a value of 1.0, and the average peak value of each harmonic was calculated and normalized to the fundamental. The frequency of occurrence of the fundamental and each harmonic was determined and converted to a percentage of occurrence. In Fig. 5 the normalized pattern is presented for type 1 behavior of group 1, and in Fig. 6 the frequency of occurrence in percent is presented for each harmonic.

Fig. 5 illustrates a predominant feature of the behavior patterns of all groups, that of an approximate exponential decay in the peak values of each harmonic. Reference 1 concluded that vibration at the higher harmonics tended to to become more random than sine wave as evidenced from amplitude histogram records of the higher harmonics. This was attributed to nominal fluctuations in the gun firing rate and harmonics. The decay in peak values, noted here, could provide another explanation in that the lower peak values at the higher harmonics would become masked by, or hidden within, the broadband random vibration leading to the type of amplitude histograms shown in reference 1. The same approximate exponential decay is noted in the data of Fig. 6, indicating that the probability of observing a response at a higher harmonic decreases with increasing harmonic number. It is noted that responses were recorded at 15f (1,000 Hz for 4,000 rounds/minute and 1,500 Hz for 6,000 rounds/minute), indicating that equipment will respond at high frequencies to gunfire, although, from Fig. 6, it is seen that responses above 9f occur less than 5% of the time.

The data for groups 2 to 10, analyzed by the same method, are shown in Figs. 7 to 24. These data are not discussed; however, the same features, as previously discussed, can be seen to occur.

Type 2: This behavior was characterized by a repetitive narrowband random vibration, with an upper band limit of 170 Hz repeating at multiples of this frequency. The data for type 2 behavior were reduced in the same manner as for type 1 except that, because of the low number of occurrences, they were analyzed for group 1 (overall) only. Figs. 25 and 26 show the normalized behavior pattern and the frequency of occurrence of the harmonics for type 2 behavior. From Figs. 25 and 26 the same approximate exponential decay can be seen as was apparent in type 1 behavior. From Fig. 25 it is seen that responses were observed out to 10f. It is noted that, although the higher harmonics occur approximately 1% of the time in group 1, for group 10, where most of the type 2 behavior was noted, these harmonics occur nearly 3 to 4% of the time, indicating that they should not be neglected when describing the vibrational response of airborne stores.

Table 11 gives the average value and standard deviation of the peak of the fundamental narrowband for group 1 and for each unit that responded with type 2 behavior. From Table 11 it is noticed that the values of the peak at the fundamental increases with distance from the gun muzzle; i.e., the air data computer, which is the furthest unit of these three from the gun muzzle, had the highest response, and the closest unit, the SIDEWINDER, had the lowest response. This is contrary to most theories predicting that the closer the unit to the gun muzzle the higher the response. No explanation for this behavior, however, was found.

Type 3: The data for type 3 behavior, which may be considered a special case of type 2 behavior, were analyzed to determine the characteristics of the peak of the narrowband random vibration at the fundamental. This peak value appeared to be the only characteristic that varied significantly from record to record or from the characteristics shown in Fig. 4. Table 12 gives the average value and standard deviation of the peak of the fundamental narrowband for group 1 (overall) and for each unit that responded with type 3 behavior. The 90% and 95% values were also calculated and given in Table 12, as was done for types 1 and 2 behavior. Since no harmonics of the fundamental occurred, no behavior pattern spectrum figures were derived, and Table 12 and Fig. 4 adequately describe the type 3 behavior. From Table 12 the same phenomena observed in type 2 behavior emerges: the air data computer again has the highest response. Since types 2 and 3 behavior occurred at different altitudes and only during gunfire at 6,000 rounds/minute rate, there are two possible explanations: (1) peculiarities exist in unit or accelerometer mounting, or

TABLE 11
Definition of Fundamental Response of Type 2 Behavior

Location	Average Magnitude $\bar{X}$ (g-Peak)	Standard Deviation σ (g-Peak)	$\bar{X} + 1.65\sigma$ (g-Peak)	$\bar{X} + 2.33\sigma$ (g-Peak)
Overall	0.8442	0.6972	1.995	2.469
Air Data Computer	1.8750	0.3535	2.458	2.699
SHRIKE	0.7633	0.1649	1.035	1.148
SIDEWINDER	0.1827	0.0358	0.242	0.266

TABLE 12
Definition of Narrowband Peak of Type 3 Behavior

Location	Average Magnitude $\bar{X}$ (g-Peak)	Standard Deviation σ (g-Peak)	$\bar{X} + 1.65\sigma$ (g-Peak)	$\bar{X} + 2.33\sigma$ (g-Peak)
Overall	0.8910	0.4817	1.686	2.013
Air Data Computer	1.3725	0.3895	2.015	2.280
SHRIKE	0.5700	0.1321	0.788	0.878

(2) the input excitation for these sensitive units is predominantly either acoustic or mechanical and the excitation for the other units is predominantly the other form. However, there are no known data to verify either of these possible explanations and this would be in conflict with the findings of reference 1.

CONCLUSIONS

On the basis of the data discussed in this paper, the following conclusions are drawn:

1. The measured vibrational response that occurred during firing of the M61A1 gun on the A-7E aircraft can be classified as three distinct types of behavior. Type 1 behavior is a discrete sine-wave vibration response at the gun-firing frequency and at several multiples of the gun-firing frequency (harmonics) superimposed upon a low-level broadband random vibration. Type 2 behavior is a repetitive, narrowband, random vibration, 80 Hz wide, rising quickly to a peak and upper limit at 170 Hz. This narrowband random vibration repeated at multiples of 170 Hz (harmonics) and was superimposed upon a low-level broadband, random vibration. Type 3 behavior is an approximately flat, high-level narrowband, random vibration 80 Hz wide, with an upper limit of 160

to 170 Hz. This random vibration decreased in level at a rate of approximately 3 db per octave from 170 Hz to 1,000 Hz, where the data levels off. (This can be considered a special case of type 2 behavior.)

2. Firing of the M61A1 gun on the A-7E aircraft significantly increases the vibration response level of the various units.

3. The vibrational response of units showing types 2 and 3 behavior during firing of the M61A1 gun on the A-7E aircraft tends to increase with distance from the gun muzzle.

4. The peak values and the frequency of occurrence of the discrete sine-wave vibrations of type 1 behavior tend to decrease exponentially with harmonic number.

5. The difference in vibrational response of units on the A-7E aircraft at the two rates of gunfire is insignificant.

REFERENCE

Hutchinson, J. A., and Musson, B. G., "Effects of Flight Conditions Upon Gunfire Induced Vibration Environment," Shock and Vibration Bulletin, December 1970, Bulletin 41, Part 4.
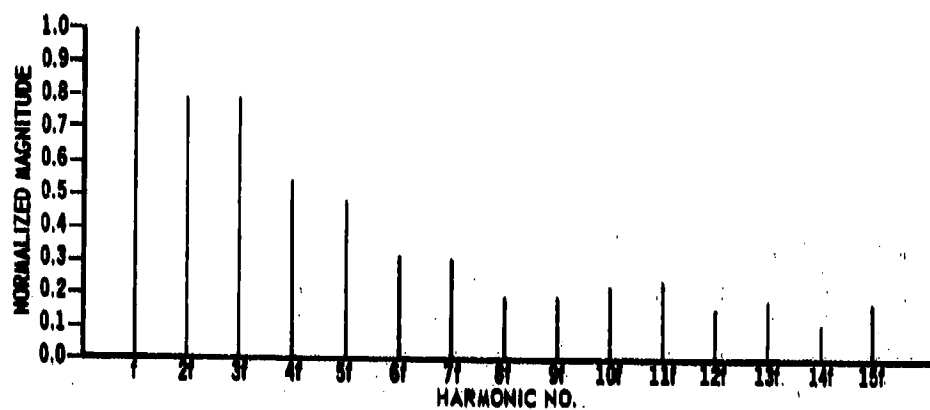
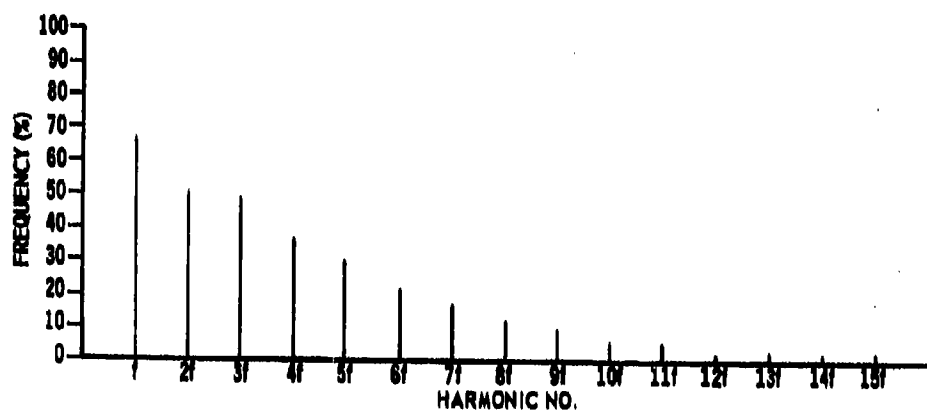Fig. 5 – Vibration Spectrum for Type 1 Behavior, Group 1

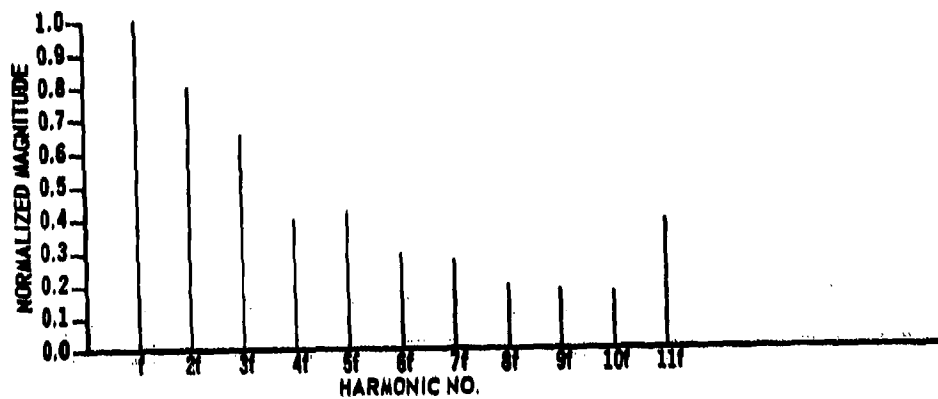Fig. 6 – Vibration Spectrum for Type 1 Behavior, Frequency of Occurrence, Group 1

83

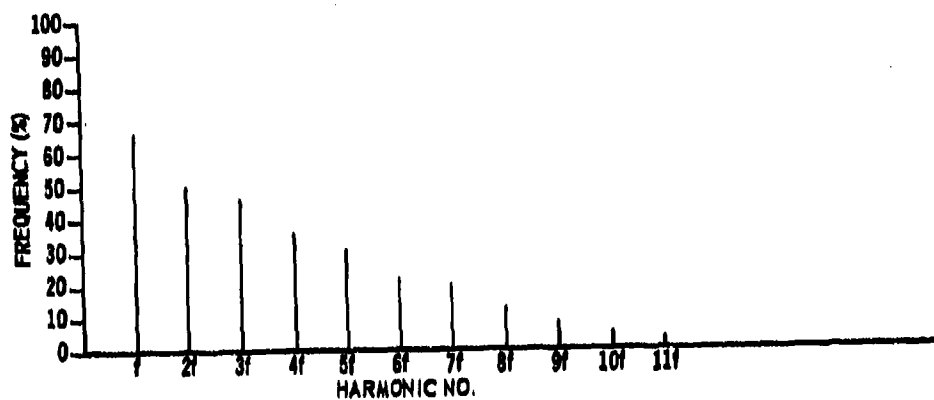Fig. 7 – Vibration Spectrum for Type 1 Behavior, Group 2

Fig. 8 – Vibration Spectrum for Type 1 Behavior, Frequency of Occurrence, Group 2
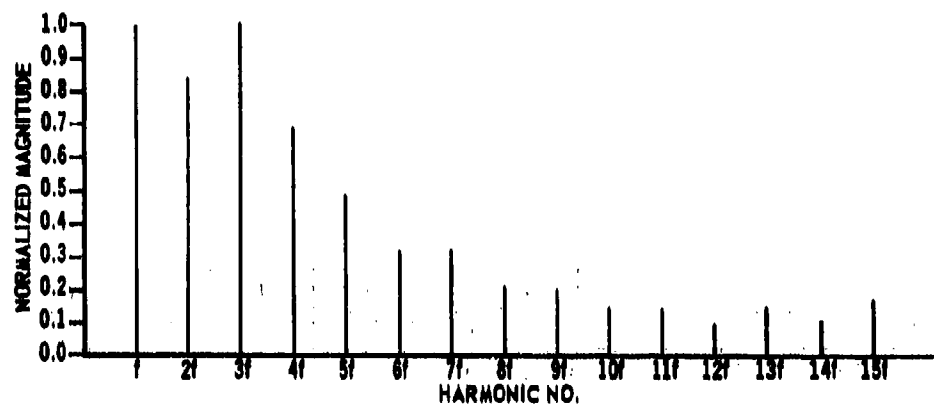
84

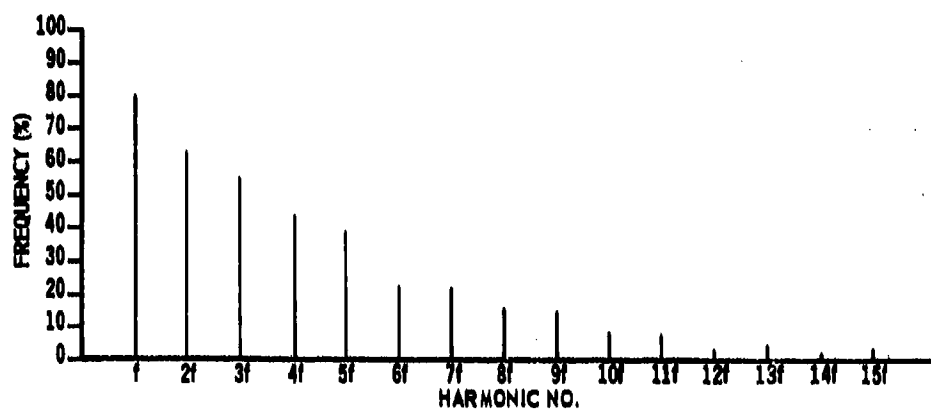Fig. 9 – Vibration Spectrum for Type 1 Behavior, Group 3

Fig. 10 – Vibration Spectrum for Type 1 Behavior, Frequency of Occurrence, Group 3
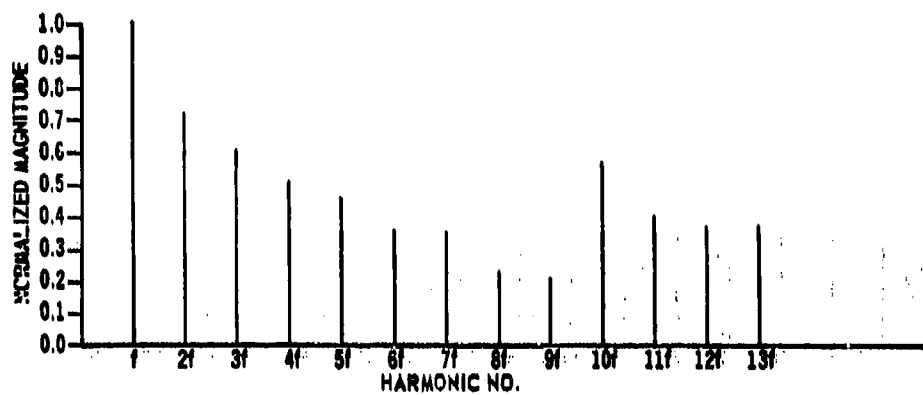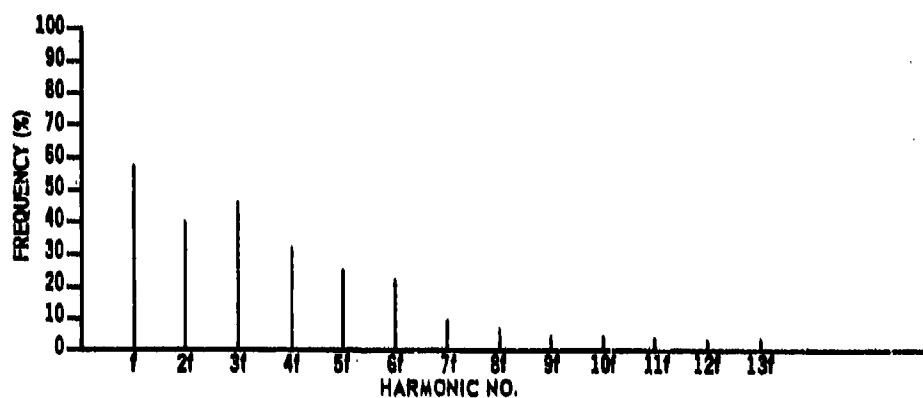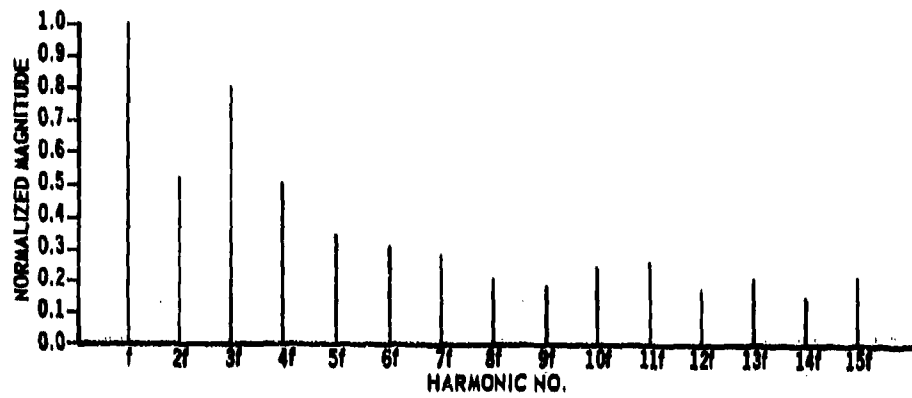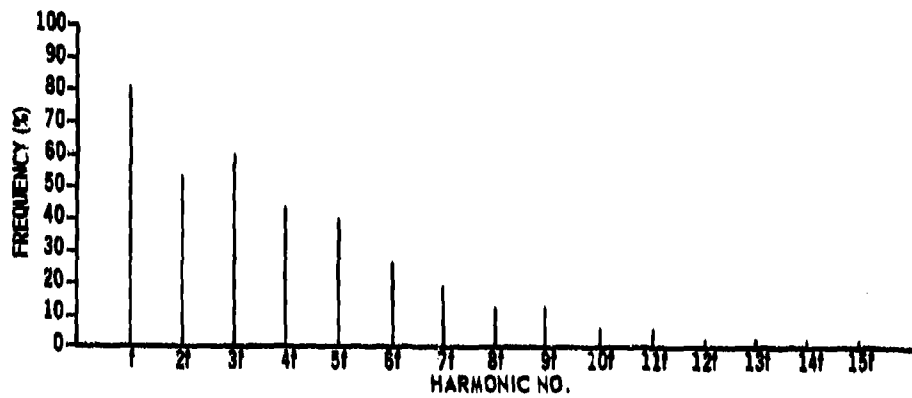
Fig. 11 – Vibration Spectrum for Type 1 Behavior, Group 4

Fig. 12 – Vibration Spectrum for Type 1 Behavior, Frequency of Occurrence, Group 4

Fig. 13 – Vibration Spectrum for Type 1 Behavior, Group 5

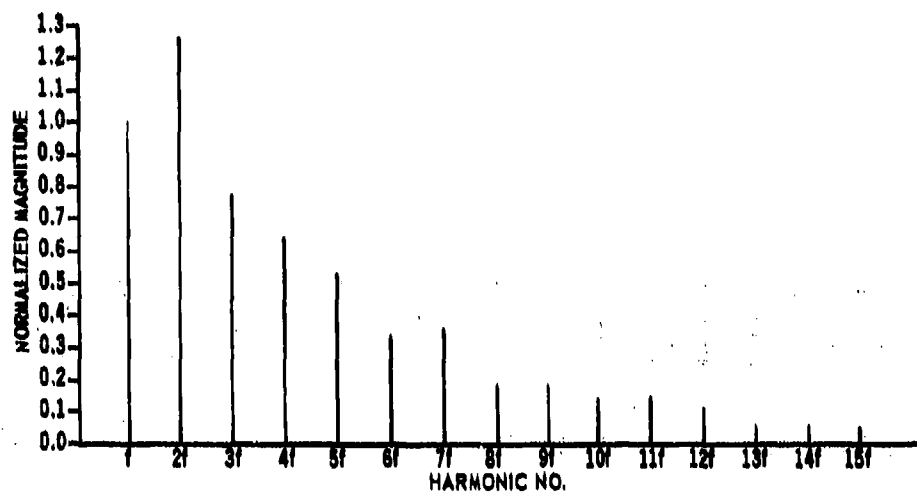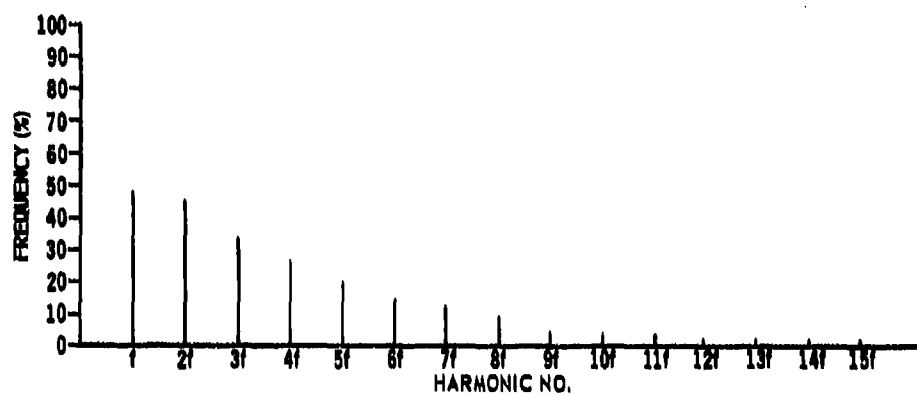Fig. 14 – Vibration Spectrum for Type 1 Behavior, Frequency of Occurrence, Group 5

Fig. 15 – Vibration Spectrum for Type I Behavior, Group 6

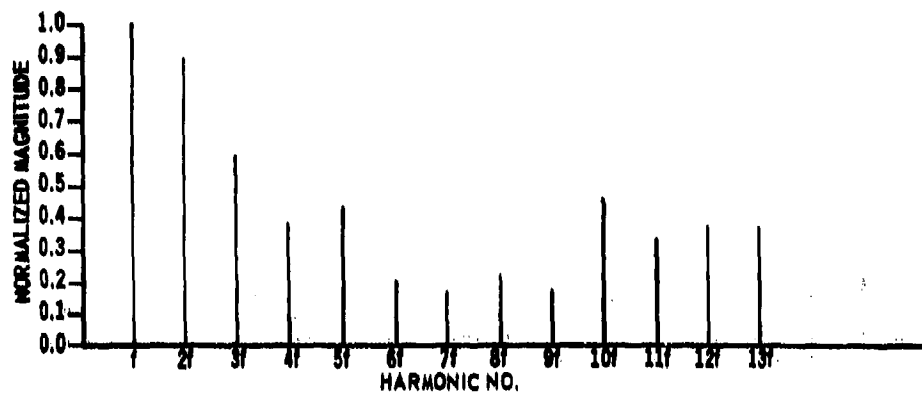Fig. 16 – Vibration Spectrum for Type I Behavior, Frequency of Occurrence, Group 6

88

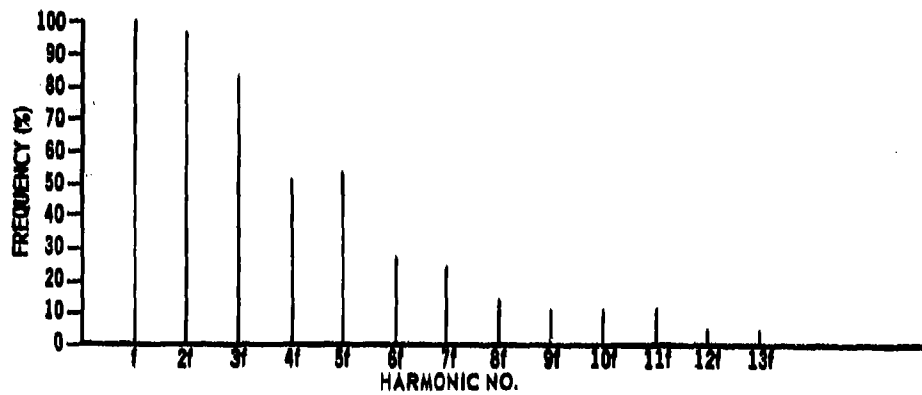Fig. 17 - Vibration Spectrum for Type 1 Behavior, Group 7

Fig. 18 - Vibration Spectrum for Type 1 Behavior, Frequency of Occurrence, Group 7
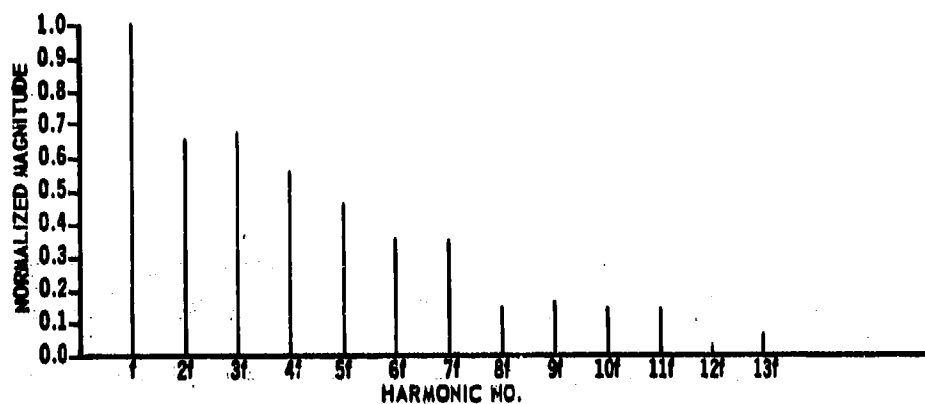
89

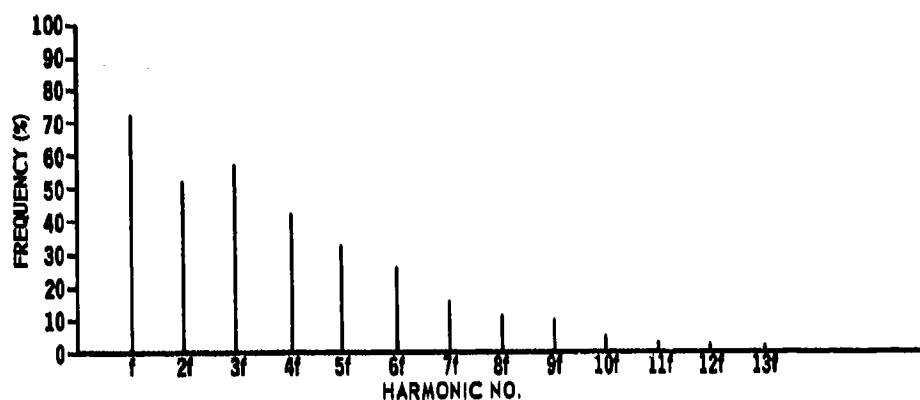Fig. 19 – Vibration Spectrum for Type 1 Behavior, Group 8

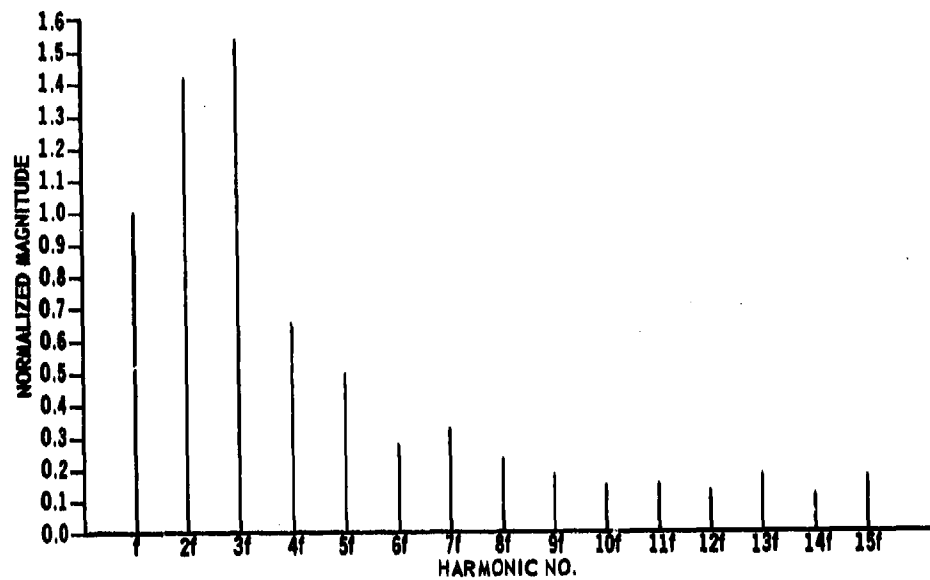Fig. 20 – Vibration Spectrum for Type 1 Behavior, Frequency of Occurrence, Group 8

Fig. 21 - Vibration Spectrum for Type 1 Behavior, Group 9
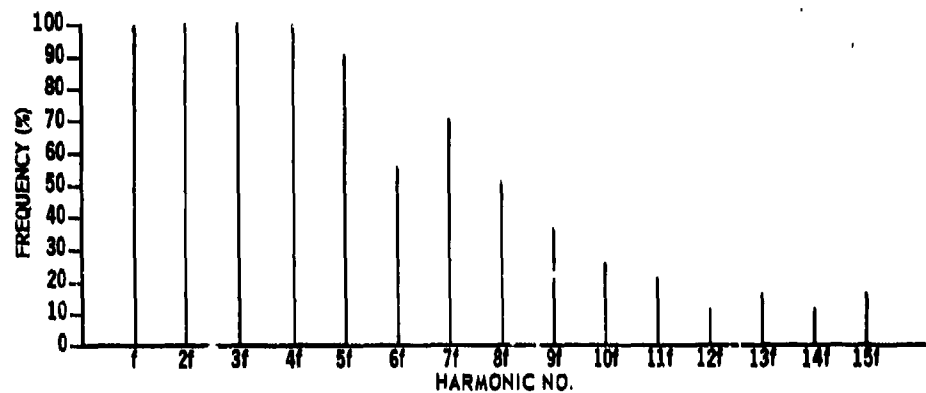

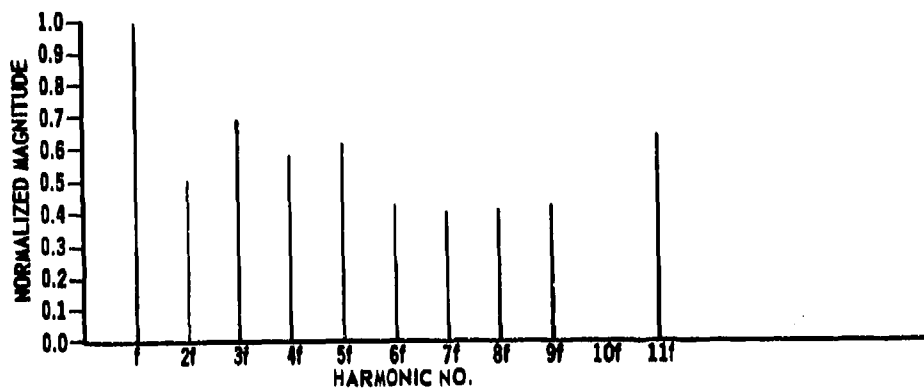Fig. 22 - Vibration Spectrum for Type 1 Behavior, Frequency of Occurrence, Group 9

91

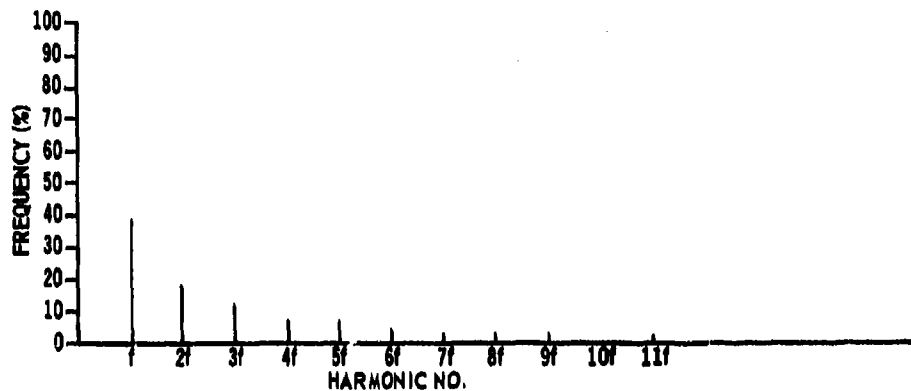Fig. 23 – Vibration Spectrum for Type 1 Behavior, Group 10

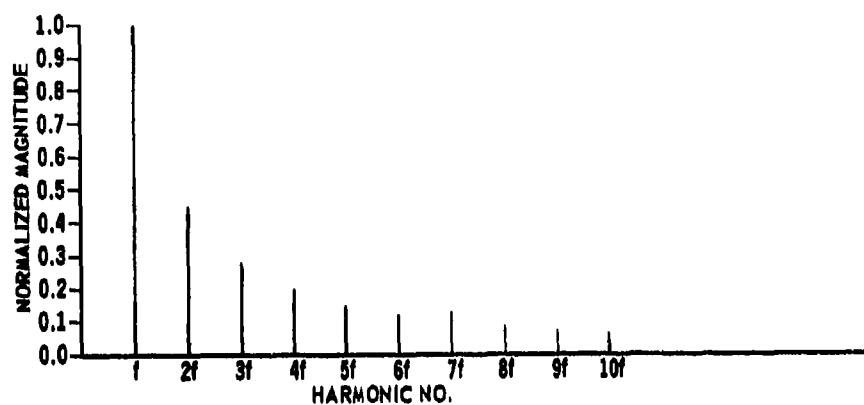Fig. 24 – Vibration Spectrum for Type 1 Behavior, Frequency of Occurrence, Group 10

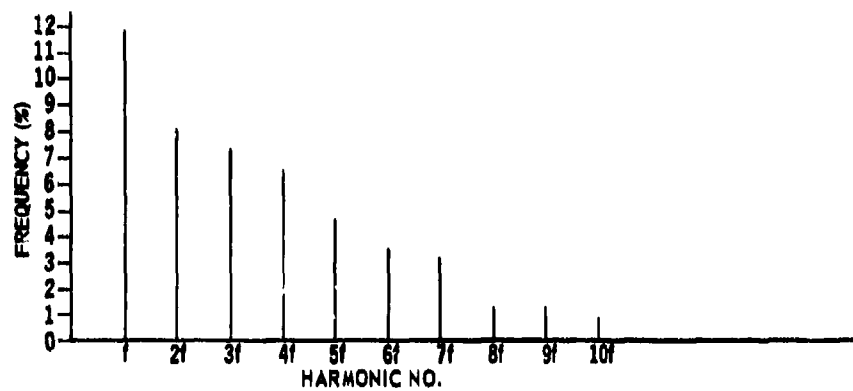Fig. 25 – Vibration Spectrum for Type 2 Behavior, Group 1

Fig. 26 – Vibration Spectrum for Type 2 Behavior, Frequency of Occurrence, Group 1

APPLICATIONS OF STRAIN GAGES TO BALLISTIC PROBLEMS

Paul D. Flynn
Pitman-Dunn Laboratory
Frankford Arsenal
Philadelphia, Pennsylvania

This paper describes several ballistic problems in which external sur-
face strain gage measurements were used to determine internal ballistic
pressures, to detect projectiles in gun barrels for the purpose of
synchronizing other instrumentation such as flash X-rays, and to study
various ballistic phenomena. A brief review of the strain gage method
is given, but the emphasis is on novel applications which may be of
general interest to ballisticians and to the shock and vibration
community.

INTRODUCTION

Electrical-resistance strain gages have
been used in ballistics ever since this type
of gage became available commercially in the
early 1940's, e.g., see Refs. [1,2]. The
principal advantages of strain gages are their
nominal cost, negligible size and weight, and
ease in mounting by using adhesives. The
chief disadvantage is that the gage output is
proportional to the strain in the part on
which the gage is cemented, and a relation
between the strain and the ballistic parameter
of interest is required.

High pressures beyond the range of avail-
able piezoelectric pressure transducers were
determined from strain gages on a caliber 0.60
high velocity launcher. During firing,
several chambers (thick-walled tubes, OD =
2.5 in., wall ratio, w = OD/ID = 2) were over-
strained and autofrettaged so that elastic
behavior was attained at pressures up to about
120 kpsi. Strain gage instrumentation was
developed for a light-gas gun to determine
chamber pressures, piston velocities, and
pressures in the central breech (OD ≈ 7 in.,
w ≈ 4.3). The central breech deformed
plastically in most rounds, and pressures as
high as 800 kpsi were estimated on the basis
of the elastic strain recovered during un-
loading.

Strain gages were cemented on various
laboratory test barrels to obtain precise
reference time signals for synchronizing flash
X-rays. An adjustable strain gaged hose clamp
was used as a simple transducer for detecting
projectiles in gun barrels during firing, and
this device eliminates the cementing of strain

gages on each barrel. These and other exam-
ples based on our experience with high
velocity guns and ammunition testing are given
in the following sections.

TEST PROCEDURES

Under certain conditions, internal ballis-
tic pressures can be determined from external
strain gage measurements. With this non-
destructive technique, the gun is not weakened
by drilling and tapping for a pressure gage,
and this is especially important at high
pressures.

Tube with Internal Pressure. From Lamé's
solution, the circumferential and radial
stresses, σ_θ and σ_r, in an elastic thick-
walled cylinder subjected to static internal
pressure, p, are [3]

$$\sigma_\theta = \frac{a^2 p}{b^2 - a^2} (1 + b^2/r^2),$$

$$\sigma_r = \frac{a^2 p}{b^2 - a^2} (1 - b^2/r^2), \tag{1}$$

where a and b are the inner and outer radii as
shown in Fig. 1. The axial stress, σ_z, de-
pends on the end conditions.

At the outer surface, r = b so that

$$\sigma_\theta = 2a^2 p/(b^2 - a^2), \quad \sigma_r = 0, \tag{2}$$

From Hooke's law

$$\sigma_\theta = E(\epsilon_\theta + \mu \epsilon_z)/(1 - \mu^2), \tag{3}$$

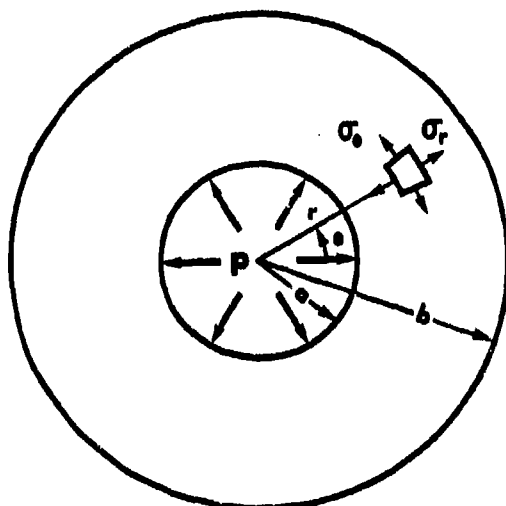where E is Young's modulus and μ is Poisson's

95

Fig. 1 - Thick-walled tube with
internal pressure

ratio, and therefore

$$p = \frac{w^2 - 1}{2} \cdot \frac{E}{1 - \mu^2} \cdot (\epsilon_\theta + \mu \epsilon_z), \qquad (4)$$

where $w = b/a = OD/ID$ is the wall ratio.

Hence, the static internal pressure, p,
can be determined by measuring the strains,
ϵ_θ and ϵ_z, on the outer surface of an elastic
thick-walled cylinder. Equation (4) can be
used to calculate ballistic pressures so long
as the loading is quasi-static, the material
responds elastically, and the gun approximates
a thick-walled tube.

Strain Gage Circuits. Potentiometer cir-
cuits [4] were used to measure the dynamic
strains so that

$$\epsilon = \frac{1 + R_g/R_b}{F} \cdot \frac{\Delta V_g}{V_g}, \qquad (5)$$

where R_g is the gage resistance, R_b is the
ballast resistance, F is the manufacturer's
gage factor, ΔV_g is the voltage change across
the gage, and V_g is the steady-state gage
voltage.

CALIBER 0.60 HIGH VELOCITY LAUNCHER

Experimental Setup. Figure 2 is an over-
all view of the gun and hypervelocity test
facility which can be used to fire projectiles
in controlled atmospheres from high vacuum to
100 psig. In a terminal ballistics program,
increased propellant charges were used to
obtain higher projectile velocities. This
produced such high ballistic pressures that a
pressure transducer was blown off the chamber.

We were asked to monitor the strain-time
response of several chambers and to determine
the highest pressure at which the gun could
operate and remain dimensionally stable.

Tubular chambers were machined from surplus
30 mm test barrels having nominal dimensions
of 1.25 in. ID and 2.5 in. OD. An "exploded"
view of Chamber No. 1, 7 in. long, is given in
Fig. 3. Holes were drilled and tapped for
mounting a Kistler quartz pressure transducer
(Model 607A) and a Frankford Arsenal piezoelec-
tric gage [5]. Three chambers without pressure
gage holes were also fired: No. 2, 7 in. long;
No. 3, 5 in. long; and No. 4, 9 in. long.
After loading each chamber with propellant, a
heavy-duty nut was used to screw the chamber
onto the caliber 0.60, smooth bore, 11.5 ft.
launch tube.

Comparison of Pressure Gages. Chamber No.
1 was used to compare the pressure-time records
obtained from strain gages with those obtained
from quartz transducers at pressures up to
75,000 psi. The pressures obtained from the
strain gages differed somewhat from the Kistler

Fig. 2 - Caliber 0.60 high velocity launcher
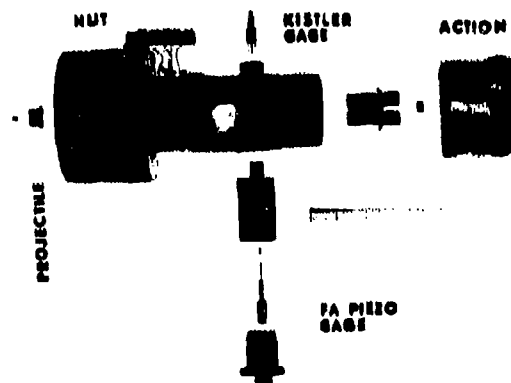and hypervelocity test facility

Fig. 3 - Chamber No.1 with pressure transducers,
strain gages, and components used in gun

TABLE 1

Caliber 0.60 High Velocity Launcher, Chamber No. 2

Round	Charge		$(\epsilon_\theta)_{max}$	$(\epsilon_z)_{max}$	p	Outside Diameter		
						OD	Δ(OD)	$(\epsilon_\theta)_{res}$
	IMR	grains	$\mu\epsilon$	$\mu\epsilon$	kpsi	in.	in.	$\mu\epsilon$
						2.5178		
70	6962	1630	1410	400	77	2.5178	0	0
71	6962	1800	2600	560	-	2.5191	0.0013	520
72	6962	1800	1960	520	106	2.5191	0.0013	520
73	6962 4895	1500 300	2970	470	-	2.5209	0.0031	1230
74	6962 4895	1500 300	2270	560	'23	2.5211	0.0033	1310

and Frankford Arsenal gages, and this was due to disturbances introduced into the strain field by the holes for the pressure gages. For the same propellant charge and projectile, the pressures calculated from Eq. (4) using strain gages on Chamber No. 2 were in good agreement with the values obtained from the Kistler gage on Chamber No. 1. This result established the validity of Eq. (4) for Chambers No. 2-4.

High Pressures and Autofrettage. Table 1 gives the pressure and the outside diameter of Chamber No. 2 for a test sequence of increasing propellant charge. Round 71 produced a large increase in $(\epsilon_\theta)_{max}$ as compared to Round 70, and permanent deformations and residual circumferential strains, $(\epsilon_\theta)_{res}$, were obtained. After Round 72, which was a repeat of Round 71, no change in diameter was observed. A higher charge, Round 73, produced additional residual strains, but when repeated, Round 74 gave practically no change. Thus, this chamber was overstrained and autofrettaged in two stages, and the strain history during these tests is shown schematically in Fig. 4. The dashed lines indicate apparent or fictitious pressures corresponding to the $(\epsilon_\theta)_{max}$'s in Rounds 71 and 73. The differences between the $(\epsilon_\theta)_{max}$'s in Rounds 71 and 72 and also in Rounds 73 and 74 are equal to the changes in residual circumferential strain.

Similar experiments were performed on Chambers No. 3 and 4. The average value of the maximum pressure at which Chambers No. 2-4 operated with dimensional stability was 122,000 psi. Assuming an elastic-plastic material and the maximum-shear theory of yielding, it can be shown [6] that a thick-walled tube becomes fully plastic at a pressure, p_{ult}, given by

$$p_{ult} = \sigma_{yp} \cdot \ln w. \qquad (6)$$

In the chambers tested, $w = 2$, $\sigma_{yp} = 124,000$ psi, so that $p_{ult} = 86,000$ psi. The operating pressures reached in these experiments exceeded
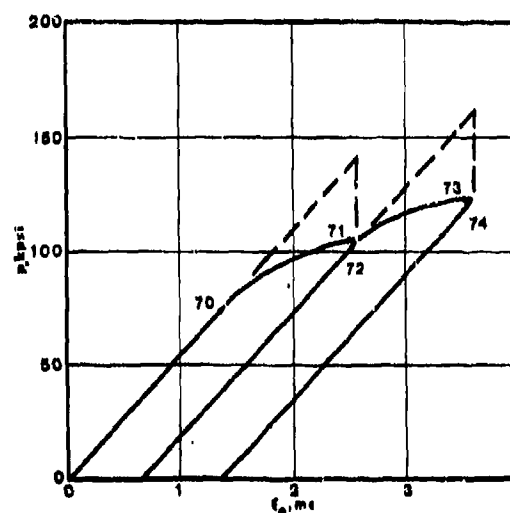
Fig. 4 - Pressure-strain history, Chamber No. 2

this elementary theoretical value, and this was due to strain hardening and other factors.

LIGHT GAS GUN

Experimental Setup. The velocity limitations of conventional propellant guns are well known [7]. Various methods have been used to obtain higher velocities, and light-gas guns are in rather wide-spread use [8]. Figure 5 is a photograph of a piston-compression light-gas gun in the hypervelocity range. The first section of the light-gas gun consisted of a 40 mm breech mechanism, chamber and barrel from a surplus naval anti-aircraft gun. The barrel was modified so that it could be coupled to a pump tube (56 in. long, 4.00 in. OD, 1.63 in. ID). A central breech or high-pressure section

Fig. 5 - Light-gas gun

TABLE 2
Light Gas Gun

Round	Helium Pressure psia	Powder Charge grams	Chamber Pressure kpsi	Piston Velocity ft/sec	Diameters at P2		P_{max} kpsi
					OD in.	ID in.	
					6.948	1.628	
8	300	227	15	1800	6.953	1.653	300
9	200	227	14	1700	6.961	1.685	370
10	100	227	14	1700	6.975	1.723	610
11	300	227	15	1800	6.976	1.727	320
12	500	227	14	1700	6.976	1.727	210
13	300	159	6	1300	6.976	1.727	130
14	300	318	40	2500	6.993	1.776	800

(13 in. long, 7 in. OD) provided the transition from the 1.63 in. ID pump tube to a caliber 0.60, smooth-bore launch tube (75 in. long).

Strain Gage Instrumentation. In order to optimize the performance of the gun in the range of projectile impacts of interest to Frankford Arsenal, strain gage instrumentation was developed to monitor the dynamic behavior of the gun [9]. Chamber pressures were determined from circumferential and longitudinal strain gages, $(\epsilon_\theta)_{p1}$ and $(\epsilon_z)_{p1}$, cemented on the outer surface of the barrel at pressure station P1 midway between the breech and first clamp. An average piston velocity was obtained from circumferential strains, $(\epsilon_\theta)_{v1}$ and $(\epsilon_\theta)_{v2}$, at velocity stations V1 and V2 on the pump tube, 12 in. apart, symmetrically placed with respect to the second clamp. Strains $(\epsilon_\theta)_{p2}$ and $(\epsilon_z)_{p2}$ were measured on the outer surface of the high-pressure section at pressure station P2 which was located 2 in. before the internal transition from 1.63 in. to caliber 0.60.

Table 2 lists the helium pressures and powder charges used in Rounds 8-14, and Fig. 6A shows typical strain vs. time traces. The circumferential strain $(\epsilon_\theta)_{p1}$ increased rather smoothly and was similar to a pressure-time curve. The longitudinal strain $(\epsilon_z)_{p1}$ increased too, but high frequency oscillations due to longitudinal waves in the gun were superimposed on this trace. Both the $(\epsilon_\theta)_{v1}$ and $(\epsilon_\theta)_{v2}$ traces exhibited a sudden increase as the piston moved past the velocity stations on the pump tube. These traces were recorded on a second oscilloscope, Fig. 6B, using a delayed and faster sweep in order to obtain a more accurate measure of the piston velocity. The circumferential strain $(\epsilon_\theta)_{p2}$ on the high-pressure section was also recorded on two oscilloscopes, Figs. 6A,B. Impact of the piston produced rather large longitudinal and circumferential strains in the gun as seen at later times on the traces in Fig. 6A, e.g., $(\epsilon_z)_{p1}$ increased abruptly and went off scale whereas $(\epsilon_\theta)_{p1}$ decreased sharply because of coupling through
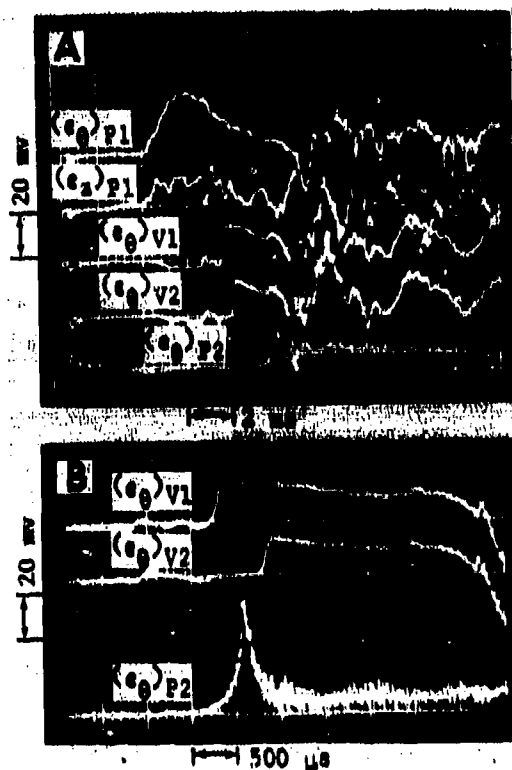
Fig. 6 - Strain-time traces, Round 11

Poisson's ratio.

Chamber Pressure. The strains $(\epsilon_\theta)_{p1}$ and $(\epsilon_z)_{p1}$ were used in Eq. (4) to calculate chamber pressures, Table 2. The chamber pressures were independent of helium pressure and increased rapidly with increasing charge. When a standard 40 mm projectile weighing 890 grams is fired with a standard charge of 318 grams of SPDN 8709 powder, the chamber pressure is 43,900 psi. For comparison, a chamber pressure of 40 kpsi was obtained in the light-gas gun when using the same charge and a piston of 820 grams.

Piston Velocity. Piston velocities, Table 2, were calculated by dividing the 12 in. base line by the time interval between the rises in the $(\epsilon_\theta)_{v1}$ and $(\epsilon_\theta)_{v2}$ traces. It is interesting to note that the values obtained were independent of helium pressure and varied linearly with charge.

High Pressure Section. The central breech was measured before and after each test, and the outside and inside diameters at strain gage station P2 are listed in Table 2. The pressures developed in the central breech during Rounds 8-11, 14 produced permanent

deformations so that Eq. (4) was not applicable. In order to estimate the maximum pressure, p_{max}, developed during compression of the helium and impact of the piston, $(\epsilon_\theta)_{max}$ was replaced by the elastic circumferential strain recovered during unloading, $(\epsilon_\theta)_{el}$. Also, ϵ_z was neglected since it was small compared to ϵ_θ. With these approximations, Eq. (4) becomes

$$ p_{max} = \frac{w^2 - 1}{2} \cdot \frac{E}{1 - \mu^2} \cdot (\epsilon_\theta)_{el}, \qquad (7) $$

and maximum pressures, Table 2 and Fig. 7, were calculated using values of w based on the dimensions after each test. Although the data in Fig. 7 are very limited, this type of graph is useful for selecting operating conditions of the light-gas gun.

SYNCHRONIZATION SYSTEMS USING STRAIN GAGES

Several methods of detecting projectiles in gun barrels are available. One method involves drilling the barrel and inserting a probe or a pressure transducer. Such modifications to the barrel may disturb the phenomena under investigation. The strain-time traces from the gages on the pump tube of the light-gas gun showed that they can be used to study the motion of the piston in the tube. This suggested that strain gages could be used to obtain a signal for synchronizing other instrumentation.

Gages Cemented on Barrels. Strain gages have been used on M14 and M16 rifles to synchronize and obtain flash X-ray pictures of the bullet in the barrel. In this work, the trigger level of the oscilloscope was adjusted so that it would sweep on the strain signal. The A gate was fed from the oscilloscope to a thyratron whose output was used to start a delayed trigger amplifier of the flash X-ray unit.
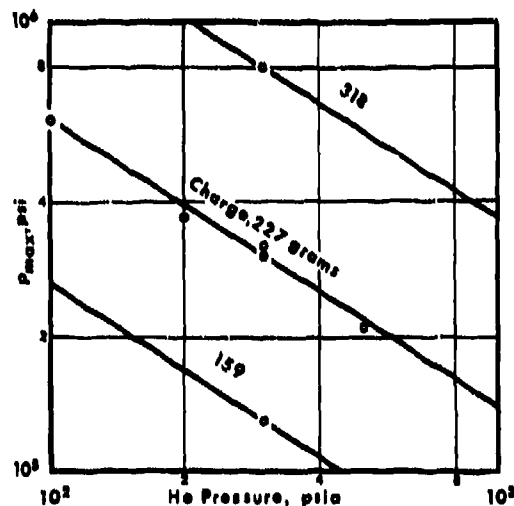

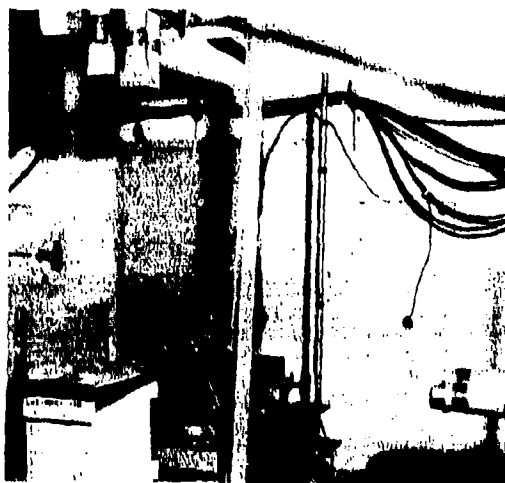Fig. 7 - p_{max} vs. helium pressure for various powder charges

99

Fig. 8 - Experimental setup for flash X-rays, strain gages cemented on test barrel

Fig. 9 - Strain gaged hose clamp

Flash X-rays can also be used to obtain pictures of projectiles near the muzzle where photo-optical methods using visible light are not applicable because of the muzzle flash. In Fig. 8, circumferential strain gages, 3.5 in. from the muzzle, were cemented on a 5.77mm test barrel (OD = 1.163 in., w = 5.12) to detect the projectile and synchronize flash X-rays. Orthogonal views were obtained using special beryllium tubes for soft and hard X-rays to study flechettes.

Strain Gaged Hose Clamp. An adjustable strain gaged hose clamp, Fig. 9, can be used as a simple transducer on a gun barrel to detect the projectile in the barrel during firing. The

hose clamp can be removed and put on other barrels, and it does not affect the performance of the weapon. Feasibility tests on the 5.77 mm barrel in Fig. 8 showed that the strain gaged hose clamp can be used to synchronize flash X-rays in the muzzle ballistic region with a reproducibility of the order of one microsecond. The simplicity of the strain gaged hose clamp and accompanying instrumentation make it very attractive for ballistic investigations and applications.

DIRECT MEASUREMENT OF $(\epsilon_\theta + \mu\epsilon_z)$

In response to a request from the Small Caliber Ammunition Modernization Program (SCAMP), consideration was given to the use of strain gages for the determination of chamber pressures in ammunition testing. Heretofore, we had measured ϵ_θ and ϵ_z independently in our laboratory experiments, but for ammunition testing, it seemed that a direct measurement of $(\epsilon_\theta + \mu\epsilon_z)$ would greatly simplify the data reduction for chamber pressures. From Eq. (3), the measurement of $(\epsilon_\theta + \mu\epsilon_z)$ is equivalent to measuring the circumferential stress in the tube at the outer surface.

The techniques of using stress gages or special stress-strain gages are well known [10], but commercially available gages of these types are relatively large and have low resistance. We, therefore, looked into the possibility of using a combination of circumferential and longitudinal strain gages to obtain $(\epsilon_\theta + \mu\epsilon_z)$. It was found that three, 1000 $\wedge$, circumferential gages (ED-DY-125AC-10C) and two, 350 $\wedge$, longitudinal gages (ED-DY-125AD-350) wired in series and connected into a potentiometer circuit will give

$$(\epsilon_\theta + 0.28\epsilon_z) = 1.20 \cdot \frac{1 + R_a/R_b}{F} \cdot \frac{\Delta V_g}{V_g}, \quad (8)$$
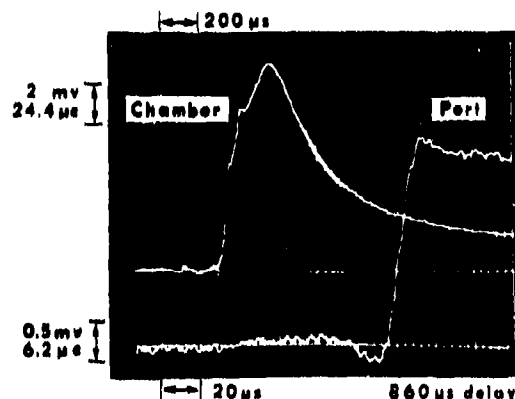

Fig. 10 - $(\epsilon_\theta + \mu\epsilon_z)$ vs. time, 5.56 mm test barrel

100

TABLE 3
40MM High Velocity Launcher, 12 ft. Smooth Bore

| Round | Propellant | | | Projectile | Pressure | Velocity, ft/sec | |
	Type	Grams	Case	grams	psi	Predicted	Measured
142	SPDN 8709 IMR 6962	100 330	Partially filled	215	47,100	6350	6360
133	SPDN 8709 IMR 4996 IMR 6962	100 200 170	Full	209	55,500	6710	6700
136	SPDN 8709 IMR 6962	100 370	Full	209	69,900	6900	6970
69	SPDN 8709 IMR 4996	250 300	Extended 3.5 in.	191	63,100	6830	6880
72	SPDN 8709 IMR 4996	200 350	Extended 3 in.	197	81,500	7020	7140

where the notation is the same as in Eq. (5). These gages are manufactured by Micro-Measurements, Romulus, Michigan, and each gage has an active area of 1/8 x 1/8 in. and a transverse sensitivity coefficient of 5.1%.

Strain gages were used on a modified 5.56 mm accuracy test barrel to determine chamber pressures at the case mouth position and port pressures. At each axial location, circumferential gages were mounted at 0°, 120°, 240° and longitudinal gages were mounted at 90° and 270°. Typical strain-time traces are shown in Fig. 10. At the chamber, it should be noted that the ballistic rise time was long compared to the time required for stress waves to travel radially through the wall of the test barrel, i.e., the dynamic response of the circumferential stress to the internal pressure was quasi-static. On the delayed and faster sweep for the port, the high frequency oscillations correspond to the period of radial waves, and the deviations from the base line are apparently due to longitudinal effects which were not completely eliminated by the strain gage circuit. Nevertheless, this combination of gages seems to be extremely effective for detecting the passage of the projectile in the bore under the gages, and we plan to use this method for difficult synchronization problems. Further work is in progress for SCAMP on the use of strain gages for ammunition testing.

40MM HIGH VELOCITY LAUNCHERS

In response to a request from Picatinny Arsenal for terminal ballistics data on cubes weighing 2000 and 3000 grains, surplus 40mm naval anti-aircraft guns were selected for use as high velocity launchers under laboratory conditions. Work began with a standard gun having a rifled barrel 6.5 ft. long. Strain gages were used to monitor the dynamic response of the gun and to determine chamber pressures. Observations of the longitudinal stress waves assisted in the design of a rigid gun mount. A series of firings were made to establish experimentally chamber pressures and projectile velocities for various propellants and charge weights. By using a slow propellant adjacent to the primer, next a medium speed propellant, and then a fast propellant, we obtained a charge which filled the case and did not exceed the maximum allowable chamber pressure during firing. Thus, we were able to modify the pressure-time curves so as to maximize the propellant charge and the projectile velocity. Next, the components of the light-gas gun (Fig. 5) were rearranged in order to obtain a 40 mm powder gun with a smooth-bore barrel, 1.630 in. ID, 12 ft. long. The combination of strain gages described in the previous section is now being used to measure $(c_\theta + \mu c_z)$ for chamber pressures.

Standard operating conditions of a 40 mm gun with a rifled barrel are: propellant charge, SPDN 8709, 318 grams; projectile, 890 grams; expansion ratio, 6.4; chamber pressure, 43,900 psi; muzzle velocity, 2890 ft/sec. Using the Frankford Arsenal interior ballistics curves [11] for the standard 40 mm gun, the predicted velocity is 2720 ft/sec. This suggested that a factor of 2890/2720 = 1.06 should be applied to the velocity graph when used for 40 mm guns. Using this correction factor, Table 3 gives a comparison of predicted and measured velocities for typical firings of the 40 mm smooth-bore gun which has an expansion ratio of 10.6. The chamber pressures as determined from strain gages were used to obtain pressure factors in the velocity calculations. Two independent systems were used to measure the projectile velocities. One system used flash X-rays, and the other employed a photo-optical system with two slit images which were recorded by a streak camera. In general, the predicted and measured velocities differed by less than 2%.

CONCLUDING REMARKS

Although the method of using external strain

101

gages to determine internal pressures is well known, the application of this method while the chamber was being overstrained and autofrettaged as in the caliber 0.60 high velocity launcher appears to be new. Transient strain-time records coupled with micrometer measurements before and after firing enabled us to establish dimensionally stable and safe operating conditions at pressures above those at which initial yielding occurred.

In the light-gas gun, chamber pressures and piston velocities were obtained readily from strain-time records, whereas the calculations for maximum pressures in the central breech involved several simplifying assumptions. The velocity measuring system showed that external strain gages can be used to detect projectiles in gun barrels. This led to the use of strain gages cemented on barrels and to the development of the strain gaged hose clamp.

The direct measurement of $(\epsilon_\theta + \mu\epsilon_z)$, which was prompted by the need for improved strain gage techniques for ammunition testing, simplifies the determination of chamber pressures. This method is now being used on the 40 mm high velocity launcher, and the predicted and measured projectile velocities are in good agreement. This technique also provides a signal which appears to be especially suitable for triggering and synchronizing other instrumentation such as flash X-rays.

ACKNOWLEDGMENTS

REFERENCES

1. M. Halio and V. H. McNeilly, "Determination of Pressure from Strain Measurements on the Outer Surface of a Gun," Ballistic Research Laboratories Memo. Rept. 421, Nov. 1948.

2. P. D. Flynn, "Some Strain Gage Applications to Ballistic Problems," Experimental Mechanics, Vol. 10, No. 7, pp. 297-304, July 1970.

3. S. Timoshenko and J. N. Goodier, Theory of Elasticity, 2nd ed., p. 60. McGraw-Hill, New York, 1951.

4. R. C. Dove and P. H. Adams, Experimental Stress Analysis and Motion Measurement, p. 92. C. E. Merrill Books, Columbus, 1964.

5. S. Fernbach, "The Piezo Gauge," Frankford Arsenal Rept. R-111, Jan. 1942.

6. S. Timoshenko, Strength of Materials, Part II, 3rd ed., p. 386. Van Nostrand, Princeton, 1956.

7. A. E. Seigel, "The Theory of High Speed Guns," North Atlantic Treaty Organization, Advisory Group for Aerospace Research and Development, AGARDograph 91, May 1965.

8. H. F. Swift, "Hypervelocity Ballistic Accelerators," Proc. 5th Symposium on Hypervelocity Impact (Denver 1961) Vol. 1, Part 1, pp. 1-22, April 1962.

9. P. D. Flynn, "Strain Gage Instrumentation for a Light Gas Gun," Proc. 3rd International Congress on Instrumentation in Aerospace Simulation Facilities, pp. 184-189. IEEE, New York, 1969.

10. F. F. Hines, "The Stress-Strain Gage," Proc. 1st International Congress on Experimental Mechanics, edited by B. E. Rossi, pp. 237-253. Pergamon Press, Oxford, 1963.

11. "Interior Ballistics of Guns", Army Material Command Pamphlet AMCP 706-150, pp. 2-41 to 2-45, Feb. 1965.

STRESS WAVE MEASUREMENT TECHNIQUE

A. J. Kalinowski
IIT Research Institute
Chicago, Illinois

A technique is presented for measuring the shock wave induced dynamic state of stress in a solid medium. The technique consists of implanting a fluid-filled spherical bladder (stress) gage) in the stressed medium and monitoring the center fluid pressure with a fluid pressure transducer positioned at the sphere center. A means is presented for inverting the fluid pressure reading into the transient free field state of stress via system transfer function.

The results of a series of experiments is presented that demonstrates the validity of the technique. The experiments consist of loading a solid block of material (including the embedded fluid bag stress gage) with   shock tube generated step wave. The transient stresses in   a block determined by the fluid bag stress gage concept are compared to an independently determined measure of the block stress. The results of the experiment demonstrate the reference state of stress and the measured stress to be in good agreement.

INTRODUCTION

The instrumentation of high-explosive field tests requires accurate measurements of the free field transmitting media motions (displacement, particle acceleration histories) and of the free field state of stress. Our primary concern is to develop a means for determining the state of stress existing in the free field. The accuracy of the stress measurement depends upon the response characteristics of the transducer, calibration procedure, and the embedding technique used to place the gage in the transmitting medium.

Fluid Bag Stress Gage

The research effort described in this paper focuses on a new stress measuring device referred to as a fluid bag stress gage. This stress gage concept consists of a fluid-filled, thin-walled, flexible sphere (bladder) and two fluid pressure transducers mounted on a small stemlike probe (Figure 1). The stem is located within the central region of the stress gage and is cantilever supported at the surface of the sphere by a boss. The initially pressurized spherical bladder is flexible enough to conform to small out-of-roundness irregularities that may exist during embedding yet is stiff enough to maintain its spherical shape (say under its own weight) during embedding handling procedures. Dynamic fluid pressure data are electronically passed to some remote aboveground recording station through a stress gage-to-recorder cable network.
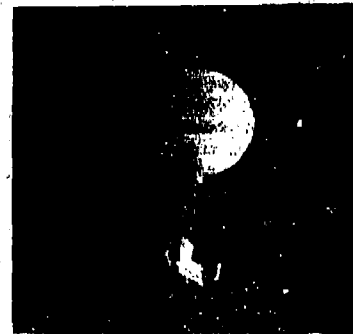
(a) The Assembled Stress Gage
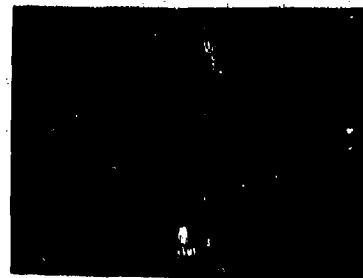
(b) Exploded View Gage Housing Assembly

Figure 1   Fluid Bug Pressure Gage

The fluid bag stress gage is intended to convey various levels of information about the state of stress existing in the free field. Each level of information depends on the amount of a priori knowledge of the free field. For example, the gage conveys the most information about the free field stress state when it is known that the primary input is made up of a plane dilatational stress wave. In such a case the full three-dimensional state of stress is determinable. In the case where the input consists of multi-input P- and S-waves resulting from reflections off of complex geological layers existing in the free field, the stress gage will give the average of the three normal stress components (i.e., the media pressure) existing in the dilatational portion of the multi-wave input.

The fluid bag stress gage first measures the dynamic fluid pressure within the bladder at a center and off-center position. Depending on the stiffness and mass properties of the fluid relative to the transmitting media, a portion of the incident wave(s) will be reflected away from the fluid inclusion and a certain portion will refract into the fluid. It is the refracted portion which results in the internal fluid pressure waveforms. Care must be taken in selecting the physical properties of the fluid (i.e., density and wave speed (or equivalently bulk modulus)) so that a large enough fraction of the incident wave refracts into the fluid to ensure the pressure transducer is registering refracted pressure and not noise in the instrumentation. The final step is to invert the center and off-center pressure readings into the free field state of stress through the system transfer function. By system transfer function we refer to the harmonic response versus frequency relationship between an incident input wave and the fluid pressure reading at some point in the fluid.

Other Stress Gages

For completeness, other stress gages that have been used to measure the dynamic state of stress in solid media are discussed. Experimenters have been interested in free field soil stress measurements for over 50 years. The Goldbeck cell, one of the first to be widely used, was reported in the literature in 1916. The earliest gages were bulky and suitable only for the measurement of static pressures in large earth masses. Over the years, the development of new instrumentation techniques has permitted the achievement of more compact gages with improved frequency response.

More recently, because of the need to measure shock response, piezoelectric materials have been used as a sensing element. They were first used for fluid pressure

transducers and were limited to short duration pulses because of the capacitive nature of the circuitry. With improved instrumentation, piezoelectric gages have been used for slowly varying stress measurements in soil (Ref. 1). Piezoresistive semiconductor material, which has some advantages over piezoelectric and other sensors, has been used in stress gage applications (Ref. 2, 3 and 4). Improved sensitivity, simple instrumentation requirements (i.e., resistance bridge) and suitability for both static and dynamic measurements are its key advantages.

This paper is not the first to employ a loaded flexible fluid container as a stress measuring device. For example, Ref. 10 reports a fluid-filled disk shaped gage. It has the drawback of having unidirectional response characteristics and poor imbedding properties relating to gage-medium contact. References 11 through 14 give similar fluid-filled gage concepts that have been tried.

Other than the fluid bag gage, the most recent stress gage to appear is the cue ball stress gage (Ref. 5). It appears to have been in the development stage at about the same time as the fluid bag concept (Refs. 6 and 7). The cue ball gage consists of a stiff solid spherical inclusion in which strain gages are embedded in three quadrants internal to the sphere. The gage has been shown to work well for static problems but according to Ref. 5 it has not worked adequately in dynamic environments. The calibration procedure for converting the strain measurements within the free field makes no use of the dynamic system transfer function (or in their terminology, dynamic influence coefficient relating free field stress to strain (or stress) in the solid sphere). These influence coefficients are frequency dependent and the use of the zero frequency influence coefficients (static values) for dynamic calibration is questionable in high-frequency rich free field environments. A further problem area encountered with the cue ball gage is that embedding the sphere in the free field and maintaining good contact over the duration of the dynamic test is a potential problem. Whereas with the fluid bag gage, the flexibility of the bladder allows some latitude in conforming too small out of roundness irregularities that may arise during the embedding procedure.

THEORETICAL BASIS OF GAGE FLUID PRESSURE-TO-MEDIUM STRESS INVERSION

Mathematical Description of Inversion

Here we address the problem of employing the center pressure measurement inside the fluid bag to estimate information about the state of stress (time history) existing in the free field.

Before proceeding to the mathematical details of the method, the assumptions on which the inversion process is dependent are listed:

- The free field medium is homogeneous in the neighborhood of the fluid bag gage (say 10-gage radii).

- The free field medium can be characterized by a linear elastic solid whose elastic constants are known.

- The gage fluid can be characterized by an inviscid acoustic fluid.

- Good normal contact is maintained between the gage bladder and solid free field media (or grout).

- The dilatational stress content of the incoming free field is planar (or spherical).

- The total center fluid pressure can be accurately measured.

- The orientation (angle ψ_d) of the input wave is known relative to a set of fixed ground coordinates (e.g., see Figure 2 for ψ_d orientation). If this is not known then the free field dilatational stress state is established only to within an unknown rotation of the stress state relative to the ground coordinates.

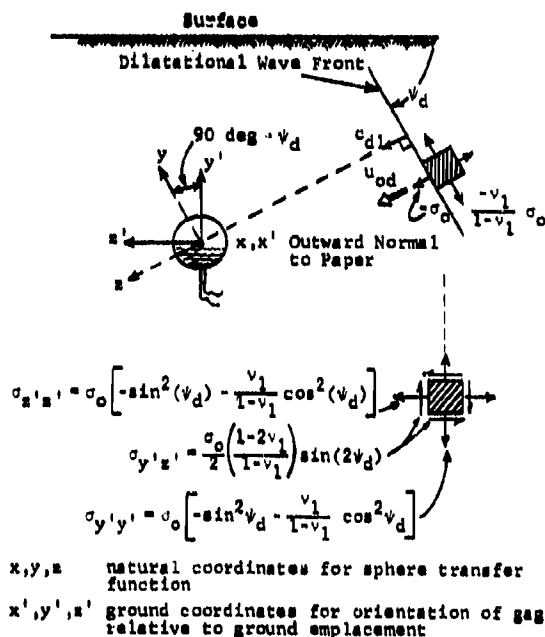The consequence of violating any of these assumptions is discussed later.

$$\sigma_{z'z'} = \sigma_o\left[-\sin^2(\psi_d) - \frac{\nu_1}{1-\nu_1}\cos^2(\psi_d)\right]$$

$$\sigma_{y'z'} = \frac{\sigma_o}{2}\left(\frac{1-2\nu_1}{1-\nu_1}\right)\sin(2\psi_d)$$

$$\sigma_{y'y'} = \sigma_o\left[-\sin^2\psi_d - \frac{\nu_1}{1-\nu_1}\cos^2\psi_d\right]$$

x,y,z natural coordinates for sphere transfer function

x',y',z' ground coordinates for orientation of gage relative to ground emplacement

Figure 2   Relationship between Local Sphere Coordinate and Ground Coordinate

In the development to follow, we will refer to the following variables

a = Cavity radius

$p^o(\tau)$ = Total fluid pressure response at origin

$p^a_d(\tau)$ = Fluid pressure dilatational response contribution at the point (c)

$p^a_T(\tau)$ = Total fluid pressure response at the point (a)

$p^i_d(\tau)$ = Dilatational input pressure (existing in free field)(i.e., sum of normal stresses $\div$ 3)

c_{d1} = Dilatational wave speed in solid medium (1)

c_{d2} = Dilatational wave speed in solid medium (2)

c_{s1} = Shear wave speed in solid medium (1)

τ = Nondimensional time (transit radii, $\tau = t\, c_{d1}/a$)

α = Nondimensional time (transit radii, $\alpha = \omega a/c_{d1}$)

f = Nondimensional circular frequency ($f = \alpha/2\pi$)

$A(\alpha,\bar{r},\theta)$ = System admittance (or transfer function) representing the harmonic pressure response at any point in the fluid $(\bar{r},\theta)$ to a unit harmonic dilatational input wave

$\bar{r} = r/a$ = Nondimensional radial spherical coordinate

θ = Angular spherical coordinate

In Ref. 7 it is shown that the response at the center of a fluid-filled spherical inclusion due to a harmonic plane shear wave input is identically zero for all values of the nondimensional driving frequency, α. Since the general transient response can be constructed by the proper summation (Fourier Integral) of all harmonic responses, it follows that the transient origin pressure response is likewise zero. Consequently, the dynamic pressure response at the origin is due only to the dilatational component of the free field input. The center pressure reading is very special in that it unscrambles the shear and dilatational response. Of course if there is no shear wave content in the input to begin with, there is nothing to unscramble and all points in the fluid respond only to the dilatational input. In Ref. 6, the relation between output (fluid bag pressure response) and input (free field pressure) is given by

Output-input for P-wave (center point, 0)

$$p^0(\tau) = \int_{-\infty}^{\infty} p_d^i(\tau-\tau')\, Y_{do}(\tau')\, d\tau'$$

with (1)

$$Y_{do}(\tau') = \int_{-\infty}^{\infty} A(-2\pi f, 0, \theta)\, e^{2\pi i f \tau'}\, df$$

Output-input for P-wave (off-center point, g)

$$p_d^g(\tau) = \int_{-\infty}^{\infty} p_d^i(\tau-\tau')\, Y_{dg}(\tau')\, d\tau'$$

with (2)

$$Y_{dg}(\tau') = \int_{-\infty}^{\infty} A(-2\pi f, \bar{r}, \theta)\, e^{2\pi i f \tau'}\, df$$

where $Y_{do}(\tau')$, $Y_{dg}(\tau')$ may be viewed as the transient pressure response to a unit impulse input pressure for the center and off-center points respectively. The center and off-center transfer functions $A(\alpha,0,\theta)$ and $A(\alpha,\bar{r},\theta)$ are defined by the following equations (Ref. 6) and represent the response to a unit harmonic input, $p = 1 \cdot e^{-i\omega t}$.

$$A(\alpha, 0, \theta) = \frac{i\alpha e^{-i\alpha}}{\bar{c}\,\bar{\rho}\left[1 - 4/(3\bar{k}^2)\right] H(\alpha)} \quad (3)$$

where

$$H(\alpha) = \frac{\alpha(\alpha+1)\, j_0(\alpha\bar{c})}{\bar{\rho}\,\bar{c}} - \left[i\alpha^2 - \frac{4(\alpha+1)}{\bar{k}^2}\right] j_1(\alpha\bar{c})$$

and

$$A(\alpha,\bar{r},\theta) = \frac{1}{\bar{\rho}\left[1 - 4/(3\bar{k}^2)\right]} \sum_{n=0}^{\infty} C_n j_n(\alpha\bar{c}\,\bar{r})\, P_n(\cos\theta) \quad (4)$$

where the mode constant C_n is determined from

$$C_n = \left[E_{11}E_{32}E_4 + E_{31}E_{42}E_1 + E_{41}E_{12}E_3 \right.$$
$$\left. - E_1 E_{32}E_{41} - E_{42}E_3 E_{11} - E_4 E_{12}E_{31}\right] \Big/$$
$$\left[E_{42}E_{31}E_{13} + E_{41}E_{12}E_{33} - E_{13}E_{32}E_{41} \right.$$
$$\left. - E_{42}E_{33}E_{11}\right]$$

with

$$E_1 = -i^n(2n+1)\left[n j_n(\alpha) - \alpha j_{n+1}(\alpha)\right]$$
$$E_2 = -i^n(2n+1)\, j_n(\alpha)$$
$$E_3 = -i^n(2n+1)\left[(n^2-n-\alpha^2\bar{k}^2/2)\, j_n(\alpha) + 2\alpha j_{n+1}(\alpha)\right]$$
$$E_4 = -i^n(2n+1)\left[(n-1)\, j_n(\alpha) - \alpha j_{n+1}(\alpha)\right]$$

$$E_{11} = n h_n(\alpha) - \alpha h_{n+1}(\alpha)$$
$$E_{21} = h_n(\alpha)$$
$$E_{31} = (n^2-n-\alpha^2\bar{k}^2/2)\, h_n(\alpha) + 2\alpha h_{n+1}(\alpha)$$
$$E_{41} = (n-1)\, h_n(\alpha) - \alpha h_{n+1}(\alpha)$$
$$E_{12} = -n(n+1)\, h_n(\alpha\bar{k})$$
$$E_{22} = -(n+1)\, h_n(\alpha\bar{k}) + \alpha\bar{k}\, h_{n+1}(\alpha\bar{k})$$
$$E_{32} = -n(n+1)\left[(n-1)\, h_n(\alpha\bar{k}) - \alpha\bar{k}\, h_{n+1}(\alpha\bar{k})\right]$$
$$E_{42} = -(n^2-1-\alpha^2\bar{k}^2/2)\, h_n(\alpha\bar{k}) - \alpha\bar{k}\, h_{n+1}(\alpha\bar{k})$$
$$E_{13} = n j_n(\alpha\bar{c}) - \alpha\bar{c}\, j_{n+1}(\alpha\bar{c})$$
$$E_{23} = j_n(\alpha\bar{c})$$
$$E_{33} = -\alpha^2\bar{k}^2\, j_n(\alpha\bar{c})/2\bar{\rho}$$

The variables $j_n(\ )$ denote spherical Bessel functions of the first kind; $h_n(\ ) \equiv j_n(\ ) + i n_n(\ )$ denote spherical Hankel functions of the first kind; $n_n(\ )$ is the spherical Neumann function; and $P_n(\cos\theta)$ denotes zeroth order Legendre polynomials of the first kind.

The transfer functions given by Eqs.(1) and (2) are for an incident dilatational wave impinging upon the fluid-filled sphere along the negative z axis defined by the local coordinate system (x,y,z) shown in Figure 3. The spherical coordinates r,θ,φ (defined relative to the set x,y,z) are the natural coordinates for the solution which display the solution in its most convenient mathematical form.
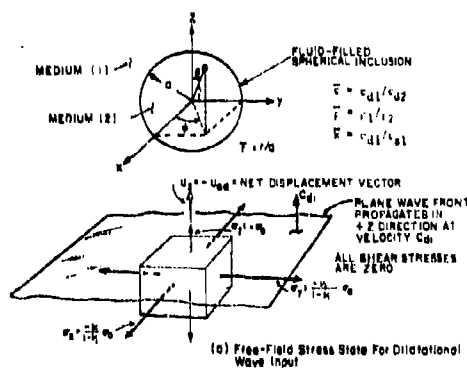

Figure 3 Orientation of Input Plane Waves

Given the center fluid pressure measurement $p^0(\tau)$, we can solve Eq.(1) for the free field dilatational pressure, $p_d^i(\tau)$. In some applications this is all we may wish to know about the input. If additional information about the state of stress is required, this can be

106

determined from the elasticity equations at the dilatational wave front (Ref. 6), namely

$$\sigma_z^1(\tau)_d = -\sigma_o(\tau);$$

$$\sigma_y^1(\tau) = \sigma_x^1(\tau) = \left[\frac{-\nu_1}{1-\nu_1}\right]\sigma_o(\tau) \qquad (5)$$

where

$$\sigma_o(\tau) = 3p_d^1(\tau)\left[\frac{1-\nu_1}{1+\nu_1}\right]$$

The stresses $(\sigma_z^1)_d$, $(\sigma_y^1)_d$ are shown* in Figure 2 in the local spherical coordinate notation for a P-wave input wherein that principal stress components are aligned along the plane wave front as shown. Upon rotating the element clockwise $(90-\psi_d)$ deg, the element is aligned with the ground coordinates. The corresponding rotated stress components are presented in Figure 2.

Later we have the need for processing some experimental data at an off-center position in the fluid-filled cavity. This is the only reason we have included Eqs. (2) and (4) and we emphasize that these equations are not needed in the normal scheme for inverting the fluid pressure-to-free field stresses.

It is noted that Eqs.(5) can be evaluated without knowledge of the dilatational wave angle ψ_d in the case of a plane wave or without knowledge of the source in the case of a spherical input dilatational wave. If the orientation of the element relative to a set of ground coordinates is desired, knowledge of the wave orientation ψ_d must be known. Experimental methods for determining ψ_d are presented in Refs. 6 and 7. Briefly, the most practical of these methods is one which consists of placing a set of motion sensing gages in the free field about 20 fluid bag gage radii away from the stress gage. By measuring arrival times of the impinging free field, the orientation of the input wave can be determined.

Numerical Evaluation of Inversion Formulas

The evaluation of the dilatational portion of the free field input requires the numerical computation of the Convolution integral equations such as Eqs.(1) and (2). In general, the analytical evaluation of these integrals is very complicated, and only in the case of evaluating Eq.(1) are we able to obtain an analytical expression for the solution. For this special case, the solution to Eq.(1) is given by the relation

---

$$p_d^1(\tau) = \frac{\bar{\rho}}{2}\left[1-4/(3\bar{k}^2)\right]\left\{(1+\frac{1}{\rho\bar{c}})p^o(\tau-1+\bar{c})\right.$$

$$+(1-\frac{1}{\rho\bar{c}})p^o(\tau-1-\bar{c})-(1-\frac{1}{\rho})\frac{1}{\bar{c}}\cdot$$

$$\left.\cdot\int_{-\bar{c}}^{\bar{c}}p^o(\tau-1-\tau')d\tau'\right\} - \frac{\bar{\rho}\left[1-4/(3\bar{k}^2)\right]}{\bar{c}\,\bar{k}^2}\cdot$$

$$\cdot\int_{-\bar{c}}^{\bar{c}}(\tau'^2+2\tau'-\bar{c}^2)\,p^o(\tau-1-\tau')d\tau' \qquad (6)$$

which is discussed in Ref. 6. Even expression (6) involves the evaluation of an integral, however the unknown no longer appears inside an integral equation with infinite limits and thus can be handled with ease.

It can be shown that if no additional dilatational shock waves are encountered (beyond the initial one), then

$$p_d^1(\tau) \longrightarrow p^o(\tau+\bar{c}-1)/A_o \qquad \text{as} \qquad \tau \longrightarrow \gg 1$$

which implies that the input and output waveforms are exactly the same (for long time) except for a $1/A_o$ multiplier where A_o is determined from the low frequency limit of Eq.(3), namely

$$A_o \equiv A(0,0,0) = \frac{1}{\left[1-4/(3\bar{k}^2)\right]\left[1+4\bar{c}^2\bar{\rho}/3\bar{k}^2\right]}$$

Consequently for long time (which may be several transit radii) the calibration procedure is very simple, wherein we need only to compute A_o and shift the time axis by $\bar{c}-1$.

Although one may use the straightforward relation, Eq.(6) to solve for the dilatational pressure input, $p_d^1(\tau)$, we selected to use the finite Fourier transform technique for evaluating $p_d^1(\tau)$. The reason for this is fourfold:

• In the event that at some future date one wishes to include the impedance mismatch of the grout or of the pressure transducer into the overall transfer function between the fluid pressure and free field media, the finite Fourier transform technique could handle this situation with relative ease (whereas Eq.(6) could most likely not be altered).

• The numerical computation scheme employing the fast Fourier transform (FFT) algorithm to implement the finite Fourier transform is computationally more efficient than evaluating Eq.(6) by some integration scheme.

---

*Where $(\sigma_x^1)_d$ is normal to the plane of the paper.

- A clear picture of the required data sampling rates in conjunction with the frequency response sensitivity of the gage system is maintained.

- A consistent numerical scheme can be used for both the evaluation of the center and off-center response Eqs. (1) and (2).

In the remainder of this subsection we concentrate on the numerical computation of the Fourier integral and/or Fourier transform integrals found in Eqs. (1) and (2). In particular, we employ the finite Fourier transform technique on its associated efficient algorithm (usually referred to as the FFT). The FFT is only a term used to describe an algorithm for efficiently computing the finite Fourier transform. This relatively new technique first appeared in literature in 1965 (Ref. 8) and was initially used to rapidly evaluate complex Fourier series. Later it was recognized that the technique could also be efficiently used to evaluate Fourier integrals and convolution integrals (Ref. 9). We draw upon the contents of Ref. 9 for the FFT methodology used to solve Eqs. (1) and (2). The details of its application are lengthy and particular attention must be paid to the range of validity of the technique. We present only a very brief sketch of the method and refer the reader to Ref. 6 for the finer details and a computer program which automatically processes the experimental fluid pressure data into free field stress calculation.

The Fourier transform pair of a general aperiodic function is given by

transform

$$\mathcal{F}[x] \equiv a(f) = \int_{-\infty}^{\infty} x(t) e^{-2\pi i f t} dt$$

inverse

$$x(t) = \int_{-\infty}^{\infty} a(f) e^{2\pi i f t} df \qquad (7)$$

The functions $x(t)$ and $a(f)$ appearing in Eqs. (7) are defined on the range $-\infty < t < \infty$ for $x(t)$ and $-\infty < f < \infty$ for $a(f)$. For our physical applications t can be viewed as the time domain and f as the frequency domain. For convenience we denote the infinite Fourier transform pair of Eqs. (7) by the notation

$$x(t) \longleftrightarrow a(f)$$

The infinite transform pair given by Eqs. (7) apply over an infinite domain time and frequency domain. For functions, say $x_p(t)$, that are periodic over a finite time domain, T, there exists a relationship similar to the infinite pair and

is given by

transform
$$a_p(n\Delta f) = \frac{1}{F} \sum_{j=1}^{N-1} x_p(j\Delta t) e^{-2\pi i j n/N} \equiv \bar{A}(n\Delta f)$$

inverse
$$T x_p(j\Delta t) = \sum_{n=0}^{N-1} a_p(n\Delta f) e^{+2\pi i j n/N} \equiv \bar{X}(j\Delta t)$$

where N is the total number of frequencies that synthesize $x_p(t)$, Δt is the time sampling, Δf is the frequency sampling, (j,n) are dummy indices, T is the period of the $x_p(t)$ function, F is the frequency range, and $i = \sqrt{-1}$. Analogous to the infinite transform pair, we use the notation

$$T x_p(j\Delta t) \longleftrightarrow a_p(n\Delta f)$$

or the equivalent

$$\bar{X}(j\Delta t) \longleftrightarrow \bar{A}(n\Delta f)$$

The $\bar{A}, \bar{X}$ terms can also be written in the canonical form usually found in most literature on finite Fourier transforms. Finite Fourier transform pair:

$$\bar{A}_n(n\Delta f) = \frac{1}{N} \sum_{j=0}^{N-1} \bar{X}_j(j\Delta t) e^{-2\pi i j n/N}$$
$$\qquad (8)$$

$$\bar{X}(j\Delta t) = \sum_{n=0}^{N-1} \bar{A}_n(n\Delta f) e^{2\pi i j n/N}$$

The purpose for the barred upper case notation in Eqs. (8) is to preserve the symmetry of the transform (i.e., avoid carrying along the troublesome T). The subscript p on the expression $a_p(n\Delta f)$ and $x_p(j\Delta t)$ is to emphasize the fact that these functions are periodic over the range F and T respectively. The sampling, interval, Δt, of the time function and the sampling interval of the frequency function, Δf, are interrelated through N, T, and F by the relations

$$\Delta f = \frac{1}{N\Delta t} = \frac{1}{T} = \frac{F}{N}$$

For physical systems, the impulse solution, $Y_{do}(\tau')$ or $Y_{da}(\tau')$ decay to essentially zero after a finite amount of time has passed. Taking advantage of this fact, we are able to apply the finite Fourier transforms pair to problems involving infinite domain, provided we truncate the infinite limit integrals at the proper point.

It can be formally shown that upon taking the infinite Fourier transform of Eq. (1), there results

108

$$c(f) = a(f) \cdot b(f)$$

where

$$p^o(\tau) \longleftrightarrow c(f)$$
$$Y_{d_s}(\tau) \longleftrightarrow b(f)$$
$$p_d^i(\tau) \longleftrightarrow a(f)$$

The counterpart of the above for the finite Fourier transform is

$$\bar{C}(n\Delta f) = T\, \bar{A}(n\Delta f)\, \bar{B}(n\Delta f) \qquad (9)$$

where $\bar{C}(n\Delta f)$ is the finite transform of the free field input pressure, $p_d^i(\tau)$, and $\bar{B}(n\Delta f)$ is the finite transform of the impulse solution, $Y_{d_s}(\tau)$. Since the Fourier transform of the impulse solution is the transfer function of the system, we may directly use Eq.(4)* for $\bar{B}(n\Delta f)$.

---

*The negative frequency portion of Eq.(4) must be extended into the second half of the frequency domain and divided by T. The reasons for doing this are explained in Ref. 6.

For forward problem types where we are given $p_d^i(\tau)$ and we wish to determine the response $p^o(\tau)$; we proceed by substituting Eq.(9) into the second of Eq.(8), we obtain the $p^o(\tau)$ time domain solution. The reader is referred to Ref. 6 for the range of validity of this solution and how the range of validity may be extended by using overlapping segments of the $p_d^i(\tau)$ function.

A similar procedure may be used to solve inverse problem types (integral equations) where we are given $p^o(\tau)$ and we wish to determine $p_d^i(\tau)$. We proceed by transposing Eq.(9) to obtain

$$\bar{A}(n\Delta f) = \frac{\bar{C}(n\Delta f)}{T\, \bar{B}(n\Delta f)}$$

and then operating on $\bar{A}(n\Delta f)$ with the second of Eqs.(8)(i.e., replace $\bar{A}_n$ in Eq.(8) with $\bar{A}(n\Delta f)$ to obtain the free field input $p_d^i(\tau)$.

The same type calculation discussed above for solutions to Eq.(2) can also be applied to Eq.(1) in the same manner. To illustrate the accuracy of the FFT type solution, we consider an example calculation relative to the forward solution of
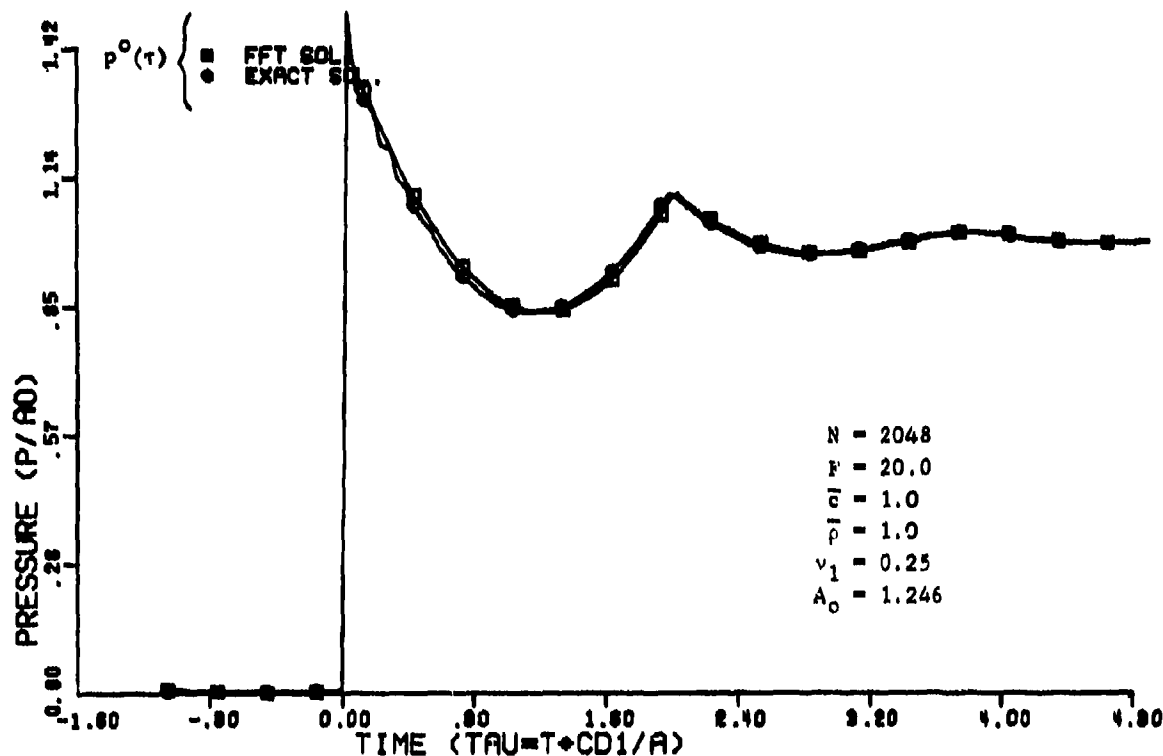

$p^o(\tau)$ { ■ FFT SOL. ● EXACT SOL.

N = 2048
F = 20.0
$\bar{c}$ = 1.0
$\bar{\rho}$ = 1.0
ν_1 = 0.25
A_o = 1.246

PRESSURE (P/A0)

TIME (TAU=T+CD1/A)

Figure 4   Convolution FFT -- Exact Solution Transient Response Solution Comparison

109

Eq. (1). A comparison is shown in Figure 4 between the exact solution (employing an exact theory solution, Ref. 6) and the solution to the above problem using the $\frac{1}{2}$FT technique.

EXPERIMENTAL VERIFICATION

The Experiment

The experiment apparatus consists of a stubby solid cylindrical block which is located at the end of IITRI's 2 ft shock tube. The block is made of a plastic-like material which consists of an epoxy resin activated with an aromatic polyamine. The material exhibits good linear elastic properties and its dynamic response is nearly strain rate insensitive. The spherical fluid bag pressure gage is embedded in the central region of the block as illustrated in Figure 5. The block is loaded with a nominal 20 to 40 psi flattop pressure wave by means of a compression chamber release device located at the end of the tube. The intent of the experiment was not only to measure the pressure in the free field (i.e., the solid test block) but to measure certain information regarding the free field shear stress content. The presence of the off-center fluid pressure transducer was to obtain backup information about the off-center fluid pressure response and is not normally needed as part of the regular gage makeup. We focus our attention on the center fluid pressure
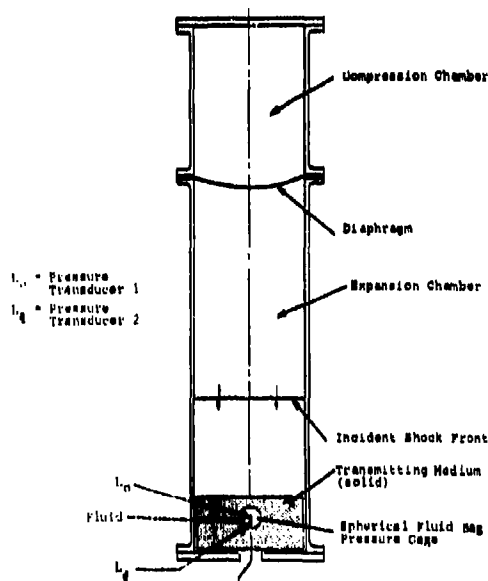
transducer and its ability to relate to the free field state of stress and/or pressure in the block via the system transfer function.

A diagram showing the instrumentation system and the location of various transducers within the test block are shown in Figure 6. The transducers denoted by L_O and L_a are the two fluid pressure transducers mentioned previously. These measure the transient pressure waveforms existing in the fluid during the shock tube experiment. The transducers denoted by A_{21} and A_{23} are strain gages whose purpose was to measure the relative arrival times of the free field incident wave for the sole purpose of determining the dilatational wave in the block. The transducers denoted by L_1 and L_2 are the air pressure gages which are imbedded in the shock tube wall. The results of these gages are used to determine the free field state of pressure loaded into the block. These measurements represent our independently determined reference state against which the spherical fluid bag gage results can be compared.

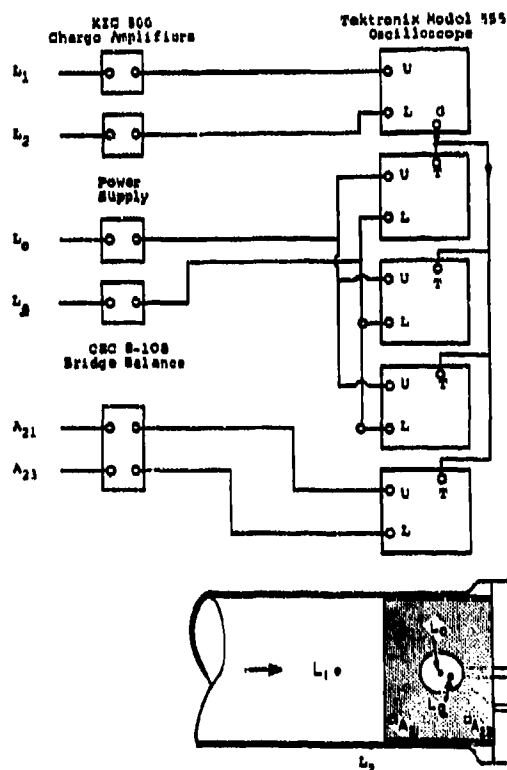Figure 5   IITRI 2-ft Shock Tube Facility with Model in Test Position

Figure 6   Block Diagram of Instrumentation System and Sketch of Transducer Locations

A series of tests employing either glycerin or water as the gage fluid were conducted using the apparatus described herein. The results of a typical test (employing glycerin as the gage fluid) are illustrated in Figure 7. The curve marked with the symbol △ is the independently determined experimental free field pressure in the solid block. This is determined from the measured reflected pressure tube. The relation between the normal reflected shock tube pressure, $p_r(\tau)$ and the pressure in the block, $p_d^i(\tau)_m$, is simply

$$p_d^i(\tau)_m = p_r(\tau)(1+\nu_1)/[3(1-\nu_1)]$$

where ν_1 is Poisson's ratio of the solid. This relation is valid prior to the arrival of the edge effect waves. The curve marked ⊙ is the fluid pressure, $p^o(\tau)$, measured by the center pressure transducer (at location L_o) within the fluid bag. It is noted that it has roughly a one-third overshoot at the arrival of this input wave. This overshoot is expected

and is mainly a result of the mismatch in impedance that exists between the fluid and solid. The curve marked ▣ represents the solid media pressure, $p_d^i(\tau)$, that was computed from the fluid bag gage's solid-fluid interaction transfer function by the FFT numerical technique. As can be seen from the figure, the comparison between the independently determined reference state, $p_d^i(\tau)_m$, and the fluid gage determined pressure, $p_d^i(\tau)$, is very good.

During the early portion of the wave arrival within the fluid (say first 20 μsec) the pressure response at the center of the fluid-filled sphere is not the same as an off-center point. This is a consequence of the fluid-solid interaction aspect of the problem. The object of the results shown in Figure 8 are to demonstrate the consistency between the computed free field input pressure, $p_d^i(\tau)$, and the measured off-center fluid response $p_m^o(\tau)$ (i.e., with the off-center transducer located in position L_m in Figure 6.
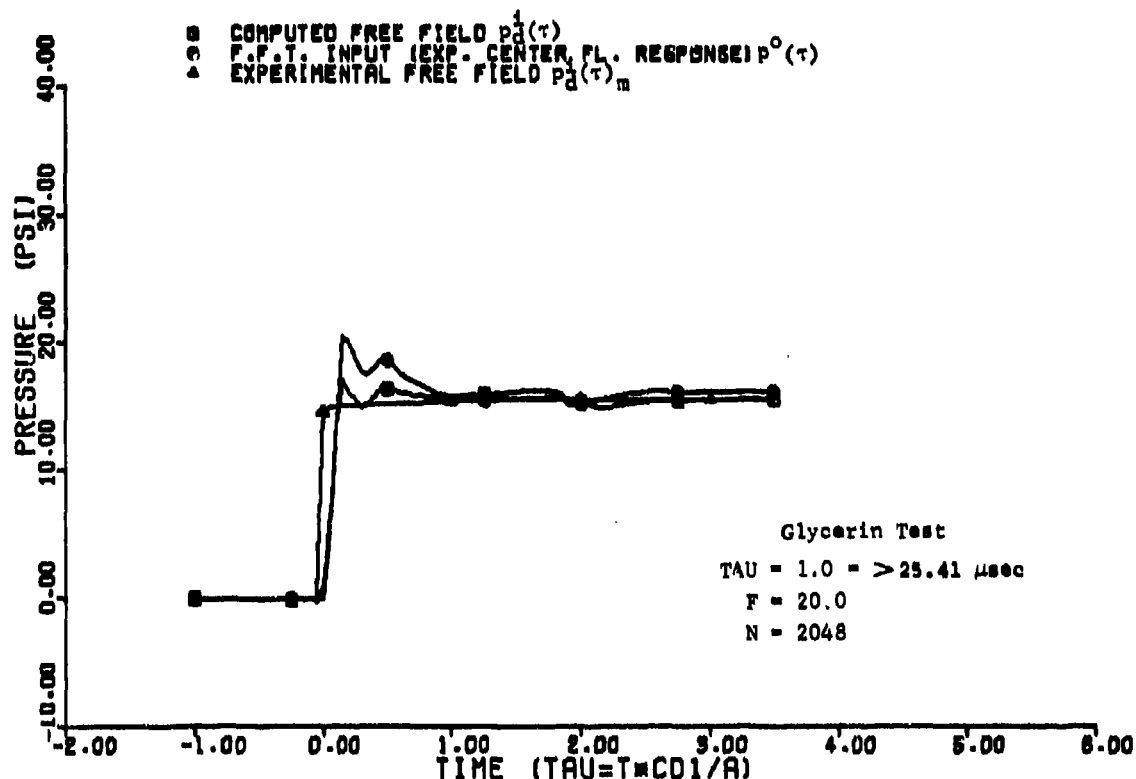

■ COMPUTED FREE FIELD $p_d^i(\tau)$
⊙ F.F.T. INPUT (EXP. CENTER FL. RESPONSE) $p^o(\tau)$
▲ EXPERIMENTAL FREE FIELD $p_d^i(\tau)_m$

Glycerin Test

TAU = 1.0 = > 25.41 μsec

F = 20.0

N = 2048

Figure 7   Free Field Dilatational Pressure in Solid
(FFT computed-to-experimental comparison)

111

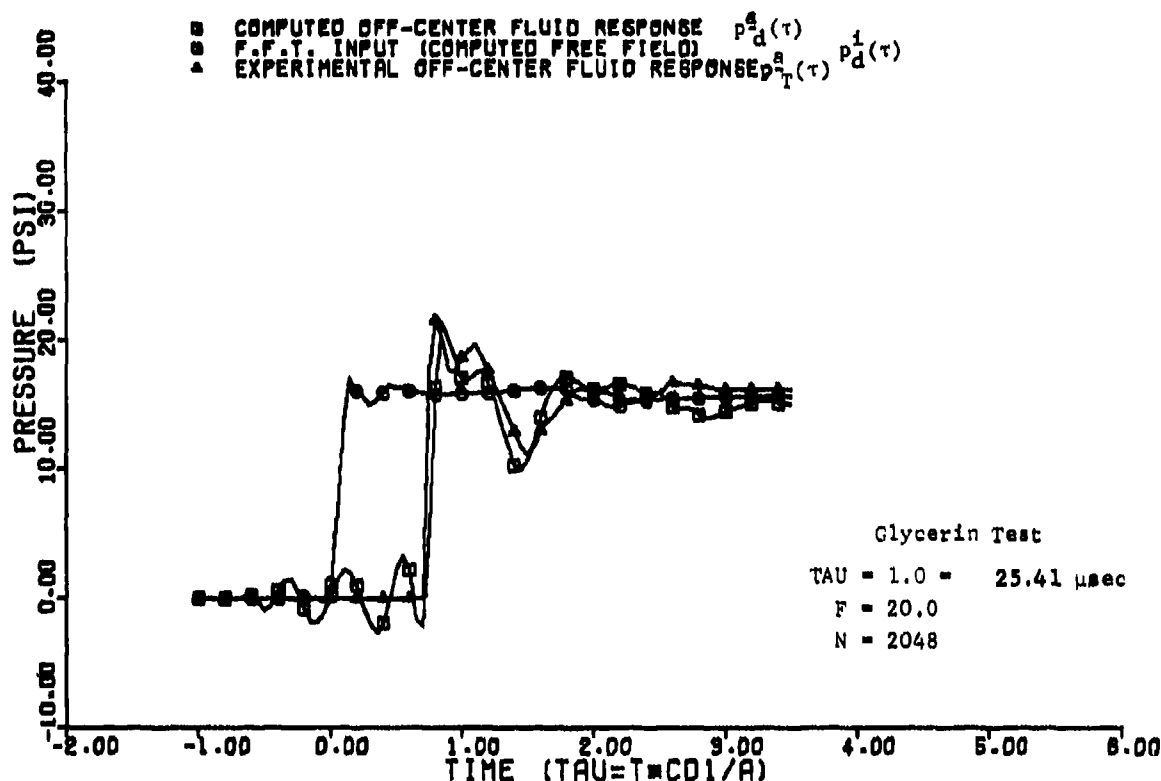Glycerin Test

TAU = 1.0 = 25.41 μsec
F = 20.0
N = 2048

Figure 8 Off-Center Fluid Pressure (FFT computed-to-experimental comparison)

In other words if the fluid gage has properly computed the correct free field pressure, then we should be able to compute (using the fluid-solid interaction transfer function) an off-center fluid pressure response, $p_d^a(\tau)$, which is in agreement with the measured off-center fluid response. By comparing the $p_d^a(\tau)$ and $p_T^a(\tau)$ curves (denoted by ▢ and △ respectively) in Figure 8, we see that very good agreement is achieved, except for a small amount of numerical noise in the early portion of the $p_d^a(\tau)$ curve. We wish to emphasize that this last exercise involving the off-center gage is only a demonstration of the validity of the fluid-solid interaction transfer function and the verification of the ability to convert free field pressure into fluid pressure or vice versa.

The curves presented in Figure 9 are photographs of the oscilloscope records taken during the glycerin fluid experiment. The fluid transducer records were only used up to the point where relief waves from edge effects entered into the problem. The point in time at which the planar form of the input in the block ceases to exist is shown in Figure 10. The dimensions of the block were specif-
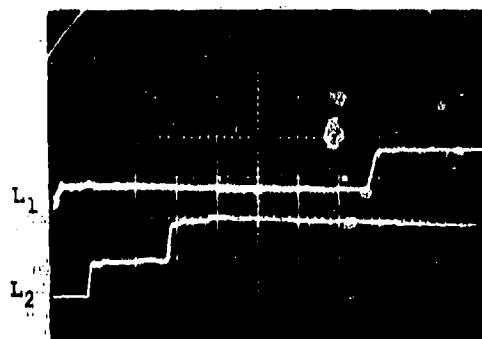
ically designed to maximize the viewing time before the edge effects arrive at the cavity. This point can be observed by noticing the sudden dropoff of pressure in the trace after about 80 μsec. For reference purposes we included the time records of the shock tube pressure and the block embedded strain gages used for determining the wave speed in the test block.

SENSITIVITY OF THE FLUID BAG GAGE

Assumptions governing the validity of the fluid pressure-to-free field stress calculations were listed. Quantitative information regarding the consequence of violating each of these assumptions can be viewed as a study of the sensitivity problem. Therefore we comment only on those assumption deviations which have a clearly understood effect on the sensitivity of the gage performance.

Variation of Media-Fluid Characteristics

There are two aspects to this problem: variations in the values of the material elastic constants affecting $\bar{c}$, ρ, and ν_1; and variations of the material behavior from the assumed linear behavior.

112

(Shock tube pressure record)
Horizontal: L_1 50 μsec/div L_2 100 μsec/div
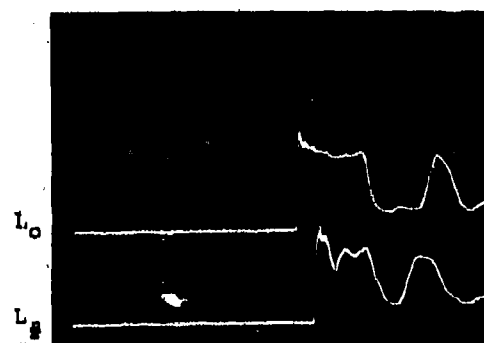Vertical: L_1 9.62 psi/div L_2 9.52 psi/div

Test Number: 61
Applied Pressure: 19.9 psi
Inclusion Fluid: Glycerin
Probe
Configuration: PCB Piezotronics
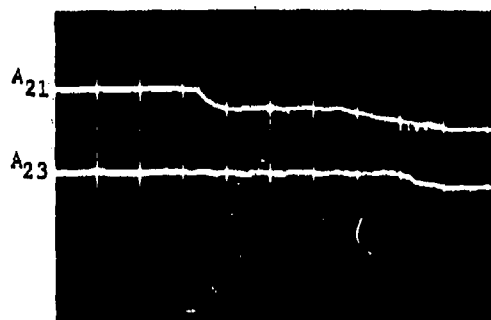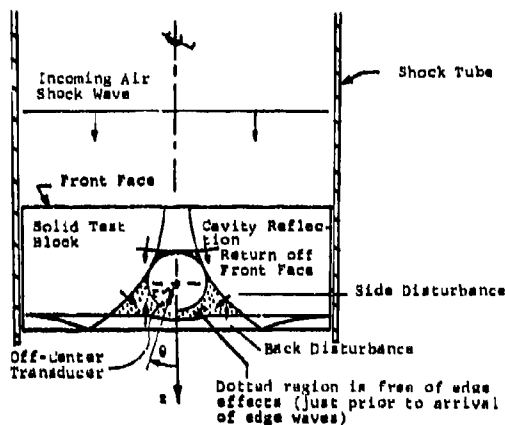

(Strain gage record)
Horizontal: A_{21} 20 μsec/div
             A_{23} 20 usec/div

(Fluid bag transducer record)
Horizontal: L_o 50 μsec/div L_a 50 μsec/div
Vertical: L_o 10.10 psi/div L_a 10.64 psi/div

Figure 9   Experiment Time Records

113

Figure 10 Valid Region of Experiment Free of Edge Effects

Location of Center Pressure Transducer $\bar{r} = 0.0$, $\theta = $ any

Location of off-Center Pressure Transducer $\bar{r} = 0.6872$
$\theta = 8.25$ deg

Note: $\bar{r} = r/a$
a = cavity radius 2.21 in.
Local coordinates θ, z are for P-wave solution.

Material Constant Variations

The solution transfer functions are complicated functions of the material constant ratios $\bar{\rho}$, $\bar{c}$, ν_1, thus it is very difficult to make general comments about the sensitivity of the dynamic response to changes (or uncertainties) in these constants. The study reported in Ref. 7 covered this problem in some detail for a range of parameters of $\bar{c} = 0.2 \rightarrow 2.0$; $\bar{\rho} = 1.0 \rightarrow 2.7$; and $\nu_1 = 0.25 \rightarrow 0.40$. No cases were found where small changes in the material constants resulted in a highly nonproportional change in the system response either for the P-wave transient step or transfer functions solutions. However, because of the nonlinear nature of the solution functional dependence on $\bar{\rho}$, $\bar{c}$, ν_1, one should still treat each problem individually and for example, reprocess the raw experimental data with several perturbations about the base case best estimate for the parameters.

One other way to observe the material sensitivity is to examine how certain key features of the system response (either steady state or transient) vary with the material parameters. For example simplified algebraic expressions for the maximum transient center fluid response (early time overshoot) to a P-wave unit step input impinging on the fluid-filled cavity is given by

$$p^o(\tau)_{max}^{in} \begin{cases} \dfrac{1}{\bar{\rho}\left[1-4/(3\bar{k}^2)\right]} & \bar{\rho}\,\bar{c} < 1 \\[3ex] \dfrac{1+e^{-2\bar{c}\gamma_0}}{\bar{\rho}\left[1-4/(3\bar{k}^2)\right]} & \bar{\rho}\,\bar{c} > 1 \end{cases}$$

where

$$\gamma_0 = \left[\coth^{-1}(\bar{\rho}\,\bar{c})\right]/\bar{c},$$

$$\bar{k} = \left[2(1-\nu_1)/(1-2\nu_1)\right]^{1/2}$$

Similarly the maximum high frequency limit $\alpha \rightarrow \infty$ for the unit amplitude input harmonic response to the same problem described above is given by (Ref. 7)

$$p^o(\alpha \rightarrow \infty) = \begin{cases} \dfrac{1}{\bar{\rho}\left[1-4/(3k^2)\right]} & \bar{\rho}\,\bar{c} < 1 \\[3ex] \dfrac{\bar{c}}{\left[1-4/(3\bar{k}^2)\right]} & \bar{\rho}\,\bar{c} > 1 \end{cases}$$

and the low frequency response $\alpha \rightarrow 0$ is given by Ref. 7

$$p^o(\alpha \rightarrow 0) = \dfrac{1}{\left[1-4/(3\bar{k}^2)\right]\left[1+\dfrac{4\bar{c}^2\bar{\rho}}{3\bar{k}^2}\right]}$$

For example these results illustrate that for $\bar{c}\bar{\rho} \sim 1$ (a hard inclusion) all three aspects of the responses discussed above either are weakly dependent or totally independent on the value of $\bar{c}$. Since $\bar{c}$ is directly related to the Young's modulus, E_1, of the materials, this has some bearing on the behavior of the gage for nonlinear material stress strain laws. This point is discussed further in the next subsection.

Material Behavior

The fluid pressure-to-stress calculations inversion process has been derived on the basis that the solid media in which the gage is embedded can be represented by a linear elastic stress strain law characterized by a constant Young's modulus E_1 and Poisson's ratio ν_1. Further the fluid was assumed to behave linear elastically. We need not concern ourselves with nonlinear variations of the fluid behavior for it will behave linearly for the range of pressures up to say 3000 psi. The solid media nonlinear material problem is a more complex problem.

Nonlinear Elastic Behavior: In this problem the stress state is assumed to be a nonlinear function of strain state, however upon release of the load, the unloading path retraces the loading path (i.e., no plastic unloading or hysteresis is present). In other words the tangent

114

modulus, E_1, is not a constant but a function of the state of strain. In the previous subsection, we have shown that the transfer functions for "hard" fluid inclusions (i.e., $\overline{\rho c} \ll 1$) are weakly dependent on $\overline{c}$. But $\overline{c}$ is related to the solid media tangent modulus, E_1, by the relation

$$\overline{c}^2 = \frac{E_1}{\lambda_2} \frac{(1-\nu_1)}{(1+\nu_1)(1-2\nu_1)\overline{\rho}}$$

where λ_2 is the bulk modulus of the fluid. Thus for a fixed λ_2, ν_1, $\overline{\rho}$, a weak dependence of the fluid response on $\overline{c}$ implies a weak dependence on the fluid response on the stress-strain law tangent modulus via the prior equation. The conjecture is that for hard inclusions, the gage system would continue to provide a sufficiently accurate fluid pressure-to-stress inversion even though different points in the solid media (in the neighborhood of the gage) are at a different stress level (hence at different $\overline{c}$ levels). The basis of the conjecture is that the response is increasingly independent of $\overline{c}$ for increasingly harder inclusions (i.e., decreasingly lower $\overline{\rho c}$ values). The conjecture must also be tempered with the fact that we are assuming all other assumptions regarding the inversion of pressure-to-stress are maintained.

Nonlinear Plastic Behavior: In this case the stress state in the solid media is assumed to be a nonlinear function of the strain state, however hysteresis is present during unloading of the stress state. The unloading path implies a stress dependent tangent modulus as in the previous discussion thus the previous subsection comments on a hard inclusion being independent of the tangent modulus holds here as well. The hysteresis has a more serious effect than mentioned above in that during the unloading, portions of the gage bladder surface, originally in contact during loading, may be separated (leave a small void) from the solid media. Short of making a separate study of this particular problem, we cannot make any routine statements regarding the effect of hysteresis on the gage response except that obviously separation of a portion of the media from the gage is not desirable, however any quantitative statements regarding what percent separation causes what percent error in the response cannot be made. There is a built-in flexibility mechanism within the gage to account for separation to some degree, namely, the partial ability of the gage to conform to irregularities in the media out-of-roundness. This is discussed further in the next section on contact.

Gage-to-Medium Contact

It is important that the gage be in contact with the solid medium during operation. A measure of the gage bladder flexibility is realized by considering an unburied free bladder subject to a net outward radial internal pressure, Δp_i. The relation between this pressure and the net radial outward displacement, σ_r, is given by the relation,

$$\delta_r = \frac{\Delta p_i \, a_b^2 \, (1-\nu_b)}{2E_b \, h_b}$$

where a_b, ν_b, E_b, h_b mean radius of the spherical bladder, Poisson's ration, Young's modulus and thickness of the spherical bladder respectively. For example, the stress gages for the study are $\sigma_r = 0.178$ in. for every 10.0 psi, Δp_i, pressure. This means that the gage can fill out to meet a 0.178 radial gap that might inadvertently occur between the gage and media. The above formula indicates that by manufacturing gages with lower h_b and E_b values, this flexibility can even be increased more than it is now. However, if it is too flexible the bladders will not remain spherical under their own weight. They will collapse like an uninflated balloon rather than maintain a spherical shape such as a basketball shell. The advantage to leaving the gage flexibility more on the stiff side is that emplacement procedures are made more easily. The tradeoff disadvantage is that increased stiffness reduces the good contact advantage.

Knowledge of Planar Input Angle ψ_d

The pressure inversion process, for the determination of the dilatational input contribution, will correctly predict the input waveform even if the presumed value ψ_d is erroneous. That is, we would have the correct pressure input, $p_d(\tau)$, but the orientation of the dilatational free field stress components relative to the ground coordinates would only be in error.

Multiwave Inputs

The pressure-to-stress inversion process will work the best when we know certain a priori knowledge about the input. However what happens when the wave encounters complicated geological states that are comprised of several layers of drastically varying material properties? The input is no longer a clean P-wave. The input impinging on the gage is more likely to be a complicated multiwave mixture of P- and S-wave reflections that resulted from multireflections off of the layered media. Such a multiwave input to

the gage will result in a net pressure reading that represents the sum total response to all P-wave input for the center response. In such situations, unscrambling P-wave pressure contributions is not possible. The center measurement does however still provide some very useful information about the dilatational component of the free field stress state. The center pressure measurement is independent of the incoming wave orientation, and as discussed earlier, independent of the planar or spherical shape of the impinging P-waves. Thus upon inverting the center pressure reading, $p^o(\tau)$, into the calculated free field dilatational pressure, $p_d^i(\tau)$, we can interpret the $p_d^i(\tau)$ calculation as the correct free field average dilatational stress (i.e., $p_d^i(\tau)$ $= -[(\sigma_x^i) + (\sigma_y^i) + (\sigma_z^i)] \div 3$) but we cannot give any information about the individual stress components that make up the average.

Experimental Fluid Pressure Measurements

Two types of fluid pressure transducers were considered during the course of the program, the PCB Piezotronics probe and the Sensotec probe. With the exception of the very early time range just after the arrival of the incoming fluid pressure wave, both transducers can accurately measure the fluid pressure to within ± 5 percent. The early time region containing the very high-frequency content input, causes the Sensotec transducer to ring whereas the PCB transducer, for the same experiment, did not.

Emplacement of the gage systems in media such as soil is not likely to have as sharp wave fronts (hence the high-frequency content is not present) as if it were placed in, say, a medium such as rock. Thus for soil type materials either transducer would probably work as well, whereas as for emplacements in rock, the PCB transducer would be better.

One advantage the Sensotec transducer has over the PCB transducer is that the former single-barrel configuration is smaller than the latter double-barrel configuration. Thus the disturbing effect of the presence of the measuring device is likely to be smaller for the Sensotec transducer by virtue of its smaller size.

A final comment on on the PCB transducer considered is that it will not measure a static pressure. This means that any initial fluid pressure present in the fluid bag for the purpose of making good contact between the medium and bladder will not register on the transducer response record. We point out however that the PCB transducer is practically a static measuring device in that it has a large time constant, $t_c = 500$ sec.

Should it become important that the static initial pressure be monitored, say during the embedding procedure, then the transducer vendor can most likely install a special static measuring device within the probe in addition to the two existing dynamic pressure transducers.

CONCLUSIONS AND RECOMMENDATIONS

During the course of this study, a fluid bag gage system was designed, and tested in a controlled shock tube experiment. Based on the results of the experiment and subsequent postprocessing of the experimental data, we have drawn these conclusions:

- The PCB pressure sensing transducers operate more accurately (without ringing) than the Sensotec pressure transducers for the early high-frequency content portion of the input records. In the lower frequency region after the shock arrival, both performed equally satisfactorily.

- The spherical bladder (or shell) of the stress gage can be made as stiff or flexible as desired to suit various embedding procedures by varying the epoxy mixture during the fabrication process. The tradeoff between maintaining roundness (with stiff bladders) and achieving good medium-to-bladder wall contact (with initially pressurized flexible bladders) must always be borne in mind when arriving at any new gage configuration.

- The fluid bag gage was able to compute the dilatational reference state (pressure or stress) existing in the solid medium with a high degree of precision (including both the shock front details and the steady state asymptote).

The scope of this effort was vast in that it touches on manufacturing problems, experimental problems and analytical problems. This study has answered some important questions regarding the feasibility of the fluid bag stress gage concept; however, it has also raised a few. Consequently, our comments are based on facts we have learned in addition to recommendations for further study to answer the questions raised by the current study.

- Upon being given the physical properties of the transmitting medium in which the stress gage is to be placed (i.e., the medium density ρ_1, dilatational wave speed c_{d1} and Poisson's ratio ν_1), a decision must be made with regard to the selection of a fluid inside the gage. We recommend selecting a fluid that has a dilatational wave speed, c_{d2}, larger than that of the transmitting medium

116

(i.e., $\bar{c} < 1$). There is an upper bound to how large the dilatational wave speed of a fluid can be, namely c_{d2} = 118,000 in./sec for a new double glycerin molecule fluid called Arlex.

● The ideal situation for the fluid-solid wave speed ratio is that c = 1. However we recommend that future bladders, and particularly the stems and stem end flange, be made of a material with a wave speed that closely matches the medium properties.

● Implementation of embedding techniques should receive further attention. Perhaps the only way this can be fully studied is to emplace a gage in the field.

● A further study of the frequency limits of the gage response should be made.

● It is recommended that further studies be made into the manner in which the procedure for inverting the fluid pressure into free field response pressure can be modified to accommodate nonlinearities in the medium constitutive relations. Another course of study could be made to determine to what extent the linear model can be used in a nonlinear medium. In either case, carefully controlled shock tube loaded experiments, like the one reported on in this paper, should be run to verify the inversion procedures.

REFERENCES

1. Selig, E. T. and Wetzel, R. A.; A Miniature Piezoelectric Gage for Static and Dynamic Soil Stress Measurements, IIT Research Institute, Contract Rept. 1-105 for U.S. Army Waterways Experiment Station, Vicksburg, Miss., Nov 1965.

2. Selig, E. T. and Tobin, H. G.; Piezoresistive Soil Stress Gage, IIT Research Institute, Tech. Rept. AFWL-TR-66-51 for U.S. Air Force Weapons Lab, Kirtland AFB, New Mexico, Sept 1966.

3. Ingram, J. K., The Development of a Free Field Soil Stress Gage for Static and Dynamic Measurements, Symp. Instrumentation and Apparatus for Soils and Rock, ASTM STP 392, 1965.

4. Lynch, R. E., Development of the University of New Mexico Soil Stress Gage, Tech. Rept. AFWL TR-65-104, Aug 1966.

5. Lew Tik, Evaluation of a Three-Dimensional Stress Cell for Granular Soils, Tech. Rept. R-758, Naval Civil Engr. Lab., Feb 1972.

6. Kalinowski, A. J., et al., Spherical Stress Gage Development, IIT Research Institute Report J6261 (to be published as AFWL Tech. Rept), Oct 1972.

7. Kalinowski, A. J., Stress Gage Feasibility Analysis, U. S. Air Force Weapons Lab., Tech. Rept. AFWL-TR-71-14.

8. Cooley, J. W. and Tukey, J. W., "An Algorithm for the Machine Calculations of Complex Fourier Series," Math. of Comput. 19, Apr 1965.

9. Cooley, W. J., Lewis, D. A., and Welch, D. D., "Application of the Fast Fourier Transform to Computation of Fourier Integrals, Fourier Series and Convolution Integrals," IEEE Transactions on Audio and Electroacoustics, AU-15(2), June 1967.

10. Nuclear Geoplasics, 1, p 38, DASA 2385, Feb 1962.

11. Underground Explosion Test Program, Final Report, 1: Soil, PX-29703, pp 2-34 Engineering Research Associates, Aug 1952.

12. Doll, E. B. and Salmon, V., Operation Jangle, Project 1(9)01, Scaled HE Test, Stanford Research Institute, Weapons Test Report, WT-377, p 16, Apr 1952.

13. Lampson, C. W., Final Report on Effects of Underground Explosions, NDRC Report A-479 and OSRD Report 6645. Cosponsored by National Defense Research Council and Office of Scientific Research and Development, Mar 1946.

14. "Development of Explosion Pressure Gages and Recording Equipment," Stanoline Oil and Gas Co., Exploration Research Laboratory, OSRD Report 1739.

ACKNOWLEDGEMENTS

DESIGN TECHNIQUES

MAXIMIZATION AND MINIMIZATION
OF DYNAMIC LOAD FACTORS

George J. O'Hara
Ocean Technology Division
Naval Research Laboratory
Washington, D.C.

This paper presents in a heuristic manner a method of determining the
maximum and minimum possible values of dynamic load factors for
damped and undamped simple oscillators responding to applied forces
defined by an amplitude tolerance curve. In the case of forcing func-
tions of long duration, limit cycles are derived to show the rates at
which resonance buildup occurs. A few sample problems are worked
out by the method of exact transformations, and the results are pre-
sented. It is demonstrated that for light damping a significant variation
can occur in dynamic load factors for band-limited pulse shapes.

INTRODUCTION

Dynamic load factor (DLF) is a common
term in structural dynamics which expresses
the ratio of the maximum absolute value of dy-
namic deflection to the statical deflection. Its
use has expanded over the years and has become
increasingly important for low-frequency sys-
tems.

There has been a tendency to attempt to
define shock pulses as a means of test speci-
fication [1]. These specifications usually define
a set of bounds within which the pulse must lie
to have an acceptable test. It then would seem
logical that a series of different tests, all within
these bounds, might produce different dynamic
load factors.

It is the propose of this paper to consider
the effects on dynamic load factor of uncertain-
ties in applied force. A set of simple problems
is explored in some detail in an effort to define
the problem, to examine some of the conse-
quences of the definition, and to present a sim-
ple, easily understood method for solution.
Therefore, only very simple pulse shapes, with
simple tolerance bounds, and simple linear os-
cillators are used in this phase of the problem
to achieve this goal. It should be understood
that the ideas and methods outlined here are not
restricted to these pulse shapes and oscillators.

There is no reason why they cannot be applied
to complicated tolerance bounds and nonlinear
systems.

In the general sense, the problem consid-
ered here is: For a prescribed second-order
ordinary differential equation in which the inde-
pendent variable is ill-defined such that only its
upper and lower amplitude bounds are known,
what are the maximum and minimum possible
values that the dependent variable may attain?
This is another way of looking at the problem of
worst and best disturbance.

Consider the linear simple oscillator shown
in Fig. 1, responding to applied forces shown in
Fig. 2. Any shaded area in Fig. 2 is meant to
convey the meaning that the applied force can
be any function of time which lies within this
area. The force is bounded by the straight lines.
In other words, $F_1 \leq F(t) \leq F$.

First the maximum possible response is
found in those cases where the duration is un-
defined; then selected problems are solved and
presented for a specified duration time.

GENERAL APPROACH

In this paper only applied forces will be
considered for convenience, since extension to
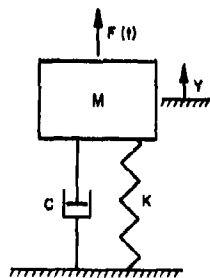base motions is straightforward.
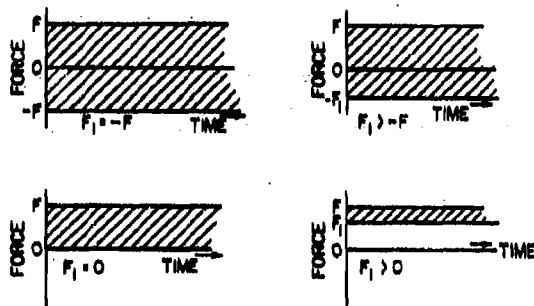
Fig. 1 - Linear simple oscillator

Fig. 2 - Bounds of example forcing functions

The differential equation of motion for the linear simple oscillator is

$$\ddot{Y} + 2\alpha\omega\dot{Y} + \omega^2 Y = \frac{F(t)}{M} , \qquad (1)$$

where $\alpha = C/C_r$ = the ratio of damping to critical damping, and $\omega^2 = K/M$ = the square of the undamped natural frequency.

First multiply both sides of Eq. (1) by $\dot{Y}$:

$$\ddot{Y}\dot{Y} + 2\alpha\omega\dot{Y}^2 + \omega^2\dot{Y}Y = \frac{F(t)\dot{Y}}{M} . \qquad (2)$$

The unit of this equation is power per unit mass. Here $F(t)$ is the independent variable and Y is the dependent variable. The power supplied to the system is the product of $F(t)$ and $\dot{Y}$. The integral of Eq. (2) is

$$\frac{\dot{Y}^2}{2} + 2\alpha\omega\int\dot{Y}^2\,dt + \omega^2\frac{Y^2}{2} + E_0 = \frac{1}{M}\int F(t)\dot{Y}\,dt , \qquad (3)$$

where E_0 is the constant of integration. This is an energy balance. The right-hand side is the energy input. The left-hand side is the system energy.

To maximize the system response, the function $F(t)$ should be chosen to provide the greatest possible energy when it helps to increase deflections and to extract the least amount of energy when it decreases deflections. To minimize the system response, the opposite scheme should be followed.

CAUTION: There are certain classes of problems in _minimization_ which require the analyst to look ahead. For example it may be necessary to input some energy early so that a prescribed part of the forcing function will complement it. The reader is referred to the literature and in particular to work concerning linear end dynamic programming such as Ref. [2].

GENERAL RESPONSE EQUATIONS

Examination of Fig. 2 and application of the preceding discussion reveal that for these simple cases the force will have a set of constant values, each value being applied for a determinable time. This is true because the bounds on $F(t)$ are horizontal lines. In more general cases, to be discussed in a companion report, this is not necessarily the situation, but it was deliberately chosen to be so here for demonstration purposes.

The response equations from Refs. 3 and 4 over any time in which a constant force is applied are

$$Y_{n+1} = Y_n e^{-\alpha\theta}\left(\cos r\theta + \frac{\alpha}{r}\sin r\theta\right)$$

$$+ V_n e^{-\alpha\theta}\frac{\sin r\theta}{r}$$

$$+ \frac{F_n}{K}\left[1 - e^{-\alpha\theta}\left(\cos r\theta + \frac{\alpha}{r}\sin r\theta\right)\right] \quad (4a)$$

and

$$V_{n+1} = -Y_n e^{-\alpha\theta}\frac{\sin r\theta}{r}$$

$$+ V_n e^{-\alpha\theta}\left(\cos r\theta - \frac{\alpha}{r}\sin r\theta\right)$$

$$+ \frac{F_n}{K}e^{-\alpha\theta}\frac{\sin r\theta}{r} , \qquad (4b)$$

where $V = \dot{Y}/\omega$. In Eqs. (4a) and (4b), $\theta = \omega\Delta t$, $r = \sqrt{1 - \alpha^2}$, Y_{n+1} and V_{n+1} are values at the end

120

of the time increment, Y_n and V_n are values at the beginning of the time increment, and F_n is the value during the time increment. In the undamped case $(\alpha = 0)$ these equations reduce to

$$Y_{n+1} = Y_n \cos\theta + V_n \sin\theta + \frac{F_n}{K}(1 - \cos\theta) \quad (5a)$$

and

$$V_{n+1} = -Y_n \sin\theta + V_n \cos\theta + \frac{F_n}{K} \sin\theta . \quad (5b)$$

RESPONSES

All of the functions of Fig. 2 can be defined as $CF \leq F(t) \leq F$, where $-1 \leq C \leq 1$. It is also assumed that the system starts from rest with zero initial conditions.

If the desire to maximize the response, then $F(t)$ must be chosen to be $+F$ when it helps to increase the deflection. Therefore, this will occur when the velocity of the mass is positive. When the velocity is negative:

1. For $C < 0$, CF has the same sign as the velocity, so the power applied is positive and its integral increases the energy; so apply CF.

2. For $C = 0$, CF does not add to or subtract from the energy of the system.

3. For $C > 0$, CF subtracts energy from the system, so apply the minimum amount possible. This discussion reveals that for these simple examples the forcing function will be a sequence of horizontal lines, and switching will occur at times corresponding to zero velocity. The times of integration are then computed by setting Eq. (4b) equal to zero:

$$-\left(Y_n - \frac{F_n}{K}\right) e^{-\alpha\theta} \frac{\sin r\theta}{r} = 0 , \quad (6)$$

since $Y_n - (F_n/K) \neq 0$, $\sin r\theta = 0$ defines the time of application of the force. Then

$$r\theta_n = \pi ,$$

so

$$\Delta t = \frac{\pi}{\omega\sqrt{1 - \alpha^2}}. \quad (7)$$

This application time is then one half the period of the oscillator. Note the because of the damping term this time can become very large.

Equation (4a) can now be used to set up a recursive relationship:

$$Y_{n+1} = -Y_n e^{-\alpha\theta_n} + \frac{F_n}{K}\left(1 + e^{-\alpha\theta_n}\right) , \quad (8)$$

Letting the half-period damping decrement be defined as

$$\phi = e^{-\alpha\theta_n} = e^{-\alpha\pi/\sqrt{1-\alpha^2}} \leq 1 \quad (9)$$

results in

$$Y_{n+1} = -\phi Y_n + \frac{F_n}{K}(1 + \phi) . \quad (10)$$

The half-period decrement ϕ is shown in Fig. 3 and is listed in Table 1.
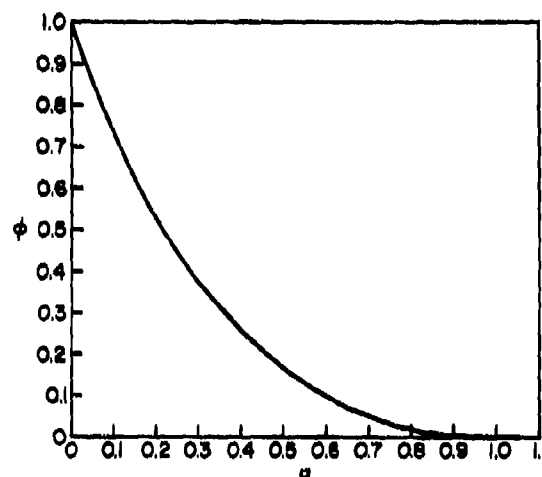

Fig. 3 - Half-period decrement

Equation (10) now can be used to calculate the response at the end of each half cycle. Letting $F/K = \delta$, where $CF \leq F(t) \leq F$, the maximum static deflection, yields the following by repeated application:

$$Y_1 = \delta(1 + \phi) ,$$

$$Y_2 = -\delta(1 + \phi)(\phi - C) ,$$

$$Y_3 = \delta(1 + \phi)(1 + \phi^2 - \phi C) ,$$

$$Y_4 = -\delta(1 + \phi)(\phi - C)(1 + \phi^2) ,$$

$$Y_5 = \delta(1 + \phi)[1 + (\phi - C)(\phi + \phi^3)] ,$$

$$Y_6 = -\delta(1 + \phi)(\phi - C)(1 + \phi^2 + \phi^4) , \text{ etc.}$$

121

TABLE 1
Half-Period Decrement ϕ for Various Amounts of Damping

Damping	Percent of Critical Damping	ϕ
None	0	1
Light	0.5	0.984415
	1	0.969071
	1.5	0.953964
	2	0.939090
	2.5	0.924443
	3	0.910019
	3.5	0.895813
	4	0.881823
	4.5	0.868042
	5	0.854468
Heavy	10	0.729248
	15	0.620871
	20	0.526621
	25	0.444344
	30	0.372326
	35	0.309190
	40	0.253627
	45	0.205346
	50	0.163034
	55	0.126324
Very Heavy	60	0.094780
	65	0.068077
	70	0.045988
	75	0.028375
	80	0.015165
	85	0.006288
	90	0.001524
	95	0.000071
Critical	100	0

By mathematical induction and by recognization that geometric series are involved, this set can be reduced to

$$Y_n = \delta(1+\phi)\left[1 + \frac{\phi(\phi - C)(1 - \phi^{n-1})}{1 - \phi^2}\right] \quad (11)$$

for n odd and to

$$Y_n = -\frac{\delta(\phi - C)(1 - \phi^n)}{1 - \phi} \quad (12)$$

for n even.

The effect of range of C can now be examined. If $C > \phi$, the maximum displacement occurs at the first half cycle with a value of $\delta[1 + \phi]$, and the deflection never becomes negative. If $C < \phi$, the deflection grows to a limit cycle such that the positive displacement is greater than $\delta[1 + \phi]$.

Taking the limit as time becomes very large $(n \to \infty)$ yields as limit cycles:

$$Y_n = \frac{\delta(1 - C\phi)}{1 - \phi} \, , \quad n \text{ odd} , \quad (13)$$

and

$$Y_n = -\frac{\delta(\phi - C)}{1 - \phi} \, , \quad n \text{ even} . \quad (14)$$

The maximum deflection is always positive (except when $C = 1$ and the values coincide) because of the way in which C was defined. Figure 4 is a plot of the maximum ratio Y/δ for two of these limit cycles and for the amplitude of the first maximum as a function of damping. There must exist a set of curves between curves "B" and "C" for various values of $C < \phi$. Inspection shows that for light damping a considerable difference in the maxima may exist. In fact the ratio is

$$1 + \frac{\psi\phi}{1 - \phi^2} \, ,$$

where $\psi = \phi - C$, a positive number. Therefore, curve "C" is the maximum value when $C \geq \phi$.

It is of some interest to compare this result with that of a sinusoidal force of amplitude F. Reference 5 presents the magnification factor as

$$\frac{Y}{\delta} = \frac{1}{\sqrt{\left(1 - \frac{\lambda^2}{\omega^2}\right)^2 + \frac{4\alpha^2\lambda^2}{\omega^2}}} \, , \quad (15)$$

where λ is the driving frequency. If this equation is differentiated with respect to λ/ω and set equal to zero, the maximum is found at the frequency

$$\lambda = \omega\sqrt{1 - 2\alpha^2} \, , \quad (16)$$

Note that a stationary value only occurs for $\alpha \leq \sqrt{2}/2$ and that the maximum value of the magnification factor after this is always one. Substitution of Eq. (16) into Eq. (15) yields
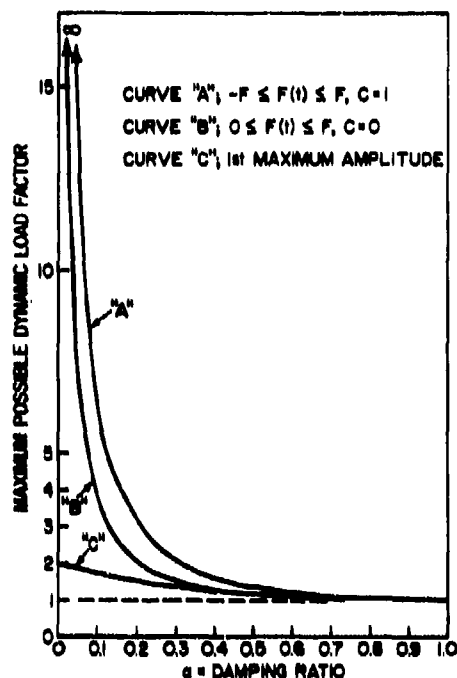
CURVE "A"; −F ≤ F(t) ≤ F, C = 1
CURVE "B"; 0 ≤ F(t) ≤ F, C = 0
CURVE "C"; 1st MAXIMUM AMPLITUDE

Fig. 4 – Maximum possible
values of DLF

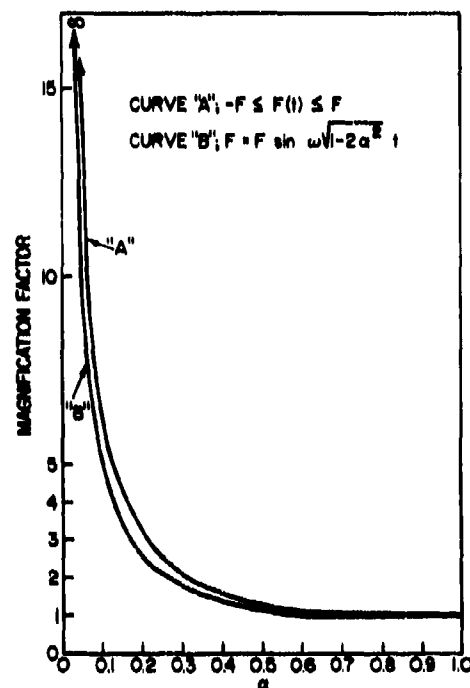CURVE "A"; −F ≤ F(t) ≤ F
CURVE "B"; F = F sin ω√1−2α² t

Fig. 5 – Comparison of maxima of
magnification factors

$$\left.\frac{Y}{\delta}\right|_{max} = \frac{1}{2\alpha\sqrt{1-\alpha^2}}, \quad \alpha \le \frac{\sqrt{2}}{2}, \quad (17)$$

and

$$\left.\frac{Y}{\delta}\right|_{max} = 1, \quad \alpha \ge \frac{\sqrt{2}}{2}, \quad (18)$$

As shown in Fig. 5, this is always less than the maximum value that is attained for a square wave at a frequency $\lambda = \omega\sqrt{1-\alpha^2}$, when $C = -1$.

RESONANCE BUILDUP

It is of interest to examine the rate at which the linear oscillator builds in amplitude under these types of hammer functions. The first case considered is that of $C = -1$, a square wave. Substituting $C = -1$ into Eqs. (11) and (12) yields

$$Y = \pm \frac{\delta(1+\phi)(1-\phi^n)}{1-\phi}. \quad (19)$$

This result is valid for all $\phi < 1$ and yields limit-cycle values of

$$Y = \delta \frac{1+\phi}{1-\phi}. \quad (20)$$

For $\phi = 1$, the undamped case, it is necessary to return to Eqs. (5a) and (5b) to find

$$Y = -2n(-1)^n \delta, \quad (21)$$

Figure 6 shows the scaled absolute values (Y/δ) of Eqs. (19) and (21) and compares them to their maximum values for selected values of the half-period decrement.

Consider now the problem of resonance buildup of an oscillator when the forcing function lies within the band $0.85\ F \le F(t) \le F$. In this case, for C to be less than ϕ, an α of 0.05 or less must be chosen (see Table 1). For values of $\alpha > 0.05$ the maximum occurs at the first half cycle, and its value can be found by adding one to the appropriate number in the ϕ
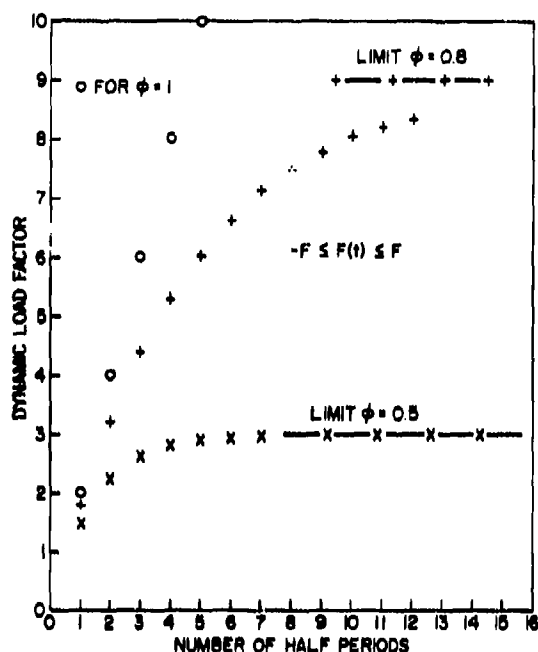
123

Fig. 6 - Resonance buildup for
a square wave

Fig. 7 - Resonance buildup for a
band-limited example

TABLE 2
Resonance Buildup for the Band-Limited
Problem for Four Damping Values

Number of Half Cycles	Dynamic Load Factor			
	$\alpha = 0$	$\alpha = 0.01$	$\alpha = 0.03$	$\alpha = 0.05$
1	2.0	1.96907	1.91002	1.85447
3	2.3	2.19628	2.01434	1.86155
5	2.6	2.40965	2.10073	1.86672
7	2.9	2.61002	2.17228	1.87049
9	3.2	2.79820	2.23152	1.87325
11	3.5	2.97491	2.28059	1.87526
13	3.8	3.14086	2.32122	1.87673
15	4.1	3.29670	2.35487	1.87780
17	4.4	3.44306	2.38274	1.87858
19	4.7	3.58049	2.40582	1.87915
21	5.0	3.70956	2.42493	1.87957
23	5.3	3.83077	2.44075	1.87988
25	5.6	3.94460	2.45386	1.88010
. . .	. . .	. . .	. . .	. . .
∞	∞	5.69980	2.51701	1.88070

column of Table 1. Table 2 and Fig. 7 show the
growth of the maximum value for every odd half
cycle (n odd). The deflection of the undamped
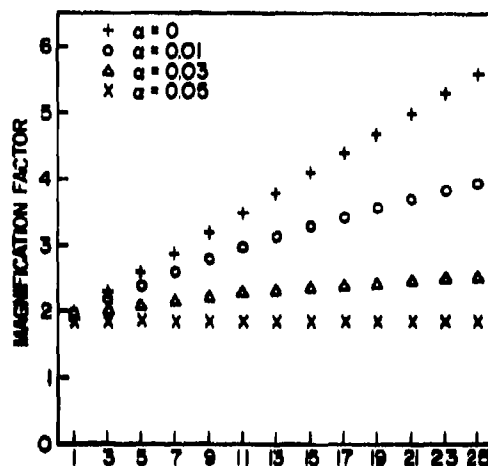oscillator increases without bound.

The addition of a small amount of damping
quickly crushes the maximum response, until
at α slightly greater than 0.05, the maximum
occurs at the first quarter cycle. For $\alpha = 0.0445$
the maximum value of 2 is attained.

PULSES OF FINITE LENGTH

The dynamic load factor is normally asso-
ciated with pulses of finite time. In this section
two simple cases will be discussed, those of
$C = -1$ and $C = 0.85$.

It was demonstrated in the section on reso-
nance buildup that the half period of the respond-
ing oscillator is an important parameter. There-
fore the pulse length will be measured in terms
of the half period. Let T_0 be the pulse length,
and let $T/2$ be the half period; then

$$\frac{T_0}{\frac{T}{2}} = \frac{2T_0}{T} = n + h, \qquad (20)$$

where n is an integer and h is a decimal. Since
time was started anew after each half period,

$$\pi h = r\theta = \omega\sqrt{1 - \alpha^2}\,\Delta t, \qquad (21)$$

In Eqs. (4) and (5). The response after the in-
put is over can be computed by setting $F_n = 0$
in these equations.

First consider the type of function (Fig. 2) $-F \leq F(t) \leq F$. If $F(t)$ were chosen identically zero for all time, there would be no response, so the minimum problem is trivial. The only remaining problem is maximization.

In the undamped case the amplitude always increases each half cycle and for any application of the force beyond a half cycle, so a simple formula results:

$$DLF = \sqrt{(2n+1)^2 + 1 - 2(2n+1)\cos\theta} \qquad (24)$$

for $\theta = \omega\Delta t = \pi h$, where n is the completed number of half periods.

In the damped case the continuation of the force beyond the half period does not guarantee an increase in amplitude, since if it is stopped too soon the damping can reduce the value below that of the previous maximum. As a result, the problem is more complex. For a given pulse the factors n, h, θ can be found. An obvious candidate for the DLF is Eq. (19). Let this candidate value be L (note the absolute value):

$$L = \frac{(1+\phi)(1-\phi^n)}{1-\phi} . \qquad (25)$$

To see if the next maximum is greater, compute by means of Eqs. (4a) and (4b)

$$Y_\Lambda = -(-1)^n \left[(L+1) e^{-\alpha\theta} \left(\cos r\theta + \frac{\alpha}{r} \sin r\theta \right) - 1 \right],$$

$$V_\Lambda = (-1)^n (L+1) e^{-\alpha\theta} \frac{\sin r\theta}{r} ,$$

and

$$\gamma = \tan^{-1} \frac{(L+1) \sin r\theta}{(L+1) \cos r\theta - e^{\alpha\theta}} ,$$

where $0 \leq \gamma \leq \pi$. Another candidate value is

$$P = e^{-\alpha\gamma}\sqrt{Y_\Lambda^2 + 2\alpha Y_\Lambda V_\Lambda + V_\Lambda^2} . \qquad (24)$$

The dynamic load factor is then the larger of the values given by the comparison of L and P.

A problem of greater interest is the banded rectangular pulse. Suppose that a measured pulse is illustrated by the jagged curve of Fig. 8. An analyst might be tempted to note that the function lies between 0.85 and 1, to draw these bounds, and to compute the response in both cases. Curves I and II of Fig. 9 would result in
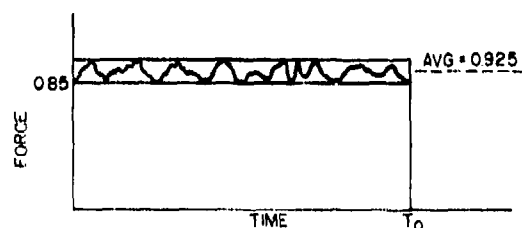

Fig. 8 - Upper and lower bounds on a pulse-type function

the undamped case. This solution is valid for maximum and minimum possible responses out to a value of $2T_0/T$ of about 2.66. However, the sequence of cliffs and plateaus of curve III results from application of the methods of this report. The sharp rises are due to energy input during the positive-velocity phase, after the minimum algebraic displacement has been achieved and after F has been applied for a sufficiently long time. The plateaus have the values presented in Fig. 7. The area bounded by curves I and III is the region of all possible solutions of Eq. (1) to inputs as given by Fig. 8 and for $\alpha = 0$.

To consider damping, note that resonance buildup can occur only for $\phi > 0.85$. Figure 10 shows the solutions for three values of damping; the values of the various plateaus can be found in Table 2.

It is now interesting to note that all possible solutions for $0 \leq \alpha \leq 0.05$ responding to the class of forcing functions of Fig. 8 lie between curves I and II of Fig. 10. All possible solutions for $0.03 \leq \alpha \leq 0.05$ lie between curves II and III, etc. The impulse I in this case is always bounded by $0.85FT_0 < I < FT_0$, or $I = 0.925FT_0 \pm 8.1\%$.

SUMMARY

In the specification of pulses for tests and dynamic analysis, tolerance bounds are sometimes prescribed. It has been shown in the banded rectangular pulse considered here that the assumption that the upper bound gives the maximum dynamic load factor is not valid for systems with small amounts of damping and whose half periods are less than 3/8 of the pulse duration.

An easily understood method for predicting the maximum or minimum possible response of
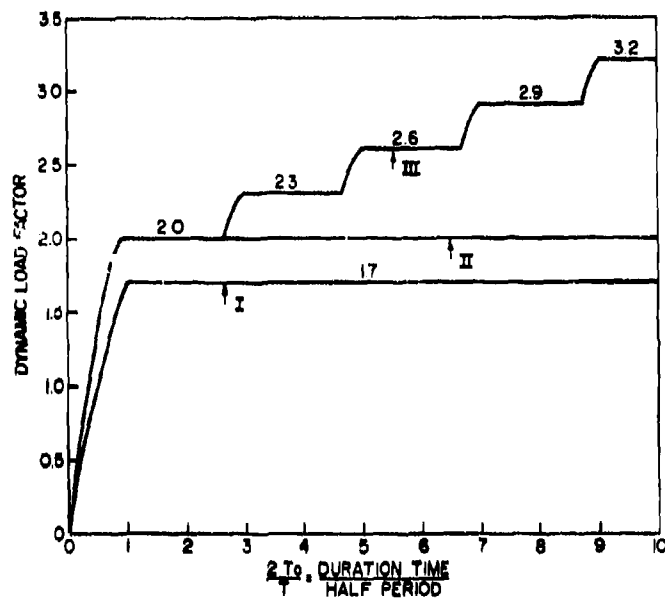
125

Fig. 9 - Ranges of solution as a function of the half
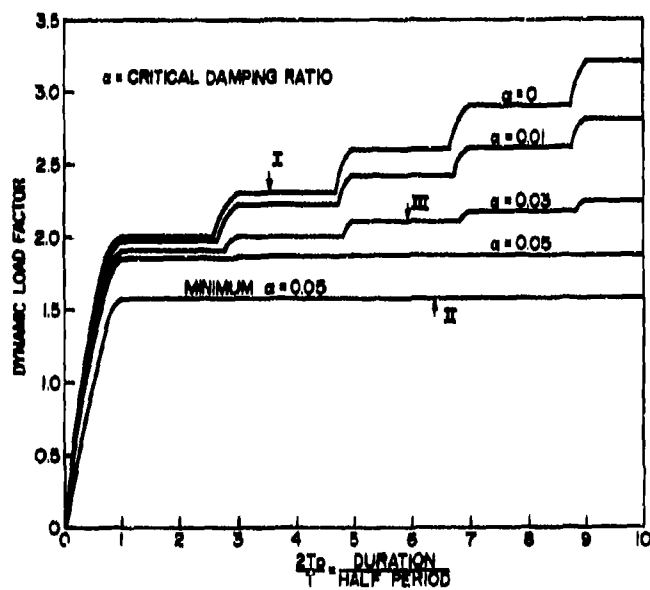period for the undamped case

Fig. 10 - Range of solution as a function of the
half period for various dampings

126

an oscillator to a loosely defined forcing function has been presented. The extension of the method seems direct. Those engineers working with pulse-type shock testing should find this to be of some value.

The examples chosen were simple and for a linear oscillator. More complex wave shapes can be considered, and these methods can be applied to nonlinear systems.

REFERENCES

[1] I. Vigness, "Specification of Acceleration Pulses for Shock Tests," Shock and Vibration Bulletin No. 35, Part 6, Apr. 1966, SVIC, NRL, Washington, D.C. 20390, p. 173.

[2] E. Sevin and W. Pilkey, "Optimum Shock and Vibration Isolation," 1971 SVM-6, Shock and Vibration Information Center, Naval Research Laboratory, Washington, D.C. 20375.

[3] G.J. O'Hara, "A Numerical Procedure For Shock and Fourier Analysis," NRL Report 5772, June 1962.

[4] G.J. O'Hara and P.F. Cunniff, "Numerical Method for Structural Shock Response," Proc. JEMD, ASCE, 51, April 1964.

[5] S. Timoshenko, Vibration Problems in Engineering, 2nd ed. D. Van Nostrand, New York, 1937, p. 38.

THE REDUCTION OF HELICOPTER VIBRATION AND NOISE PROBLEMS

BY THE ELIMINATION OF THE BLADE TIP VORTEX

Richard P. White, Jr.
Rochester Applied Science Associates, Inc.
Rochester, New York

(U) The significant reduction or the elimination of the high vibratory loads and acoustic output created by the concentrated vortices trailed from helicopter rotor systems in forward flight has been an unattainable goal in the past. After more than four years of research, RASA has developed a technique whereby the concentrated trailed tip vortex can be eliminated efficiently without affecting the performance characteristics of the helicopter rotor. This paper will present the benefits that accrue as regards helicopter vibration and acoustic output by the elimination of the concentrated trailed tip vortices.

SYMBOLS

C-(i) — Primary coupled chordwise bending modes of the helicopter blade (i=first, second, etc.)

F-(i) — Primary coupled flapwise bending modes of the helicopter blade (i=first, second, etc.)

R — Radius of rotor blade (ft)

r — Radial distance to a given location on the rotor blade (ft)

T-(i) — Primary coupled control-blade torsion modes of the helicopter blade (i=first, second, etc.)

V — Forward speed of the helicopter (ft/sec)

v — Flapwise bending deflection normalized by generalized mass

w — Chordwise bending deflection normalized by generalized mass

$\mu = \dfrac{V}{\Omega R}$ — Advance Ratio

ϕ — Torsional deflection normalized by generalized mass

ψ — Azimuth angle in rotor disk, degrees

Ω — Rotational frequency of the helicopter rotor system (radians/sec)

ω — Frequency of a blade natural coupled mode (radians/sec)

INTRODUCTION

(U) Since the first successful flight of the helicopter, the "dynamic" characteristics of these vehicles have been well-known to those who have been either riding in the aircraft or to those striving to construct a successful rotor system or vibration-free structure. During the early years of the development of the helicopter, the important dynamic effects produced by the vortex wake had to be ignored in deference to the more urgent need to solve problems of stability, control, performance and structural integrity. Once these goals were achieved, however, then vibrations, a more reasonable structural life, and most recently, noise considerations led to the need to define the nature of the vortex wake.

(U) In order that helicopter blades could be properly designed in the past on the basis of these considerations, the aerodynamic loadings associated with the interaction of the blade with the nonuniform flow field arising from the trailed and shed vorticity had to be defined more precisely. The early theoretical attempts to predict the instantaneous induced-velocity field [1] and the oscillatory aerodynamic loading [2,3] of helicopter rotors represented significant advances in that era but these advances were hampered by the lack of application of suitable high-speed, high-capacity digital computers. In the early sixties, however, Miller [4] and DuWaldt and Piziali [5] undertook the problem with all its complexities and used high-speed, high-capacity digital computers to obtain marked improvement in the prediction of the periodic aerodynamic loads. The results of both of these investigations, while not showing ideal correlation with experimental data, did show a vast improvement over previous predictions.

(U) The prediction of the dynamic loads of helicopter rotor systems continues to receive a great deal of attention in the V/STOL industry. Considerable research effort has centered around the development of improved analysis procedures for predicting the dynamic air loads developed by helicopter rotor blades. A majority of these analyses are concerned with the flow field in the vicinity of the rotor system and the helicopter fuselage which is immersed in the rotor vortex wake. Current research in the development of computational programs in this area allow the position of the "free, distorted wake" to be predicted in the vicinity of the helicopter rotor and fuselage for single, tandem and coaxial rotor systems. This research has been and continues to be aimed at improving significantly the prediction of the aerodynamic and dynamic loads generated by the rotor blades while the aircraft is in either a steady-state or maneuver flight mode. References 6 and 7 present examples of the current state-of-the-art in the prediction of the aerodynamic environment in which a helicopter blade operates in forward flight. The benefits that have accrued to the V/STOL industry through the use of the more sophisticated methods of wake prediction are to be found in the increased efficiency, performance and reliability of rotor blades and their control systems that can now be designed.

(U) While these previously mentioned research programs have been associated with predicting the effects of the concentrated vortex, considerable effort has also been expended by the V/STOL industry in an attempt to understand the characteristics of the structure of the blade tip vortex and its interaction with a lifting surface because of its great influence on blade dynamic loads problems, and the generation of rotor impulsive noise. When impulsive noise ("blade slap") is obtained, it is the predominant source of noise of a helicopter rotor system. Its contribution to the noise signature of a helicopter is of particular importance in detection problems associated with military operations and in annoyance problems associated with civil operations. Blade slap may occur under various flight conditions and in particular it generally occurs during low-speed power descents due to blade-vortex interaction as the aircraft settles through its wake. Severe blade slap can also occur during a coordinated right or left-hand turn or during a pull-up when the rotor system is rotated into its own wake. Some of the approaches attempted by research engineers in the V/STOL industry and more recently, in the fixed-wing industry to modify the trailed concentrated tip vortex are categorized in Fig. 1, and Fig. 2 presents conceptual sketches of the various modifications of the lifting surfaces that have been attempted to test the validity of these diverse approaches.

(U) Some of the approaches are categorized as hopefully accomplishing more than one kind of modification. For example, porous tips are listed both as capable of spreading concentrated vorticity and also dissipating the strength of the vorticity. Lifting surface tip spoilers are listed in the same category. End plates are categorized as both spreading and relocating the concentrated vorticity. The effect of gulled outer panels [8] is to divide the total concentrated vorticity into two vortices, each of lesser strength, at two different spanwise locations, (one at the juncture of the gulled tip and main lifting surface and the other at the tip), and also to relocate the tip vortex with respect to a dimension normal to the wing chord plane because of the deflection of the tip of the gulled section.

(U) While the porous tip spreads the vorticity in the near wake [9], it also has the potential of dissipating the vortex because of the turbulence generated by the flow passing through the porous sections. As might have been expected, the dissipation obtained with the porous tips was not significant because of the small turbulence wavelength generated, and thus investigators

have found that the concentrated vortex reappeared downstream with its apparent strength unchanged. The wing tip spoilers, by which Chigier at NASA/Ames attempted to modify the tip vortex [10], seems to produce the same end result as the porous tip at a downstream location, again apparently because of the small turbulence wavelength that was generated.

(U) Spanwise blowing tried by Scheiman and others [11,12], seemed to have no effect other than to relocate the position of the trailed vortex.

(U) Investigations, to date, of the effect of jet engine location in the vicinity of the tip vortex have not been notably successful. Dr. John Olsen of Boeing [13] and the NASA investigators [14,15] who have tried this approach, placed the turbulent jet in the irrotational regimes of the vortex. Thus, its potential dissipative action was weakly coupled with that part of the vortex which contains the concentrated rotational energy, the vortex core.

(U) Based on the results of associated research being conducted by RASA in 1968, it was believed that the injection of an unstable aerodynamic mass flow into the core of a swirling tip vortex would significantly increase the viscous dissipation of that vortex. As indicated in Fig. 1, this vortex modification technique has the sole objective of dissipating the strength of the concentrated vorticity rapidly by the generation of a jet flow instability.

(U) After more than four years of research and a number of research programs [16-22] it has been shown by the RASA investigators that the strength of the concentrated tip vortex can be rapidly dissipated. Fig. 3 presented photographs of the visualized concentrated vortex with and without the mass injection system operating. These visualized flow pictures obtained by the use of neutrally-buoyant soap bubbles filled with helium, show how the concentrated tip vortex is rapidly dissipated and only a turbulent flow field is left. In the photographs, the centerline of the vortex is clearly depicted by the white line which is formed by the bubbles in rectilinear motion. The swirling motion of the vortex about its center is shown by the helical motion of the flow. Comparison of the visualized flow field before and after injection shows that the concentrated vortex is immediately affected while the overall flow field over the tip section is not changed significantly. Fig. 4 presents the results of

quantitative measurements made in the wake at a downstream position which corresponds to a time after vortex formation of 0.075 sec (6-1/2 chord lengths downstream at the tunnel speed of the tests). The results that are presented were obtained by measuring all the vorticity in the wake and then integrating the measured vorticity to obtain the circulation. The results presented in this figure show that the sonic injection nozzle is much more efficient in dissipating the strength of the tip vortex than the subsonic injection nozzle. Figure 5 presents typical performance results that were obtained for the lifting surface that generated the tip vortex as a function of injected mass flow using a subsonic injection nozzle. As can be seen from the results presented, the performance characteristics are not altered when the vortex is injected with the unstable jet.

(U) While the means of rapidly dissipating the energy of the concentrated tip vortex has been demonstrated and a somewhat optimal system has been developed during the previously noted research programs, the benefits that will be derived as regards dynamic loads and acoustic output of helicopter rotor systems have not as yet been demonstrated by tests of full-scale hardware with the injection system installed. In preparation for the full-scale tests which will be initiated in the near future, sophisticated theoretical analysis procedures were used to evaluate the benefits that would be derived by the elimination of the concentrated tip vortex trailed from the blade tips of helicopter rotor systems. Some of the results of these theoretical investigations are the subject of the present presentation.

TECHNICAL DISCUSSION

Analysis Procedures Used in Investigations

(U) In order to determine the location and strength of the trailed vortex field generated by a helicopter rotor system in forward flight, a theoretical analysis developed by RASA for NASA [6,7] was used to calculate the position and strength of the free vortex wake and the dynamic loads generated by the rotor blades operating in the aerodynamic environment created by this wake. The predicted results of this analysis have been correlated with experimental results obtained with full-scale helicopters and it has been demonstrated that the predicted and experimental results are in excellent agreement when the helicopter is in steady-state flight

131

condition and when it is a coordinated turn, pull-up or roll maneuver. The results of this theoretical analysis were used in conjunction with a theoretical acoustic prediction analysis [23,24] by which the acoustic pressure time history generated by a helicopter rotor can be predicted at various observer locations during hover or flyby. The accuracy of the predictions generated by this analysis procedure have been well established [24].

Helicopter and Flight Condition Analyzed

(U) The helicopter that was used to demonstrate the benefits of eliminating the vortex trailed by the tip of the blades of a helicopter rotor system was the first of the series of the Huey Helicopter, the UH-1. The flight condition that was analyzed was a 1.5g left-hand turn at an advance ratio of $\mu=0.24$ (forward flight velocity of 120 MPH). This flight condition was analyzed since it had been demonstrated experimentally that a strong blade vortex interaction occurred which created higher harmonic dynamic loads and blade slap. The coupled symmetric and antisymmetric dynamic modal shapes of the helicopter rotor that was analyzed are shown in Fig. 6.

Results of Calculations

a. Change in Aerodynamic Flow Field

(U) Fig. 7 presents a planview plot to the paths of the tip vortex trailed from each of the two blades of the UH-1 rotor. The plot has been made for the instant of time at which blade number 2 is intersecting the wake generated by blade number 1. The age of the wake generated by blade number 1 is approximately 0.15 seconds when blade number 2 intersects it, or approximately twice the age for which measurements have been made in the wind tunnel (Figs. 3 and 4). It can be seen from this plot that blade number 2 intersects the wake at approximately the same time over much of its radius and thus produces a very strong pressure and loading pulse. Fig. 8 clearly illustrates this somewhat simultaneous interaction of the vortex across the blade radius. As can be seen in Fig. 8, the induced velocity (the velocity generated at the blade by the wake) has a large perturbation centered around an azimuth angle ψ of 295 degrees along the majority of of the radius. The peak to peak variation of the induced velocity is about 40 ft/sec along the blade radius which is approximately twice the value of the

induced velocity anywhere else in the azimuth. It can thus be concluded that the induced effect on blade number 2 is indeed a very strong one.

(U) Fig. 9 presents a polar plot of lines of constant induced velocity in the plane of the rotor. While there is considerable variation of the induced velocity around the azimuth, the rapid change caused by the blade vortex interaction is obvious in the area noted. The associated polar plot of angle of attack is shown in Fig. 10. Since this rapid variation of induced velocity and angle of attack occurs over a very narrow range of azimuth, aerodynamic loadings in the higher harmonics of rotor speed are generated primarily which excite the higher rather than the lower dynamic modes of the helicopter blade. In addition, since the pressure pulse generated by the blade vortex interaction is of short duration the acoustic output caused by the blade vortex interaction is very high.

(U) Figs. 11 and 12 present the polar plots of induced velocity and angle of attack, respectively, after the tip vortex has been eliminated by jet mass injection. Comparison of these plots with their counterparts when the tip vortex is present (Figs. 9 and 10, respectively), will show that while there has been some change on the advancing side of the rotor disk, the very rapid change in the induced velocity and angle of attack on the retreating side caused by blade vortex interaction has been eliminated. It can also be noted that for a given radial station in the azimuth range from $\psi=270$ to $\psi=360$ degrees there is very little change in induced velocity or angle of attack.

b. Change in the Aerodynamic Loading

(U) When a helicopter is flying in steady-state flight, level or in a coordinated maneuver, it is assumed that all the load variations repeat periodically and therefore, it is convenient to analyze the loads in terms of the harmonics of the rotor speed. In order to properly analyze the harmonics of induced velocity and loads, the harmonic content of these parameters generated by motions of the helicopter control system and not the wake must be considered. For example, the collective blade pitch control is used to control the zeroth harmonic of thrust and thus the zeroth harmonic of induced velocity and loads are not associated primarily with the concentrated rotor wake. The one/per/rev cyclic pitch of the control systems tilts the rotor and helps to smooth out

the load variation caused by the variation of the free-stream velocity over the rotor when the helicopter is in forward flight. This velocity is given by

$$V_T = \Omega r + V \sin \psi$$

Since the dynamic pressure on a blade section is a function of the velocity squared, the cyclic pitch control will generate loading functions through the third harmonic of rotor speed. Therefore, harmonics of the induced velocity and loadings through the third are primarily controlled by the blade pitch control system, and the harmonics above the third are primarily a function of the concentrated tip vortices in the wake.

(U) The harmonics of the induced velocity on the rotor blade at V/R=0.87, with and without the tip vortex are presented in Fig. 13 and those for the aerodynamic loadings at that radius are shown in Fig. 14. It can be seen that while there is some variation in the induced velocity in the zeroth and first two harmonics, these aerodynamic loadings are not changed significantly as they are primarily controlled by the control system. It is noted that the induced velocity in the third harmonic generated by the tip vortex was almost completely eliminated when the tip vortex was destroyed but the third harmonic of loading was basically unaltered. This result points out that the third harmonic of loading is caused primarily by the cyclic control system and the varying velocity field and not the induced effect of the concentrated wake. Except for the sixth harmonic, all of the harmonics of both the induced velocity and loading are significantly reduced when the concentrated tip vortices are eliminated. Apparently the sixth harmonic of the induced velocity and loading is created by the vortex wake flow not associated with the concentrated tip vortices and thus when the induced effects of the tip vortices were removed their relieving induced effects were cancelled and the harmonic loading increased.

(U) While it might seem that the higher harmonic loadings are relatively small even when the tip vortices are present and thus the reduction achieved by the elimination of the tip vortex may not be of significance, it is noted that the higher harmonic loadings are the ones that determine the lift of the helicopter blade and thus the reductions achieved are very significant. This becomes more obvious when it is realized that the natural coupled modes of the

blade (Fig. 6) are all close to the harmonics of the loadings and thus when the excitation forces are significantly reduced, the dynamic response and associated stresses of these modes are also reduced significantly.

c. Change in Acoustic Signature

(U) The evaluation of the change in the acoustic output of the rotor system when blade slap is eliminated by the destruction of the tip vortices was conducted for a flyby of the helicopter when the highly directional "poping" noise was directed toward a fixed location of the observer. Fig. 15 shows the pressure time history of the acoustic signal received by the observer at this time. This acoustic signature not only has rotational noise generated by the blade lift and that caused by blade-vortex interaction but also has the noise generated by the broadband (nonharmonic) oscillatory forces on the blade. The spike caused by the blade vortex interaction is very apparent in this signature. Since the acoustic output of a blade-vortex interaction is associated with nonbroadband forces, the broadband force output was removed from the signature and the resulting signature plotted at the top of Fig. 16. The sharp acoustic spike generated by the interaction of the blade and the tip vortex is very apparent in this signature. The signature at the bottom of Fig. 16 is that generated by the helicopter blade when the concentrated tip vortices have been eliminated. The change in the acoustic signature is obvious.

(U) The spectrum of the total acoustic signature (with broadband nonharmonic oscillatory forces included) is presented in Fig. 17. Also shown is a curve of the threshold of hearing for the human ear in an ambient background environment. It can be seen that above about 20 cps the acoustic output is significantly above the threshold of hearing. The humping of the acoustic spectrum is caused by ground reflection effects since the observer ear is located five feet from the ground. The spectrum of just the rotational noise, with blade-vortex interaction, is presented in Fig. 18. In comparing the spectrums presented in Figs. 17 and 18, it can be seen that in the frequency range 0 to 200 cps there is little difference in the spectrums, from 200 to 600 cps the broadband noise contributes about 5 db and in the frequency range of 500 to 1000 cps the broadband noise contributes about 10 db. The acoustic signature of the rotor rotational noise

when the tip vortices have been eliminated is shown in Fig. 19. Comparing the spectrums presented in Figs. 18 and 19, it can be seen that there is a significant change in the acoustic output with the elimination of the blade vortex interaction, particularly in the frequency range of 50 to 400 cps. It is the frequencies in this range that propagate for large distances and thus are the most significant as regards detectability. In order to further demonstrate the significance of the reduction achieved, it is noted that if there are two independent sound sources and one is approximately 10 db higher than the other, then the weaker sound source is not heard. Thus the 10 to 15 db reduction in acoustic output that was achieved can be concluded to be very significant.

CONCLUDING REMARKS

(U) The effect of eliminating the concentrated tip vortices from a helicopter rotor system has been shown to be very beneficial as regards the reduction in the dynamic loads that determine the life of helicopter blades and in the reduction of the acoustic output of "blade slap" which dominates the helicopter rotor noise when it occurs. While the present paper was based on theoretical analyses using techniques that have been well refined, it is expected that the noted benefits will be realized when the vortex injection system is installed and tested on a full-scale rotor system in the near future.

REFERENCES

1. K. W. Mangler, "Calculation of the Induced Velocity Field of a Rotor," RAE Report No. Aero 2247, 1948.

2. M.A.P. Willmer, "The Loading of Helicopter Rotor Blades in Forward Flight," RAE Report Naval 2-N-76935, No. 8, 1959.

3. W. Castles, and W. L. Durham, "The Computed Instantaneous Velocities Induced at the Blade Axes by the Skewed Helical Vortices in the Wake of a Lifting Rotor in Forward Flight," ASTIA Document No. AD-210613, 1959.

4. R. H. Miller, "Unsteady Airloads on Helicopter Rotor Blades," The Royal Aeronautical Society Fourth Cierva Memorial Lecture, October 1963.

5. R. A. Piziali, and F. A. DuWaldt, "Computation of Rotary Wing Harmonic Airloads and Comparison With Experimental Results," Presented at AHS Eighteenth Annual National Forum, Washington, D.C., May 1962.

6. S. Gene Sadler, "Development and Application of a Method for Predicting Rotor Free Wake Positions and Resulting Rotor Blade Airloads," NASA CR 1911, 1971.

7. S. Gene Sadler, "Main Rotor Free Wake Geometry Effects on Blade Airloads and Response for Helicopters in Steady Maneuvers, Volume I - Theoretical Formulation and Analysis of Results," Rochester Applied Science Associates, Inc., RASA Report 71-13, NASA Contract NAS1-8448, NASA CR 2110, September 1972.

8. Raghuveera Padakannaya, "Effect of Wing Tip Configuration on the Strength and Position of a Rolled-up Vortex," A Thesis in Aerospace Engineering, NASA CR 66916, March, 1970.

9. R. H. Spencer, H. Sternfeld, and B. W. McCormick, "Tip Vortex Core Thickening for Application to Helicopter Rotor Noise Reduction," U. S. Army Aviation Material Labs., R-403-A, September 1966.

10. N. A. Chigier and V. R. Corsiglia, "Tip Vortices - Velocity Distributions," Paper presented at the 27th Annual National Forum of the American Helicopter Society, Preprint No. 522, May 19-21, 1971, Washington, D.C.

11. James Scheiman and James P. Shivers, "Exploratory Investigation of the Structure of the Tip Vortex of a Semispan Wing for Several Wing-Tip Modifications," NASA/Langley Research Center, NASA TN D-6101, February 1971.

12. J. J. Cornish, III., "High-Lift Applications of Spanwise Blowing," Paper presented at the Seventh Congress of the International Council of the Aeronautical Sciences, Consiglio Nazionale Delle Ricerche, Roma, Italy, ICAS Paper No. 70-09, September 14-18, 1970.

13. John Olsen, "Aircraft Configuration Effects on Wake Turbulence," Paper presented at FAA Symposium on Turbulence, March 22, 23, 24, 1971 in Washington, D.C.

14. James C. Patterson, Jr., and Stuart G. Flechner, "An Exploratory Wind-Tunnel Investigation of the Wake Effect of a Panel Tip-Mounted Fan-Jet Engine on the Lift-Induced Vortex," NASA TN D-5729, May 1970.

15. William A. McGowan, "NASA Aircraft Trailing Vortex Research," Presented at the Federal Aviation Administration Symposium on Turbulence, March 22-24, 1971, Washington, D.C.

16. Stephen A. Rinehart, "Study of Modification of Rotor Tip Vortex by Aerodynamic Means," Rochester Applied Science Associates, Inc., RASA Report 70-02, ONR Contract No. N00014-59-C-0169, January 1970, AD 704804.

17. Stephen A. Rinehart, John C. Balcerak and Richard P. White, Jr., "An Experimental Study of Tip Vortex Modification by Mass Flow Injection," Rochester Applied Science Associates, Inc., RASA Report 71-01, ONR Contract N00014-69-C-0169, January 1971, AD 726736.

18. Richard P. White, Jr. and John C. Balcerak, "An Investigation of the Mixing of Linear and Swirling Flows," Rochester Applied Science Associates, Inc., RASA Report 72-04, ONR Contract N00014-71-C-0226, February 1972.

19. Richard P. White, Jr. and John C. Balcerak, "Investigation of the Dissipation of the Tip Vortex of a Rotor Blade by Mass Injection," Rochester Applied Science Associates, Inc., RASA Report 72-03, USAAMRDL Technical Report 72-43, August 1972.

20. Rochester Applied Science Associates, Inc., "Investigation of the Transonic Effects of Mass Injection to Restructure a Trailing Tip Vortex," Department of the Navy, Office of Naval Research, Contract No. N00014-71-C-0226, March 1972-March 1973.

21. Rochester Applied Science Associates, Inc., "Elimination of the Trailed Tip Vortex From a Helicopter Rotor Blade," NASA/Langley Research Center, Hampton, Virginia, Contract NAS1-11409, March 1971-May 1973.

22. Rochester Applied Science Associates, Inc., "Wind Tunnel Tests to Reduce Tip Vortex Strength," USAAMRDL Contract No. DAAJ02-72-C-0097, June 1972-March 1973.

23. H. Kevin Johnson and Walter M. Katz, "Investigation of the Vortex Noise Produced by a Helicopter Rotor," USAAMRDL Technical Report 72-2, February 1972.

24. H. Kevin Johnson, "Helicopter Noise Prediction Program," Rochester Applied Science Associates, Inc., RASA Report 72-08, USAAMRDL Contract No. DAAJ02-71-C-0064, to be published, 1973.

I. Spreading of Concentrated Vorticity
   A. End plates
   B. Gulled outer panels
   C. Tip planform variations
   D. Porous Tips
   E. Lifting surface tip spoilers
   F. Spanwise or angled blowing

II. Dissipation of the Concentrated Vorticity
   A. Porous tips (small-scale turbulence)
   B. Lifting surface tip spoilers (small-scale turbulence)
   C. Jet engine exhaust in the vicinity of the wing tip
   D. Reverse swirl
   E. Linear turbulent mass injection developed by RASA

III. Relocation of the Concentrated Vorticity
   A. End plates
   B. Gulled outer panels
   C. Spanwise or angled blowing

Figure 1.   Categorization of Basic Approaches
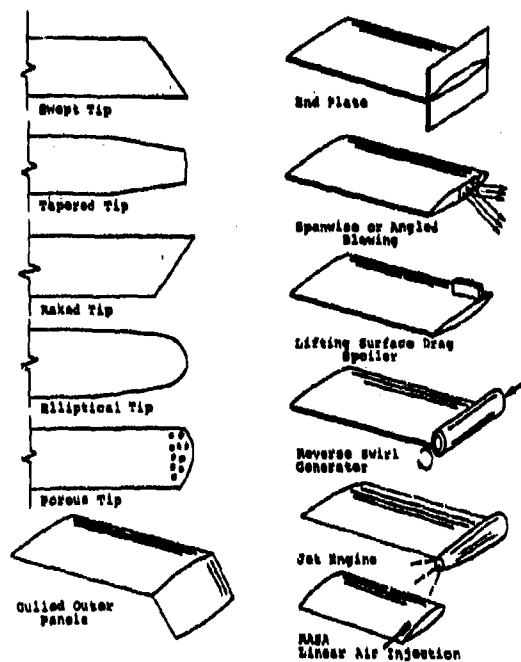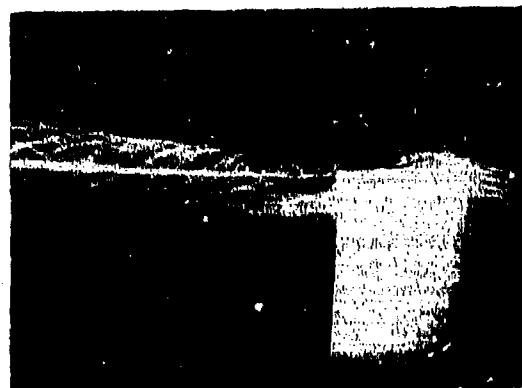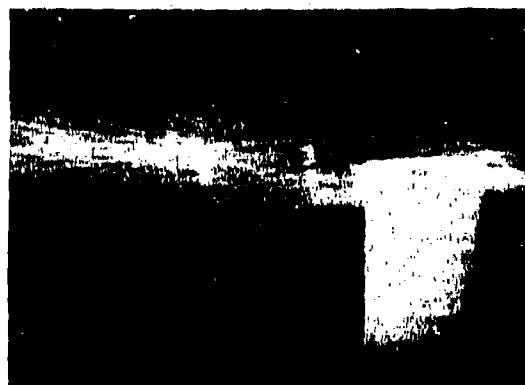
Figure 2. Wing Tip Configurations for
Distributing, Dissipating or
Relocating Tip Vortices

Without Mass Injection

With Mass Injection

Figure 3. Influence of Mass Injection
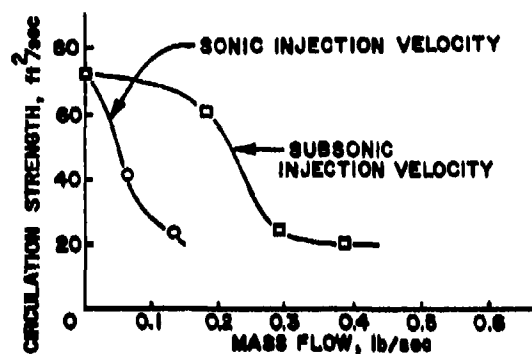on the Flow Field Behind a
Rotor Blade Tip
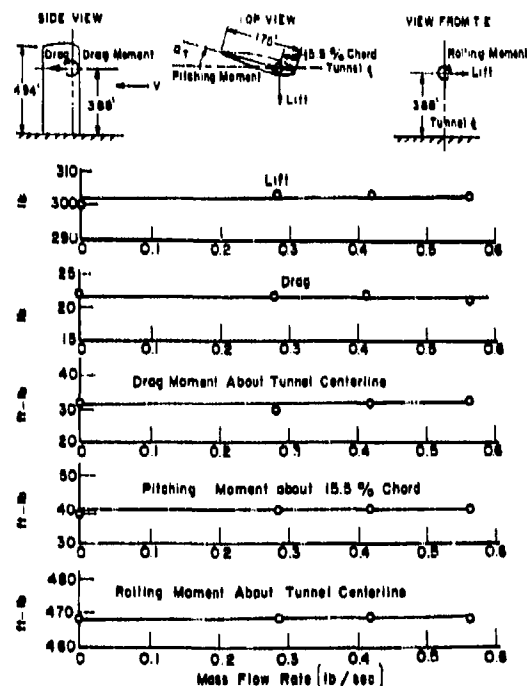
Figure 4. Circulation Vs. Mass Flow

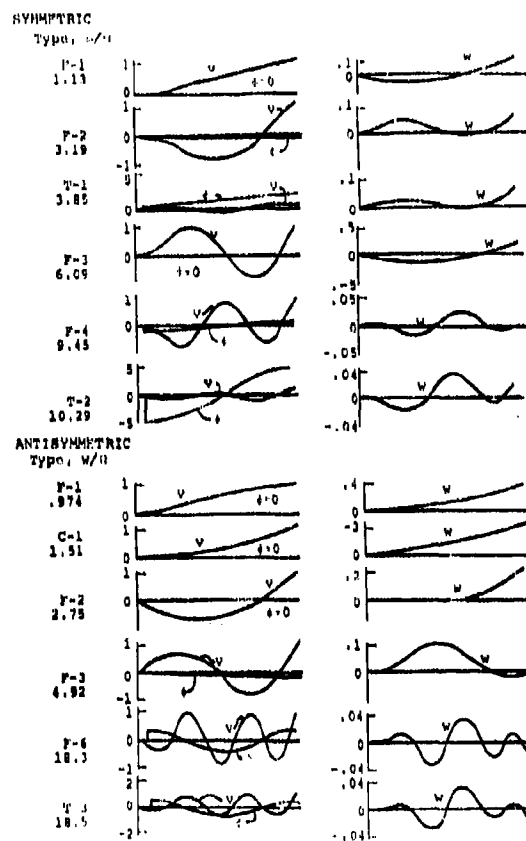Figure 5. Net Balance Measurements Versus Mass Flow Rate, V=225 ft/sec, α_T=9.5°

Figure 6. UH-1 Coupled Mode Shapes and Frequencies; v and w Normalized by m/(m v_{tip}), ϕ in rad/(m v_{tip}), Ω=32.88
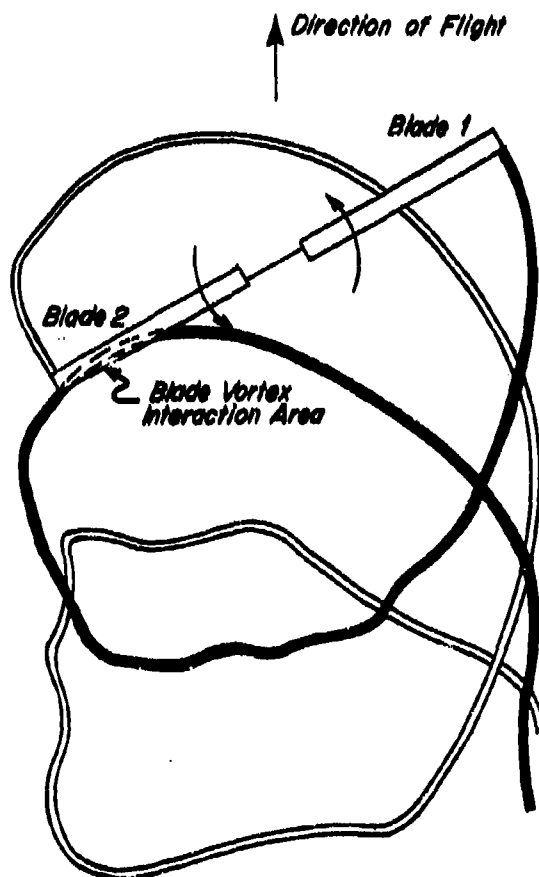
Figure 7. Planview of Deformed UH-1
Wake For a 1.5g Left-hand
Turn, μ=0.24
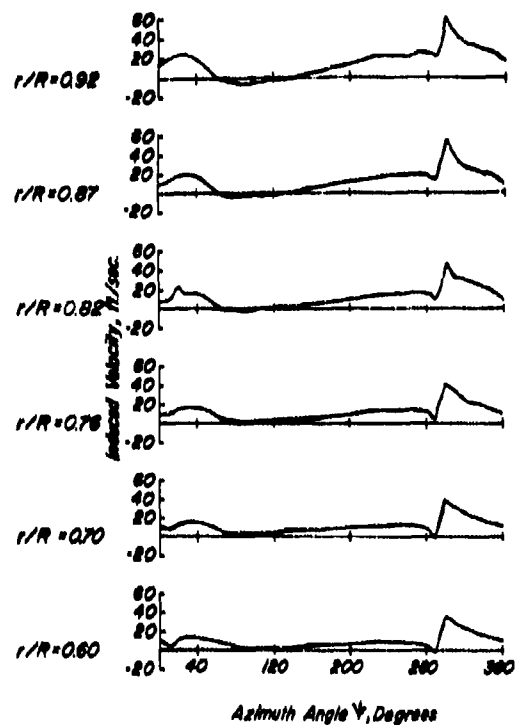
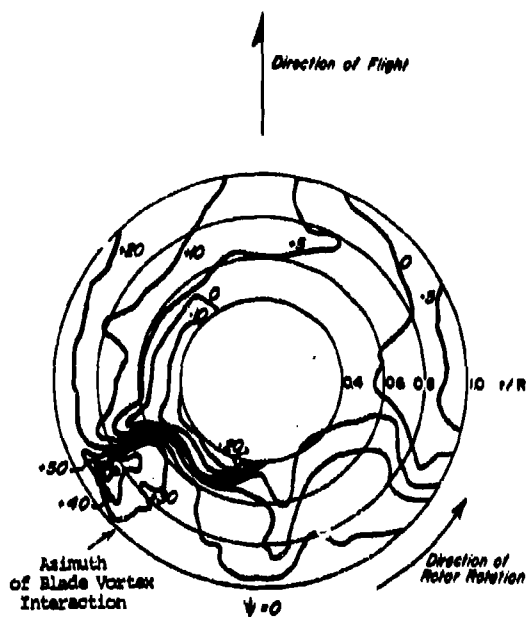Figure 8. Induced Velocity Vs. Azimuth
Angle UH-1, 1.5g Left-hand
Turn

138

Figure 9. Polar Plot of Induced
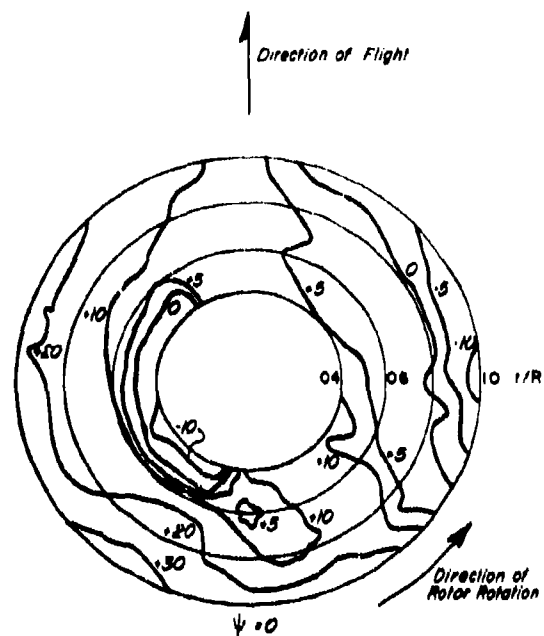Velocity With Blade Vortex
Interaction

Figure 11. Polar Plot of Induced
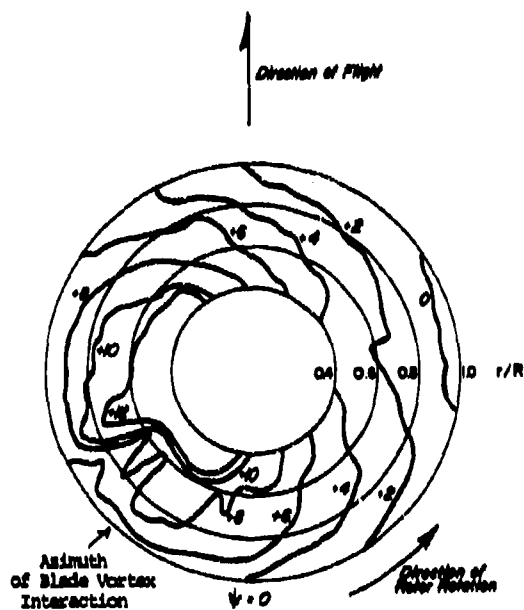Velocity With Concentrated
Tip Vortex Eliminated

Figure 10. Polar Plot of Aerodynamic
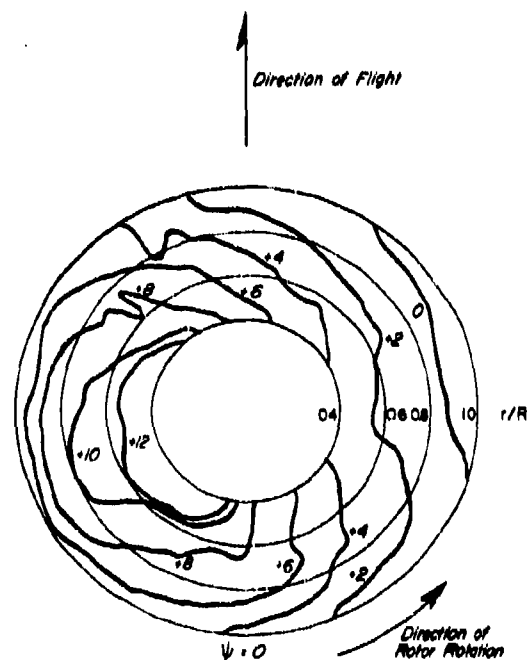Angle of Attack With Blade
Vortex Interaction

Figure 12. Polar Plot of Aerodynamic
Angle of Attack With
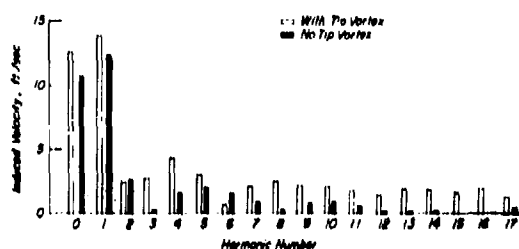Concentrated Tip Vortex
Eliminated

139

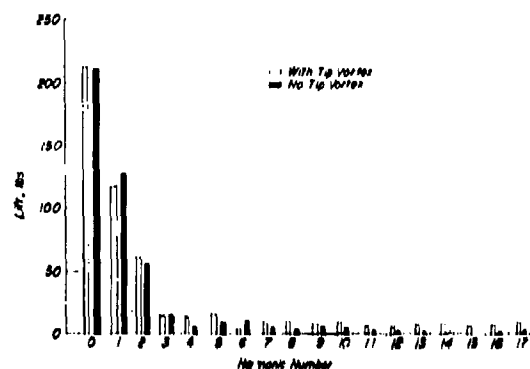Figure 13. Harmonics of Induced
Velocity for UH-1, r/R=0.87

Figure 14. Harmonics of Section Lift
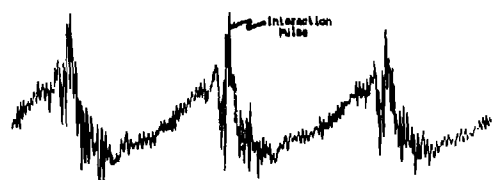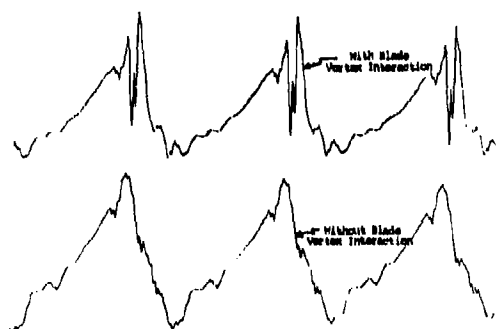for UH-1, r/R=0.87

Figure 15.

Figure 16. Acoustic Pressure Time
History of UH-1 Helicopter
in 1.5g Left-hand Turn
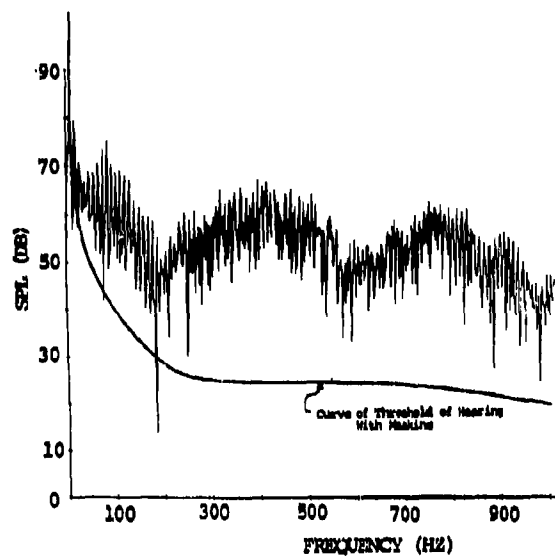

Figure 17. Spectrum of Total Acoustic
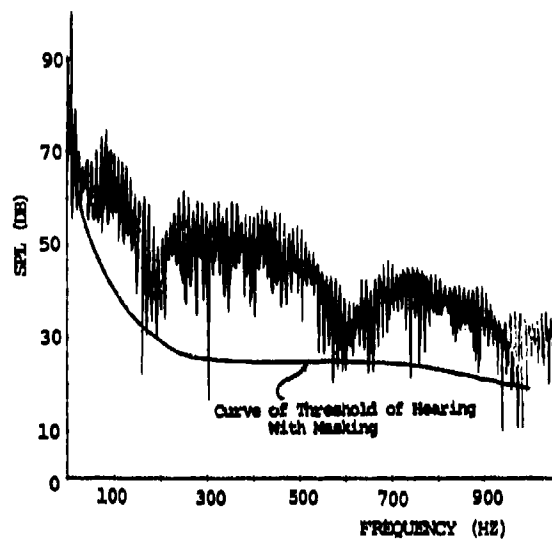Signature With Blade Vortex
Interaction

140

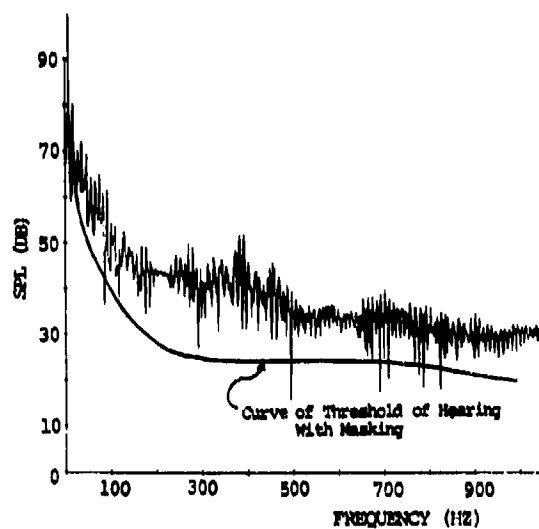Figure 18. Spectrum of Rotational Noise
With Blade Vortex Interaction

Figure 19. Spectrum of Rotational Noise
With Tip Vortex Eliminated

141

MATHEMATICAL MODEL OF A TYPICAL FLOATING SHOCK PLATFORM
SUBJECTED TO UNDERWATER EXPLOSIONS

R. P. Brooks, and B. C. McNaight
Naval Air Engineering Center
Philadelphia, Pa.

A lumped parameter, finite difference method in common usage at the
Naval Air Engineering Center has been utilized to model a typical
floating shock platform and its dynamic response to underwater
explosions.

The method is a non-iterative time domain approach especially
adaptive to the treatment of non-linear systems. The use of a non-
matrix serial integration technique provides substantial gains in
computer time and memory requirements, and thus permits analysis
of systems which contain a large number of degrees-of-freedom.

The three-dimensional model is divided into four parts: (1) the
floating shock platform, (2) the shock fixture for decking simulation,
(3) the test specimen, a tied-down A4C aircraft, (4) an underwater
blast input. The analytic results of the model are compared to
actual test records.

INTRODUCTION

Ordinary and partial differential equations
which describe structural dynamic problems
have been solved numerically for some time by
the use of digital computers. Matrix methods
and finite difference techniques have become
standard in the repertoire of the dynamicist.
However, the treatment of structural disconti-
nuity phenomena (such as clearances), non-
linearities, resonance, damping, wave travel
and reflections, has proven difficult with these
methods. An accepted practice is to totally
"linearize" the structure to be analyzed and
design the mathematical model for projected
"worst case" conditions.

The lumped parameter, finite difference
technique refined by the Naval Air Engineering
Center has been directed toward the understand-
ing, and incorporation of these physical phe-
nomena. This non-matrix method has evolved
as a deterministic procedure that minimizes
mathematical and computing restraints, and
permits analysis of systems which are imprac-
tical to solve by other methods because of a
prohibitive number of degrees-of-freedom

required for definition and non-linear complex-
ities. The basic scheme uses time domain
definitions.

The method has been applied at NAEC to a
wide range of problems; i. e. beams, cable
dynamics, hydraulics, and heat transfer. To
establish validity, each physical problem
modeled was compared with classic solutions
and actual end results where possible. Excel-
lent agreement was obtained in each study. It
was shown that continuous mass systems could
be discretely modeled to achieve practically
any degree of accuracy desired. Samples of
these efforts are documented in Refs. [1], and
[2]. In these specific cases, the method utilizes
the ability of the high speed digital computer to
perform routine iterative calculations on the
finite elements of which all complex structures
are made. All that is required of the analyst
is to model the system as a set of finite mass
elements connected by springs and dampers.
Thus, these finite elements are dynamically
coupled such that the response of all these ele-
ments is equivalent to the response of the total
system under consideration.

This paper outlines in detail how the method was employed in the mathematical modeling of a complex three-dimensional structure subjected to a severe dynamic shock environment. The interpretation, definition and modeling of a typical floating shock platform, an A4C aircraft test specimen, and a complex shock wave/gas globe loading function is derived step by step to the final model. The resulting computer program is then discussed, and the analytic results and correlation presented.

In order to demonstrate the capability of the method in treating such a complex structure as the floating shock platform, a particular test series was modeled. This was a modified MIL-S-901C test of a tied-down A4C aircraft conducted at the San Francisco Bay Naval Shipyard, (SFBNSY) Hunters Point, California, in April of 1969.

During the course of the project several literature searches were made through the Defense Documentation Center to research the field of underwater explosions. Although many reports were ordered and carefully studied, Cole's "Underwater Explosions" was used as the primary source of phenomena definition.

METHODOLOGY

The lumped parameter, finite difference method applied to the solution of the floating shock platform (FSP), is essentially an application of the same method rigorously developed in Refs. [1 and 2]. However, a short review of the method, abstracted from these reports, with the addition of the specialized FSP requirements, is in order.

Finite difference methods, like many numeric techniques used today for the solution of structural dynamics problems, are not new. Most of these techniques and their properties were derived, documented, and published, literally centuries ago. Leonhard Euler (1707-1783) that prolific mathematician and physicist, with his polygonal curve methods, was probably the first to apply the concept of finite differences to the solution of differential equations. With the advent of the modern digital computer, these methods have been revived, refined and become standard tools for the analyst.

The method of finite differences is most commonly used in solving the governing partial differential equations of boundary value problems. With this method the partial differential equations are replaced by approximating difference equations, and the continuous region in which the solution is desired, is replaced by a set of discrete points. By this approach the

overall problem is reduced to a finite set of algebraic equations, although a large number of unknowns may be involved. The power of the digital computer to then perform the necessary repetitive calculations at high speeds becomes the answer to modern structural dynamic analysis.

As a direct applicative example, Timoshenko's theory of beam bending supplies the following basic equations:

$$M - EI \frac{\partial \theta}{\partial x} = 0, \tag{1A}$$

$$F - A s G \left(\frac{\partial y}{\partial x} - \theta \right) = 0 \tag{1B}$$

$$\frac{\partial M}{\partial x} - F + \rho I \frac{\partial^2 \theta}{\partial t^2} = 0, \tag{1C}$$

$$\frac{\partial F}{\partial x} - \rho A \frac{\partial^2 y}{\partial t^2} = 0, \tag{1D}$$

The first two equations relate loading to movement. Equation (1A) expresses the relationship between internal bending moment (M) and relative cross-sectional rotation ($\partial \theta / \partial x$). Equation (1B) stipulates the relationship between the vertical shear force on a beam cross-section (F), and the shear angle ($\partial y / \partial x - \theta$).

The latter two equations relate accelerations to loading. Equation (1C) defines the effect of rotary inertia ($\rho I \partial^2 \theta / \partial t^2$) developed by considering rotational motion of beam elements during vibration. Equation (1D) considers translation motion of the beam elements.

From consideration of Fig. (1), the finite difference form of the equation set is

$$M_i = \frac{EI}{X} (\Delta \theta_i - \Delta \theta_{i+1}), \tag{1A}$$

$$F_i = \frac{A s G}{X} \left\{ (\Delta Y_{i+1} - \Delta Y_i) - \Delta x \left[\frac{\Delta \theta_{i+1} + \Delta \theta_i}{2} \right] \right\}, \tag{1B}$$

$$\ddot{\theta} = \left\{ -\Delta x \left(\frac{F_{i-1} + F_i}{2} \right) + M_{i-1} - M_i \right\} \Big/ \Delta x \rho I, \tag{1C}$$

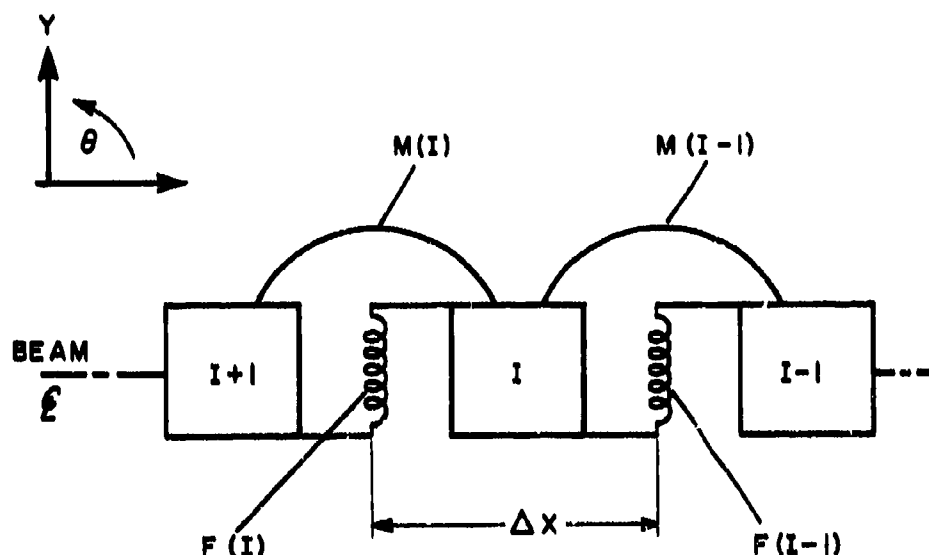$$\ddot{Y} = (F_i - F_{i+1}) \Big/ \rho A \Delta x$$

Fig. 1 - Spring-mass model for Timoshenko Beam Equations

Equations (1A) and (1B) now form the static set, and equations (1C) and (1D) the dynamic set. The integration scheme which is applied to each mass in the model, in readily programable form is:

$$
\begin{array}{ll}
\text{Dynamic} \\
\text{equation} \\
\text{loop}
\end{array}
\left[
\begin{array}{ll}
\text{ACC}_i & = \dfrac{\text{(forces or moments)}}{\text{(mass or inertia)}} \\[2mm]
\text{VEL}_i & = \text{VEL}_i + \text{ACC}_i\,(\Delta t) \\[2mm]
\Delta\text{DISP}_i & = \text{VEL}_i\,(\Delta t)
\end{array}
\right.
$$

$$
\begin{array}{ll}
\text{Static} \\
\text{equation} \\
\text{loop}
\end{array}
\left[
\begin{array}{ll}
\Delta\text{LOAD}_i & = K\,(\Delta\text{DISP}_i - \Delta\text{DISP}_{i-1}) \\[2mm]
\text{LOAD}_i & = \text{LOAD}_i + \Delta\text{LOAD}_i
\end{array}
\right.
$$

The dynamic and static program loops are typical of the sets for each degree-of-freedom considered in a model. If all six degrees-of-freedom are included, then; six accelerations, three translational and three rotational, are calculated. This is done by a simple summation of forces or moments, divided by the mass or mass moment of inertia, of the particular mass point under consideration. These accelerations are then integrated to incremental changes in translational or rotational velocity by the product of acceleration and Δ t. The new velocity for this increment becomes the sum of the old velocity and the incremental change. The resulting new velocity is then integrated to incremental displacement by the by the product of velocity and Δ t.

After the dynamic equation loop has been repeated for each mass in the model, the method proceeds to the static equation loop. For six degrees-of-freedom the static set will contain twelve equations, corresponding to twelve loads; six moments and six forces. Each incremental load is calculated based on incremental displacements of adjoining masses and the spring stiffness between them. The change in load is then added to the load that existed at the end of the preceeding time increment, and the new load is obtained. Again, the equation set is repeated for each mass in the model. At the conclusion of the static equation loop all the calculations for the time increment are completed. Time is then updated and the process repeated, until the desired simulation time, or other criteria is reached.

With this method of integration it is not necessary to iterate within the time increment. This is because the load and motion equations are coupled and compensate for each other as the problem solution proceeds from time increment to time increment.

The method by itself is an entity in the respect that its application involves a continuous region. But because the method may be

145

readily inserted into a master logic flow, and phenomena observed during each time increment, the ability to handle structural complexities is practically unlimited. For example, whenever a discontinuity, such as a gap, or interaction with other structure due to physical excursion, is encountered at a certain time or condition, the logic can be corrected, or redirected to include the new phenomena. And to delete it when it is no longer present. Also, any type of spring may be easily incorporated on a time increment basis, providing its governing function is known.

It is these options and the serial integration scheme undertaken in the incremental time analysis, probably more than anything else, that make this method invaluable for the dynamic analysis of complex structures.

THE FLOATING SHOCK PLATFORM MODEL

The floating shock platform (FSP) was designed to realistically test heavyweight shipboard equipment which has exceeded the capabilities of the standard Navy shock machines. [Ref. 5]

The equipment to be tested is subjected to a standard series of underwater explosions varying from light to severe intensity. After each attack the platform is boarded and a damage inspection made of the test specimen.

The basic structure of the platform is the type of double-bottom construction common to a surface ship hull. (Fig. 2) However, because of the allowable freedom in the design of the support structure and mountings for the equipment to be tested, it is possible to simulate a wide range of ship locations. Shock intensity is controlled by the size of the explosive charge and standoff distance from the platform. (Fig. 3). A protective canopy is used during most FSP tests to protect the equipment from the weather and explosion produced plume spray. (Fig. 2).

The idealization of the platform as a spring-mass system presented no especially difficult problems. Because of the flat, double bottom construction, the basic platform could be considered as a series of parallel I-beams or a series of parallel box beams joined along their length. (Fig. 4). The I-beam analogy
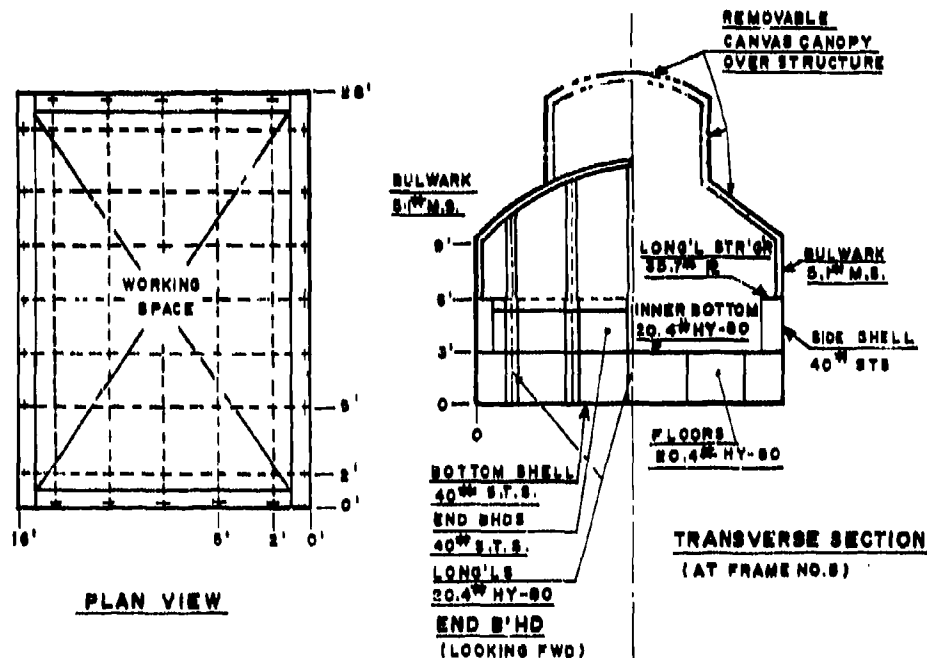

PLAN VIEW

TRANSVERSE SECTION
(AT FRAME NO.5)

Fig. 2 - Floating shock test platform
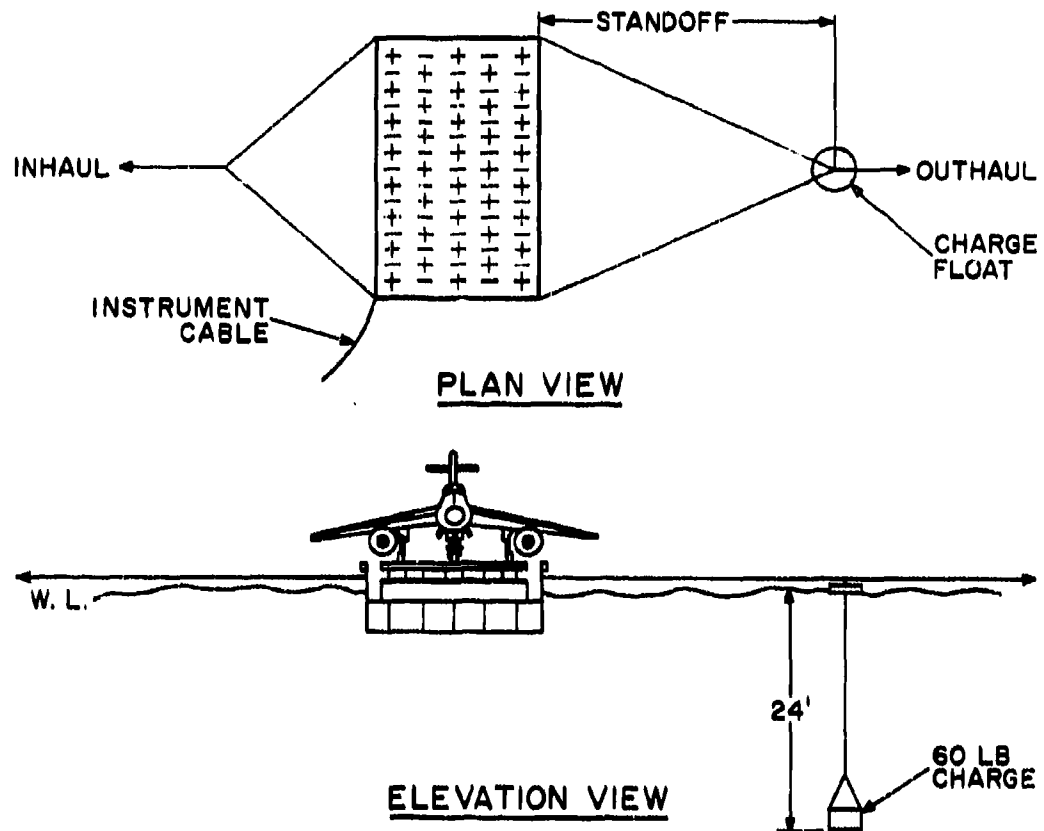
146

PLAN VIEW

ELEVATION VIEW

Fig. 3 - Floating shock platform test geometry

was decided upon because its definition provided mass points on the webs of the beams. The standard properties of the I-beams determined by this philosophy were then calculated for the model, with the exception of the torsional rigidity. For this value the torsional rigidity of the box beam was used to more accurately define the inherent stiffness of the platform. The athwartships members were represented by considering the local increases in mass and stiffness of the beams. Accordingly, five parallel beams were defined for the FSP model; three identical central beams, and two reversed identical end beams.

The finite difference beam equations refered to in Ref. [2] were expanded for the platform model to include shear and moment in two perpendicular directions, torsion, tension and compression, and the effect due to shear center offset. These expansions resulted in governing beam equations with six degrees-of-freedom. Fig. 5 shows a spring-mass diagram of a

typical FSP mass. The double subscripts K, I, refer to beam number (K), and beam mass (I). There are three compression/tension springs and three rotational springs between each pair of masses, although for ease of viewing they are not duplicated.

The coupling of the parallel I-beams along the top and bottom flanges required the mutual transmission of three moments and three forces between corresponding beam masses. A more detailed explanation of the finite difference equation set used for the basic FSP model is given in the appendix.

The dx or axial spacing of the masses along the beams was determined by two considerations. First, the number of masses necessary to accurately depict the possible beam motions. And second, the provision of dynamic loading points which are formed by the perpendicular projections of the mass points to the outside edges of the platform
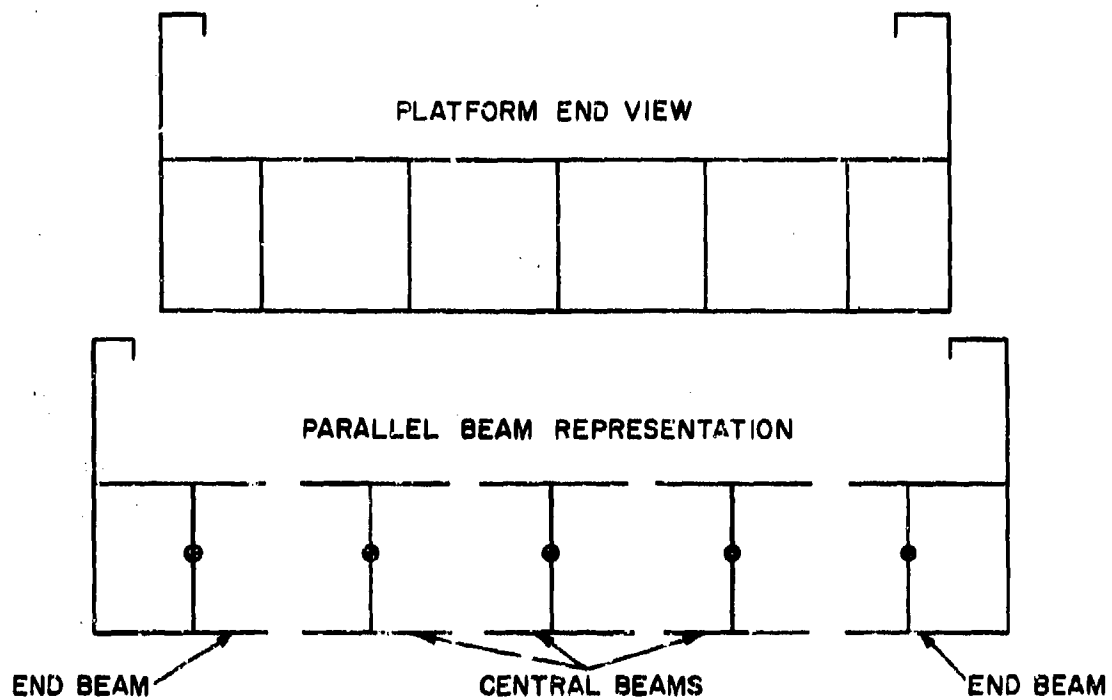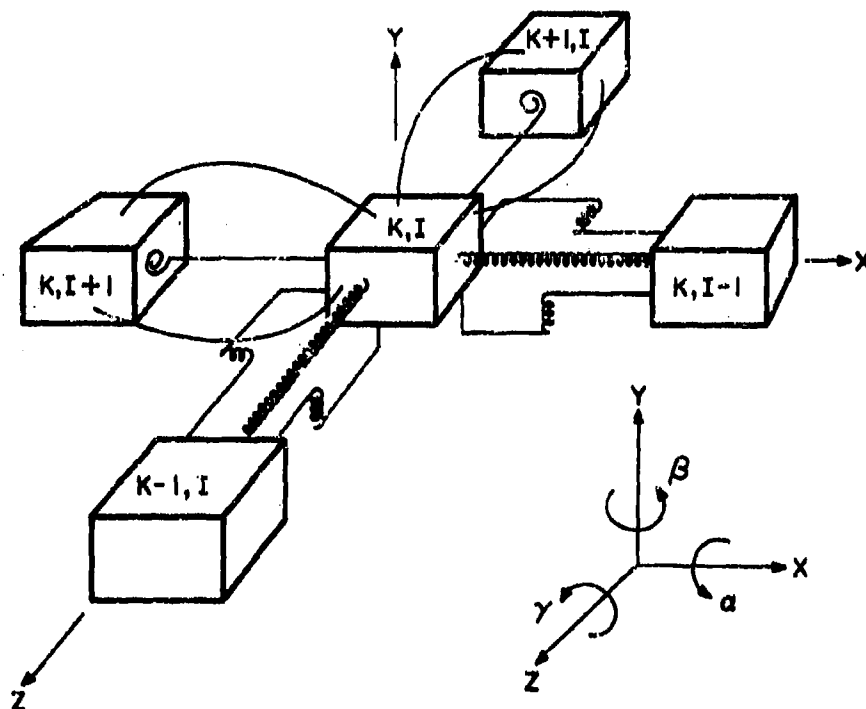
147

Fig. 4 - Floating shock platform model

Fig. 5 - Spring - mass model of a typical (K, I) mass point

148

bottom and side hull plating. Thirty masses per beam, 11.5 inches apart, was the final spacing chosen for the model.

A total of 150 mass points (5 beams with 30 masses per beam) is then arrived at for the basic FSP model. With six degrees-of-freedom per mass, a 900 degree-of-freedom system is described.

When the A4C FSP test series was conducted at SFBNSY the protective canopy was not used because of the protruding wing span (the A4C, unlike other naval aircraft, has no wing folds). And of course, the A4C test simulations computed for this analysis do not include the canopy and its effects. Although, to provide for the simulation of tests which would employ the canopy, a simplified canopy model was constructed to supplement the FSP model. For this model, 66 masses were distributed about the perimeter of the FSP. These masses were connected to the side and end bulwarks with bi-linear springs to represent the difference between the tensile and compressive forces exerted on the platform.

The selection of the number and configuration of elements to define any given system is determined by many considerations. Two of the more important factors are accuracy definition and required frequency. Detailed discussions of these considerations are presented in Ref. [2], which demonstrates that perturbation transmittal and reflection time are controlled by both the spacing and the number of elements. The total number of elements and configuration selected for the FSP application was arrived at (for initial modeling) by consideration of the above factors. The good correlation achieved with the raw test results available indicated that the chosen element configuration was adequate.

THE SHOCK FIXTURE MODEL

If a piece of equipment is to be tested in the floating shock platform which has a normal shipboard location other than the inner bottom level, a special mounting fixture is employed to simulate the intervening structure and its shock attenuation characteristics.

During the A4C aircraft shock test series a shock fixture designed for the FSP testing of flight and hangar deck equipment was used (Fig. 6). In general the fixture may be classified as four parallel beams joined along their lengths at the top flanges and mounted on simple end supports.

The modeling scheme used for the shock fixture was essentially the same as that for the floating shock platform (Fig. 6). The fixture was divided into four parallel I-beams joined along their entire length at the top flange only. A $d x$ axial mass spacing, of 12 in. was decided upon for the shock fixture beams, yielding a total of 20 masses per beam. Basically the same beam coupling equations that were used for the platform were also used for the shock fixture. Slight variances are realized due to the differences in cross-sectional geometry between the platform and shock fixture beams. As in the platform model, the entire six degrees-of-freedom are allowed for all beam masses in the fixture.

For the end supports of the fixture beams, only vertical degrees-of-freedom were included in the model. A stress analysis of the supports to determine spring rates had shown the contribution of the other components to be negligible. The additional mass of the supports was added to the platform connection masses.

THE AIRCRAFT MODEL

The A4C aircraft which was shock tested on the FSP, was a full scale, flyable aircraft. It was secured to the shock fixture deck with a normal weather tie-down configuration, representative of standard flight and hangar deck stowage (Fig. 7). The fuel tanks were filled to bring the gross weight of the aircraft to approximately 18,000 lbs. and the landing gear and tires were serviced for carrier flight operation [Ref. 3].

The objectives of the test series performed were "To evaluate the effects on aircraft tie-downs due to underwater shock, and also the interaction effects between tied down aircraft and simulated carrier (CVA) decks".

Because the resultant loads and motions of the aircraft model would become the main basis for comparison with the physical FSP test records, a great deal of effort was put into the small but sophisticated aircraft model. The shock test reports, detailed drawings of the test arrangements, and high speed motion picture films of the tests, were all carefully studied.

Although the aircraft model was derived for a specific aircraft and test series, it is completely general in nature. Floating shock platform tests of any naval aircraft may be simulated by simple changes of the required input data.

149

EQUIPMENT TEST DECK

END SUPPORT

BASIC FSP DECK

SHOCK FIXTURE SIDE VIEW

BASIC FSP DECK

SHOCK FIXTURE CENTER END VIEW

END BEAM   CENTRAL BEAM   END BEAM

END   SUPPORT   SPRINGS

BASIC FSP DECK
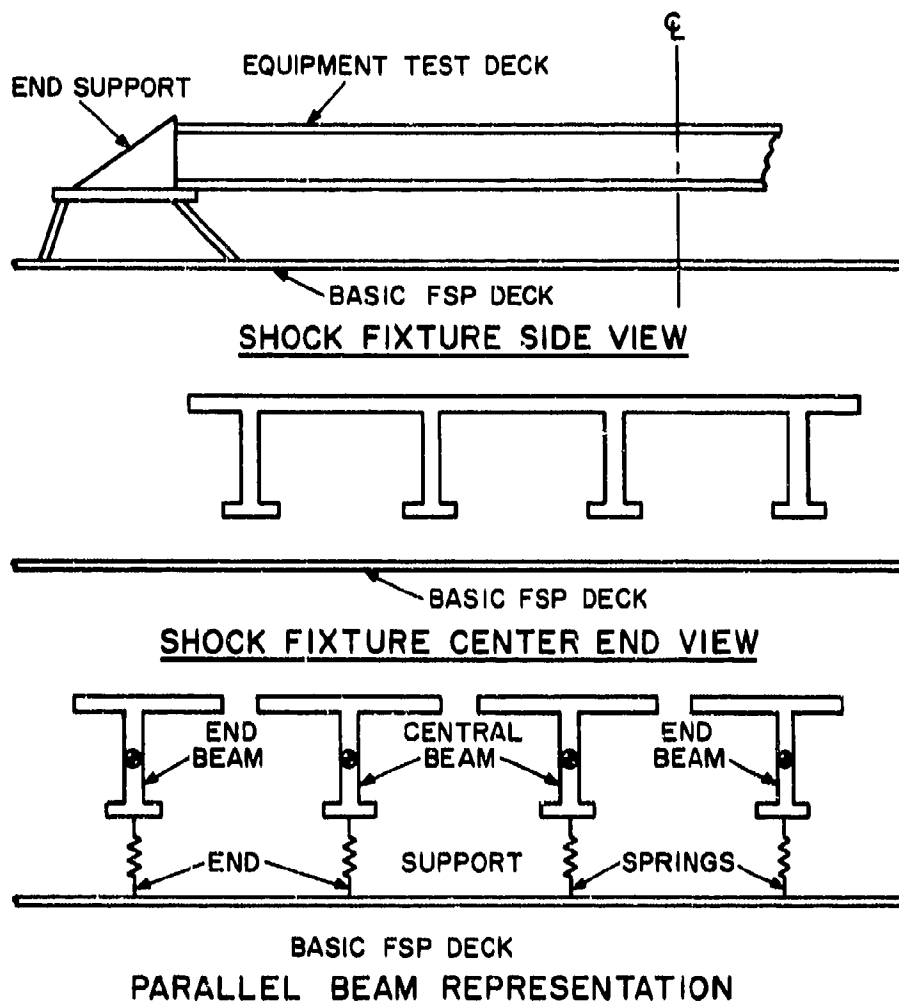
PARALLEL BEAM REPRESENTATION

Fig. 6 - Shock fixture model

Four masses were used to model the aircraft. Each landing gear of the aircraft was modeled as one mass, and a fourth was located at the center of gravity. Only vertical degrees-of-freedom were assigned to the gear masses, while the C.G. mass has vertical, pitch, and roll degrees-of-freedom.

The aircraft tires were modeled as non-linear springs by incorporation of available load versus stroke curves. Tire damping was generated by the product of a variable tire damping coefficient and the square of the wheel vertical velocity.

The aircraft landing gears were modeled as the tires, with the additional consideration of packing friction.

Tie-down chains are defined as linear springs with a finite breaking strength. If a load is calculated which exceeds the breaking strength, that chain is effectively "removed" from the model. Each chain is defined by its aircraft attachment point, the horizontal component of its length, and the plane angle to the deck anchor point. Double chains are formed by the input of two single chains with the same identification coordinates. Only the vertical components of the chain loads are used in determining the aircraft and wheel dynamics. The contribution of the horizontal component is ignored.

Fig. 7 shows a general view of the tie-down configuration used for the A4C test simulations. Two double chains are attached
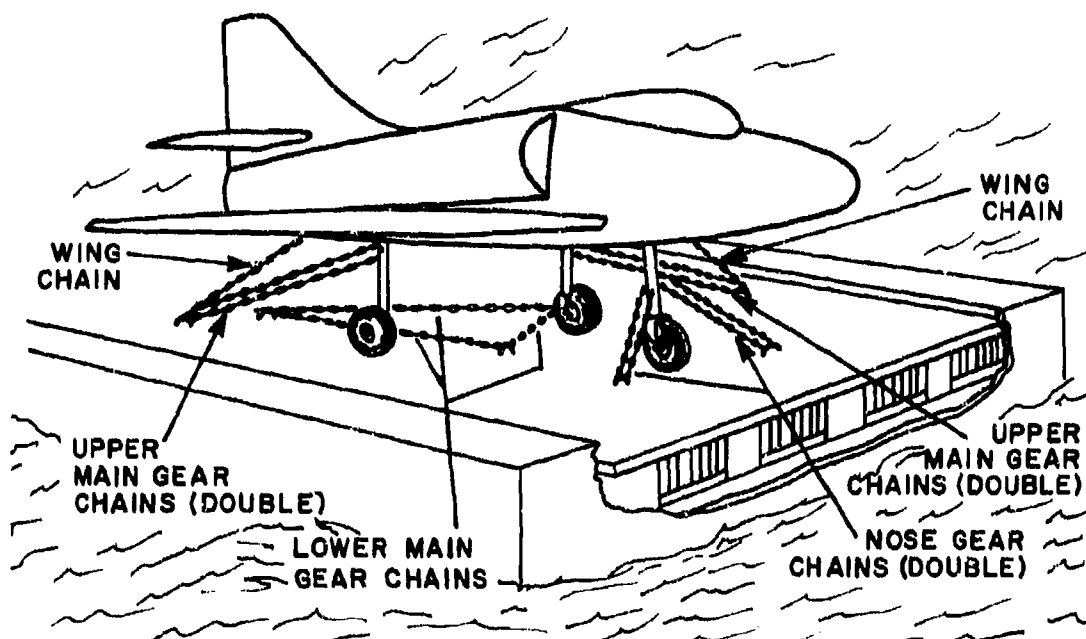
150

Fig. 7 - Aircraft shock model tie-down configuration

to the upper part of the nose gear. A double chain is also used for each upper main gear. Two single chains are attached to each lower main gear, and one to each wing tie-down point.

The model also includes wing flexibility. For the A4C test simulations, this data was provided by the McDonnel-Douglas Corporation.

Figure 8 shows a starboard view of the aircraft pitch model. All gear and tir springs are assumed to be vertical at all times, and as has been noted, only the vertical components of the chain springs are considered. The nose gear chains are attached to the upper portion of the nose gear and do not directly influence the motion of the nose gear mass. The upper main gear chains are similarly attached to the upper portion of the main gear and do not directly influence the motion of the main gear masses. The lower main gear chains, however, are attached in the vicinity of the main gear axle, and as such are included in the force balance equations about the main gears, but are not included in vertical force or pitching moment equations about the aircraft C.G. The aircraft pitch angle is computed dynamically from the pitch moment balance and is defined as the angle between the Fuselage Reference Line

(FRL) and the ground (not the deck, which can also pitch), and is positive nose up.

Figure 9 shows a front view of the Aircraft Roll Model. Again, all gear and tire springs are assumed to be vertical and only the vertical components of the chain springs are considered. Also, as in the pitch model, the lower main gear chain springs do not directly influence the roll motion of the aircraft.

The aircraft roll angle is computed dynamically from the roll moment balance and is defined as the angle between the wing line and the ground. Roll angles are defined positive starboard wing down.

THE UNDERWATER EXPLOSION/
HYDRODYNAMIC MODEL

To provide the dynamic input necessary for the response simulation of an FSP test, a semi-empirical model of an underwater explosion and the resulting hydrodynamic forces was constructed.

The mechanism of an underwater explosion and the phenomena produced is well understood and thoroughly documented. Probably the
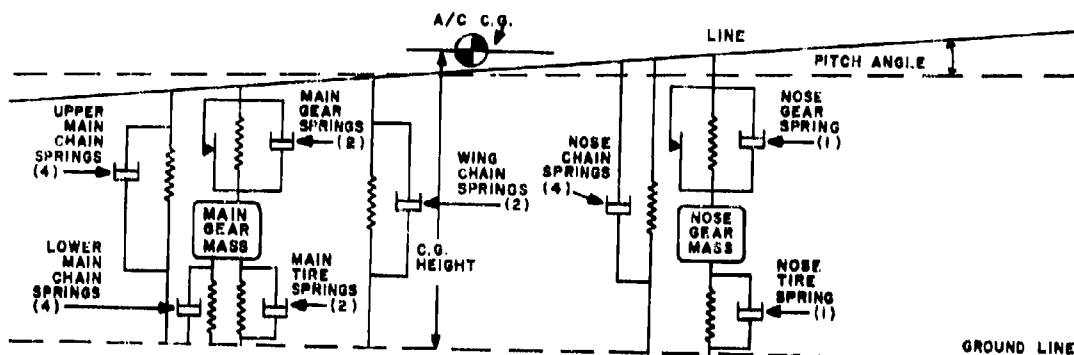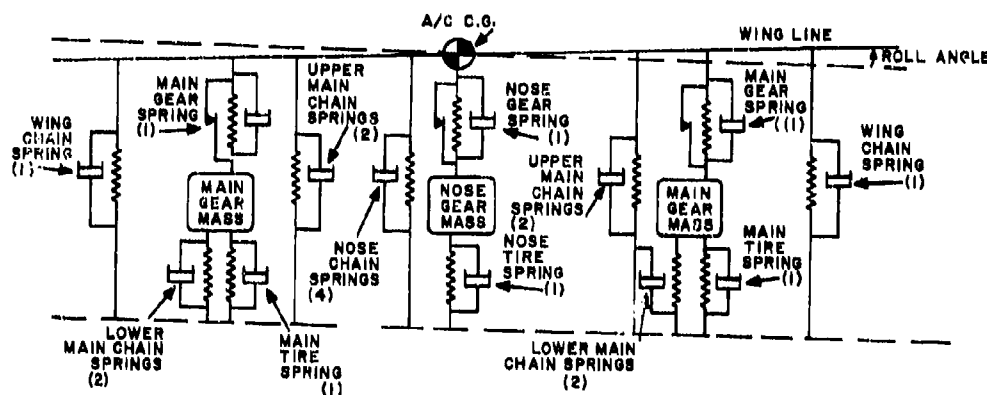
151

Fig. 8 - Aircraft pitch model (Starboard View)

Fig. 9 - Aircraft roll model (Front View)

most inclusive work on the subject is R.H. Cole's "Underwater Explosions". [Ref. 4], although many other articles and reports are available on the subject. It is not the purpose of this paper to present another treatise on underwater explosions, but only to mention briefly those important phenomena which influence the FSP test simulations.

The sequence of events following an underwater explosion is briefly; the charge detonation and conversion of the solid explosive material to a gas at extremely high temperature and pressure, the emission of a steep fronted shock wave, and the later formation of a bubble, or gas globe. The gas globe then expands and contracts several times emitting further pressure pulses following the shock wave. Migration of the gas globe usually takes place during this phase which further complicates the problem. There are other phenomena which may take place depending, i.e., upon different charge shapes, charge magnitudes, proximity of the free surface, the bottom, or objects. However, for FSP tests, only the shock wave, the pulsating, migrating gas globe, and the further effects they generate, are of interest.

The Shock Wave

The initial, and most violent response of the FSP is caused by the shock wave. For most analyses, only the shock wave needed be considered, as most damage to test equipment will occur within 50 milliseconds from FSP impingement. During this time period the FSP is responding solely to the shockwave.

Ref. [4] includes the analysis of an infinite, free, air-backed plate impinged upon

152

normally by a shock wave. This analysis was adopted in general theory and the aspect of non-normal impingement added to it. Fig. 10 shows a plate section being struck by a shock wave at an angle δ with the normal. Assuming the angle of incidence will equal the angle of reflection, and applying the principle of continuity of flow, the incident water particle vertical velocity is equated to the sum of reflected water particle vertical velocity and the plating vertical velocity so that:

$$v_i \cos \delta = v_R \cos \delta + v_{PL} \qquad (1.1)$$

From the theory of propagation of waves in an ideal fluid, water particle velocity may be expressed by:

$$v_{wp} = \frac{P}{\rho c} \qquad (1.2)$$

where;

P is overpressure

ρ is density

and, c is propagation velocity

rewriting equation (1.1),

$$\frac{P_i \cos \delta}{\rho c} = \frac{P_R \cos \delta}{\rho c} + v_{PL} \qquad (1.3)$$

The total force P_T acting on a unit area of plating is equal to:

$$P_T = P_i + P_r \qquad (1.4)$$

$$P_T = 2P_i - \frac{\rho c v_{PL}}{\cos \delta} \qquad (1.5)$$

The relationship,

$$P = P_0 e^{-t/\theta} \qquad (1.6)$$

is an empirical formula which may be used to describe the pressure decay, at a point in the medium, from the initial shock wave peak pressure.

Where,

   P   is pressure

   Po   is shock wave peak pressure

   and, θ is the time for the pressure to decay to a value of Po/e

Po and θ are related to the charge weight-W (in lbs. of tnt) and the distance from the charge center-R (in feet) by the following empirical formulae:

$$P_0 = 21,600 \left[\frac{W^{1/3}}{R}\right]^{1.13}, \text{ PSI} \qquad (1.71)$$

$$\theta = .058 W^{1/3} \left[\frac{W^{1/3}}{R}\right]^{-.22}, \text{ millisec} \qquad (1.72)$$

All these functions have been validated many times by independent experiments. Substituting equation (1.6) into equation (1.5)

$$P_T = 2 P_0 e^{-t/\theta} - \frac{\rho c v_{PL}}{\cos \delta} \qquad (1.8)$$

$$m \frac{dv_{PL}}{dt} = P_T$$

and,

$$m \frac{dv_{PL}}{dt} = 2 P_0 e^{-t/\theta} - \left[\frac{\rho c v_{PL}}{\cos \delta}\right] \qquad (1.81)$$

A linear, ordinary differential equation of first order is derived for plate motion. Applying the method of integrating factors the solution for plate vertical velocity is:

$$v_{PL} = \frac{2 P_0 \cos \delta}{c (x \cos \delta - 1)} \left[(e)^{-t/x\theta \cos \delta} - (e)^{-t/\theta}\right] \qquad (1.82)$$

And the pressure acting on the same unit area of plate is:

$$p = \frac{2 P_0}{(x \cos \delta - 1)} \left[x \cos \delta (e)^{-t/\theta} - (e)^{-t/x\theta \cos \delta}\right] \qquad (1.83)$$

In the early stages of the FSP project, the general equation (1.83) was applied individually to each wetted plating mass point in relationship to time of shock wave impingement, forming a family of particular equations of form (1.83) as the shock wave loading function. However, the FSP response calculated from the application of this loading function seemed excessive. This was attributed to the fact that the infinite free plate analysis, from which equation (1.83) was derived, assumed no occurrence, transmission, or reflection of internal elastic waves in the plate. To include these
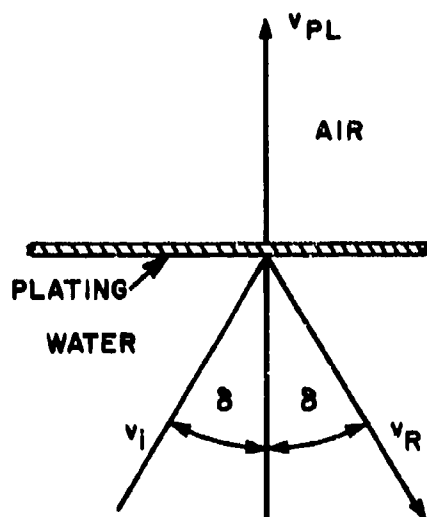
153

Fig. 10 - Shock wave/plating interaction model

effects, which are provided by the finite difference models of the FSP and shock fixture, equation (1.8) was employed as a time increment, corrective input. This type of loading function, on the same per mass, impingement time basis, includes the mass point vertical velocity, if any, caused by the elastic waves traveling through the structure. With this approach, the influence of FSP elasticity mitigating the impinging shock wave was taken into account. Results from this analysis showed significant reductions in impingement pressure, particularly at the FSP center bottom plating where reductions of up to 30% were observed. Accordingly, comparison with the test records showed increased agreement.

Equation (1.8) indicates that the pressure on the FSP plating can drop to zero. If this occurs, cavitation takes place, the plating separates from the water, and the shock-wave-plating interaction is terminated. The suction force on the FSP that cavitation produces is treated in the model by consideration of each bottom plating mass. The vertical displacement of the individual mass is followed. If a positive value is sensed, a suction force created by the difference between atmospheric and bulk cavitation pressure is applied to that masspoint. A bulk cavitation pressure of 4 psi, that of seawater, was used.

The Gas Globe

The gas globe formed by the detonated charge during a standard 901C FSP test,

migrates to the surface. Several expansion and contraction cycles take place before the gas globe reaches the surface and vents.

As a first attempt at including this phenomena in the explosion model, the hydrodynamic equations, which predict the pressure pulsations caused by the cycles, were extracted from Ref. [4]. These equations were rewritten in finite difference form, coded in fortran, and computed as a separate program. To evaluate the new equation forms, and the program logic, the results were compared with values listed in Ref. [4] and found to be identical.

To date, time has not permitted the addition of this subprogram to the main logic of the FSP program. For this reason, the equations, and their development, are not shown here.

Water Resistance

Water resistance to platform horizontal motion, opposite the shot side is provided by a Bernoulli type equation of the form:

$$P = \frac{v^2 \gamma}{2 g}$$

where,

P is pressure

and, v is velocity

this variable force is also computed on a per mass basis, and applied to the platform side or end plating accordingly.

RESULTS

The computer program which resulted from the project was written in straightforward fortran. It is over two thousand statements in length. And for that reason it is not listed in this paper.

The program was computed on a Univac 1108, although it is readily transferable to any computer of comparable core size. Execution time for a 50 ms. simulation with the total 1386 degree-of-freedom model was approximately 280 cpu seconds. For longer simulations the same general ratio will apply.

Whenever the program is run for an FSP 901C test simulation, only charge standoff and

154

the selection of side or end shot, is specified. No other changes are required.

Comparison of analytic results with the published test data has shown good agreement. Fig. (11) and Fig. (12) depict the calculated values of FSP inner bottom vertical velocity versus the velocity meter instrumentation output, for 40 ft. and 50 ft. standoffs. Although the velocity meter traces are uncorrected for inherent instrument errors, the strong correlation is readily apparent.

Fig. (13) shows the calculated vertical velocity of the shock fixture for a 40 ft. standoff test simulation. The predominant frequency response of the fixture is seen to be about 35Hz. This frequency is in agreement with the fundamental natural frequency of 33Hz published in Ref. [3].

The strong correlation noted between the computed and test results for both the 40 and 50 ft. standoff cases, gave confidence to the analytical approach and simulation model.
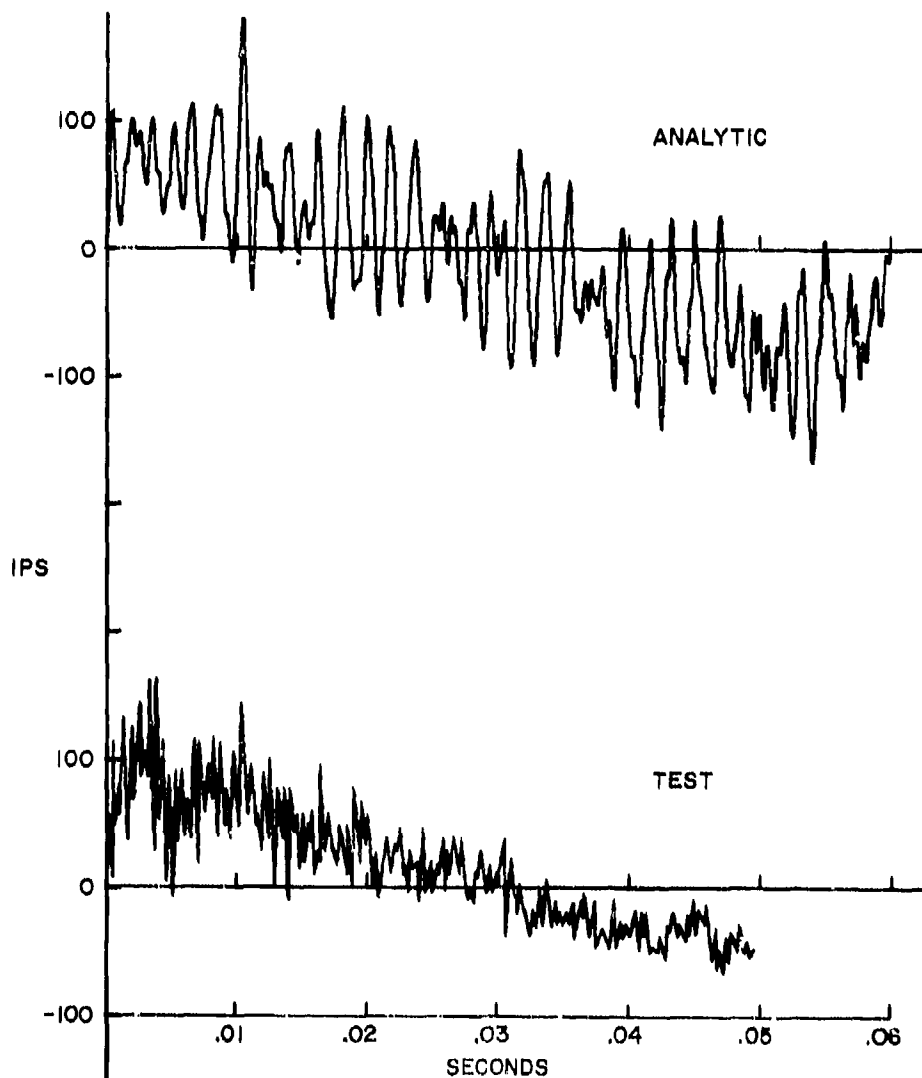

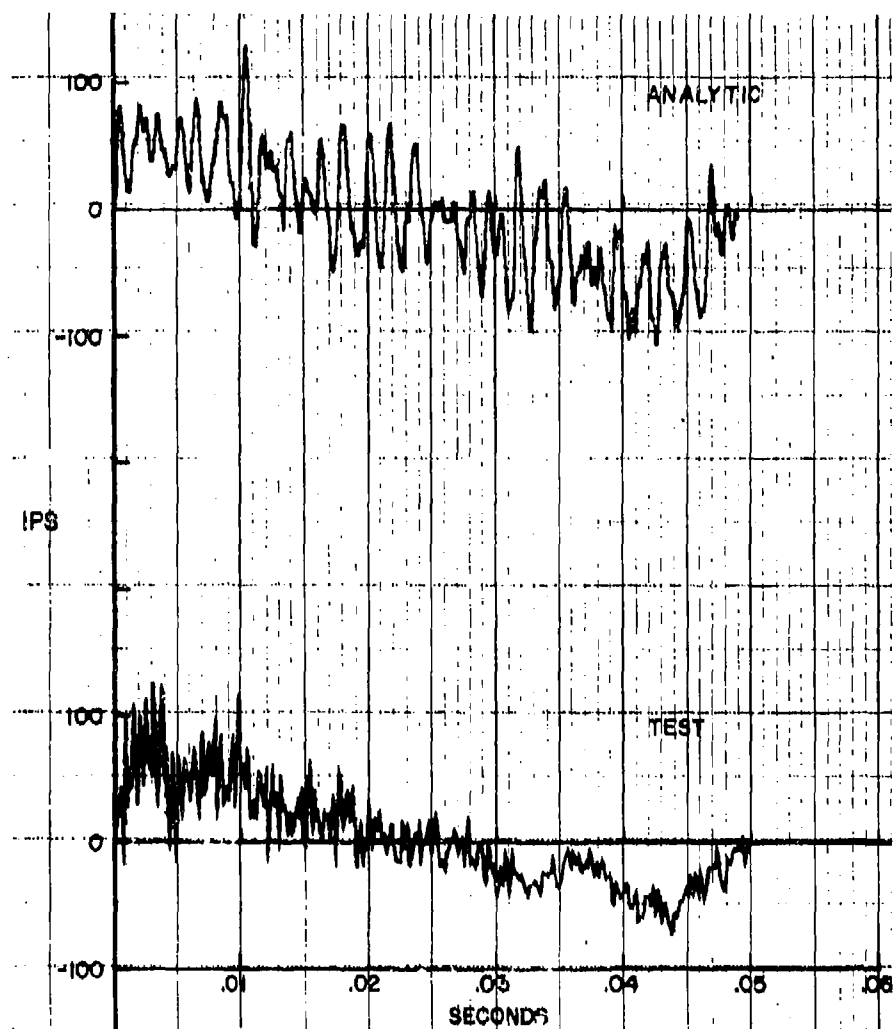Fig. 11 - 40 ft. standoff F.S.P. test of A-4C A/C

Fig. 12 - 50 ft. standoff F. S. P. test of A-4C A/C

This confidence provided encouragement to apply the analytic model to an untested case. Thus an untested 20 ft. standoff case was simulated.

An examination of the data from this run in the 0 to 60 millisecond range reveals high dynamic loads for the aircraft main gear. Although the results show bottoming of the gear and possible damage, the aircraft model may be lacking in sophistication to predict such a failure. A more realistic approach to the determination of failure or non-failure in this instance would be to rerun the case, and print out the shock fixture motions loading the

main gear. This load history could then be applied to a more sophisticated mathematical model of the gear.

An interesting phenomena observed in the cases computed is the mitigating effect of platform elasticity and motion upon the shock wave inpingement function.

The inclusion of bottom plating vertical velocity on a per mass, iterative basis in the impingement function precipitates significant reductions in the initial pressure applied to the center platform masses over the pressure predicted by formula (1. 83).
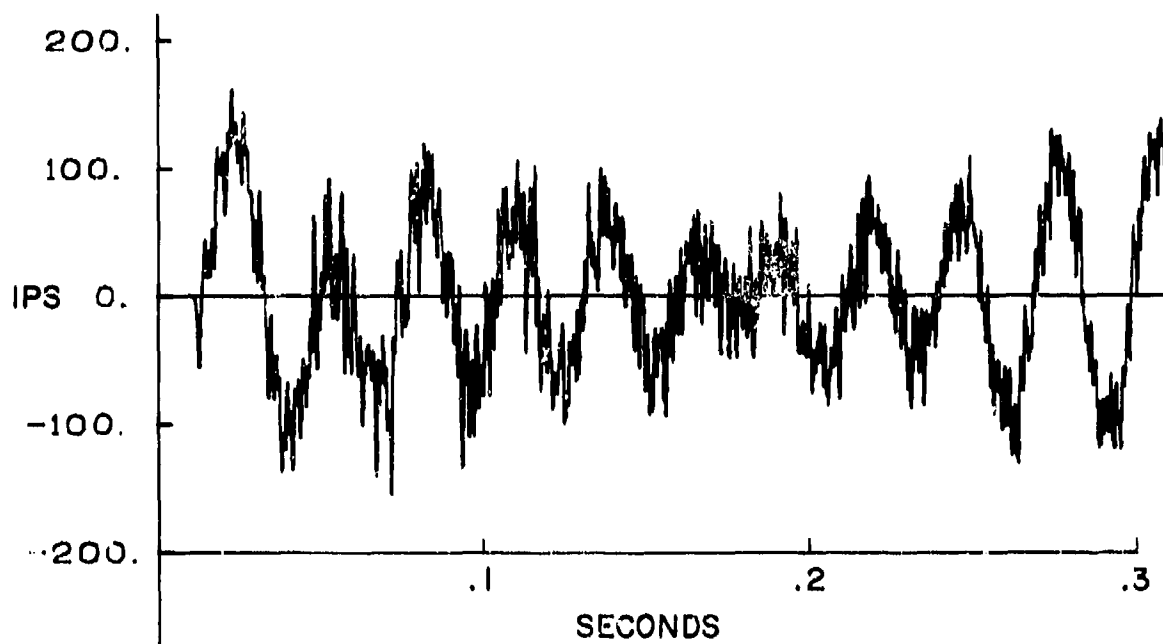
Fig. 13 · 40 ft. standoff F. S. P. test of A-4C A/C

Compression waves from earlier shock wave impingements, travelling through the steel structure of the platform are responsible for the imparting of motion to the individual masses before they themselves are struck by the shock wave.

There are, of course, numerous results from the program output. Those selected for inclusion in this paper were a representative cross section.

SUMMARY AND CONCLUSIONS

Viewing the entire project in retrospect, and the paths which led to the final model, the authors feel it is reasonable to state; that with the finite difference method, a floating shock

platform test can be modeled to predict the total dynamic response.

Although the results of the analysis are numerous, two factors were found to be of major importance in achieving the correct response of the platform to blast loading; they are:

1. The large, sophisticated model was necessary because the total elasticity of the platform must be accounted for to obtain the sum affect of internal stress waves in creating perturbation.

2. In order to obtain the correct shock wave loading function, the mitigating effect of the calculated platform vertical velocity must be included on a per mass basis.

REFERENCES

1. Brooks, R. P. and Thomas, A. "Development of an Analytic Method for Dynamic Beam Analysis," Report NAEC-ENG-7579, Naval Air Engineering Center, Philadelphia, Pa.   February 28, 1969

2. Brooks, R. P. "Advanced Development of a Lumped Mass, Finite Difference Method for Dynamic Beam Analysis," Report NAEC-ENG-7676, Naval Air Engineering Center, Philadelphia, Pa.   November 13, 1970

3. Vogensen, S. E. "Shock Test of Aircraft Tie-Downs (Type TD-1A), Navships Item No. 216," Technical Report No. H13-69, San Francisco Bay Naval Shipyard, Hunters Point, San Francisco, California, April, 1969

4. Cole, R. H. "Underwater Explosions," Princeton, New Jersey: Princeton University Press, 1948

5. "The Floating Shock Platform," UERD Report No. 7-61, Underwater Explosions Research Division, David Taylor Model Basin, Portsmouth, Va. May, 1961

*   *   *

APPENDIX

The following is the equation set for the six degree-of-freedom parallel beams described in the floating shock platform section. The Equations are derived for the typical K, I mass model depicted in Fig. (5).

DEFINITION OF SYMBOLS FOR EQUATIONS OF THE K, I MASS

$\ddot{X}_{K,I}$ is the acceleration in the X direction of the I mass in the K beam

$\ddot{Y}_{K,I}$ is the acceleration in the Y direction of the I mass in the K beam

$\ddot{Z}_{K,I}$ is the acceleration in the Z direction of the I mass in the K beam

$\ddot{\alpha}_{K,I}$ is the acceleration in the α direction of the I mass in the K beam

$\ddot{\beta}_{K,I}$ is the acceleration in the β direction of the I mass in the K beam

$\ddot{\gamma}_{K,I}$ is the acceleration in the γ direction of the I mass in the K beam

$FBX_{K,I}$ is the force in the X direction between K, I and K + 1, I

$FBY_{K,I}$ is the force in the Y direction between K, I and K + 1, I

$FBZ_{K,I}$ is the force in the Z direction between K, I and K + 1, I

$AMBX_{K,I}$ is the moment about the X axis between K, I and K + 1, I

$AMBZ_{K,I}$ is the moment about the Z axis between K, I and K + 1, I

$FX_{K,I}$ is the force in the X direction between K, I and K, I + 1

$FY_{K,I}$ is the force in the Y direction between K, I and K, I + 1

$FZ_{K,I}$ is the force in the Z direction between K, I and K, I + 1

$AMX_{K,I}$ is the moment about the X axis between K, I and K, I + 1

$AMY_{K,I}$ is the moment about the Y axis between K, I and K, I + 1

$AMZ_{K,I}$ is the moment about the Z axis between K, I and K, I + 1

$SCX_{K,I}$ is the spring constant in the X direction

$SCY_{K,I}$ is the spring constant in the Y direction

$SCZ_{K,I}$ is the spring constant in the Z direction

$SC\alpha_{K,I}$ is the spring constant in the α direction

$SC\beta_{K,I}$ is the spring constant in the β direction

$SC\gamma_{K,I}$ is the spring constant in the γ direction

$SCBX_{K,I}$ is the spring constant between beams in the X direction

$SCBY_{K,I}$ is the spring constant between beams in the Y direction

$SCBZ_{K,I}$ is the spring constant between beams in the Z direction

$SCB\alpha_{K,I}$ is the spring constant between beams in the α direction

$SCB\beta_{K,I}$ is the spring constant between beams in the β direction

$SCB\gamma_{K,I}$ is the spring constant between beams in the γ direction

$M_{K,I}$ is the mass

$MIX_{K,I}$ is the mass moment of inertia about the X axis

$MIY_{K,I}$ is the mass moment of inertia about the Y axis

$MIZ_{K,I}$ is the mass moment of inertia about the Z axis

$FWY_{K,I}$ is the water force in the Y direction

$\triangle LB$ is the distance between the CG's of adjacent beams

$\triangle L$ is the distance between masses on the same beam

EZ is the shear center offset in the Y direction

DEFINITIONS OF CONSTANTS

$$M = (\rho)(\triangle L)(A)$$

$$MIX = \rho \triangle L \left[IX + \frac{(\triangle L)^2 A}{12} \right]$$

$$MIY = \rho \triangle L \left[IY + \frac{(\triangle L)^2 A}{12} \right]$$

$$MIZ = \rho \triangle L \left[IZ + \frac{(\triangle L)^2 A}{12} \right]$$

$$SCX = \frac{AE}{\triangle L}$$

$$SCY = \frac{\alpha AG}{\triangle L}$$

$$SCZ = \frac{\alpha AG}{\triangle L}$$

$$SC\alpha = \frac{KG}{\triangle L}$$

$$SC\beta = (IY) E/\triangle L$$

$$SC\gamma = (IZ) E/\triangle L$$

$$SCBX = \alpha AG/\triangle LB$$

$$SCBY = \alpha AG/\triangle LB$$

$$SCBZ = AE/\triangle LB$$

DEFINITIONS OF CONSTANTS, Cont'd.

$$SCB\alpha = (IX)E/\triangle LB \qquad\qquad SCB\gamma = KG/\triangle LB$$

$$SCBB = (IY)E/\triangle LB$$

EQUATION SET FOR A K, I BEAM MASS

EQUATION

#1. $\triangle FX_{K,I} = (SCX)(\triangle X_{K,I+1} - \triangle X_{K,I})$

#2. $\triangle FY_{K,I} = (SCY)\left(\triangle Y_{K,I+1} - \triangle Y_{K,I} + \left(\triangle\gamma_{K,I+1} + \triangle\gamma_{K,I}\right)\left(\frac{\triangle L}{2}\right)\right)$

#3. $\triangle FZ_{K,I} = (SCZ)(\triangle Z_{K,I+1} - \triangle Z_{K,I} - (\triangle\beta_{K,I+1} + \triangle\beta_{K,I}\left(\frac{\triangle L}{2}\right) + (EZ)$

$\left(\triangle a_{K,I+1} - \triangle a_{K,I}\right)$

#4. $\triangle AMZ_{K,I} = (SC\gamma)\left(\triangle\gamma_{K,I} - \triangle\gamma_{K,I+1}\right)$

#5. $\triangle AMY_{K,I} = (SC\beta)\left(\triangle\beta_{K,I} - \triangle\beta_{K,I+1}\right)$

#6. $\triangle AMX_{K,I} = (SC\gamma)\left(\triangle\gamma_{K,I} - \triangle\gamma_{K,I+1}\right)$

#7. $\triangle FBZ_{K,I} = (SCVZ)\left(\triangle Z_{K+1,I} - \triangle Z_{K,I}\right)$

#8. $\triangle FBY_{K,I} = (SCBY)\left(\triangle Y_{K+1,I} - \triangle Y_{K,I} - \left(\triangle a_{K+1,I} + \triangle a_{K,I}\right)\left(\frac{\triangle LB}{2}\right)\right)$

#9. $\triangle FBX_{K,I} = (SCBX)\left(\triangle X_{K+1,I} - \triangle X_{K,I} + (\triangle\beta_{K+1,I} + \triangle\beta_{K,I})\left(\frac{\triangle LB}{2}\right)\right)$

#10. $\triangle AMBX_{K,I} = (SCB\alpha)\left(\triangle a_{K,I} - \triangle a_{K+1,I}\right)$

#11. $\triangle AMBY_{K,I} = (SCB\beta)\left(\triangle\beta_{K,I} - \triangle\beta_{K+1,I}\right)$

#12. $\triangle AMBZ_{K,I} = (SCB\gamma)\left(\triangle\gamma_{K,I} - \triangle\gamma_{K+1,I}\right)$

EQUATION

#13. $\ddot{X}_{K,I}$ $= \left(FBX_{K,I} - FBX_{K-1,I} + FX_{K,I} - FX_{K,I-1} \right) \Big/ m$

#14. $\ddot{Y}_{KI}$ $= \left(FWY_{K,I} + FBY_{K,I} - FBY_{K-1,I} + FY_{K,I} - FY_{K,I-1} \right) \Big/ m$

#15. $\ddot{Z}_{K,I}$ $= \left(FZ_{K,I} - FZ_{K,I-1} + FBZ_{K,I} - FBZ_{K-1,I} \right) \Big/ m$

#16. $\ddot{\alpha}_{K,I}$ $= \left(AMBX_{K-1,I} - AMBX_{K,I} + \left(FBY_{K-1,I} + FBY_{K,I} \right) \dfrac{\Delta LB}{2} + AMX_{K,I-1} \right.$

$\left. - AMX_{K,I} - (EZ) \left(FZ_{K,I-1} - FZ_{K,I} \right) \right) \Big/ MI_X$

#17. $\ddot{\beta}_{K,I}$ $= \left(AMBY_{K-1,I} - AMBY_{K,I} + AMY_{K,I-1} - AMY_{K,I} - \left(FBX_{K-1,I} + FBX_{K,I} \right) + \right.$

$\left. \dfrac{\Delta LB}{2} + \left(FZ_{K,I} + FZ_{K,I-1} \right) \dfrac{\Delta L}{2} \right) \Big/ MI_Y$

#18. $\ddot{\gamma}_{K,I}$ $= \left(AMBZ_{K-1,I} - AMBZ_{K,I} + AMZ_{K,I-1} - AMZ_{K,I} - \left(FY_{K,I-1} + FY_{K,I} \right) + \right.$

$\left. \left(\dfrac{\Delta L}{2} \right) \right) \Big/ MI_Z$

EXCITATION, RESPONSE, AND FATIGUE LIFE ESTIMATION

FOR STRUCTURAL DESIGN OF EXTERNALLY BLOWN FLAPS

Eric E. Ungar
Bolt Beranek and Newman Inc.
Cambridge, Massachusetts

Relations are presented for prediction of the fluctuating pressure
spectra experienced by flaps exposed to fan-jet engine exhausts
and for estimation of the resulting maximum stresses induced in
skin-stringer and in honeycomb-core sandwich flaps. These stress
estimates are combined with expressions representing fatigue data,
to obtain relations between fatigue life and the important struc-
tural and engine exhaust parameters and to suggest structural de-
sign approaches.

INTRODUCTION

Short take-off and landing (STOL)
aircraft concepts have been attracting
much attention in the past several years,
because of their potential operational
advantages over more conventional air-
craft. Of the several STOL configura-
tions that have been given very serious
consideration, those incorporating "ex-
ternally blown" flaps (e.g., see Fig. 1)
have recently found increasing favor,
and EBF aircraft technology currently
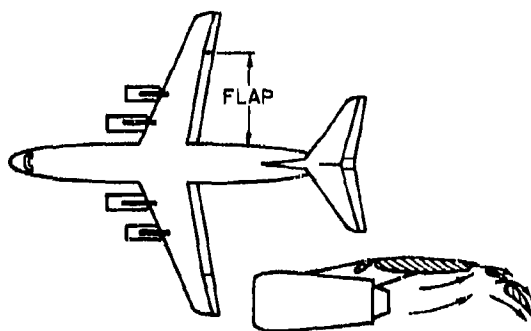is the subject of extensive study and
evaluation.

Fig. 1. Externally-Blown-Flap STOL
Airplane (from Ref. 1)

Because the flaps of EBF aircraft
are exposed to the direct impingement of
the engine exhaust streams, the effects
of the associated fluctuating pressures
must be taken into account in the design
of the flap structures. It is the pur-
pose of this paper to summarize means
for estimating the "sonic" fatigue life
of such structures, to display relations
that indicate the effects of the impor-
tant structural and engine exhaust para-
meters, and to suggest structural design
approaches. This paper in essence is a
condensed version of the primary part of
Ref. [1]; it has been prepared in order to
make the salient information of that pub-
lication more readily and more widely
available.

FLUCTUATING PRESSURES ON EBF SURFACES

Jet Configuration

Velocity profiles (e.g., as appear
in Ref. [2]) indicate that at several
core-nozzle diameters aft of the nozzle
exit plane, the flow field produced by
fan-jet engines is dominated by that due
to the core jet. It is reasonable there-
fore to estimate the fluctuating pres-
sures produced by the exhaust from a
fan-jet engine on the basis of the pres-
sures associated with the core jet, and
to make use of the extensive information
available concerning ideal circular jets.

The configuration of an ideal circular jet, as sketched in Fig. 2, shows a converging conical "potential flow region", surrounded by a diverging conical "mixing region". The total angle 2α subtended by the jet boundary typically is between 25 and 30 degrees [3]. The length of the potential core is given [4] by

$$X_c \approx 3.45 \ D(1 + 0.38 \ M)^2 \ , \qquad (1)$$

where D denotes the diameter of the (engine core) nozzle and M represents the Mach number of the exhaust stream.

Velocity Fluctuations in Jets

For estimation purposes it is also convenient to assume that the velocity fluctuations that are present in the jet in absence of an inserted flap are not altered substantially in the presence of the flap, and one may then interpret available velocity fluctuation data in terms of the pressure fluctuation information one requires. Figure 3 indicates how the axial turbulence intensity

$$I = \sqrt{\overline{u^2}}/U_0 \qquad (2)$$

varies along the axis of a jet, and Fig. 4 shows how this intensity varies along the radial coordinate. Here U_0 represents the jet exit velocity (which, for a fan-jet engine is taken to be the core engine exit velocity) and $\overline{u^2}$ denotes the mean-square axial fluctuating velocity.

As is evident from Fig. 3, the intensity I on the jet axis is at approximately its maximum value of 0.11 at $X/D \approx 10$. Figure 4 shows that for $X/D \geq 8$, I does not exceed approximately 0.12. From examination of the peak values of Fig. 4 one may determine, in fact, that for $X/D > 9$, the maximum value of I obeys

$$I_{max} \approx 0.165 - 0.0044 \ X/D \qquad (3)$$

and occurs at a radial coordinate r_{peak}, given by

$$\frac{r_{peak}}{D} \approx 0.15 \ \frac{X}{D} - 1.0 \ . \qquad (4)$$

Thus, for the regions of interest with respect to blown flaps, $I \approx 0.12$ may be expected to represent an upper bound suitable for conservative design purposes.
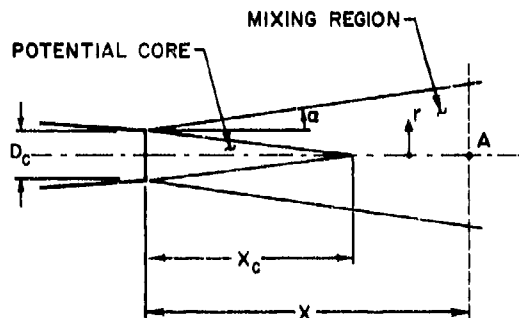

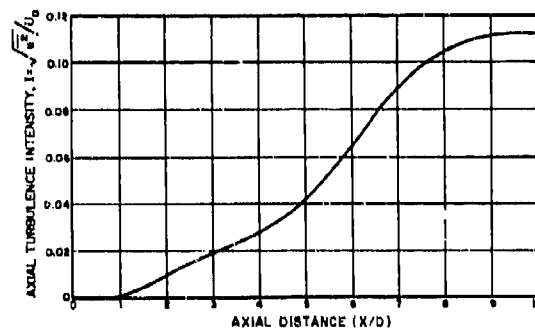Fig. 2. Configuration of Ideal Jet

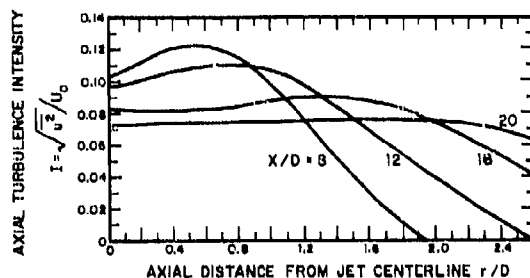Fig. 3. Variation of Axial Turbulence Intensity Along Jet Axis (from Ref. 5)

Fig. 4. Variation of Axial Turbulence Intensity with Distance from Jet Centerline (from Ref. 5)

166

Pressure Fluctuations on Flap Surfaces

Normally impinging jets. — For flap surfaces on which the jet flow impinges essentially normally, one may take the momentum flux in the flow to be annihilated at the structural surface. With this assumption, the mean-square fluctuating pressure $\overline{p^2}$ is found to be related to the mean-square fluctuating velocity $\overline{u^2}$ as

$$\overline{p^2} = 4\rho^2 U^2 \overline{u^2} = (4qI)^2 , \qquad (5)$$

where ρ denotes the local fluid density and U the local mean velocity. For most locations of interest for EBF's, the local velocity U is nearly equal to the exit velocity U_0 and the local gas density ρ differs little from the density ρ_0 at the exit. With these assumptions one obtains the above indicated equality, where

$$q = \frac{1}{2} \rho_0 U_0^2 \approx \frac{1}{2} \rho U^2 \qquad (6)$$

represents the dynamic pressure at the exit.

The frequency-spectral density $\Phi_p(\omega)$ of the fluctuating pressure is shown in Ref. [1] to be of the same form as that of the fluctuating velocity component, and to obey*

$$\Phi_p(\omega) = \frac{1}{2\pi} \Phi_p(f) = \overline{p^2} \ \frac{T_f/\pi}{1 + T_f^2 \omega^2} , \qquad (7)$$

where T_f represents a typical time scale (or inverse frequency) of the pressure or velocity fluctuations and obeys

$$T_f \approx 0.1 \ X/U_0 , \qquad (8)$$

and where ω denotes the radian frequency.

From Appendix A of Ref. [1] one also finds that the pressure cross-correlation function $\phi_{p_1 p_2}(s,\tau)$ for two points on the flap surface near the jet axis separated by a distance s obeys

$$\phi_{p_1 p_2}(s,\tau) = \overline{p^2} \ e^{-s/L} \ e^{-|\tau|/T_f} , \qquad (9)$$

where L denotes a length scale, called

---

*The spectral density $\Phi_p(\omega)$ represents the mean-square pressure per rad/sec, whereas the spectral density $\Phi_p(f)$, expressed in cyclic rather than radian frequency, represents the mean-square pressure per Hertz.

the correlation length, and is given by

$$L \approx 0.025 \ X . \qquad (10)$$

Near-tangentially impinging jets. — For flap surfaces along which the engine exhaust flows essentially tangentially, the assumption of momentum flux annihilation would tend to overestimate the mean-square fluctuating pressure. From Figs. 5 and 6, which show how $\sqrt{\overline{p^2}}/q$ varies in the stream-wise and cross-wise directions along a plate inclined at various angles to an impinging jet, one finds that $\sqrt{\overline{p^2}}/q$ does not exceed 0.1 for $X/D > 9$ and for angles between the plate surface face and flow-normal greater than 30°. This value of 0.1 is considerably smaller than the value of $\sqrt{\overline{p^2}}/q = 4I \approx 4(0.12) = 0.48$ one obtains from Eq. (5) for a normally impinging jet with the near-maximum turbulence intensity $I = 0.12$.
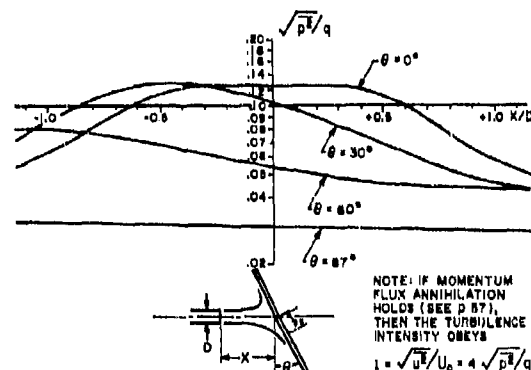

Fig. 5. Variation of Surface Pressure Fluctuation on a Flat Plate due to Jet Impingement with Location, at $X/D = 7$ and Several Angles of Inclination (from Ref. 6)
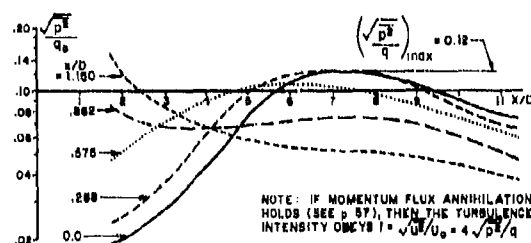

Fig. 6. Variation of Surface Pressure Fluctuation on a Flat Plate due to Normal Jet Impingement ($\theta = 0°$) with X/D, at Several Locations along Plate (from Ref. 6)

The frequency-spectral density $\phi_p(\omega)$ of the fluctuating pressures associated with nearly tangential flows may again be approximated by Eqs. (7) and (8). The pressure cross-correlation function here is more complex, however, being characterized (see Appendix A of Ref. [1]) by different correlation lengths (or "eddy decay scales") L_x and L_y in the streamwise and transverse directions, with

$$L_x \approx 13.5 \ V_c/\omega$$
$$L_y \approx 2.0 \ V_c/\omega \ , \tag{11}$$

where

$$V_c \approx 0.45 \ U_0 \tag{12}$$

represents the convection velocity of the flow.

Design Pressure Spectra

Maximum mean-square pressure.— Although one may use the data shown in Figs. 3-6, together with the previously given equations, to estimate the fluctuating pressure that occurs at any specific location, one usually need not consider all this detail for design purposes. By inspection of Figs. 3 and 4 one finds that for $8 \leq X/D \leq 20$, corresponding to typical locations where EBF surfaces may be expected to be placed normal to the flow, the turbulence intensity does not exceed 0.12. Since one also may note that in the high-turbulence region, i.e. for $r/D \leq 1$, the turbulence intensity decreases slowly with X/D, approximately according to Eq. (3), one may choose $I = 0.12$ for general conservative design purposes.

With this value of I, Eqs. (5) and (6) reduce to

$$\overline{p^2} = (0.24 \ \rho_0 U_0^2)^2 \ ; \tag{13}$$

this then may be used to estimate the pressure on surfaces on which a jet impinges normally.

From Figs. 5 and 6 one may similarly deduce that for surfaces on which jets impinge more nearly tangentially, $\sqrt{\overline{p^2}}/q \leq 0.12$, so that for conservative estimation purposes one may take

$$\overline{p^2} = (0.12 \ q)^2 = (0.06 \ \rho_0 U_0^2)^2. \tag{14}$$

Clearly, the assumption of normal incidence leads to mean-square pressures that are higher by a factor of 16 than the pressures one obtains for more tangential incidence, and structures that can withstand the normal incidence pressures for a given period may be expected

in general to survive the tangential incidence pressures for a longer period.

Pressure spectrum (spectral density). — The frequency spectral density $\phi_p(\omega)$ of the fluctuating pressures, for both the normal and tangential incidence cases, as has been stated, is given by Eqs. (7) and (8). The maximum value of the spectral density, which value is obtained for $T_f\omega \ll 1$, obeys

$$\phi_{max}(f) = 2\overline{p^2}T_f = \frac{0.2X}{U_0}\overline{p^2}$$

$$= 0.0115 \ X\rho_0^2 U_0^3 \ , \tag{15}$$

where the last expression has been obtained by substitution of Eq. (13).

For high frequencies, on the other hand, — that is, for $T_f\omega \gg 1$, — Eqs. (7), (8), and (13) yield

$$\phi_{hi \ freq}(f) \approx \frac{\overline{p^2}}{2\pi^2 T_f f^2} = \frac{U_0\overline{p^2}}{0.2\pi^2 X f^2}$$

$$= 0.029 \ \frac{\rho_0^2 U_0^5}{X f^2} \ , \tag{16}$$

where $f = \omega/2\pi$ denotes the cyclic frequency.

FATIGUE LIFE OF SKIN-STRINGER STRUCTURES

Overview of Estimation Approach

Conventional aircraft structures consist of skins, reinforced by stringers, frames, and bulkheads (Fig. 7). Fluctuating pressures acting on the skins tend to induce complex vibratory deflections in the entire assembly, resulting in associated stresses, which — in turn — lead to structural fatigue.
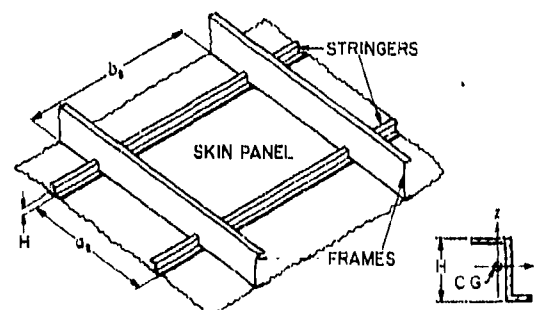

Fig. 7. Typical Bay of Skin-Stringer Structure, and Typical Stringer Cross-Section

Because of the complexities of the excitations and responses, currently available "sonic fatigue" design methods* are based on analyses developed on the basis of simplifying assumptions, coupled with empirically derived relations. These analyses in essence focus on one bay (i.e., one skin panel) at a time, ignore the complex spatial and temporal distribution of the exciting pressure by assuming the pressure always to be completely in phase over the entire panel, and compute the mean-square displacement response of the panel (mode by mode) to this spatially uniform but time-wise random pressure. They then calculate the maximum stresses from the panel modal displacements, and finally relate these calculated stresses to experimentally measured stresses and fatigue data.

In dealing with the panel responses and stresses, the reinforcing structures (i.e., stringers and frames) are considered essentially only as boundary conditions. They are in effect assumed to deflect very little — an assumption that is likely to be well justified in many practical cases. Once the panel motions have been determined, the sonic fatigue analysis method proceeds to determine the stresses induced in the stringers as the result of the loads imposed on them by the vibrating panels, and it then compares these calculated stresses with experimental stress and fatigue data.

Skin

Relation between dynamic and static stress. — In Ref. [7] analysis of the response of elastic structures to random pressure fields is discussed in general terms, and simplified results are presented for the case where:

(1) One mode predominates in the frequency range of interest.
(2) The excitation pressure is in phase over the entire structure of interest.
(3) The spectrum of the excitation does not change rapidly in the vicinity of the resonance frequency of the dominant mode.

*Although these methods were developed to cope with the problem of fatigue induced by acoustic excitation, they may be expected also to be applicable (at least approximately) in many other cases of fluctuating-pressure excitation, including generally that due to impinging jets and tangential flows. In all cases, of course, the quality of the estimate depends on how well the actual situation matches the various underlying assumptions.

It is shown in Ref. [7] that if the foregoing conditions hold, then the root-mean-square stress σ induced at a given location in a structure (or panel) by a random pressure field may be expressed in terms of the stress σ_0 induced at that same location by a uniformly distributed static pressure of unit magnitude as

$$\sigma = \sqrt{\frac{\pi}{2n} f_n \Phi_p(f_n)} \, \sigma_0 . \qquad (17)$$

Here n represents the structural loss factor (of the dominant mode at its resonance), f_n denotes the (cyclic) resonance frequency of the dominant mode, and $\Phi_p(f_n)$ represents the spectral density of the exciting pressure at the frequency f_n.

Resonance frequencies of flat rectangular panels. — A method for determining the natural frequencies of multibay systems, taking into account the flexural and torsional stiffnesses of the various stringers, is presented in Ref. [8]. An alternate method, applicable to structures with many equi-spaced identical stringers between flexurally stiff frames, is summarized in Ref. [9]. These methods, however, are relatively complex; — perhaps too complex for preliminary design purposes. It is likely also that they give results whose precision is much greater than necessary, in view of the considerable uncertainty in (1) the estimated pressure spectra, (2) the validity in any practical case of the assumptions involved in the development of Eq. (17), and (3) the boundary conditions operative in practical structures. Furthermore, fatigue data have been accumulated only for the lowest modes, so that application of this data to fatigue prediction for any given structure of a material or configuration different from those for which data is available or for higher modes is likely to introduce greater errors than those due to the use of simpler, less precise, resonance frequency estimates.

Many measurements of the random responses of panels (e.g., Refs. [7], [10-13]) have shown these responses to be dominated by the fundamental panel mode. Data on realistic aircraft structures (e.g., Refs. [14,15]) and related analyses (summarized in Ref. [9]) have indicated that the responses of skin-stringer configurations generally† are

†However, some data are available [Refs. 16,17] which show that the fundamental panel mode response does not always predominate.

dominated by modes in which each *panel* vibrates in a fundamental mode corresponding to a boundary condition (at each edge) that lies between the fully clamped and the simply supported. It is therefore reasonable to focus on the fundamental panel mode, and to omit the more complex higher modes from consideration.

From a curve presented in Ref. [10] (on page 224) one may find that the experimentally observed variation with aspect ratio of the fundamental resonance frequencies of rectangular panels of skin-stringer configurations correspond very nearly to the geometric average of the resonance frequencies for clamped and for simply supported panels.

The fundamental frequency of a simply supported panel of thickness h and edge lengths a and b is given by*

$$f_s = \frac{\pi}{2} \sqrt{\frac{D}{m}} \left(\frac{1}{a^2} + \frac{1}{b^2} \right) \quad , \quad (18)$$

and that of a clamped panel obeys [10]

$$f_c \approx \frac{2\pi}{3} \sqrt{\frac{D}{m}} \ \frac{F(b/a)}{ab} \quad , \quad (19)$$

where m denotes the mass per unit area of the panel and D its flexural rigidity, and

$$F(b/a) = [2 + 3b^2/a^2 + 3a^2/b^2]^{1/2} \quad . \quad (20)$$

For homogeneous panels,

$$D = \frac{Eh^3}{12(1 - \nu^2)} \quad , \quad (21)$$

$$m = \rho_s h \quad , \quad (22)$$

where E represents Young's modulus, ν Poisson's ratio, and ρ_s the density of the structural material. One may thus estimate the fundamental natural frequency of a skin-stringer panel from*

$$f = \sqrt{f_s f_c} = \frac{h c_L}{a^2} G(b/a) \quad (23)$$

where

$$G(b/a) = \frac{\pi}{6} \left[\frac{a}{b} \left(1 + \frac{a^2}{b^2} \right) F(b/a) \right]^{1/2}$$

$$\approx \begin{cases} 1.25 & \text{for } b/a = 1 \\ 0.69 & \text{for } b/a \gg 1 \end{cases} \quad (24)$$

and where $c_L = \sqrt{E/\rho_s}$ represents the longitudinal wave velocity[†] in the panel material.

Resonance frequencies of cylindrically curved panels. — The fundamental natural frequency f_R of a cylindrically curved panel with radius of curvature R is related to the natural frequency f of a flat panel with the same thickness h and edge dimensions as**

$$\frac{f_R}{f} \approx \left[1 + \frac{0.006(b^2/hR)^2}{A^4 + 0.61A^2 + 1} \right]^{1/2} \quad ,$$

where $A = b/a$, and a denotes the length of the flat edge of the panel, and b the length of its curved edge. The above relation was developed semi-empirically, on the basis of experimental data on structures with realistic boundary conditions, and is valid only for $h/a \leq 1/100$ and for aspect ratios in the range $0.3 < b/a < 3.0$, and for $a/R \leq 0.35$.

Maximum root-mean-square stress in flat panels. — In a simply supported panel, the maximum flexural stress associated with uniform loading or with the first vibratory mode occurs at the panel center. In a rectangular panel that is clamped on all edges, the corresponding maximum stress occurs at the middle of the longer edge. In practical skin-stringer structures, panel fatigue failures typically occur along the edges, at the rivet line or at the ends of stringer flanges or doublers [10,18]; thus, the panel stress associated with fatigue corresponds more closely to the maximum stress in a clamped panel than to that in a simply supported panel.

The maximum flexural stress $\sigma_{0\ max}$ induced in a clamped panel with $b \geq a$ by a uniformly distributed static pressure of unit magnitude is given [10] by

$$\sigma_{0\ max} = \frac{12}{\pi^2}\left(\frac{b}{h}\right)^2 F^{-2}, \qquad (26)$$

where $F = F(b/a)$ is given by Eq. (20).

If one substitutes the foregoing for σ_0 into Eq. (17), and if one takes the natural frequency f to be equal to that for a clamped plate, one obtains the maximum rms stress as

$$\sigma = 1.185\sqrt{\frac{c_L\Phi_p(f)}{a\eta}}\left(\frac{b}{h}\right)^{3/2}F^{-3/2}. \qquad (27)$$

On the other hand, if one uses the expression (23) corresponding to more realistic boundary conditions, one finds

$$\sigma = 1.10\sqrt{\frac{c_L\Phi_p(f)}{a\eta}}\left(\frac{b}{h}\right)^{3/2}\left(\frac{a}{b}+\frac{b}{a}\right)^{1/4}F^{-7/4}. \qquad (28)$$

In Ref. [10] there is derived yet another expression for σ_{max}, on the basis of a regression analysis of experimental data, arranged in nondimensional groups of variables deduced from ideal clamped-edge panel analysis. This expression (when rewritten in consistent units) corresponds to

$$\sigma = 0.24\sqrt{\frac{c_L\Phi_p(f)}{a\eta}}\left(\frac{b}{h}\right)^{7/4}\eta^{-0.06}F^{-1.88}. \qquad (29)$$

Comparisons of the stress estimates one obtains from the three foregoing equations for realistic configurations indicate that the stress one calculates by use of Eq. (27) is higher by a factor of about 1.2 than the stress estimate one finds from Eq. (28), that Eq. (29) increases more rapidly with b/h than Eq. (27), and that the stress estimates one obtains by use of Eq. (29) on the average are about 30% lower than those one obtains on the basis of Eq. (27), and thus about 20% lower than those one finds from Eq. (28).

It is important to note, however, that Eq. (29) was derived on the basis of experimental data [10] on test panels with aspect ratios a/b between 1.0 and 3.0 only, so that the validity of this relation for larger aspect ratios remains uncertain. Furthermore, the test data points (see Fig. 69, p. 138 of Ref. [10]) exhibit a good deal of scatter, with a considerable number of the points deviating considerably from the regression line. It thus is not clear whether the use of the somewhat more complex Eq. (29) is justified instead of Eq. (27) with a reduced coefficient that makes this equation correspond more closely to the available data for $b/a \leq 3.0$.

In view of the fact that Eq. (29) has gained some acceptance, has been reduced to nomograph form, and has been compared with some experimental data other than that on the basis of which it was derived, it seems logical to retain it for stress estimation purposes. However, for the purpose of studying trends and parametric dependences, the simpler Eq. (27), with the coefficient 0.85 replaced by 0.90 is likely to be advantageous.

Maximum root-mean-square stress in curved panels. — On the basis of analytically developed expressions, in which empirically derived corrections have been included, the maximum root-mean-square stress σ_R (at the middle of the straight edge) in a cylindrically curved panel with radius of curvature R has been found [8,10] to be related to the corresponding stress in a similar flat panel as

$$\frac{\sigma_R}{\sigma} = \left[\frac{f_R}{f}\right]^{-1/2}$$
$$\left[1 + 0.453\left(\frac{b^2}{hR}\right)\left(\frac{A^2+0.034}{A^4+9.62A^2+1}\right)\right] \qquad (30)$$

where, as before, $A = b/a =$ length of curved edge/length of straight edge and f/f_R is given by Eq. (25).

The applicability of this relation is limited to $0.3 \leq b/a \leq 3.0$, $a/h \geq 100$, and $a/R \leq 0.35$. On the whole, stress estimates for curved panels obtained on the basis of Eq. (30) or corresponding nomographs correlate more poorly with test data than similar estimates for flat panels (e.g., see Fig. 5.2 of Ref. [9]); the estimates tend to be too high — by as much as a factor of 5 at low stress values, generally less at higher stresses. Means for improving the estimates are not available at present.

Panel loss factors. — References 19 and 20 suggest a method for estimating the loss factors of panels with riveted edges, taking account of such parameters as rivet spacing, width of contact area, and panel wavelength (as a function of frequency). However, this method may be somewhat too cumbersome

for preliminary design purposes. Abundant experimental evidence* indicates that for conventional aircraft structures (i.e., for structures not provided with special damping treatments), η differs little from 10^{-2}. This value may therefore be taken as a reasonable estimate, unless measured data for the particular structure under consideration are available.

It should be noted, however, that air flow along a panel may extract energy from the panel vibrations, and thus increase the effective structural loss factor — or that this flow may feed energy into panel vibrations (under conditions approaching panel flutter), and thus decrease the effective loss factor. At present there is available no means for estimating this effect, and one can do little better than to evaluate it on the basis of experimental measurements.

From the curves of the above-mentioned Fig. 34 of Ref. [10] one may determine that the number N of cycles that a panel survives before failing is related to the maximum root-mean-square stress σ according to

$$\log N = -\alpha \log\left(\frac{\sigma}{\sigma_{ref}}\right) + \log \beta \qquad (31)$$

or

$$N = \beta(\sigma/\sigma_{ref})^{-\alpha} , \qquad (32)$$

where σ_{ref} is a reference stress value, here taken as 10^3 psi, and where α and β are constants whose values are listed in Table I.

Although the time-variation of a randomly varying parameter like the panel stress is not a simple sinusoid, and

TABLE I

VALUES OF CONSTANTS FOR FATIGUE-CYCLES/STRESS RELATIONS

	Skin-Stringer		Honeycomb-Core Sandwich	
	Panel 7075-T6	Stringer 7075-T6	Facing 7075-T6	Core* 5052-H39
α	4.60	2.74	4.06	7.05
$\log \beta$ for C = -95%	9.38	6.98	9.22	11.76
$\log \beta$ for C = -50%	9.75	7.57	9.53	12.16
$\log \beta$ for C = 0	10.04	7.94	9.75	12.76

*Note: Honeycomb core fatigue expression contains additional factor accounting for core density.

Cycles to failure; survival probability. — One may expect that the number of stress reversals a panel can withstand decreases as the stress amplitude increases. Related test data, corresponding to skin-stringer panels of 7075-T6 aluminum alloy exposed to random noise, are given in Fig. 34 of Ref. [10], together with curves representing various statistical confidence limits. Later test data [8] were found to fall within these same confidence limits; the design nomographs given in Refs. [8] and [10] are based on these confidence limit curves.

one cannot speak of cycles in the strictest terms, one may expect the panel vibrations to be approximately sinusoidal in time as long as they are dominated by a single mode — as was previously assumed in the response analysis. One may then consider the stress signal between successive zero crossings as a half cycle, with the signal varying approximately like a sinusoid at the natural frequency of the system. Knowing this frequency and the number of cycles N that produce failure, one may calculate the fatigue life.

Fatigue life. — For failure probability distributions that are symmetric about the mean, (50 - C/2)% of the samples fail under fewer stress cycles than the number corresponding to the -C% confidence limit [22]. Thus, for example, if N = 10^7 cycles corresponds to a confidence limit of -50% for a given panel design exposed to a given excitation, one may expect 25% of all panels to fail at less than 10^7 cycles

(i.e., one may expect 75% of all panels to survive after 10^7 cycles).

The fatigue life of a structure obviously must be defined in terms of a failure probability or similar statistical measure. Here it is convenient to use the fatigue life corresponding to the −C% confidence limit, which one may find from

$$T_C = N_C/f , \qquad (33)$$

where N_C is obtained from Eqs. (31) or (32) for the confidence limit in question and f denotes the natural frequency of the panel under consideration.

Stringers

In typical skin-stringer structures, fatigue failures of stringers usually occur at the clip attachment (where the stringer is joined to the frame or bulkhead), because of the presence of stress raisers in that location. Because of the general complexity of the problem, little analytical work has been done on stringer fatigue, and since stringer failures generally occur in the interior of practical structures, there appears to exist no quantitative field data. Reference [8] contains the most definitive available analytical and experimental information; it is on that report that the following discussion is based.

Analytical estimate of maximum root-mean-square stress. — The analysis of stringer stresses presented in Ref. [8] is based on the following assumptions: (1) The total force acting on a stringer corresponds to the net shear force (integrated distribution minus corner reactions) that acts at the edge of a simply supported panel, which is deflecting in its first mode, in response to a pressure that is uniformly distributed over the panel, but varying randomly in time. (2) The force acting on a stringer is distributed uniformly along its length and acts on the rivet line. (3) The maximum stress in the stringer occurs in flexure at the clip attachment point, where the stringer is taken to be clamped with respect to bending.

With these assumptions one finds that the maximum root-mean-square stress in a stringer obeys*

---

*This relation follows from Eq. (67) of Ref. [8]. However, there the numerical coefficient, which here is $2^{3/2}/3\pi^{7/2} \approx 0.0171$, was erroneously omitted.

$$\sigma_b = \frac{2^{3/2}}{3\pi^{7/2}} \frac{Hb_s^3}{I^*} \sqrt{\frac{f\Phi_p(f)}{\eta}} \left(\frac{b_s}{a_s} + \frac{a_s}{b_s}\right)^{-1} , \quad (34)$$

where b_s denotes the stringer length (which is usually, but not necessarily always, the longer panel edge length), a_s the distance between the rivet lines of adjacent stringers, H the stringer depth (see Fig. 7) and I^* an effective moment of inertia of the stringer cross-section, given by

$$I^* = I_{xx} - \frac{I_{xz}^2}{I_{zz}} . \qquad (35)$$

Here I_{xx} denotes the centroidal moment of inertia of the stringer cross section about an axis perpendicular to the panel surface (see Fig. 7), I_{zz} represents a similar moment of inertia about an axis parallel to the panel surface, and I_{xz} denotes a similar mixed moment of inertia.† As previously, f denotes the fundamental resonance frequency of a skin panel, η represents its loss factor, and $\Phi_p(f)$ denotes the spectral density of the fluctuating excitation pressure (at the frequency f).

Correction of rms stress estimate on basis of test data. — Since the various assumptions involved in the derivation of Eq. (34) are likely to represent only rather poor approximations of conditions occurring in practical structures, one would expect predictions made on the basis of Eq. (34) to deviate from corresponding experimental results. Comparison of such predictions with experimental data [8] indicates that the experimentally observed root-mean-square stress σ_e on the average is related to the corresponding σ_b calculated from Eq. (34) as

$$\frac{\sigma_e}{1 \text{ psi}} = 900 \left(\frac{\sigma_b}{1 \text{ psi}}\right)^{1/5} . \qquad (36)$$

The above relation was derived on the basis of calculated σ_b values ranging from about 150 to 3000 psi; its applicability to values outside this range remains to be established.

Cycles to failure; survival probability; fatigue life. — Data presented in Fig. 44 of Ref. [8] indicate that

---

†That is, $I_{xx} = \int_A z^2 dA$, $I_{zz} = \int_A x^2 dA$, $I_{xz} = \int_A xz dA$, where A represents the area of the stringer cross-section. Appendix I of Ref. [8] gives expressions for these moments of inertia for zee, channel, and hat sections.

173

the number N of cycles that a stringer
survives before failing is related to
the experimentally observed maximum rms
stress σ_e by an equation of the same
form as Eq. (31), but with different
constants, as shown in Table I.

The discussion and the relation
between confidence limits and failure
probability presented (in relation to
panel failures) in the paragraphs fol-
lowing Eq. (32) apply equally well to
stringer failures, as does the discus-
sion of fatigue life. One may thus find
the stringer fatigue life corresponding
to the -C% confidence limit by use of Eq.
(33), keeping in mind that the stringer
motion is dominated by the panel reso-
nance, so that the natural frequency f
of the *panel* again enters this relation.

FATIGUE LIFE OF HONEYCOMB-CORE SANDWICH FLAPS

Overview of Estimation Approach

The fatigue of flat, rectangular
panels of honeycomb sandwich construc-
tion is discussed in Ref. [10] on the
basis of classical thin-plate theory.
Earlier data cited in that report indi-
cate that this theory yields good ap-
proximations to observed vibration and
stress responses associated with the
fundamental panel mode, and that shear-
ing of the core plays no important role,
unless this core is very flimsy.

A flap element, however, may be ex-
pected to behave more like an end-sup-
ported beam than like an edge-supported
panel. The analytical results available
for panels thus do not apply to flap
elements directly, although one may hope
that honeycomb panel fatigue data will
also be useful for honeycomb beam fa-
tigue life estimation. The following
paragraphs, therefore, summarize the re-
sults of a corresponding beam analysis
and then apply related available fatigue
data to develop a fatigue life estima-
tion approach.

Beam Response

Resonance frequency. — In order to
simplify the analysis, it is useful as a
first approximation to assume the fluctu-
ating excitation pressure to be uniform-
ly distributed over (one surface of) a
flap element, and to consider only the
response of the first mode of that ele-
ment modeled as a uniform beam — in a
manner somewhat analogous to that used
in skin-stringer panel analyses or
honeycomb sandwich panel analyses [10].

The resonance frequency of the
first mode of a beam is given (e.g. Ref.
[23]) by*

$$f_1 = \frac{\gamma}{L^2} \sqrt{\frac{B}{\mu}} \quad , \qquad (37)$$

where L denotes the beam's length, B its
bending stiffness, and μ its mass per
unit length. The parameter γ represents
a constant that depends on the boundary
conditions; for a beam that is simply
supported on both ends, $\gamma = \pi/2 \approx 1.57$,
and for a clamped-clamped (or free-free)
beam, $\gamma \approx 3.56$. Since in a realistic
flap element the boundary conditions are
likely to be somewhere between simply
supported and fully clamped, one may rea-
sonably take $\gamma \approx \sqrt{(1.57)(3.56)} \approx 2.36$ as
a first estimate, in absence of better
information.

Resonant response of fundamental
mode. — If one assumes the beam response
to be dominated by the first mode — as
was done for panels — , one may apply
classical modal analysis techniques
(e.g., Ref. [24]) and the well-known ex-
pression (e.g., Refs. [24,25]) for the
response of simple modal systems to ran-
dom excitation, in order to determine
that the (time-average) root-mean-square
displacement of the beam obeys

$$u_{rms} = \phi(x) \sqrt{\frac{\pi f_1 \phi_F(f_1)/2\eta_1}{(2\pi f_1)^2 M_1}} \quad , \qquad (38)$$

Here η_1 denotes the loss factor of the
beam in its first mode and M_1 the total
beam mass. The function $\phi(x)$ represents
the mode shape associated with the first
mode, normalized for unit average value
of its square over the beam length.

ϕ_F denotes the spectral density of
the modal force $F_1(t)$, which is given by

$$F_1(t) = ep_0(t)J_1 \qquad (39)$$

where

$$J_1 = \int_0^L \phi(x)dx \quad , \qquad (40)$$

for a pressure $p_0(t)$ that is uniform over

_____

*This expression is based on the
assumption that shear effects are negli-
gible. As shown in Ref. [4], the finite
shear stiffness of a beam reduces its
natural frequency, but in most practical
cases this reduction is insignificant.

174

(on side of) the beam. As indicated in Fig. 8, e represents the beam's width. Since the spectral density Φ_F of the force is proportional to the mean-square force, Φ_F is related to the spectral density Φ_p of the pressure $p_0(t)$ as

$$\Phi_F = e^2 J_1^2 \Phi_p \ . \qquad (41)$$
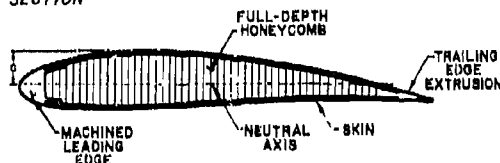
ISOMETRIC SKETCH
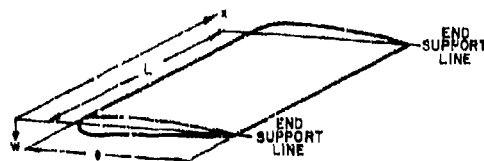
SECTION

Fig. 8.   Typical Honeycomb-Core Sandwich Flap Element.

Maximum root-mean-square stress in skin. - For a given amount of beam flexure, the greatest skin tensile and compressive stresses occur in those fibers that are farthest from the beam's neutral surface. If c denotes the distance from the neutral surface to the farthest fiber (see Fig. 8), then one may write the maximum rms stress associated with beam vibrations in the fundamental mode as

$$\sigma_1 = Ec(u''_{rms})_{max} \ . \qquad (42)$$

where the primes indicate differentiation with respect to the lengthwise coordinate x and E denotes the modulus of elasticity of the skin material.

If one combines Eqs. (38), (41) and (42), one finds that the maximum root-mean-square skin stress obeys

$$\sigma_1 = \frac{ecEJ_1 \phi''_{max}}{\pi^{3/2} 2^{5/2} \mu L f_1^2} \sqrt{\frac{f_1 \Phi_p(f_1)}{\eta_1}} \ , \qquad (43)$$

where ϕ''_{max} represents the maximum absolute value of $\phi''(x)$.

The term $J_1 \phi''_{max}$ depends only on the mode shape, and thus only on the boundary conditions. By use of information given in Refs. [24] and [26] one may find that

$$J_1 \phi''_{max} = \begin{cases} 4\pi/L \approx 12.6/L \\ \text{for simply supported ends} \\ 37.4/L \\ \text{for clamped ends.} \end{cases} \qquad (44)$$

If one uses the geometric average (21.7/L) of the above values, in view of the uncertainty of the actual boundary conditions, one may rewrite Eq. (43) as

$$\sigma_1 \approx 0.69 \ \frac{eCE}{\mu L^2 f_1^{3/2}} \sqrt{\frac{\Phi_p(f_1)}{\eta_1}}$$

$$\approx 0.19 \ \frac{ecEL}{(\mu B^3)^{1/4}} \sqrt{\frac{\Phi_p(f_1)}{\eta_1}} \ , \qquad (45)$$

where the latter expression is obtained by substitution of Eq. (37) with $\gamma = 2.36$.

Maximum root-mean-square shear stress in core. - In Ref. [1] it is shown by means of an analysis that parallels that presented in Ref. [27] that, for a simply supported sandwich beam, the ratio of the maximum shear stress τ in the core to the maximum tensile stress in the skin obeys

$$\frac{\tau}{\sigma_1} = \frac{\pi B}{LACE} \approx \pi \ \frac{t_s}{L} \ , \qquad (46)$$

where A represents the cross-sectional area of the beam. The approximate equality applies for a beam with a rectangular cross-section, with skin of thickness t_s; this approximate expression may suffice for the evaluation of a rough estimate in cases where not enough information is available to apply the more complete expression.

For beams with other than simply supported boundaries, the simple analytical approach leading to Eq. (46) does not work and results like the above cannot be obtained readily. It is nevertheless suggested that Eq. (46) be used for estimation purposes for all boundary conditions.

Loss factors. - The available data pertaining to loss factors of honeycomb core sandwich structures are extremely limited. Reference [10] reports test results for about 30 different panels vibrating in their fundamental modes. Their loss factors were found to lie between about 0.03 and 0.05, and to be comparable to a value of about 0.04 measured on panels obtained from aircraft

175

development programs.

In absence of more directly applicable data, an estimate of $n_1 = 0.04$ appears to be reasonable.

Fatigue Life

Facing Sheets. — From Fig. 51 of Ref. [10], which summarizes the results of a regression analysis of data obtained on panels with 7075-T6 aluminum alloy facing sheets, one may deduce that the relation between the maximum skin stress σ_1 and the number of cycles N that the skin can withstand without failing is of the same form as Eq. (31), with the constants as given in Table I.

The discussion that follows Eq. (32) applies here again; the fatigue life T_C of the facing sheet corresponding to the -C% confidence limit may be found from Eq. (32), but the natural frequency f must be replaced by the fundamental natural frequency f_1 of the sandwich beam.

Core. — Only very few core shear fatigue failure data points appear to be available; the data do not suffice for regression analysis, and thus one cannot establish confidence limits.

Perhaps the best one can do at present is to accept the design data indicated in Fig. 86 of Ref. [10], although the basis for that figure is not indicated. From the curves in that figure one may deduce the following relation between the number of cycles N_h that will induce failure in 5052-H39 aluminum alloy honeycomb core, the maximum rms core shear stress τ, and the core density d:

$$\log N_h = 12.76 - 7.05 \log \left(\frac{\tau}{\tau_{ref}}\right)$$
$$+ 10.58 \log \left(\frac{d}{d_{ref}}\right) \quad (47)$$

or

$$N_h \approx 5.7 \times 10^{12} \left(\frac{\tau}{\tau_{ref}}\right)^{-7.05} \left(\frac{d}{d_{ref}}\right)^{10.6}. \quad (48)$$

Here $\tau_{ref} = 1$ psi is a reference value of shear stress and $d_{ref} = 1$ lb/ft^3 is a reference value of density.

Since not enough data are available for the determination of confidence limits, it appears reasonable to assume

that the foregoing expressions pertain to the 0% confidence limit. In order to estimate the numbers of cycles to failure corresponding to the -50% and -95% confidence limits (probably conservatively), one may multiply the value of N_h obtained froms Eqs. (47) or (48) by 0.4 and 0.1, respectively.

The honeycomb fatigue life, of course, may be calculated from Eq. (32), again using the fundamental natural frequency f_1 of the sandwich beam in place of f.

DEPENDENCE OF FATIGUE LIFE ON JET AND STRUCTURAL PARAMETERS; DESIGN CONSIDERATIONS

Skin-Stringer Flaps

Skin panels. — In order to display typical parametric dependences most simply, it is useful to focus on commonly used skin-stringer configurations that have aspect ratios b/a > 2.5. For such configurations, the function F(b/a) of Eq. (20) may be approximated by $\sqrt{3(b/a)}$ and the function G(b/a) of Eq. (24) may be taken as equal to 0.69.

If one takes the maximum panel stress to be given by Eq. (27), with the coefficient 0.59 replaced by 0.42 in accordance with the discussion presented after Eq. (29), then one finds by use of the above indicated approximations that

$$\sigma \approx 0.39 \left|\frac{c_L a^2 \phi_p(f)}{h^3 n}\right|^{1/2} \quad (49)$$

and that the fundamental natural frequency of the skin panel obeys

$$f \approx 0.69 \, hc_L/a^2. \quad (50)$$

Substitution of Eq. (49) into (32), and substitution of the result and of Eq. (50) into Eq. (33) gives the panel fatigue life as

$$T = 110 \, \beta \, \frac{h^{5.90}}{a^{2.60} \, c_L^{3.30}} \left(\frac{n\sigma_{ref}^2}{\phi_p(f)}\right)^{2.30}. \quad (51)$$

If the panel resonance frequency f is in a range where $\phi_p(f)$ varies little with changes in f, then Eq. (51) exhibits all of the dependences on panel parameters. On the other hand, if $\phi_p(f)$ depends significantly on f, the dependence of f on the panel parameters will also affect these dependences. From Eqs. (8), (15) and (16) one finds that

$$\phi_p(f) \approx \begin{cases} 0.0115 \, \rho_0^2 U_0^3 X & \text{for } f \ll f_T \\[2ex] 0.29 \, \rho_0^2 U_0^5 / X f^2 & \text{for } f \gg f_T \end{cases} \quad (52)$$

where the transition frequency f_T obeys*

$$f_T \approx 1.5 \, U_0 / X \, . \qquad (53)$$

Substitution of Eq. (52) into (51) and use of Eq. (50) results in

$$\frac{T}{10^3 \sigma_{ref}^{4.60} \beta} \approx \begin{cases} 3.2 \times 10^3 \left(\dfrac{h^{5.90} \, \eta^{2.30}}{a^{2.60} \, c_L^{3.30}} \right) \left(\dfrac{1}{X^{2.30} \, \rho_0^{4.60} \, U_0^{6.90}} \right) & \text{for } f \ll f_T \\[3ex] 1.9 \left(\dfrac{h^{10.50} \, \eta^{2.30} \, c_L^{1.30}}{a^{11.60}} \right) \left(\dfrac{X^{2.30}}{\rho_0^{4.60} \, U_0^{11.50}} \right) & \text{for } f \gg f_T \end{cases} \quad (54)$$

where the first parentheses enclose all relevant panel parameters, whereas the second enclose the jet parameter terms.

Stringers. — Again for the purpose of exhibiting the salient parametric effects most simply, it is useful to consider the common case where the stringer length is the same as the greater of the two panel edge lengths, and where the spacing between stringers is equal to the shorter panel edge length. With $b_S = b$ and $a_S = a$, assuming $b/a > 3$, and

using Eq. (50) in Eq. (34), one may obtain an approximate expression for the "theoretical" maximum stress. If one corrects this according to Eq. (36), in order to obtain a better representation of the actual (experimentally observed) maximum stress σ_e, one finds

$$\frac{\sigma_e}{\sigma_{ref}} \approx 1.5 \left[\frac{Hb^2}{I^* \sigma_{ref}} \sqrt{\frac{hc_L \phi_p(f)}{\eta}} \right]^{1/5} . \quad (55)$$

By combining Eqs. (55), (50), (32), and (33) one obtains the stringer fatigue life T as

$$T = 0.488 \, \frac{a^2}{(hc_L)^{1.274} \, b^{1.096}} \, .$$

$$\left(\frac{I^* \sigma_{ref}}{H} \right)^{0.548} \left(\frac{\eta}{\phi_p(f)} \right)^{0.274} . \quad (56)$$

If one again uses Eq. (52) to account for the dependence of $\phi_p(f)$ on the panel resonance frequency f, which frequency again may be approximated by Eq. (50), one may find that

$$\frac{T}{\sigma_{ref}^{0.548} \beta} = \begin{cases} 1.6 \left(\dfrac{a^2}{b^{1.096}} \dfrac{(I^*/H)^{0.548} \, \eta^{0.274}}{(hc_L)^{1.274}} \right) \left(\dfrac{1}{X^{0.274} \, \rho_0^{0.548} \, U_0^{0.822}} \right) & \text{for } f \ll f_T \\[3ex] 0.55 \left(\dfrac{a^{0.904}}{b^{1.096}} \dfrac{(I^*/H)^{0.548} \, \eta^{0.274}}{(hc_L)^{0.726}} \right) \left(\dfrac{X^{0.274}}{\rho_0^{0.548} \, U_0^{1.370}} \right) & \text{for } f \gg f_T \end{cases} \quad (57)$$

Design considerations. — As is evident from Eqs. (51) and (56), the fatigue lives of skin panels and of stringers increase as the excitation — represented by the pressure spectral density $\phi_p(f)$ — decreases. This behavior is as one would expect intuitively, of course. Since this spectral density decreases with increasing frequency, as indicated in Eq. (7), one should design the skin panel to

have as high a fundamental resonance frequency f as possible. In view of Eq. (50), this implies that one should choose the largest admissible panel thickness h

and the smallest panel edge length a. One might also consider choosing materials with large longitudinal wavespeeds c_L, but most acceptable structural materials have wavespeeds that differ by no more than about 10% from each other, so that one stands to gain little by choosing alternate materials on this basis.

From the exponents appearing in Eq. (57) one may readily determine by what factors the fatigue life of a blown flap *panel* may be expected to change as the result of changing the various parameters.

---

*For the typical values of $U_0 = 750$ ft/sec and $X = 10$ ft, one finds $f_T \approx 110$ Hz.

Thus, for example, one finds that a change in the skin thickness h by a factor of 1.50 (i.e., a 50% increase) would increase the high-frequency fatigue life by a factor of 71; similarly, decreasing the panel edge length a by 20% would lengthen the fatigue life by a factor of 14, whereas doubling the damping η would increase that life by a factor of 4.9.

As evident from Eq. (54), relatively small changes in h and a can lead to quite considerable changes in panel fatigue life; the effects of changes in the other structural parameters are much less significant. Small changes in the distance X of the flap from the engine exit have relatively little effect on the fatigue life, and changes in the gas density (associated with exhaust temperature changes) that can occur with a given engine also are likely to have only minor significance. On the other hand, the exit velocity U_0 is of great importance; a mere 10% increase in this velocity can reduce the panel fatigue life to about one-third of its original value.

From the exponents appearing in that part of Eq. (57) that applies for $f \gg f_T$, one may observe, for example, that doubling of the panel edge length a (which is also equal to the spacing between the stringers) increases the *stringer* fatigue life by a factor of 1.91, whereas doubling the stringer length b reduces the fatigue life to 0.47 of its former value.

By comparing Eqs. (54) and (57) one finds that the panel fatigue life is much more sensitive to parameter changes than is the stringer fatigue life. It is also evident that increases in h and c_L, as well as decreases in a, serve to increase the panel fatigue life, while they result in reductions in the stringer fatigue life.

From Eqs. (51) and (56) one may determine that the ratio of panel to stringer fatigue life obeys

$$\frac{T_p}{T_s} \approx 230 \left(\frac{\beta_p}{\beta_s}\right)\left(\frac{h}{a}\right)^{4.60}\left(\frac{Hb\,h}{I^*}\right)^{0.548} \times$$

$$\left(\frac{h\eta\sigma_{ref}^2}{c_L\phi_p(f)}\right)^{2.026}, \qquad (58)$$

where the subscripts P and s refer to panel and stringer parameters, respectively.

If one introduces $\phi_p(f)$ as given by Eq. (52) for $f \gg f_T$, if one substitutes for f from Eq. (50), and if one takes

$I^* \sim H^3h/2$ (which corresponds to an I-beam of height and flange width H, with flange thickness h), one finds that one may approximate the above expression by

$$\frac{T_p}{T_s} = 81 \left(\frac{\beta_p}{\beta_s}\right)\left(\frac{h}{a}\right)^{10.68}\left(\frac{b}{H}\right)^{1.096} \times$$

$$\left[\left(\frac{\sigma_{ref}}{q_0}\right)^2\left(\frac{X}{a}\right)\left(\frac{a}{U_0}\right) \cdot \eta\right]^{2.026} \qquad (59)$$

for the purpose of making order-of-magnitude estimates. Substitution of the middle values of β_p and β_s given in Table I and of typical orders of magnitude of the various ratios then leads to

$$\frac{T_p}{T_s} \approx 81 \left(\frac{5.6 \times 10^9}{3.7 \times 10^7}\right)\left(\frac{1}{100}\right)^{10.7}\left(\frac{20}{1}\right)^{1.1} \times$$

$$\left[\left(\frac{10^3}{2}\right)^2\left(\frac{20}{1}\right)\left(\frac{25}{1}\right)(0.01)\right]^2 \approx 2.1 \times 10^{-4},$$

which indicates that stringers typically have much longer fatigue lives than skin panels — in agreement with experimental observations.

Thus, one generally should first design the panels so that they have adequate fatigue lives, and then verify that the stringer design one selects (usually on the basis of other than fatigue considerations) has a fatigue life that is no less than that of the panels.

Honeycomb-Core Sandwich Flaps

Facing sheets (skin). — If one substitutes into the fatigue life expression of Eq. (33) the number of cycles to failure as given by Eq. (32) and the natural frequency expression of Eq. (37) — with γ = 2.36, to account for boundaries that are neither simply supported nor fully clamped, — and if one also uses the second stress expression of Eq. (45), which applies for the same boundary conditions, one finds that the facing sheet fatigue life obeys

$$T \approx 360\beta \; \frac{\mu^{1.515}B^{2.545}}{L^{206}} \left(\frac{\sigma_{ref}}{ecLE}\right)^{4.06}\left(\frac{\eta_1}{\phi_p(f_1)}\right)^{2.03}$$

$$\approx 360\beta \left(\frac{L^2}{c_f r}\right)\left(\frac{Ar}{ecL}\right)^{4.06}\left(\frac{\eta_1 r\sigma_{ref}^2}{c_f\phi_p(f_1)}\right)^{2.03}. \qquad (60)$$

The second form of this expression involves the useful newly defined effective flap density $\rho_f = \mu/A$, effective radius of gyration $r = \sqrt{B/EA}$, and effective longitudinal wavespeed $c_f = \sqrt{E/\rho_f}$.

Equation (60) exhibits all structural parametric dependences for the low-frequency case, where $\phi_p(f_1)$ is essentially independent of frequency. But, since $\phi_p(f_1)$ does vary significantly at the higher frequencies, the aforementioned equations need to be modified. If one substitutes for $\phi_p(f)$ from Eq. (52) and again uses Eq. (37) with $\gamma = 2.36$, one obtains

greater fatigue life by designing the flap element to have a higher fundamental resonance. In view of Eq. (37), a high fundamental resonance results from use of short unsupported spans L and of large stiffness/mass ratios B/μ.

As evident from Eqs. (61) and (63), reductions in L can result in quite dramatic increases in fatigue life, provided that the flap element's fundamental

$$
\frac{T}{10^5 \sigma_{ref}^{4.06}} \approx
\begin{cases}
31 \left(\dfrac{\mu^{1.515} B^{2.545} \eta^{2.03}}{L^{6.12} (ecE)^{4.06}} \right) \left(\dfrac{1}{\chi^{2.03} \rho_0^{4.06} U_0^{6.09}} \right) & \text{for } f \ll f_T \\[20pt]
1.45 \left(\dfrac{B^{4.57} \eta^{2.03}}{\mu^{0.515} L^{14.24} (ecE)^{4.06}} \right) \left(\dfrac{\chi^{2.03}}{\rho_0^{4.06} U_0^{10.15}} \right) & \text{for } f \gg f_T
\end{cases}
\tag{61}
$$

As previously, the first set of parentheses in each expression encloses the structural parameters, the second the jet parameters.

Core. — By substitution of the cycles-to-failure relation of Eq. (32) and the natural frequency expression of Eq. (37), again using $\gamma = 2.36$, into the fatigue life equation, Eq. (33), and by using also the stress expressions of Eqs. (45) and (46), one may find that the honeycomb core fatigue life T obeys

$$
\frac{T}{9.3 \times 10^{13}} \approx \left(\frac{L^2}{c_f r} \right) \left(\frac{d}{d_{ref}} \right)^{10.6} \left(\frac{A}{er} \right)^{7.05} \times
$$
$$
\left(\frac{r \eta_1 \tau_{ref}^2}{c_f \phi_p(f_1)} \right)^{3.525} . \tag{62}
$$

If one again substitutes for ϕ_p from Eq. (52), one obtains

frequency f_1 is above the transition frequency f_T. If $f_1 < f_T$, then the facing sheet fatigue life increase produced by a given amount of length reduction is somewhat less dramatic — and this length reduction may indeed by expected even to reduce the core's fatigue life.

From Eqs. (60) and (62) one may determine that

$$
\frac{T_h}{T_f} \approx \frac{2.6 \times 10^{11}}{B} \left(\frac{A}{cr} \right)^{2.99} \left(\frac{cL}{r^2} \right)^{4.06} \left(\frac{d}{d_{ref}} \right)^{10.6} \times
$$
$$
\left(\frac{\tau_{ref}}{\sigma_{ref}} \right)^{7.05} \left[\frac{\eta_1 r \sigma_{ref}^2}{c_f \phi_p(f_1)} \right]^{1.495} , \tag{64}
$$

where the subscript h refers to the honeycomb core and f to the facing sheet.

$$
\frac{T}{10^{18} \tau^{7.05} d_{ref}^{-10.6}} =
\begin{cases}
640 \left(L^2 \left| \dfrac{\mu}{B} \right|^{2.26} \left| \dfrac{A}{e} \right|^{7.05} d^{10.6} \eta^{1.52} \right) \left(\dfrac{1}{\chi^{3.525} \rho_0^{7.05} U_0^{10.575}} \right) & \text{for } f \ll f_T \\[20pt]
3.1 \left(\dfrac{d^{10.6} (A/e)^{7.05} \eta^{3.525}}{L^{12.1} (\mu/B)^{1.265}} \right) \left(\dfrac{\chi^{3.525}}{\rho_0^{7.05} U_0^{17.625}} \right) & \text{for } f \gg f_T
\end{cases}
\tag{63}
$$

Design considerations. — Equations (60) and (62) show that the fatigue lives of facing sheets and honeycomb cores increase with decreasing exciting pressure spectral density (evaluated at the flap element's fundamental natural frequency). This trend is as one would expect intuitively. Since the spectral density decreases with increasing frequency, as indicated by Eq. (9), one may obtain

From Eqs. (37) and (52) one may determine that for $f \gg f_T$,

$$
\frac{\eta_1 r \sigma_{ref}^2}{c_f \phi_p(f_1)} \approx 4.8 \eta_1 \left(\frac{\sigma_{ref}}{q_0} \right)^2 \left(\frac{r}{L} \right)^3 \left(\frac{\chi}{L} \right) \left(\frac{c_f}{U_0} \right). \tag{65}
$$

For typical orders of magnitude for the various parameters, one finds that

179

$$\left(\frac{\sigma_{ref}}{q_0}\right)^2 \left(\frac{r}{L}\right)^3 \left(\frac{X}{L}\right)\left(\frac{c_f}{U_0}\right) \sim \left(\frac{10^3}{2}\right)^2 \left(\frac{1}{30}\right)^3 (1)\left(\frac{5}{1}\right) \approx 46$$

so that, for the middle value of β

$$\frac{T_h}{T_f} \approx \frac{2.6 \times 10^{11}}{3.4 \times 10^8} (15)^{2.99} (50)^{4.06} (1)^{10.6} \times$$

$$\left(\frac{1}{10^3}\right)^{7.05} \left|(4.8)10^{-2}(46)\right|^{1.495}$$

$$\approx 4.6 \times 10^{-9} .$$

Thus, one generally would expect core shear fatigue failures to occur long before facing sheet failures.* In designing a flap element it thus appears logical first to select a core that has the required fatigue life, and then to verify that the facing sheet will endure at least for the same time span.

From the exponents appearing in Eqs. (61) and (63) one may determine the factors by which the facing-sheet and honeycomb-core fatigue lives change as the result of changes in the various structural and jet parameters. Clearly, the one most significant structural parameter is the unsupported span length L; a mere 10% decrease in L may be expected to increase the fatigue life of the skin by a factor of about 4.5, and that of the core by about 3.6.

Changes in the flap element's flexural rigidity and mass per unit length may be seen to have somewhat lesser effects on these two fatigue lives. On the other hand, the core density affects the core's fatigue life very significantly, with a 10% increase extending the fatigue life by a factor of about 2.7. Again, the jet exit velocity is the most important jet parameter, with a 10% decrease in U_0 leading to increases in the skin and core fatigue lives by factors of 2.9 and 6.4, respectively.

Fatigue Life Corrections for Other Aluminum Alloys

The various fatigue life estimates presented so far were obtained on the basis of experimental data on structures made of only one kind of material — namely, 7075-T6 aluminum for skin/stringer structures and for the facing sheets of honeycomb sandwich structures, and

---

*No comparable experimental data appear to be available. Such data as are available [Ref. 10] pertain to panels, rather than beams, and are affected by stress raisers (e.g., fasteners) that reduce the skin fatigue life.

5052-H39 aluminum for honeycomb cores. This section suggests how one may correct the estimates pertaining to the aforementioned materials so as to obtain corresponding estimates for other aluminum alloys.

Similarity of S-N curves. — The fatigue behavior of materials generally is described by so-called "S-N" curves, which are plots of the fully reversed stress amplitude S versus the number of stress cycles N at which a specimen fails when subjected to cyclic stress of that amplitude. When plotted on log-log scales, the S-N curves for most aluminum alloys appear very nearly like parallel straight lines, at least in the low stress and large N region; e.g., see Ref. [28] and Table 3.3.1(c) of Ref. [29]. Although the classical S-N curves are obtained from experiments where the stress amplitude is held constant (for each data point), whereas the S-N curves represented by Eq. (31) correspond to random stress variations with a given mean-square value, one may expect the latter log-log curves for various alloys to be parallel, if the former are parallel.

If one assumes that the root-mean-square stress σ that different alloys can withstand for a given number of cycles is proportional to the "fatigue stress" S of the material, then for two different materials (indicated by subscripts 1 and 2),

$$\frac{\sigma_2}{\sigma_1} = \frac{S_2}{S_1} . \qquad (66)$$

For materials that exhibit a definite endurance limit (i.e., a stress amplitude that the material can withstand essentially for an unlimited number of cycles), one would be inclined to take the endurance limit as the fatigue stress. Aluminum alloys do not have endurance limits, in general [29,30]; for such alloys one needs to define S as corresponding to any fixed number of cycles, say $N = 10^8$.

Correction for fatigue stress. — If one rewrites Eq. (32) as

$$\frac{\sigma_1}{\sigma_{ref}} = \left(\frac{N}{\beta}\right)^{-1/\alpha} \qquad (67)$$

and introduces Eq. (66), one may obtain

$$\frac{\sigma_2}{\sigma_{ref}} = \frac{S_2}{S_1} \frac{\sigma_1}{\sigma_{ref}} = \frac{S_2}{S_1} \left(\frac{N}{\beta}\right)^{-1/\alpha} . \qquad (68)$$

Then, the number N of cycles that material 2 can withstand is found to obey

$$N = \beta \left(\frac{\sigma}{\sigma_{ref}}\right)^{-\alpha} \left(\frac{S_2}{S_1}\right)^{\alpha} = N_1 \cdot k_m, \quad (69)$$

where N denotes the number of cycles one calculates for the basic material — i.e., by use of Eq. (32) — and where

$$k_m = (S_2/S_1)^{\alpha} \quad (70)$$

is a correction factor that accounts for differences in the material's fatigue properties.

Since the fatigue life is proportional to the number of cycles to failure, one may obtain the fatigue life of a structural component of any aluminum alloy by multiplying the life one calculates for that component on the basis of Eqs. (32) by the appropriate correction factor k_m. The exponent α, of course, depends on the component — i.e., on which of the aforementioned equations apply.

Estimation of fatigue stress ratio. — Unfortunately, S-N curves are available for only a few alloys. For alloys for which no fatigue data are available, one may use the rough approximation that

$$\frac{S_2}{S_1} \approx \frac{Y_2}{Y_1} , \quad (71)$$

where Y represents the yield stress of the material [30]. As demonstrated in Ref. [1], this approximation is very close for some materials, but may be about 20% too high or too low for others. Nevertheless, in absence of better information, one can do no better than to use the above relation.

Materials other than aluminum. — It should be noted that the procedure suggested here for aluminum alloys cannot readily be extended to other materials, unless their S-N curves have the same slopes (on a log-log plot) as those for aluminum. Unfortunately, most other materials have different slopes and many — notably steels — have segments of greatly differing slopes. For such materials, further analysis and/or experimental investigation is required.

CONCLUDING REMARKS

The approach suggested here for estimation of fluctuating pressures associated with engine exhausts is based on extrapolation of nondimensionalized fluctuating pressure data obtained from sim-

ple jets and on interpretation of similar velocity distribution data from measurements in the exhausts of a very limited number of fan-jet engines. Clearly, the availability of data on the fluctuating pressure distribution in the exhaust of the engine to be used in any particular application may be expected to improve the characterization of these pressures and to increase the confidence one has in fatigue life estimates based on these pressures.

The response, stress, and fatigue life estimation approaches presented in this report follow the earlier literature in assuming only the fundamental mode of the structure to be of importance. Although this assumption may lead to conservative designs and life estimates in many cases, one can easily visualize practical situations where higher modes predominate. Such cases are particularly likely to occur with engine exhaust excitation, where the excitation pressures are correlated over small areas, have spectral peaks at frequencies considerably higher than the fundamental structural resonance, and convect along the structural surface. Indeed, there also exists some experimental evidence that shows that higher structural modes play important roles in responses to flow excitation. Of course, the importance of higher modes in determining fatigue life is also enhanced by the higher fatigue damage accumulation rates associated with their higher resonance frequencies. Thus, it appears advisable to use the response, stress, and fatigue estimation approaches suggested here with some caution.

Any but the most grossly empirical fatigue life prediction method must be based on information concerning how the number of loading cycles that a structure can withstand varies with the fluctuating stress. The method suggested in this report is based on sonic fatigue data derived from tests on panel specimens of only one material for each panel type. In particular, the data pertaining to the fatigue of honeycomb-core sandwich structures is extremely limited. Thus, although one may expect the suggested prediction technique to yield good results for structures that are closely related to those whose fatigue data were used in development of the technique, its reliability is much reduced for other structures.

181

REFERENCES

1. E.E. Ungar, K.L. Chandiramani, and J.E. Barger, "Excitation, Response, and Fatigue Life Estimation Methods for the Structural Design of Externally Blown Flaps," NASA CR-112216, Oct. 1972.

2. R.G. Dursch, W.J. Kreim, and W.A. Olsen, "Externally Blown Flap Noise," AIAA Paper No. 72-129, Jan. 1972.

3. L.D. Landau and E.M. Lifshitz, *Fluid Mechanics*, p. 133, Pergamon Press, London, 1959.

4. L.C. Sutherland et al., "Sonic and Vibration Environments for Ground Facilities — A Design Manual," Wyle Laboratories, Research Staff Report No. WR 68-2, pp. 6-13, March 1968.

5. J.C. Laurence, "Intensity Scale and Spectra of Turbulence in Mixing Region of Free Subsonic Jet," Lewis Flight Propulsion Laboratory, Cleveland, Ohio, Report No. 1292.

6. D.R. Strong, T.E. Siddon, and W.T. Chu, "Pressure Fluctuations on a Flat Plate with Oblique Jet Impingement," UTIAS Note No. 107, Feb. 1967.

7. B.L. Clarkson, "Stresses in Skin Panels Subjected to Random Acoustic Loading," AFML-TR-67-199, June 1967.

8. F.F. Rudder, Jr., "Acoustic Fatigue of Aircraft Structural Component Assemblies," AFFDL-TR-71-107, Feb. 1972.

9. A.G.R. Thomson, "Acoustic Fatigue Design Data, Part I," AGARDograph 162, May 1972.

10. J.R. Ballentine, F.F. Rudder, Jr., J.T. Mathis, and H.E. Plumblee, Jr., "Refinement of Sonic Fatigue Structural Design Criteria," AFFDL-TR-67-156, Jan. 1968.

11. L.W. Lassiter and R.W. Hess, "Calculated and Measured Stresses in Simple Panels Subject to Intense Random Acoustic Loading Including the Near Noise Field of a Turbojet Engine," NACA Report No. 1367, 1958.

12. J.F. Wilby, "Random Excitation of a Simple Panel, Some Experimental Results," University of Southampton, AASU Report No. 231, Jan. 1963.

13. J.R. Ballentine, H.E. Plumblee, Jr., and C.W. Schneider, "Sonic Fatigue in Combined Environment," AFFDL-TR-66-7, May 1965.

14. B.L. Clarkson and R.D. Ford, "The Response of Typical Aircraft Structure to Jet Noise," J. Royal Aeronautical Soc., Vol. 66, pp. 31-40, Jan. 1962.

15. B.L. Clarkson and R.D. Ford, "An Experimental Investigation of the Random Excitation of a Tailplane Section by Jet Noise," ASD-TDR-62-680, July 1962.

16. D.R.B. Webb, A.R. Keeler, G.R. Allen, "Surface Pressures and Structural Strains Resulting from Fluctuations in the Turbulent Boundary Layer of a Fairey Delta 2 Aircraft," R.A.E. Tech. Note Structures 313, May 1962.

17. J.F. Wilby, W.V. Baht, F.L. Gloyna, "Airplane Fuselage Response to Turbulent Boundary Layers," ASME Paper 70-WA/DE-10, Nov. 1970.

18. G. Bayerdörfer, "Experimental Investigations to Establish Acoustic Fatigue Design Charts," J. Sound Vib., Vol. 17, pp. 55-62, 1971.

19. E.E. Ungar, "Damping of Panels," Chapter 14 of *Noise and Vibration Control*, L.L. Beranek, Ed., McGraw-Hill Book Co., Inc., New York, 1971.

20. E.E. Ungar and J.R. Carbonell, "On Panel Vibration Damping due to Structural Joints," AIAA Journal, Vol. 4, pp. 1385-1390, Aug. 1966.

21. L. Cremer and M. Heckl, Chapter 3 of *Körperschall*, Springer Verlag, Berlin, 1967.

22. S.H. Crandall, "Measurement of Stationary Random Processes," Chapter 2 of *Random Vibration*, S.H. Crandall, Ed., The M.I.T. Press, Cambridge, Mass., 1963.

23. J.P. Den Hartog, *Mechanical Vibration*, p. 432, McGraw-Hill Book Co., Inc., New York, Fourth Edition, 1956.

24. E.E. Ungar, "Mechanical Vibrations," Section 6 of *Mechanical Design and Systems Handbook*, H. Rothbart, Ed., McGraw-Hill Book Co., Inc., New York, 1964.

25. S. H. Crandall, "Statistical Properties of Response to Random Vibration," Chapter 4 of *Random Vibration*, S.H. Crandall, Ed., The M.I.T. Press, Cambridge, Mass., 1958.

26. R.E.D. Bishop and D.C. Johnson, *Vibration Analysis Tables*, Cambridge University Press, Cambridge, 1956.

27. C.E. Wallace, "Stress Response and Fatigue Life of Acoustically Excited Sandwich Panels," pp. 228-244, *Acoustical Fatigue in Aerospace Structures*, W.J. Trapp and D.M. Forney, Jr., Eds., Syracuse University Press, 1965.

28. P.R. McGowan, et al., "Structural Design for Acoustic Fatigue," Fig. 48, p. 92, ASD-TDR-63-820, Oct. 1963.

29. Anon., *Strength of Metal Aircraft Elements*, MIL-HDBK-5, Armed Forces Supply Support Center, Washington, D.C., March 1961.

30. V.M. Faires, Chapter IV of *Design of Machine Elements*, The Macmillan Co., New York, Third Edition, 1955.

DETUNING AS A MECHANICAL DESIGN APPROACH

Charles T. Morrow
Advanced Technology Center, Inc.
Dallas, Texas 75222

Under some conditions coincidence or near coincidence of mechanical resonance frequencies can lead to catastrophic failures of equipment during exposure to a shock or vibration environment. Detuning is then a powerful method for improving reliability, but it should be applied with full appreciation of the fact that resonance frequencies may depend on the mechanical impedance of the structure or test platform to which the equipment is mounted. Fortunately, detuning can often be accomplished in such a way that it is effective for a wide variety of mounting impedances.

INTRODUCTION

It has been common, in designing equipment for reliability under severe shock or vibration conditions, to deal with potential failure points as if they were subject merely to static stress. In fact, design to an equivalent static acceleration has been proposed as a routine approach for gaining reliability. According to this approach, if a part fails or malfunctions, the designer must fasten it tighter, stiffen it, brace it, or devise a way of distributing the stress in the part.

All rules of thumb, however valuable, have their limitations. A conspicuous example of the breakdown of this one is found when a light and flexible part such as a potentiometer wiper is mounted to something more massive and rigid, having a resonance frequency in coincidence or near coincidence, and chatters in consequence. Only small increases in stiffness or preloading of the wiper may be permissible if it is to perform without excessive friction. Yet, a small increase, if the wiper resonance happens to be on the low side of coincidence, may actually aggravate any tendency to lose contact.

Under such circumstances, planned detuning may be a much more powerful approach than designing for a greater static acceleration. This can be illustrated in terms of two linear simple mechanical resonators coupled in tandem. (The wiper can be considered to be a linear mechanical element up to the chattering point.)

Previous papers, Refs. [1] and [2], showed at some length the conditions under which a detuning policy is preferable to a stiffening policy, on the assumption of no loading of the first resonator by the second. These papers were written at a time when shock and vibration engineers tended to think of shock and vibration excitation sources as having infinite impedance, that is, a capability to control the applied motion to the same time function regardless of the nature of the equipment excited. Investigators were preoccupied primarily with design and environmental test within this restriction. The idea of testing to a controlled force (zero impedance) was still in a very preliminary exploratory state, and the phrase "mechanical impedance" was just beginning to become familiar.

The possibility of alternate source impedances brings with it the chance that two resonance frequencies that are successfully staggered for one source impedance may be close to coincidence for another. Then, even if the equipment passes an environmental test, it may be far from an optimum design for practical application.

Fortunately, it is easier to maintain acceptable detuning under a variety of conditions than it would be to maintain, for any reason, a precise coincidence.

CASE OF ZERO MECHANICAL LOADING

To facilitate gaining insight into this situation we will calculate from a lumped-element two-resonator model that includes no damping, an

in Fig. 1, and explore the effect of source impedances on the resonance frequencies. The masses m_b, m_1 and m_2 are in order of descending magnitude. For the first investigation, we will simplify the model further by assuming that the first resonator, which consists of two masses and a spring and is driven, experiences no mechanical loading from the simple resonator attached to it. Under this assumption, the two system resonances are simply those of the two resonators, and only the first is affected by source impedance.

$$f_2 = \frac{\omega_2}{2\pi} = \frac{1}{2\pi}\sqrt{k_2/m_2} \tag{1}$$

That of the first resonator is

$$f_1 = \frac{\omega_1}{2\pi} = \frac{1}{2\pi}\sqrt{k_1/m_1} \tag{2}$$

for infinite source impedance (velocity V_b as the excitation) and, according to Appendix 1, a zero impedance source (force F_b as the excitation) shifts this to

$$f = \frac{\omega}{2\pi} = \sqrt{f_1^2 + f_{b1}^2} \quad , \tag{3}$$

where

$$f_{b1} = \frac{\omega_{b1}}{2\pi} = \frac{1}{2\pi}\sqrt{k_1/m_b} \quad . \tag{4}$$
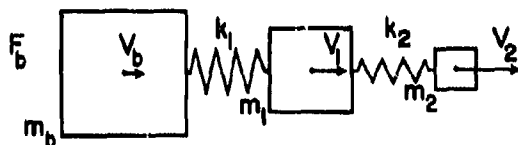
Fig. 1 - Undamped Three-Mass Two-Spring Mechanical System

Note that decreasing the source impedance from infinity to zero increases the resonance frequency of the first resonator. Consequently, an equipment that failed an infinite-impedance shock or vibration test because of close resonance frequency coincidence might fail a zero-impedance test instead if the designer stiffened the second resonator. We observed in the introduction that, even with constant source impedance, a stiffening of the second resonator without examination of existing resonance frequency relationships could aggravate a reliability problem by bringing the frequencies closer together. We now have a more general reason to discourage indiscriminate stiffening.

For optimum design by mechanical detuning, the designer should decrease f_2, which runs counter to his instincts, or increase f_1, if

coincidence or near coincidence is observed for an infinite-impedance source, unless he has the privilege of making large shifts, or f_{b1} is so low that the system resonances are, for practical purposes, insensitive to source impedance.

For example, suppose a designer who observes $f_1 = f_2 = 1000$ Hz, for an infinite-impedance source, shifts f_2 to 1250 Hz for the purpose of detuning, and then observes resonances for a zero-impedance source. The second resonance remains $f_2 = 1250$ Hz. If, by chance, $f_{b1} = 750$ Hz, the first resonance becomes $f = 1250$ Hz. Coincidence is avoided for the infinite-impedance source but reoccurs for the zero-impedance source. If he increases f_2 to 1500 Hz, coincidence does not reoccur, but the margin is less for zero impedance.

Alternately if he shifts f_2 to 750 Hz or even to a lower frequency, coincidence can not reoccur. The margin is in fact greater for zero source impedance than for infinite source impedance.

Conversely, suppose a designer who observes $f = f_2 = 1250$ Hz for a zero-impedance source, shifts f_2 to 1000 Hz for the purpose of detuning and then observes resonances for a zero-impedance source. The second resonance remains $f_2 = 1000$ Hz. If, by chance, $f_{b1} = 750$ Hz, the first resonance becomes $f_1 = 1000$ Hz. Coincidence is avoided for the zero-impedance source but reoccurs for the infinite-impedance source. If he decreases f_2 further, coincidence is avoided, but the margin is less for the infinite than the zero source impedance.

Consequently, he should increase f_2 or decrease f, unless he has the privilege of making large shifts, if coincidence is observed for a zero-impedance source.

CASE OF SMALL LOADING

We now generalize to permit mechanical loading of the first resonator by the second, but we assume the loading to be so small that it does not reduce transmission to the second resonator so much that coincidence ceases to be a critical factor

The resonances of the complete system now become somewhat different in frequency than those of the individual resonators. It is shown in Appendix 2 that the system resonance frequencies for an infinite impedance source are obtainable from the formula

$$f^2 = \frac{(f_1^2 + f_{12}^2 + f_2^2) \pm \sqrt{(f_1^2 + f_{12}^2 + f_2^2)^2 - 4f_1^2 f_2^2}}{2}$$

$$= \frac{(f_1^2 + f_{12}^2 + f_2^2) \pm \sqrt{(f_1^2 - f_2^2)^2 + 2(f_1^2 + f_2^2)f_{12}^2 + f_{12}^4}}{2} \quad , \tag{5}$$

and those for a zero impedance source are
obtainable from

$$f^2 = \frac{(f_1^2+f_{12}^2+f_2^2+f_{b1}^2) \pm \sqrt{(f_1^2+f_{12}^2+f_2^2+f_{b1}^2)^2 - 4(f_1^2 f_2^2+f_{12}^2 f_{b1}^2+f_2^2 f_{b1}^2)}}{2}$$

$$= \frac{(f_1^2+f_{12}^2+f_2^2+f_{b1}^2) \pm \sqrt{(f_1^2-f_2^2)^2+2(f_1^2+f_2^2)f_{12}^2+(f_{12}^2-f_{b1}^2)^2+2(f_1^2+f_2^2)f_{b1}^2}}{2},$$

(6)

with

$$f_{12} = \frac{1}{2\pi}\sqrt{k_2/m_1} \; , \tag{7}$$

and

$$f_{b1} = \frac{1}{2\pi}\sqrt{k_1/m_b} \; . \tag{8}$$

Since the square roots of Eqs. (5) and (6) can never be zero, exact coincidence in terms of system resonances is impossible, regardless of the values of f_1 and f_2. Nevertheless, for small loading, the system resonance frequencies can be close enough to create a reliability hazard.

Let us now explore what may be sufficient to make the zero-impedance separation equal or greater than the infinite-impedance separation. This is crudely equivalent to requiring that the additional positive terms under the radical of Eq. (6), in comparison with Eq. (5), be larger than the additional negative terms, or

$$f_1^2 > f_2^2 + f_{12}^2 - f_{b1}^2 \; . \tag{9}$$

That increasing f_{b1} should be beneficial was an unexpected result. Decreasing m_b implies more of a redesign, in most cases, than the designer would be permitted to make. However, decreasing k_1 helps in two ways – by increasing f_1 and by increasing f_{b1}.

From the conditions assumed at the beginning, both f_{12} and f_{b1} are rather small compared to f_2. Consequently, Eq. (9) is very similar to the prescription for no loading – detune f_1 and f_2 so that $f_1 > f_2$. However, Eq. (9) is not a quantitative expression of the sufficient condition but merely an indicator that was convenient to calculate. It indicates the direction in which detuning should go – the same as in the case of no loading – but the actual detuning should, if anything, be made greater than suggested by the formula.

ARBITRARY SIMPLE REACTIVE IMPEDANCE

At this point, it is natural to inquire whether separation of system resonance frequencies can be maintained over a greater variety of source impedances than zero and infinity. We will limit ourselves to simple reactances such as those of a mass or a stiffness.

The impedance presented to the excitation source by the dissipationless three-mass resonant system is shown in Appendix 3 to be

$$Z_b = F_b/V_b$$

$$= \frac{j2\pi f[f_{b1}^2 f_{12}^2+f_{b1}^2 f_2^2+f_1^2 f_2^2-(f_1^2+f_{12}^2+f_2^2 f_{b1}^2)f^2+f^4]}{f_1^2 f_2^2-(f_1^2+f_{12}^2+f_2^2)f^2+f^4}$$

(10)

The general character of this expression is shown in Fig. 2. The poles, indicated by crosses on the frequency axis, correspond to the system resonances for infinite source impedance, and the zeros, indicated by dots on the frequency axis, correspond to the system resonances for zero source impedance.
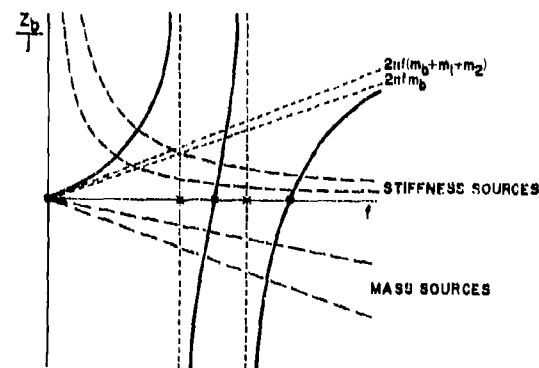

Fig. 2 – Impedance Presented to the Source

187

System resonance frequencies for other sources occur when Z_b is equal in magnitude but opposite in sign to the source reactance. In the absence of damping, these correspond to maximum response of m_2. Consequently, if the source reactance is shown reflected to the opposite side of the frequency axis, its intersections with Z_b determine the corresponding system resonance frequencies, and, in the absence of damping, the frequencies of maximum response of m_2. This reflection has been performed for simple mass reactances, which appear as dashed straight lines extending from the origin below the frequency axis, and for simple stiffness reactances, which appear as dashed hyperbolas above the frequency axis. It is apparent that <u>system resonances that are well separated for both zero and infinite source impedances will also be well separated for these alternate simple source reactances.</u>

Damping of the three-mass resonator would decrease the hazard associated with coincidence or near coincidence but increase the amount of detuning that must be carried out before significant benefit results. Heavy damping would also shift the frequencies of maximum response.

CONCLUSION

If the system resonance frequencies of a three-mass resonant system with masses m_b, m_1, and m_2 in order of descending magnitude are staggered sufficiently for infinite source impedance and zero source impedance, wide separation can also be maintained for intermediate simple reactances. The favorable direction for detuning is the one that increases f_1 or decreases f_b, if coincidence is observed for an infinite-impedance source. The reverse is true if coincidence is observed for a zero-impedance source.

Prescription of exact amounts of detuning for various situations would require more analysis than was given here but would not be proportionately helpful to the mechanical designer. He would not usually possess in advance all the data required for more sophisticated prediction. After a test failure, he may be able to effect a remedy more quickly by skillful cut and try, guided by system resonance frequency measurements for zero and infinite source impedances, than by detailed computation based on more complete measurements of dynamics and environmental response.

However, this study reinforces the concept of detuning as a powerful tool for design for reliability under shock or vibration excitation by showing that detuning can be made effective for a wide variety of source impedances. Inspection of the theory for shock (especially Fourier transform or spectrum) and for random vibration shows that if detuning is beneficial for periodic excitation, it is beneficial for these more subtle excitations as well.

Furthermore, situations frequently arise such that servo control system stability is dependent on relationships between mechanical resonance frequencies of a device as mounted to aerospace or other structure. This study should provide the control system designer with beneficial insights into that type of problem.

REFERENCES

1. C. T. Morrow, "Effect of Detuning in Coupled Systems Excited by Single-Frequency Sweeps," Bulletin No. 29, Shock, Vibration and Associated Environments, Part 4, (June 1961), pp. 226-240.

2. C. T. Morrow, B. A. Troesch and H. R. Spence, "Random Response of Two Coupled Resonators without Loading," Jour. Acous. Soc. Amer., Vol. 33, No. 1, (January 1961), pp. 46-55.

APPENDIX 1

RESONANCE FREQUENCIES FOR CASE OF NO MECHANICAL LOADING

If the simple resonator comprising k_2 and m_2 does not load the rest of the mechanical system, the corresponding system resonance frequency, ω_2, as measured on an infinite impedance mount, is unaffected by the impedance of the source at m_c.

The other system resonance frequency is source-impedance sensitive and is calculable from the remainder of the system with k_2 and m_2 ignored.

For the case of an applied force F_b,

$$j\omega m_b V_b + k_1 (V_b - V_1)/j\omega = F_b , \qquad (11)$$

RESONANCE FREQUENCIES FOR CASE OF NO MECHANICAL LOADING (Concluded)

and

$$j\omega m_1 V_1 + k_1(V_1 - V_b)/j\omega = 0 \ , \qquad (12)$$

where

$$\omega = 2\pi f \ , \qquad (13)$$

and V_1 and V_b are the complex vibrational velocities of the appropriate masses.

Let

$$\omega_{b1}^2 = k_1/m_b \ , \qquad (14)$$

and

$$\omega_1^2 = k_1/m_1 \ . \qquad (15)$$

It follows that

$$-\omega^2 V_b + \omega_{b1}^2 V_1 = j\omega F_b/m_b \ , \qquad (16)$$

and

$$-\omega^2 V_1 + \omega_1^2(V_1 - V_b) = 0. \qquad (17)$$

Hence

$$V_b = (\omega_1^2 - \omega^2) \ V_1/\omega_1^2, \qquad (18)$$

and

$$V_1 = \omega_1^2 F_b/(\omega_1^2 + \omega_{b1}^2 - \omega^2)j\omega m_b \qquad (19)$$

so that, for a zero-impedance source,

$$\omega^2 = \omega_1^2 + \omega_{b1}^2 \ , \qquad (20)$$

which is equivalent to Eq. (3).

APPENDIX 2

RESONANCE FREQUENCIES WITH MECHANICAL LOADING

The complete equations for the mechanical system of Fig. 1 are:

$$j\omega m_b \ V_b + k_1(V_b - V_1)/j\omega = F_b \ , \qquad (11)$$

$$j\omega m_1 \ V_1 + k_1(V_1 - V_b)/j\omega + k_2(V_1 - V_2)/j\omega = 0 \qquad (21)$$

189

RESONANCE FREQUENCIES WITH MECHANICAL LOADING (Concluded)

and

$$J\omega m_2 V_2 + k_2(V_2-V_1)/J\omega = 0 , \qquad (22)$$

or

$$-\omega^2 V_b + \omega_{b1}^2(V_b-V_1) = j\omega F_b/m_b , \qquad (16)$$

$$-\omega^2 V_1 + \omega_1^2(V_1-V_b) + \omega_{12}^2(V_1-V_2) = 0 , \qquad (23)$$

and

$$-\omega^2 V_2 + \omega_2^2(V_2-V_1) = 0 , \qquad (24)$$

where

$$\omega_2^2 = k_2/m_2 \qquad (25)$$

$$\omega_{12}^2 = k_2/m_1 \qquad (26)$$

and V_2 is the complex vibrational velocity of m_2.

From Eq. (24),

$$V_1 = \frac{(\omega_2^2-\omega^2) V_2}{\omega_2^2} . \qquad (27)$$

Substitution in Eq. (23) yields

$$V_2 = \frac{\omega_1^2\omega_2^2 V_b}{\omega^4-(\omega_1^2+\omega_{12}^2+\omega_2^2)\omega^2+\omega_1^2\omega_2^2} , \qquad (28)$$

which, for an applied V_b has poles at

$$\omega = \frac{(\omega_1^2+\omega_{12}^2+\omega_2^2) \pm \sqrt{(\omega_1^2+\omega_{12}^2+\omega_2^2)^2-4\omega_1^2\omega_2^2}}{2} , \qquad (29)$$

which is equivalent to Eq. (5).

Alternately, for an applied V_b, substitute Eqs. (27) and (29) into Eq. (16) to obtain

$$V_2 = \frac{\omega_1^2\omega_2^2 F_b/j\omega m_b}{\omega^4-(\omega_1^2+\omega_{12}^2+\omega_2^2+\omega_{b1}^2)\omega^2+\omega_1^2\omega_2^2+\omega_{12}^2\omega_{b1}^2+\omega_2^2\omega_{b1}^2} . \qquad (30)$$

This has poles for

$$\omega^2 = \frac{(\omega_1^2+\omega_{12}^2+\omega_2^2+\omega_{b1}^2)\pm \sqrt{(\omega_1^2+\omega_{12}^2+\omega_2^2+\omega_{b1}^2)^2-4(\omega_1^2\omega_2^2+\omega_{12}^2\omega_{b1}^2+\omega_2^2\omega_{b1}^2)}}{2} \qquad (31)$$

which is equivalent to Eq. (6).

190

IMPEDANCE PRESENTED TO THE SOURCE

Substitute Eq. (28) into Eq. (23) to eliminate V_s.

$$V_1 = \frac{\omega_1^2 V_b}{\omega_1^2 + \omega_{12}^2 - \omega^2 - \omega_{12}^2 \omega_2^2/(\omega_2^2 - \omega^2)}$$

$$= \frac{\omega_1^2 (\omega_2^2 - \omega^2) V_b}{(\omega_1^2 + \omega_{12}^2 - \omega^2)(\omega_2^2 - \omega^2) - \omega_{12}^2 \omega_2^2} \tag{32}$$

Substitute Eq. (32) into Eq. (16)

$$V_b = \frac{j\omega F_b/m_b}{(\omega_{b1}^2 - \omega^2) - \omega_1^2 \omega_{b1}^2 (\omega_2^2 - \omega^2)/[(\omega_1^2 + \omega_{12}^2 - \omega^2)(\omega_2^2 - \omega^2) - \omega_{12}^2 \omega_2^2]}$$

$$= \frac{(j\omega F_b/m_b)[(\omega_1^2 + \omega_{12}^2 - \omega^2)(\omega_2^2 - \omega_1^2) - \omega_{12}^2 \omega_2^2]}{(\omega_{b1}^2 - \omega^2)[(\omega_1^2 + \omega_{12}^2 - \omega^2)(\omega_2^2 - \omega^2) - \omega_{12}^2 \omega_2^2] - \omega_1^2 \omega_{b1}^2 (\omega_2^2 - \omega^2)}$$

$$= \frac{(F_b/j\omega m_b)[\omega_1^2 \omega_2^2 - (\omega_1^2 + \omega_{12}^2 + \omega_2^2)\omega^2 + \omega^4)}{\omega_{b1}^2 \omega_{12}^2 + \omega_{b1}^2 \omega_2^2 + \omega_1^2 \omega_2^2 - (\omega_1^2 + \omega_{12}^2 + \omega_2^2 + \omega_{b1}^2)\omega^2 + \omega^4}$$

Therefore

$$Z_b = \frac{j\omega m_b [\omega_{b1}^2 \omega_{12}^2 + \omega_{b1}^2 \omega_2^2 + \omega_1^2 \omega_2^2 - (\omega_1^2 + \omega_{12}^2 + \omega_2^2 + \omega_{b1}^2)\omega^2 + \omega^4]}{\omega_1^2 \omega_2^2 - (\omega_1^2 + \omega_{12}^2 + \omega_2^2)\omega^2 + \omega^4} \tag{33}$$

which is equivalent to Eq. (10).

Note that for ω large

$$Z_b = j\omega m_b , \tag{34}$$

whereas for ω small,

$$Z_b = \frac{j\omega m_b (\omega_{b1}^2 \omega_{12}^2 + \omega_{b1}^2 \omega_2^2 + \omega_1^2 \omega_2^2)}{\omega_1^2 \omega_2^2} = j\omega(m_b + m_1 + m_2) . \tag{35}$$

EARTHQUAKE RESPONSE OF SHOCK-MOUNTED
COMMUNICATIONS EQUIPMENT

N. J. DeCapua, G. Nevrincean, E. F. Witt

Bell Laboratories
Whippany, New Jersey

This paper describes the case history of a shock-mount failure caused by an earthquake excitation. The failure resulted from large pendulum-mode displacements of the ceiling suspended equipment. Auxiliary leaf spring isolators were designed to eliminate this pendulum mode and still maintain adequate protection against nuclear blast. A test program was conducted using actual communications equipment excited by an input more severe than the El Centro Earthquake. The design objectives were met and the hardware functioned without damage.

INTRODUCTION

A significant portion of the long distance network of the Bell System is designed to resist the effects of a nuclear detonation. Buildings along such routes are usually underground, and equipment within many of these structures is shock-mounted to isolate it from the high frequency, high acceleration motions associated with a nuclear blast environment. The basic objective in shock-mounting is, of course, to convert a relatively high frequency system, such as equipment bolted directly to a building, into a low frequency system by placing shock-mounts between the equipment and the building. This low frequency system isolates the equipment from the blast environment and exposes it to only modest, nondamaging accelerations.

Although a low frequency system provides isolation from high frequency inputs, it is vulnerable to low frequency excitations. Thus, since a nuclear environment also includes a low frequency oscillatory ground motion, the behavior of the shock-isolated system must be such that induced displacements are not excessive. The vertical and horizontal frequencies of the shock-mounted system must be chosen so that they are low enough to isolate blast induced accelerations and yet high enough to avoid excessive ground motion induced displacements.

These problems of frequency tradeoffs become even more critical when a shock-mounted installation is in an earthquake area. It is possible that low frequency induced displacements can be greater in a severe earthquake environment than in a nuclear ground motion environment.

The L3 carrier repeater station is an example of a hardened facility (1964) where recent events vividly demonstrated the need to consider severe low frequency motion in designing shock-isolated systems. A number of repeater stations located in Southern California were exposed to the San Fernando Earthquake in February 1971. Although communication service was maintained, a number of the suspension shock-mounts illustrated in Fig. 1 were broken or damaged at one station (located on the seismic contour map shown in Fig. 2).

Low frequency systems such as the above must be avoided. This paper describes how this particular system was modified to eliminate the pendulum mode while maintaining blast protection. The test program conducted to corroborate design objectives and qualify new hardware is also described.

THE REPEATER STATIONS

In these underground structures, measuring approximately 10 ft long by 6 ft wide with 8 ft ceilings, equipment is shock-isolated with ceiling-suspended coil spring mounts, as indicated in Fig. 1. This provides vertical isolation to keep nuclear blast induced accelerations of the equipment below a 3g level. Communications equipment is designed to withstand accelerations up to 3g's in a vibratory environment. The vertical frequency of this system is approximately 3 Hz. The frequency in the lateral direction is about 0.45 Hz. In the longitudinal direction, the geometric configuration is such that the pendulum swing is at least 1 ft, with a frequency of less than 0.90 Hz. There are other rocking modes which will be discussed later.
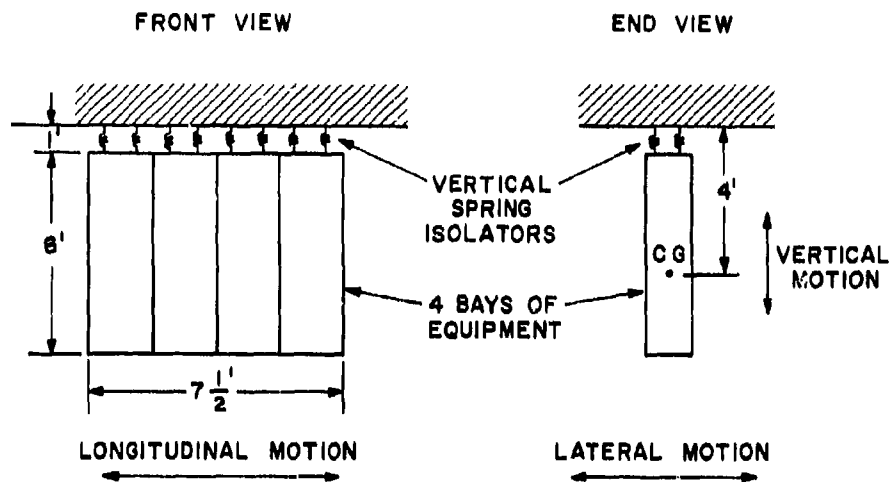
FRONT VIEW   END VIEW

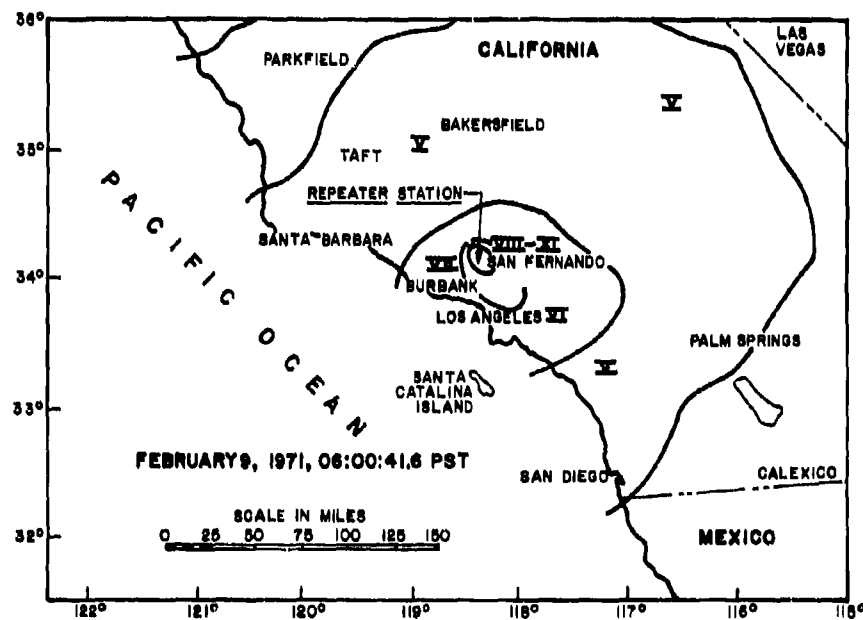Fig. 1 - Shock isolation system for blast protection

Fig. 2 - Seismic intensity contours for the San Fernando Earthquake

194

Lateral clearance between the equipment and adjacent walls is a minimum of 6 in.

EARTHQUAKE EXCITATIONS

As shown in Fig. 2, the shock-mount failure occurred in an area experiencing an earthquake of Richter Magnitude 6.6 with a duration of 12 seconds. A more severe earthquake probably would have resulted in equipment impacting against adjacent walls, possibly causing loss of service. Thus, it is advisable to provide protection against more severe earthquake motions. The El Centro Earthquake [1], 1940 N-S component, is an example of what is generally considered a severe earthquake and is used to establish design limits. The duration of the El Centro record was 30 seconds with a peak acceleration of 0.30g and a Richter magnitude of 7.3. The 1 percent damped displacement shock spectrum of El Centro is shown in Fig. 3.
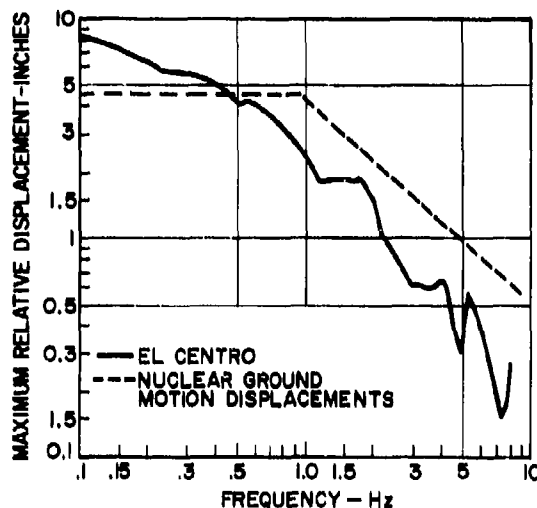
Fig. 3 - 1 Percent damped displacement shock spectra

A typical spectrum for nuclear blast induced ground motion [2] is also shown for comparison. This represents an envelope of spectra for overpressures up to 50 psi produced by a 20 MT detonation. Note the similarities in low frequency response. The earthquake excitation would cause the equipment center of gravity to displace about 4.5 in. laterally and 2.5 in. longitudinally. The resulting motion at the base of the equipment would be at least 9 in. laterally and 2.5 in. longitudinally. The corresponding values for nuclear blast would be similar. These displacements exceed the 6-in. clearance

limit for the equipment assembly. However, before this limit is reached, the vertical shock-mounts would probably fail since they were not designed to experience such large lateral displacements. Lateral restraints are required to avoid damage to the equipment during the maximum expected earthquake and nuclear blast effects.

RESTRAINING METHOD

The requirements for the additional restraints were:

1. Must limit horizontal and vertical motion under El Centro Earthquake conditions to about ±2.0 in.

2. Horizontal frequencies limited to 3 Hz maximum to ensure protection from nuclear blast shock.

3. Existing vertical isolation should not be affected.

After considering a number of alternative designs, the authors decided that the existing vertical shock-mounts should remain attached and that auxiliary leaf spring isolators would be placed at each of the four corners of the equipment, as shown in Fig. 4. This arrangement is easy to install, low in cost, and requires no maintenance.

DESIGN OF AUXILIARY LEAF SPRING ISOLATORS

A relatively simple dynamic analysis was performed to assist in determining the characteristics of the proposed auxiliary leaf spring isolators. Since the equipment is essentially a rigid structure compared to the flexibility of the vertical coil springs and the proposed horizontal leaf springs, a dynamic lumped-mass model was easy to describe. For design purposes, it was assumed that longitudinal and lateral motions could be decoupled. Thus, two separate models were used to describe the system, as shown in Fig. 5. All members in the models are rigid except the springs. The location and magnitude of the mass points were chosen to duplicate the mass and inertia of the communications equipment.

The ultimate configuration of the auxiliary leaf spring isolators, as indicated in Fig. 6, evolved from an attempt to achieve the same frequency (of approximately 3 Hz) in both the longitudinal and lateral directions. This was achieved by increasing the moment of inertia of one side. A leaf spring with constant moment of inertia would yield different longitudinal and lateral stiffnesses, as indicated by the following relationships:
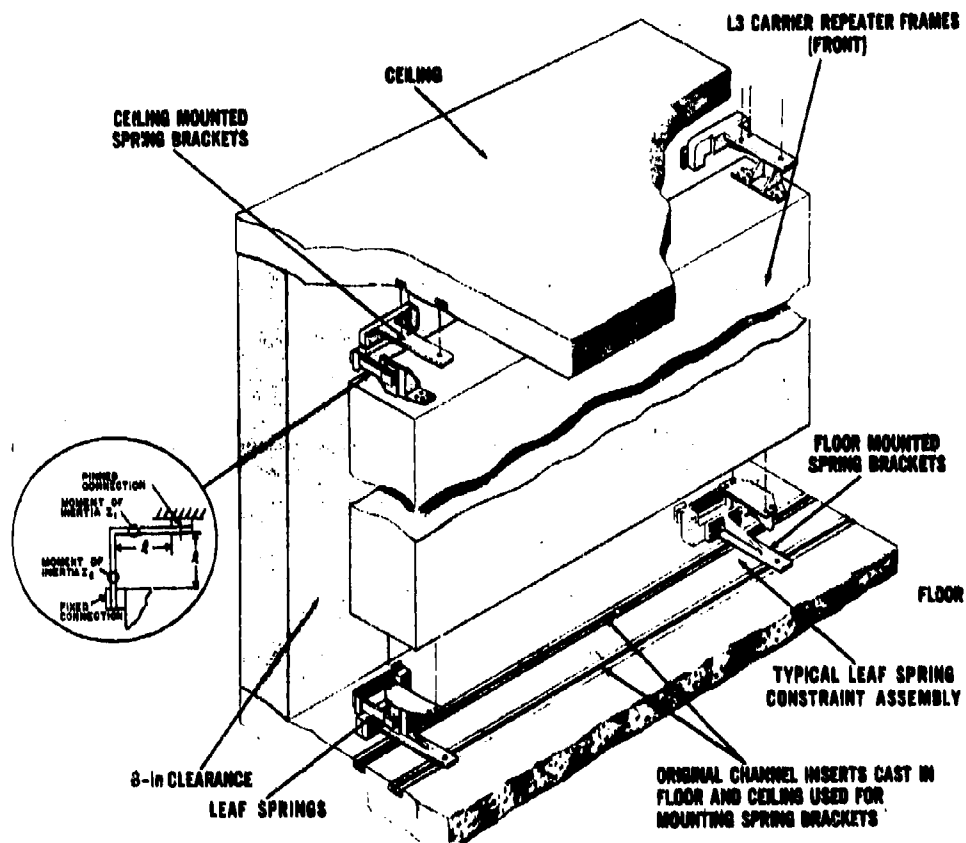
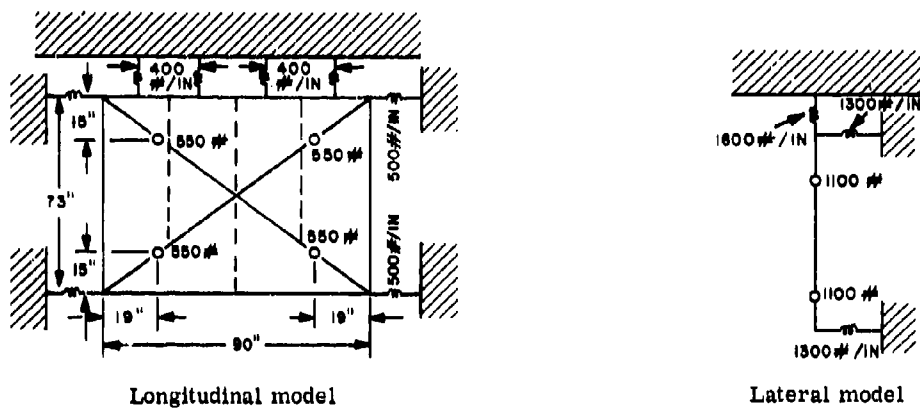Fig. 4 - Shock-mounting for blast and earthquake protection
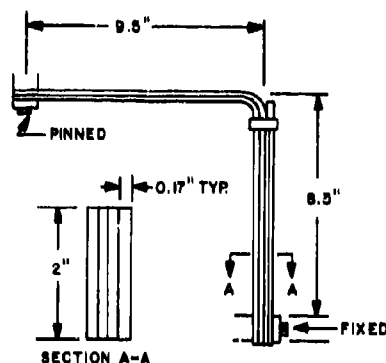

Longitudinal model

Lateral model

Fig. 5 - Dynamic models

Fig. 6 - Auxiliary leaf spring isolator

$$k_{long.} = \frac{EI_2}{\ell^3} \frac{1}{\left[\frac{1}{3} - \frac{1}{4}\left(1 + \frac{I_2}{I_1}\right) \right]}, \quad (1)$$

and

$$k_{lat.} = \frac{EI_1}{\ell^3} \frac{1}{\left[\frac{1}{3} - \frac{1}{4}\left(1 + \frac{I_1}{4I_2}\right) \right]} \quad (2)$$

where ℓ is the effective length of each side of the leaf spring, and I_1 and I_2 are the moments of inertia of each side, as shown in Fig. 4. Thus, by increasing the moment of inertia of one side, the longitudinal and lateral stiffnesses were made approximately equal.

As shown in Fig. 6, the isolator has one fixed connection and one pinned connection. Tests indicated that a single pinned connection was sufficient to allow the existing vertical isolation system to be unaffected by the additional horizontal restraints.

Mode shapes and frequencies (eigenvalues and eigenvectors) were determined for the two models indicated in Fig. 5 using a computer program based on a stiffness matrix analysis. [3] As shown in Fig. 7, each model experiences three predominant modes of vibration: vertical, horizontal, and rocking. As a result of the decoupling assumption, one rotational mode was not computed. The response of the corner points in the model to an earthquake input was obtained by employing a modal analysis [4] program which accepts as input the previously determined frequencies and mode shapes, as well as joint masses, modal damping, and a digitized acceleration history of the earthquake.

Fig. 7 indicates the computed and measured (test) frequencies. The primary goal of a 3 Hz longitudinal and lateral frequency was adequately satisfied.

The peak accelerations for the lower corner of the equipment, as determined from the modal analysis, were 0.75 g, 0.57 g, and 0.52 g in the lateral, longitudinal, and vertical directions respectively. Similarly, peak displacements were 0.65 in., 0.6 in., and 0.7 in., well below the 2-in. maximum displacement requirement.

In these design calculations, there were several modeling assumptions which should be emphasized. One rotational mode was not modeled, and this would affect the computed

TRANSLATION

VERTICAL
2.7 (2.9) Hz

LONGITUDINAL
3.0 (2.7) Hz

LATERAL
3.4 (2.9) Hz

ROTATION

IN-PLANE
3.6 (3.5) Hz

NOT MODELED

OUT-OF-PLANE
6.8 (6.0) Hz
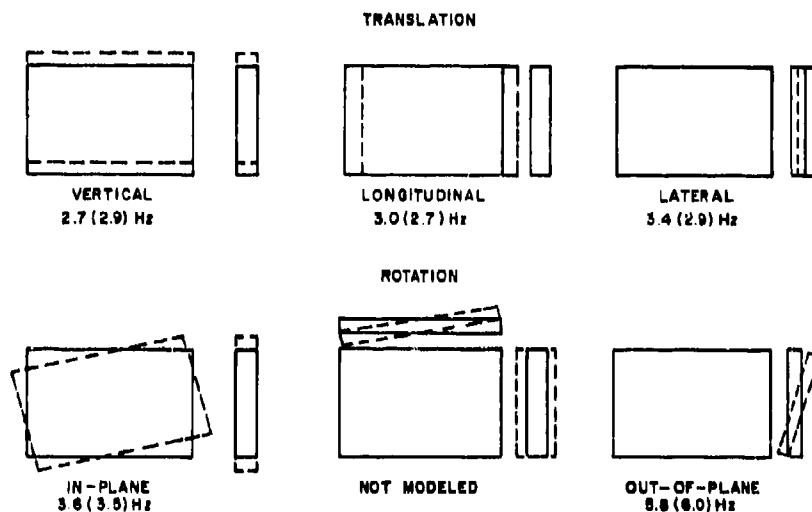
NUMBERS IN PARENTHESES ( ) ARE OBSERVED VALUES

Fig. 7 - Vibrational modes and resonant frequencies

197

responses. The horizontal stiffness of the existing vertical coil springs was also neglected, and the leaf spring isolators were assumed to act only as linear springs, when in fact they tend to exert other forces which excite rotational modes. However, since these calculations were made only to aid in the hardware design and in the planning of the test program, the model was considered satisfactory.

TEST PROGRAM

A test program, employing the Wyle Laboratories Earthquake Simulator at Huntsville, Alabama was devised to corroborate the basic design objective of the shock isolation system with the auxiliary leaf spring isolators. The size of the test table (6 ft by 16 ft) permitted testing of the actual equipment used in the field. Four frames were bolted together into one rigid assembly and, since equipment is ceiling suspended in the actual sites, the assembly was suspended from the bottom of the test bed, as shown in Figs. 8A and 8B.

Inputs of vertical and horizontal motions were applied simultaneously and, by orienting the equipment at 45 degrees to the input, it was possible to simulate the earthquake motions along three axes. The full earthquake was applied horizontally, and 2/3 of this motion was fed vertically [4]. Accelerations were measured with two tri-axial accelerometers located as shown, and displacements were obtained from analysis of movies taken during the test. In addition, sine sweeps from 0.5 Hz to 20 Hz were run to determine modal frequencies. These observed values are compared to the computed values in Fig. 7.

It was anticipated that the Wyle Simulator would reproduce El Centro conditions in the range of 0.5 to 20 Hz, a range sufficient to test the equipment both with and without the auxiliary leaf spring isolators. However, preliminary test records indicated that the El Centro environment was not reproduced at low frequencies (below 2 Hz), and it was decided to check the simulator. A shock spectrum was made from the El Centro input data, and the same analyzer was used to produce a spectrum for the table motion resulting from this same input. The gain to the simulator was adjusted until the table spectrum exceeded the El Centro input spectrum above 2 Hz, as shown in Fig. 9. This meant that the table motion was more severe than the actual El Centro data for frequencies above 2 Hz. Thus, since the system frequencies are all above 2 Hz when the leaf springs are attached, the equipment will see a more severe environment under test conditions than indicated by the El Centro data.

As a result of the tests, the configuration of the isolator was modified somewhat. Initially, the configuration tested was similar to that shown in Fig. 6 but without the additional leaves.

However, a sine sweep indicated a longitudinal frequency of approximately 2.2 Hz, which was considered too close to the 2-Hz limit, below which the simulator could not accurately reproduce earthquake motions. Additional leaves were used to increase the longitudinal frequency to about 3 Hz. As shown in Fig. 6, the leaves were added to stiffen the longitudinal direction but to have less effect in the lateral direction, which was already close to 3 Hz.

The test demonstrated that the leaf spring arrangement with one end pinned and one end clamped performed satisfactorily. The vertical frequency did not increase beyond 3 Hz, and the leaf spring isolators functioned under maximum expected vertical displacements.

LOW FREQUENCY RESPONSE OF EQUIPMENT WITHOUT AUXILIARY LEAF SPRING ISOLATORS

As a result of the simulator's poor response at frequencies below 2 Hz, it could not test the equipment without the isolators. Thus, it was not possible to reproduce the pendulum mode which had caused the shock-mount failures observed in California. However, a severe low frequency environment was artificially simulated with a sinusoidal input excitation of 1/3 Hz, which forced the equipment into violent motions and did cause shock-mount failures.

RESPONSE OF CONSTRAINED EQUIPMENT TO EARTHQUAKE

Test table displacements and accelerations corresponding to the simulated earthquake input spectrum of Fig. 9 are shown in Fig. 10. Fig. 11 shows the first 20 seconds of accelerations measured at the upper corner of the constrained equipment frame. A summary of accelerometer-measured peak accelerations, as well as displacements obtained from analysis of film, are given in Table 1.

The measured values are higher than those indicated by the design calculations because the test table motion was more severe than the El Centro data. Other factors contributing to these differences were that one rotational mode was not modeled and that the modeled rotational modes were not excited in the design calculations while they were excited in the test.

CONCLUSIONS

It has been shown that a shock isolation system which includes a low frequency pendulum mode is extremely vulnerable to earthquake-type excitations. Excessive horizontal displacements up to 10 in. could be induced, possibly causing shock-mount failure and/or impact of equipment against adjacent objects.
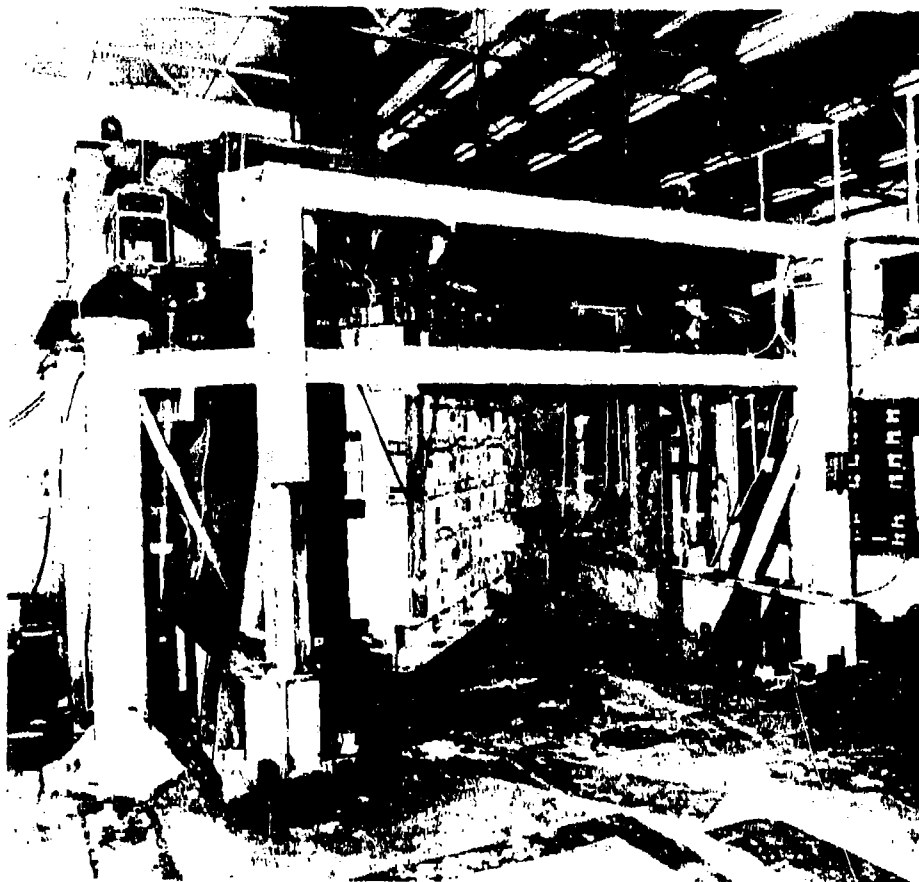
198

Fig. 8A - Wyle Laboratories Earthquake Simulator
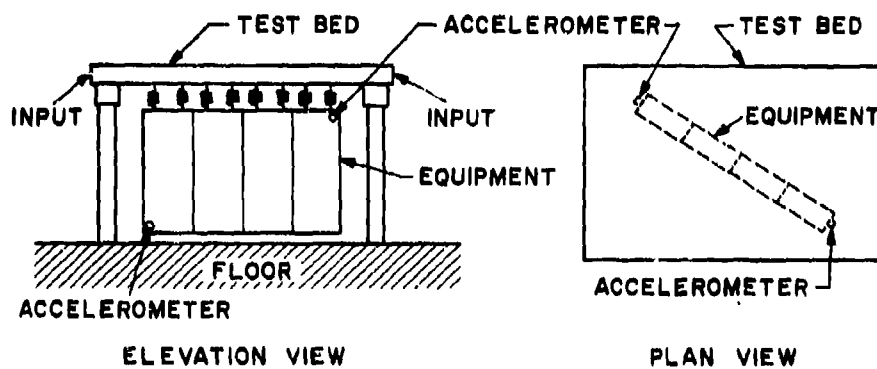

ELEVATION VIEW   PLAN VIEW

Fig. 8B Test configuration

Auxiliary leaf spring isolators were designed to increase the pendulum frequencies from less than 1 Hz to approximately 3 Hz. This system restricts earthquake induced displacements to less than 2 in. and still provides acceptable blast protection.

A test program employing an earthquake simulator was used to corroborate basic design objectives and qualify new hardware. The test environment was more severe than the El Centro Earthquake for frequencies above 2 Hz. Design objectives were met and all hardware functioned properly.
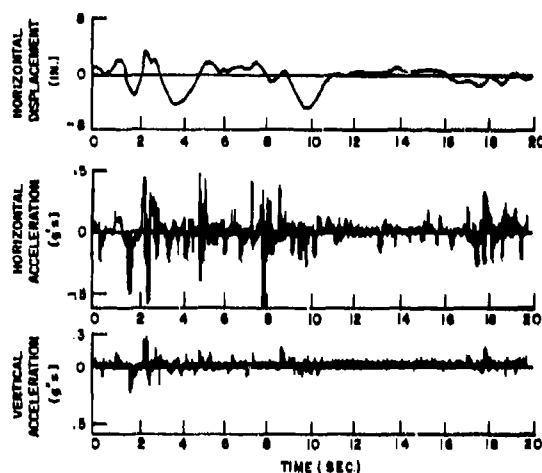
Fig. 9 - Test spectra

Fig. 10 - Table motions
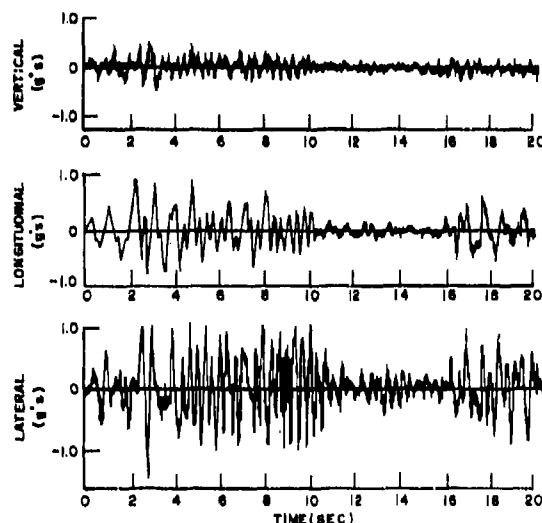
Fig. 11 - Measured equipment accelerations

Table 1
Earthquake Induced Responses

Location	Peak Accelerations (g's)			Peak Displacements
	Vert.	Lat.	Long.	
Upper Right	0.45	1.4	0.9	Vertical and horizontal displacements were between 1 and 1.25 in.
Lower Left	0.85	2.0	1.0	

200

REFERENCES

1. G. W. Housner, R. R. Martel, and J. L. Alford, "Spectrum Analysis of Strong Motion Earthquakes," Bulletin of Seismological Society of America, Vol. 43, pp. 97-119, Apr. 1953.

2. F. M. Sauer, "Nuclear Geoplosics, Part Four-Empirical Analysis of Ground Motion and Cratering," DASA-1285 (IV), May 1964.

3. B. Wada, "Stiffness Matrix Analysis," Tech. Rept. No. 32-774, Jet Propulsion Laboratories, Oct. 31, 1965.

4. J. M. Biggs, Structural Dynamics, pp. 329-332. McGraw-Hill, New York, 1964.

5. C. V. DiPol, "Seismic Design Criteria for Nuclear Power Plants," ASCE Preprint 791, National Meeting on Water Resources Engineering, Feb. 1969.

THE REDUCTION OF IMPACT INDUCED PRESSURES IN FUEL TANKS*

Peter J. Torvik
and
James W. Clark
Air Force Institute of Technology
Wright-Patterson Air Force Base, Ohio 45433

The use of porosity to reduce the pressures generated by projectile impact was considered both theoretically and experimentally. Flame retardant polyurethane foam was found to give some improvement, attributed to the casual introduction of air. A freon-filled dacron material (not suggested for actual application) shows that significantly greater attenuations can be achieved.

INTRODUCTION

The catastrophic damage to fuel tanks brought about by projectile penetration is receiving much attention in the design of modern military aircraft. The processes contributing to such a catastrophic destruction are many, and are not simple. Neither analytical nor experimental approaches have been entirely successful in leading to a complete understanding of the phenomenon often referenced to as the "hydraulic ram" effect.

The process of projectile penetration can be divided into at least three major portions. First, the generation of a shock wave at the instant of initial impact of the projectile on the fluid or the tank wall, and secondly, the creation of a pressure field within the tank by the quasi-steady motion of the projectile through the fluid. Finally, as the projectile approaches the opposite tank wall, the influence of the second wall becomes significant, and perhaps predominant, as the fluid set in motion by the moving projectile encounters the second wall. Other investigators, such as Williams [1] and Bristow [2] have sub-divided the process even further, but these three will suffice for the present discussion.

It has long been known that porous or foamed metals lead to rapid attenuation of large pressure disturbances [3]. The rapid attenuation of strong disturbances in soils [4] may well be due to an inherent porosity. It is therefore evident that the introduction of porosity should be considered as a means of reducing the peak pressures and therefore reducing the damage due to projectile impact in fuel tanks. Reticulated polyurethane foams have been inserted into tanks as a flame

suppressant, and pressures due to impact have been measured in tanks containing foams. Clark [5] reported a reduction by one-half in pressure when polyurethane foam was added to water, while Williams [1] found that pressures actually increased when foam was added. We assume that the introduction of even a reticulated foam into a tank of liquid will lead to the inclusion of porosity in the mixture through small air or vapor particles within the foam-fuel mixture. Other experiments have been conducted with foams or gas bubbles introduced into tanks, and have led Bristow [2] to state that the introduction of such materials into fuel cells is not an effective means of controlling the hydraulic ram effect.

It was the purpose of this study to reconsider the role of porosity in the reduction of pressures. The primary attention in the analytical portion of the work was given to the first (impact-induced shock) phase of the phenomenon, with the experiments being conducted so as to gain further information about the effectiveness of porosity in both this phase and in the quasi-steady phase of the process.

In the next section, results of the analysis will be briefly described, and in the following section the results of the experimental program will be given.

203

ANALYSIS

As assume that a projectile penetrating the tank wall generates a shock wave which propagates into the fluid. For the purpose of determining pressures at points along the extension of the original trajectory, we assume the front to be hemi-spherical. It is further assumed that the shock wave is similar to that which would be generated by the instantaneous deposition of energy at a point, i.e., the instantaneous detonation of a small spherical charge. If these assumptions are valid, a theory previously developed [6] in order to predict the attenuation of shock pressures by hypervelocity impact on solid metal targets can be applied. In that work, the Taylor blast wave theory was so modified as to take into account the fact that the material through which the shock is propagating is not a perfect gas being shocked to the limiting compression, but rather that the pressure-density states at the shock front are those of the Hugoniot curve of the material. The required Hugoniot pressure-density relationship was determined for water-polyurethane mixtures and water-polyurethane-air mixtures by using a simple mixture theory described elsewhere [7]. In this adiabatic mixture theory, it is assumed that no energy is transferred from one component of the mixture to another during the short time required for the passage of the shock wave. An alternative or isothermal theory, in which it was assumed that each component of the mixture acquires the same temperature during shock passage was also developed, but was shown [8] to lead to predictions which differ but little from those of the adiabatic theory. Typical results of these calculations are shown in Figure 1 for mixtures of several different volume fractions. Details of the calculations and further results are given in [8]. It can be seen that the inclusion of the polyurethane foam typically leads to slightly higher shock pressures. On the other hand, if a small amount of air is introduced into the mixture, the calculations show that a slight, but not substantial reduction in peak shock pressure is to be expected. These calculations all show a pressure decaying with distance as an inverse power less than two.
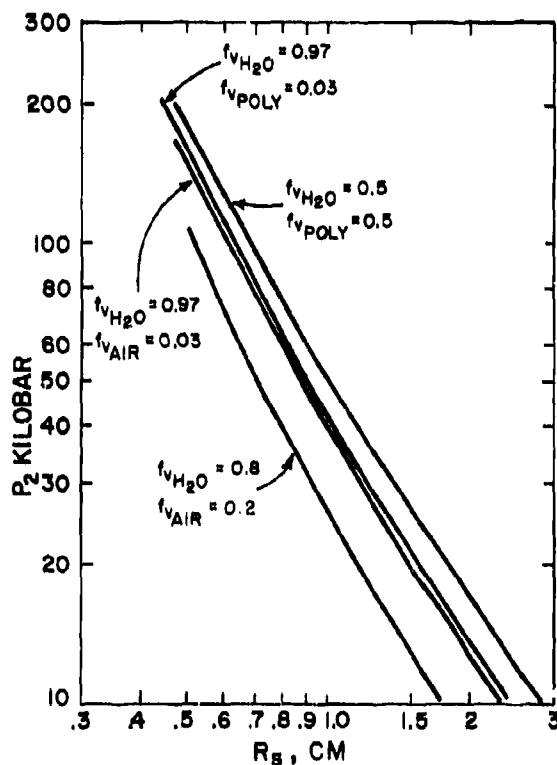
It has been found [3], however, that in the case of metals, an approach such as this in which a porous material is approximated by an equivalent hydrodynamic material can be expected to give accurate results only at early times, that is, at short distances and high shock pressures. At greater distances, i.e., longer times and lower pressures, it has been shown [9] for one dimensional (planar) shock waves that a simple theory, known as the "snowplow" model gives better agreement with the detailed code calculations. Consequently, the possibility of developing a simple model analogous to the "snowplow" model which would be applicable to spherical shock waves was undertaken. The results of this effort are given in another report [10]. It was found that a spherical "snowplow" model could be developed from conservation of momentum and would predict a pressure decay as the inverse sixth power of distance. Other simplified models, based on conservation of energy, were found to lead to the prediction that pressure should decay as the inverse fourth power of distance. Either of these models would seem to suggest that the introduction of even a small amount of porosity will lead to a large increase in the rate of attenuation of spherical shock waves.

Based on these analysis, we conclude that the presence of porosity should lead to increased attenuation of the shock waves in a fuel tank, particularly at large distances and long times. The contradictions in the experimental data, with regard to the beneficial effect of foams, would be resolved if one investigator had succeeded in achieving a liquid-polyurethane mixture without trapped air

Figure 1 Peak Pressure Versus Distance from Impact for Water-Air and Water-Polyurethane Mixtures, E_0 = 1000 joules

204

pockets, and the other had not. Porosity which is not sufficiently uniform throughout the fluid might also not produce the expected benefits. Further, a reduction in the pressure of the shock wave generated by the initial impact does not necessarily insure improved attenuation of the pressures generated in the later stages of the impact and penetration process. As these later phases appear to be less amenable to analysis and may well be the more significant in the creation of damage, the experimental program to be described in the next section includes an attempt to measure the pressures generated in the quasi-steady phase.

EXPERIMENTS

Water was used as the first target material in order to establish a baseline against which the results for the mixtures containing porosity could be compared. The second material selected was a mixture consisting of reticulated polyurethane foam and water. This foam is currently used in some aircraft fuel cells in order to prevent explosions in vapor filled tanks. The material used had a density of 1.3 lb/cu-ft, about 15 pores per lineal inch, and a volume fraction of 1.8%. Measurements showed about 6% by volume of air to be present in a tank otherwise filled with foam and water. The material is shown in Figure 2a. The third target material used was water

Figure 2a Reticulated Polyurethane Foam

and Pneumacel, a new Du Pont tradenamed product now in pilot production and currently used in rug pads. It is a mat made of Dacron fibers inflated with approximately 12% by weight Freon gas. This particular material was selected only because it provided a simple means of insuring a uniform distribution of gas throughout the liquid, and is not suggested for application to fuel tanks. It is estimated that the

Pneumacel and trapped air occupied 14% of the tank volume. The manufacturer has indicated the material will withstand pressures of 3000 psi without damage. The material is shown in Figure 2b. The density of the individual

Figure 2b Pneumacel

strands are 0.023 gm/cm^3, and the diameter about 0.05 cm.

Target materials were contained in a rectangular tank measuring 23 1/2 in. high, 29 1/2 in. wide, and 24 in. deep. The top, bottom and sides were 1/4 in. steel plates, reinforced by bands of angle iron. The front and back plates were removable and were made of 0.125 in. 2024 aluminum. A 4 in. diameter hole was cut in the center of the front plate and covered with 0.0005 in. Mylar sheet.

Two pressure transducers were positioned 5 cm from the front plate at opposite sides of the projectile path, 7.5 cm and 15 cm respectively from the impact point. A third was located 20 cm above the path of the projectile and 30 cm from the point of impact. The first two gages were placed so that the pressures created by the initial impact would be sensed. The third gage was placed further from the wall so that the pressure field generated by the passing projectile would be dominant. The arrangement of the pressure gages was as shown in Figure 3.

Kistler 603-A quartz transducers with model 105H connector adapters connected to Kistler 504-A charge amplifiers were used to measure the pressures. Data were recorded on a Sangamo Model 3562 portable recorder/reproducer, and later interpreted by playback through a Honeywell Visicorder and a storage oscilloscope. Steel ball bearings weighing 128.5 grains were fired into the tank through
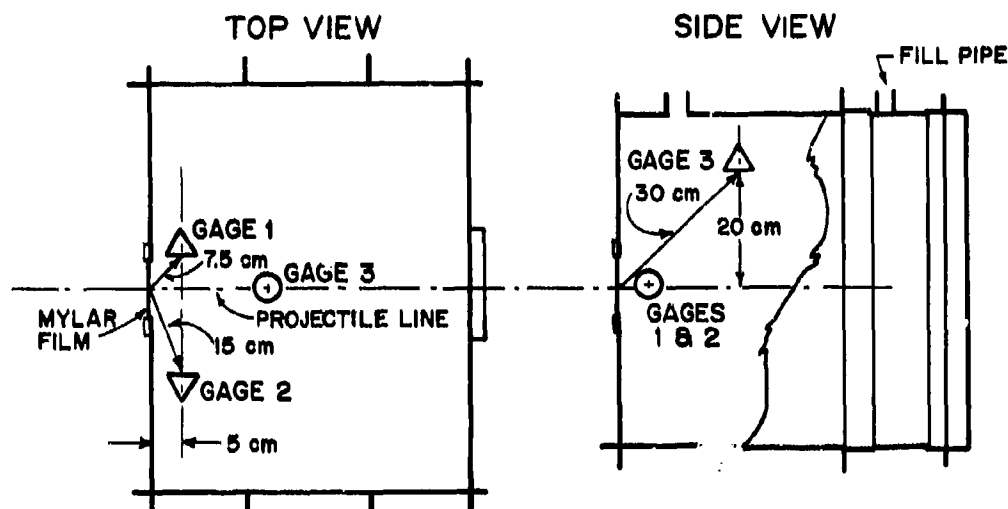
Figure 3 Gage Location

TABLE 1

Shot No.	Material	Impact Velocity (fps)	P_1 -psi (r = 7.5 cm)	P_2 -psi (r = 15 cm)	P_3 -psi (r = 30 cm)
1W	Water	1571	210	80*	100
2W	Water	2219	210	110*	140
3W	Water	2516	210	80*	160
4W	Water	2896	245	100*	150
5P	Pneumacel	1566	140	6	4
6P	Pneumacel	2230	175	8	8
7P	Pneumacel	2869	155		8
8F	Polyurethane	1612	175		22
9F	Polyurethane	2219	185		90
10F	Polyurethane	2823	210		45
11F	Polyurethane	1460	215	80	75
12F	Polyurethane	2180	180	65	185
13F	Polyurethane	2759	145	50	142
14P	Pneumacel	1333	45	8	8
15P	Pneumacel	1816	140	10	10
16P	Pneumacel	2740	130	14	14
17W	Water	1650	240	65	145
18W	Water	1459	225	50	80
19W	Water	2040	210	105	180
20W	Water	2747	240	130	200

Experimental Results

* Data questionable

the mylar film at various velocities using a powder gun. A more detailed description of the experimental apparatus and procedure is given elsewhere [11].

A total of 20 shots were fired: eight into water, six into the water-polyurethane mixture, and six into the water-Pneumacel mixture. Some data was lost due to an intermittent failure of gage 2, as is indicated in the tabulation of results, Table 1. Visicorder traces obtained by replaying the recorded data for representative shots are shown in Figure 4.

Much scatter in the data is evident, but it is felt that certain general trends can be deduced from the results. Comparisons of the magnitude of pressures at gage 1 for the various target materials show that typical pressures in the polyurethane foam mixtures were less than those in water, and that pressures in the water Pneumacel mixtures were still less. Of a greater interest, however, is the rate at which these pressures diminish with distance into the tanks. The experiments on water show that the pressures at 15 cm from impact are reduced by about a factor of two from the pressure at 7.5 cm. On the other hand, the pressures at 30 cm are typically about 50% greater than those at 15 cm. We take the increase of pressure with distance to be an indication of the development of a pressure field around the moving projectile as conjectured by previous investigators. It can also be seen from the tabulated data that a pressure drop of typically a factor of three occurs between gage 1 and 2 for the polyurethane foam, while a reduction of a factor of 10 or more in going from 7.5 cm to 15 cm into the Pneumacel-water mixture is typical. These results are taken as confirmation of the predictions that a porous material should be beneficial in the reduction of pressures due to the initial impact.

The limited data indicate a higher pressure at gage 3 (30 cm) than at gage 2 (15 cm) in the polyurethane foam, just as in the case of water. On the other hand, pressures in the Pneumacel-water mixture at gage 3 were found to be at the same low level as at gage 2. These data suggest that the Pneumacel is also effective in attenuating the pressures caused by the moving projectiles.
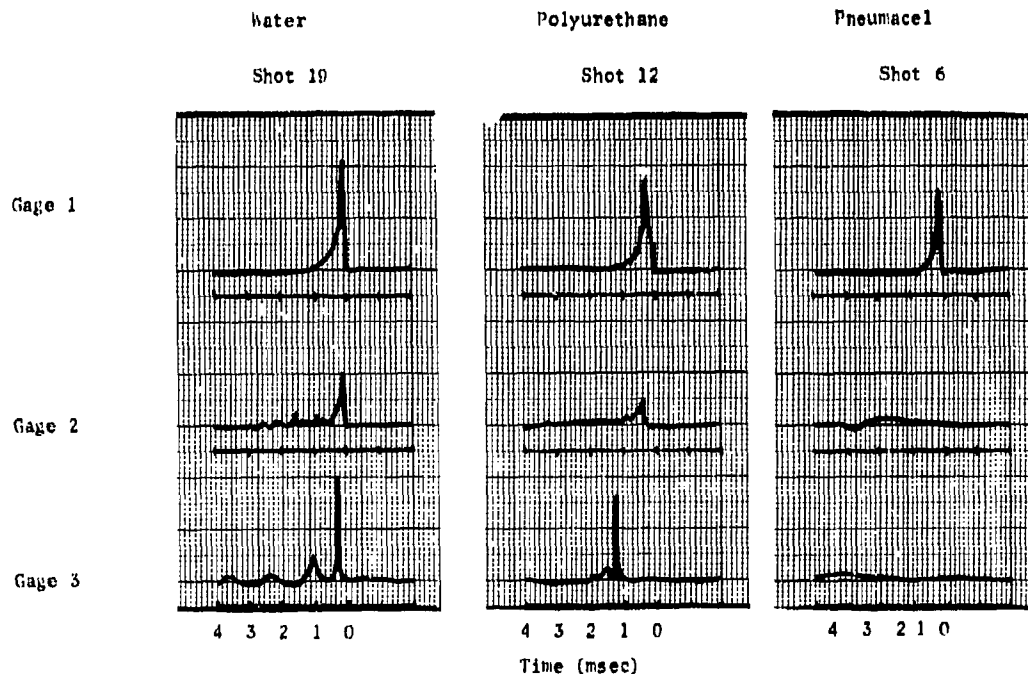

	Water	Polyurethane	Pneumacel
	Shot 19	Shot 12	Shot 6

Time (msec)

Figure 4   Pressure Time History at Several Stations

207

SUMMARY AND CONCLUSIONS

The introduction of porosity into a liquid was considered as a means of reducing the pressures caused by projectile impact. The use of simple analytical models showed that a small amount of porosity should lead to some increase in the rate of pressure attenuation near the point of impact and a greater increase at larger distances. A limited experimental study was also undertaken using as targets water, water in the expanded polyurethane foam used as a flame retardant, and a mixture of water and Dacron tubes containing freon gas (Pneumacel). In each of the mixtures, it is assumed that some unknown and unpredictable amount of air is also trapped as bubbles, contributing to the porosity. The results of the experiments showed consistently lower pressures in the porous mixtures. In the case of the polyurethane mixtures, we attribute the lower pressures to some degree of attenuation brought about by the trapped air bubbles. The even greater attenuation in the Pneumacel mixture is attributed to two causes. First, the more uniform distribution of porosity obtainable with gas filled fibers than is obtained by relying on the casual introduction of trapped air bubbles. Secondly, since the limiting compressibility of freon is much greater than that of air because of a lower ratio of specific heats, a given volume fraction of freon can be expected to lead to a greater attenuation than a similar volume fraction of air.

It is particularly significant that the experimental results show lower pressures in the porous mixtures than in water even in the region where it is expected that pressures are not due to a quasi-spherical shock wave generated by the initial impact, but rather due to the quasi-steady motion of the projectile through the fluid. It should be noted that in these experiments less volume (~ 86%) was available for the liquid when Pneumacel was used to introduce the porosity than the 92% available when polyurethane foam was used. As fuel is a superior wetting agent to water, it is expected that less air bubbles will be present in a fuel foam mixture than in a water foam mixture.

The results of this study indicate that porosity should receive further consideration as a means of reducing pressures in fuel tanks, but that it is likely to be essential to have a uniform distribution. The freon filled dacron product used in this study is not suggested for actual application, but was used only because it is a currently available material having the desired properties.

REFERENCES

[1] Roger F. Williams, "Shock Effects in Fuel Cells," Stanford Research Institute Project No. PGD 7708, Stanford Research Institute, October 1969.

[2] R. J. Bristow, "Design of Hydraulic Ram Resistant Structure," Army Symposium on Solid Mechanics, Ocean City, Md, October 1972.

[3] W. Herrmann, "Constitutive Equation for the Dynamic Compaction of Ductile Porous Materials," Journal of Applied Physics, Vol. 40, pp. 2490-2499, May 1969.

[4] P. Weidlinger, "Analytical and Experimental Studies on Locking Media," Shock and Vibration Bulletin, No. 29, Part III, pp. 30-39, July 1961.

[5] G. O. Clark, "Gunfire Testing of a Rigid Fuel Container to Determine the Shock Attenuation Values of Foam," Report No. 2-59920/OR-8380, Dallas, Texas. Vought Aeronautics Division, LTV Aerospace Corporation, August 1970.

[6] P. J. Torvik and R. F. Prater, "A Simple Model for the Shock Wave Induced by High-Speed Impact," Journal of Spacecraft and Rockets, Vol. 9, pp. 13-18, January 1972.

[7] P. J. Torvik, "A Simple Theory for Shock Propagation in Homogeneous Mixtures," Air Force Institute of Technology TR 70-3, May 1970.

[8] Richard F. Fischer, "A Theoretical Investigation of Shock Waves in Water and Water-Polyurethane Foam Mixtures," MS Thesis, Air Force Institute of Technology, Wright-Patterson Air Force Base, Ohio, June 1971.

[9] W. Herrmann, "Equation of State of Crushable Distended Materials," Sandia Laboratory Research Report SC-RR-66-2678, March 1968.

[10] P. J. Torvik, "On the Attenuation of Diverging Shock Waves in a Porous Material," Air Force Institute of Technology TR 71-4, November 1971.

[11] J. W. Clark, "An Experimental Study of Shock Waves in Three Mixtures," MS Thesis, Air Force Institute of Technology, Wright-Patterson Air Force Base, Ohio, June 1972.

A TREATMENT OF A NON-STATIONARY RANDOM PROCESS -

LOAD TRANSFER AT SEA

H. S. Zwibel and D. A. Davis
Naval Civil Engineering Laboratory
Port Hueneme, California

A treatment of a non-stationary random process is presented. By way of example, an offshore cargo transfer problem is solved in order to demonstrate the approach. It is found that for high sea states the statistical uncertainty in load pendulation is quite large.

INTRODUCTION

Many of the problems in shock and vibration are random in nature. The majority, representable as stationary stochastic processes, are analyzable by a variety of analytical techniques. There are, however, situations for which the process is non-stationary, e. g., transient phemonena, time variation of control parameters, etc. For these non-stationary processes most of the analytic tools used for stationary processes are not applicable. In this paper, we treat a system that is non-stationary because of time varying parameters.

In a previous study, Zwibel [1] treated the stationary stochastic problem of load oscillation with fixed load suspension line length. In most load handling operations, however, a non-stationary problem arises during offshore cargo handling operations. A load is raised, shifted and than lowered by a crane mounted on a floating platform. Horizontal boom motion (caused by wave-induced platform motion) forces the load line system to oscillate. Due to raising and lowering of the load, the physical properties of this pendulum change with time. The magnitude of this induced oscillation for both random sea conditions and swell is of interest. For swell, the system is not random; however, for a wind developed sea the system is stochastic due to the randomness of the forcing function. Both situations are discussed in this paper.

THEORY

A heavy load suspended by a wire from a boom acts like a pendulum, and a swinging motion of the load can be initiated by horizontal accelerations of the boom. The mathematical analysis of this forced pendulation is complicated for several reasons: first, the length of the pendulum is changing with time due to raising and lowering of the load; second, the

boom acceleration is a random function of time. This randomly forced pendulum therefore falls under the category of non-stationary stochastic processes. In fact, if one considers the possibility of large amplitude oscillations, then the equation of motion is also non-linear. There are analytical means for determining the statistics of stationary stochastic processes; unfortunately for some non-stationary random processes there are no comparable methods available[2]. One must use the "brute force" method of simulating the random input function and numerically integrating the equation of motion to obtain the output. In order to get statistical information it is necessary to repeat this procedure for a number of inputs. Statistical accuracy increases with the total number of simulations.

The equation of motion is obtained by equating the time rate of change in the load angular momentum to the applied torque. This yields the following equation:

$$\frac{d^2\theta(t)}{dt^2} = -2\frac{dL(t)}{dt}\frac{1}{L(t)}\frac{d\theta(t)}{dt} - \frac{g}{L(t)}\left[\sin\theta(t) + \frac{1}{g}\frac{d^2X_s(t)}{dt^2}\cos\theta(t)\right] \quad (1)$$

where

t = time

$\theta(t)$ = angle of lifting line with respect to the vertical

L(t) = length of lifting line (this is a deterministic, specified function of time)

$X_3(t)$ = horizontal position of boom (the attachment point for the lifting line)

g = acceleration of gravity

209

For a given $L(t)$ and $X_g(t)$ it is a simple matter to numerically integrate the above equation. The complication arises because of the random nature of $X_g(t)$.

In order to numerically integrate Equation (1) it is necessary that $X_g(t)$ be a known, deterministic function of time. $X_g(t)$ depends on the crane-barge motion, which in turn depends on the sea surface motion. The sea surface -- for wind generated waves -- can be approximated as a stationary, Gaussian random process. Its power spectral density function, $S_g(\omega)$, takes a variety of forms; we use the Pierson-Moskowitz spectrum. The deep water form of this spectrum is given by:

$$S_g(\omega) = \frac{A}{\omega^5} e^{-\bar{B}/\omega^4}$$

where $A = 0.0081g^2$ and $\bar{B} = 33.56/H_{1/3}^2$. Here $H_{1/3}$ is the "significant" wave height, and it represents the average of the 1/3 highest waves in the random sea.

The barge motion is assumed to depend linearly on the surface elevation, hence the various motions, heave, pitch, surge, etc. are also stationary Gaussian random processes. If $RAO(\omega)$ is the response operator for the boom tip motion, then

$$S(\omega) = \left| RAO(\omega) \right|^2 S_g(\omega)$$

is the power spectral density function for the boom tip horizontal motion. The RAO is the response of the boom due to unit amplitude incident waves.

It is now possible to simulate $X_g(t)$ by using Monte Carlo techniques. [3]. The method used is the most "intuitive" of the various possible approaches. The desired stochastic variable, e. g., the sea surface elevation is represented as a sum of waves, each with a different frequency. The phase of each wave is independently chosen at random from the uniform distribution, and the amplitude of each wave is chosen so that the power spectral density function of the process is a specified function. Mathematically, the simulation of $X_g(t)$ is described by the following equation:

$$X_g(t) = 2 \sum_{n=1}^{N} \left[S(\omega_n)\Delta_n \right]^{\frac{1}{2}} \cos\left(\omega_n t + \varphi_n\right) \tag{2}$$

where

ω_n = is the circular frequency at the midpoint of nth frequency interval.

Δ_n = is the width of the nth interval.

φ_n = is the randomly chosen phase of the nth wave.

N = is the total number of individual waves.

$S(\omega_n)$ = is the power spectral density for the horizontal motion of the boom.

The boom acceleration obtained from $X_g(t)$ is

$$\ddot{X}_g(t) = -2 \sum_{n=1}^{N} \omega_n^2 \left[S(\omega_n)\Delta_n \right]^{\frac{1}{2}} \cos\left(\omega_n t + \varphi_n\right) \tag{3}$$

and is used as the forcing acceleration for the load pendulation.

It should be noted that a given set of N random phases yields a simulation of $X_g(t)$ that is a deterministic function of time. It represents one member from an ensemble of boom motion. The pendulation time history obtained by integrating the equation of motion is, therefore, only representative, and statistical inferences must be made by sampling many members from the ensemble. For some applications thousands of sample functions must be used. [4]. In this paper such extremes are not required since high accuracy is not necessary.

TYPICAL PROBLEM

Consider the case of the YD-225, a Navy 100-ton yard crane, unloading containers from a ship moored in the open sea. The 140-foot long barge has a beam of 70 feet, a mean draft of 6.0 feet and displaces 1,540 long tons. Both ship and crane are headed bow-on into the incident unidirectional sea. A lighter lies between the crane and ship and serves as a receiving platform for off-loaded containers. The crane lifts the upper most container from a stack of three resting on the deck of the ship, raises the container 10 feet at a constant line rate of 79 fpm and then immediately lowers the container at the same line rate to the well deck of the lighter. To actually accomplish this transfer, the crane boom must either be rotated or raised to position the container over the lighter. The theory, however, does not account for changes in boom position during a load transfer, and this variable is ignored in the analysis that follows. Figure 1 depicts the crane, lighter and ship at the instant that the load is lifted. The crane boom is positioned normal to the barge longitudinal axis, and the point of line suspension is 61 feet above the top of the container. For the sake of simplicity, the center of gravity of the container, spreader bar and hook is assumed to be located at the geometric center of the 8 foot high container; thus the effective line length at the beginning of the load cycle is $61 + 4 = 65$ feet. The well deck of the lighter is one foot below the water surface, hence the effective line length when the container is released is 116 feet. The problem statement is completed by noting that the mean water depth at the unloading site is assumed to be 100 foot and that the crane barge moorings are assumed to have no effect on the barge motion for the frequency range of interest.

The RAO for the horizontal boom tip acceleration, $\ddot{X}_g$, is required for both regular and random waves. It and the RAO's for X_g and $\dot{X}_g$ - the boom tip horizontal displacement and velocity - were computed using the NCEL ship motion computer code, (RELMO). The results are given in Figures 2 through 4.
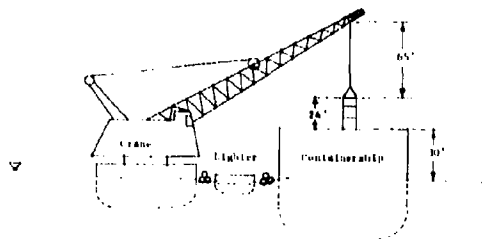
210

Figure 1.   Unloading containerized cargo with
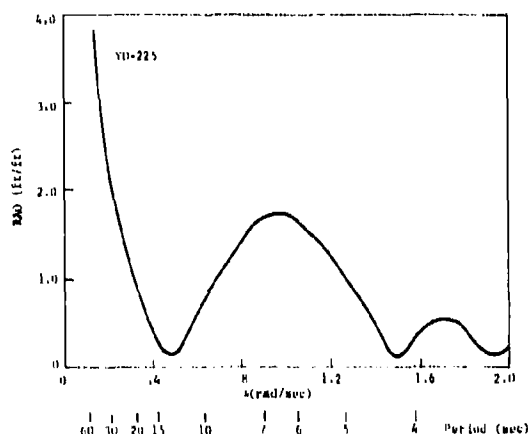100-ton Navy yard crane.

Figure 2.   Horizontal displacement response
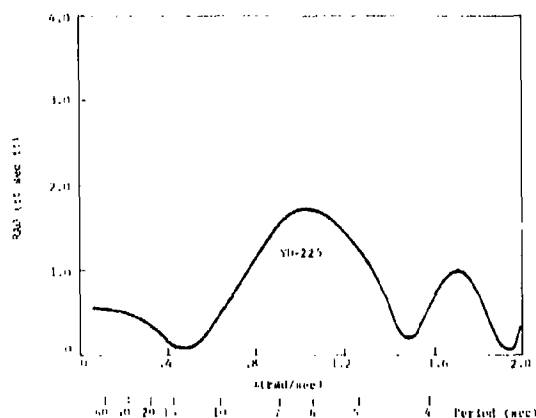amplitude operator for crane boom.

Figure 3.   Horizontal velocity response
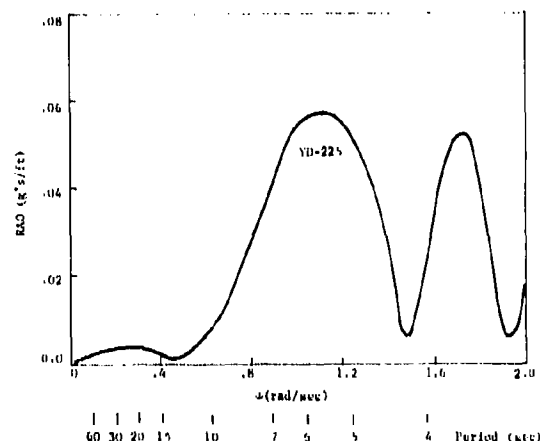amplitude operator for crane boom.

Figure 4.   Horizontal acceleration response
amplitude operator for crane boom.

The load displacement amplitude operators
for five different wave periods are shown in
Figure 5. The results were obtained from an
analytical model (code named SWING) which com-
putes load oscillation for simple harmonic
excitation of the load suspension point. The
abscissa in each graph is expressed as time (in
seconds) from the beginning of the load transfer
cycle. Thus at time 7.6 seconds the load has
been lifted 10 feet from the containership deck,
and at 53.9 seconds from lift-off the load is
resting on the well deck of the lighter. The
ordinate of each trace is expressed as the
ratio of load displacement over boom displace-
ment amplitude.

For a boom period of 6 seconds (or less),
the motion of the load is comparatively small,
and there is no evidence of resonant behavior.
Considerably more motion occurs for 8 second
period excitation, and a maximum response occurs
for excitation of 9.5 seconds. In the latter
case, the unrestrained load is seen to pendulate
with an amplitude equal to 15 times the boom
displacement amplitude. Resonant behavior is
far less evident in the plot for 12 second
excitation, and at 16 seconds the load response
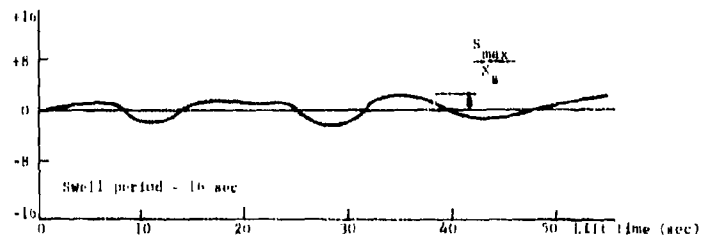is comparable in magnitude to that noted for 6
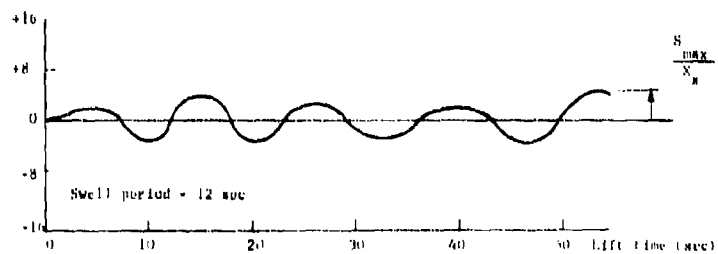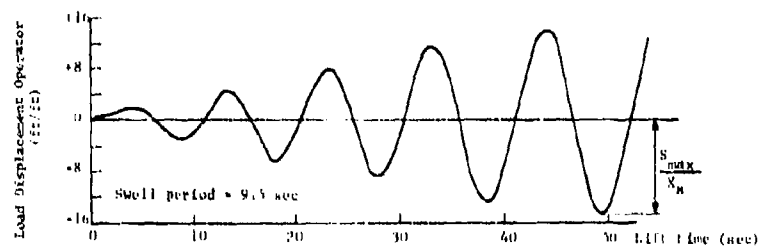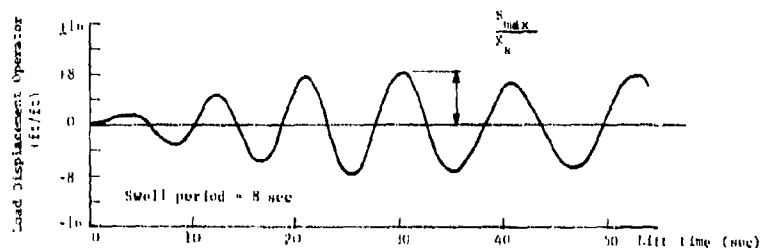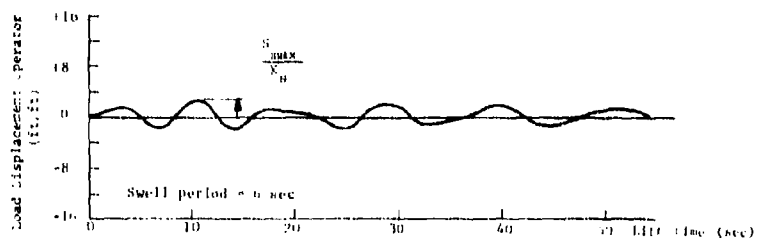second excitation.

211

Figure 5. Load absolute displacement operator in regular swell

If one scans the frequency dependent load displacement operators in Figure 5 and selects from each of these the maximum swing amplitude that occurs during each load transfer cycle (regardless of when it occurs during the cycle), then a plot can be formed such as the lower trace in Figure 6. Two additional traces for slower line speeds, 50 fpm and 25 fpm, are also shown in this figure. It is clear from these results that faster line handling rates result in a lowering of the load displacement amplitude operator.

The product of the boom tip horizontal displacement amplitude operator and the maximum load displacement amplitude operator produces the useful result shown in Figure 7. It is apparent from this plot that regular swell having a period of 9 seconds produces the maximum load amplitude, about 14.5 feet per foot of wave amplitude.

Motion in Random Waves

Random Waves. Estimates of the load suspension point motion in random seas were computed using the NCEL ship motion analysis.[*] The results appear in Figures 8 through 10 as plots of the average of the 1/3 highest displacement amplitude as a function of the deep water significant wave height, $H_{1/3}$.

As noted earlier, the solution of Equation (1) for the angular deflection of a wire suspended load in a random sea (with variations allowed in the suspension line length) was complicated by the dependency of this solution on the random nature of $X_s(t)$, the time dependent horizontal boom displacement. The function $X_s(t)$, however, can be simulated as shown in Equation (2), and the result in turn used to simulate the motion of the load, the independent variable of interest.

Thus, with the same load cycle as before (line speed = 79 fpm) and with random selection of wave phase angles for each simulation, a series of plots can be generated such as those which appear in Figures 11 and 12. These two simulations from the infinitely large ensemble of simulations differ markedly. This illustrates the dependency of the solution on the random selection of wave phase angles. Obviously, accurate statistical estimates of the load motion are impossible without a substantial number of motion simulations. On the basis of nine simulations for each of three different line speeds (25.0, 50.0 and 79.0 fpm) the estimates for S_{max} (maximum load amplitude per load cycle) are plotted in Figure 13. It is apparent that the effect of increasing the crane line speed is to reduce the magnitude of load oscillation, although the reduction in magnitude is not as great as that noted earlier for pendulation in regular waves (Figure 6).

[*] The sea is described by a fully developed Pierson-Moskowitz spectrum.

For different values of significant wave height, $H_{1/3}$, load motion simulations were made to determine the relationship between maximum load amplitude and seastate. The results, for a line speed of 79 fpm, appear in Figure 14. Although only five simulations were made for each value of $H_{1/3}$, it is apparent that S_{max} (and the spread in predicted amplitude as well) increases with seastate. It's clear that, for the higher sea states, many more samples would be needed in order to obtain reliable statistics. It is also interesting to note that very large swinging motion may be induced, even with a random excitation and a varying pendulation length.

FINDINGS AND CONCLUSIONS

1. A theory has been developed for predicting the horizontal response of an unrestrained wire suspended load in regular and random seas. The line length is allowed to vary; thus the load response in random seas is a non-stationary random process.

2. The non-stationary nature of the load response in random seas, coupled with the short duration of each lift cycle (1-2 minutes) requires multiple load response simulations for accurate results. Additional study is required to relate accuracy of prediction with total simulation time.

3. Results from the analysis for a Navy 100-ton yard crane, operating at a maximum line rate of 79 fpm, indicate that the maximum load displacement amplitude to be expected in a seastate 3 is at least 2 times as great as the significant wave height ($H_{1/3}$ = 5.0 feet).

4. The corresponding maximum load displacement amplitude to be expected in 5 foot high, 9 second period regular swell (critical swell period for the crane) is about 7.5 times as great as the swell height.

5. The predicted unrestrained load response for the 100-ton crane is clearly unacceptable for reasons of safety and for the adverse effect it would have on the rate of cargo transfer. Positive tagline control is required at all times to control load pendulation.

6. Faster line handling rates have a mitigating influence on unrestrained load oscillations. For the 100-ton crane, the maximum load displacement amplitude for a 79 fpm line rate is about half of that for a rate of 25 fpm.

FUTURE PLANS

1. Extend the theory to include motion in more than one plane.

2. Investigate predictive accuracy in random seas as a function of total simulation time.

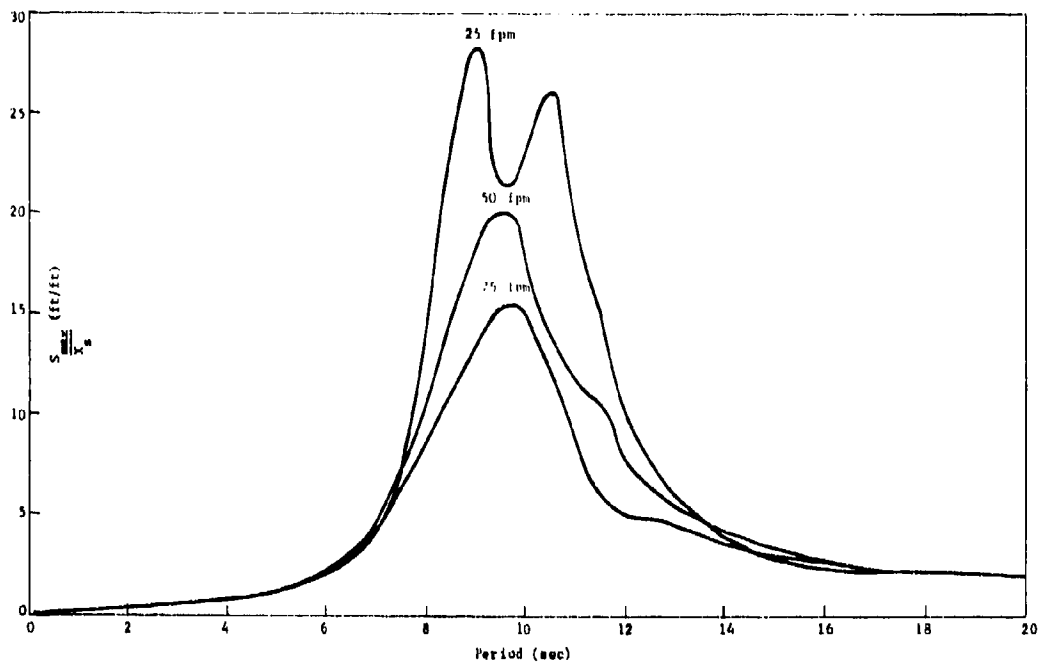3. Extend the theory to include the effects of linear tagline restraint.

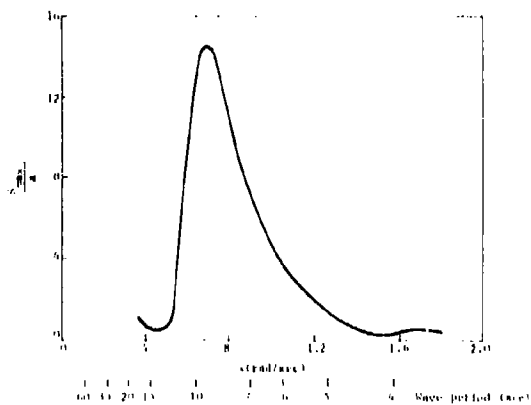Figure 6. Maximum load amplitude operator in regular swell.

Figure 7. Ratio of maximum load displacement
amplitude to incident swell amplitude expressed
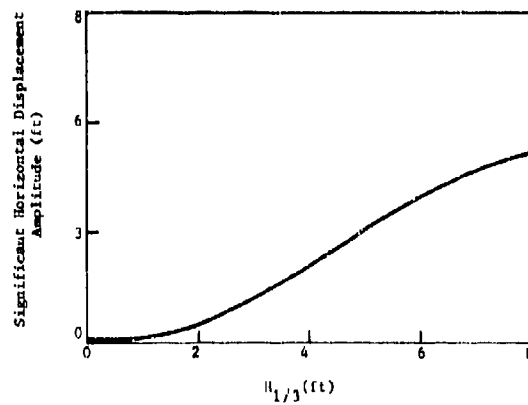as a function of swell frequency.

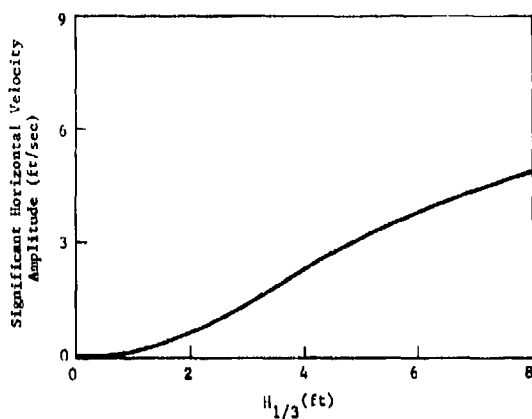Figure 8. Random crane boom horizontal
displacement.

214

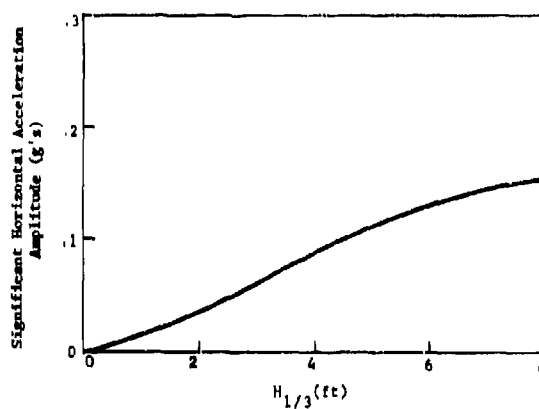Figure 9. Random crane boom horizontal velocity.

Figure 10. Random crane boom horizontal acceleration.
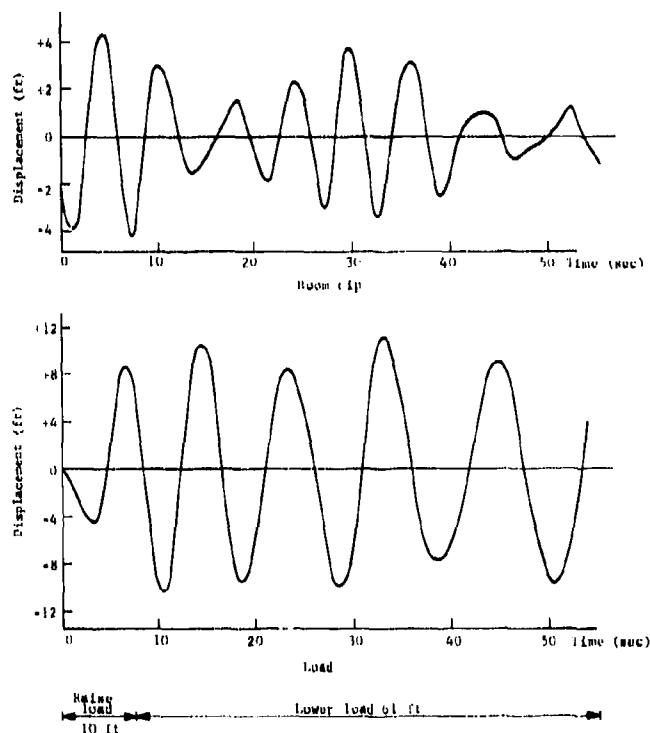

Figure 11. Typical simulation of random boom tip and load displacement ($H_{1/3} = 5.0$ ft).
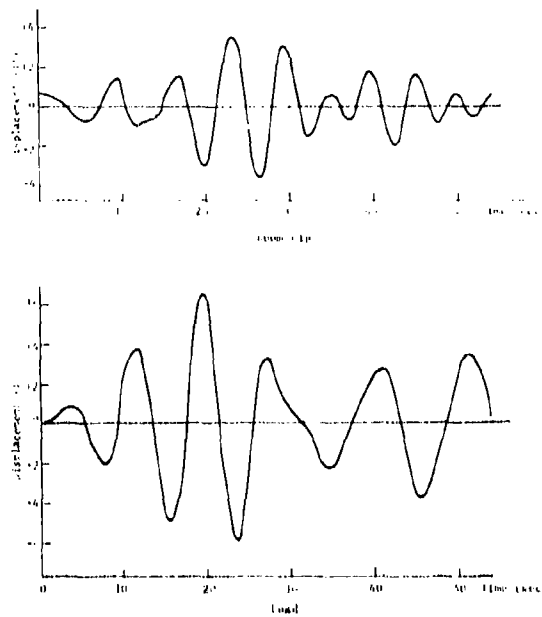
Figure 12. Typical simulation of random boom tip and
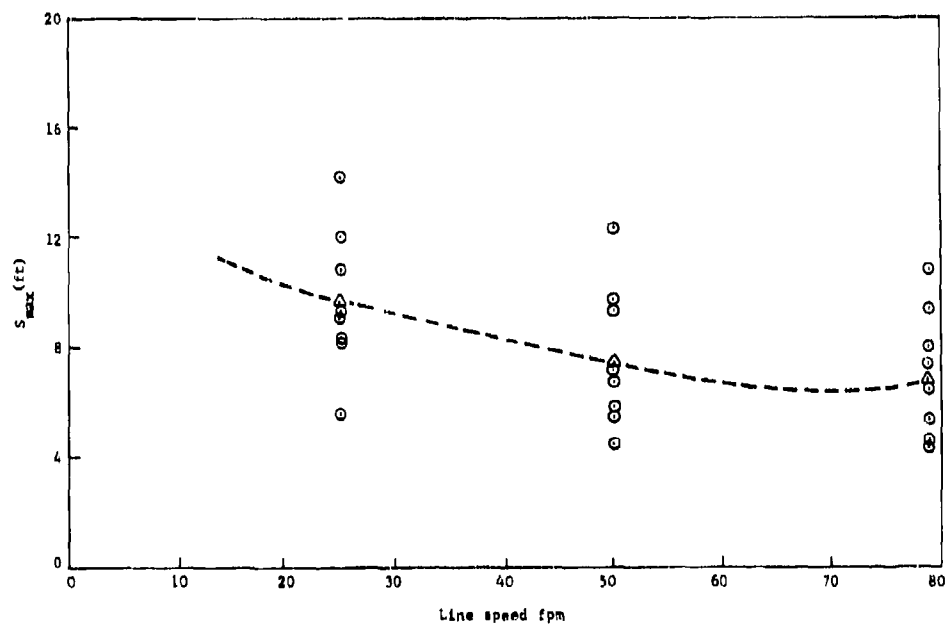load displacement ($H_{1/3}$ = 5.0 ft).
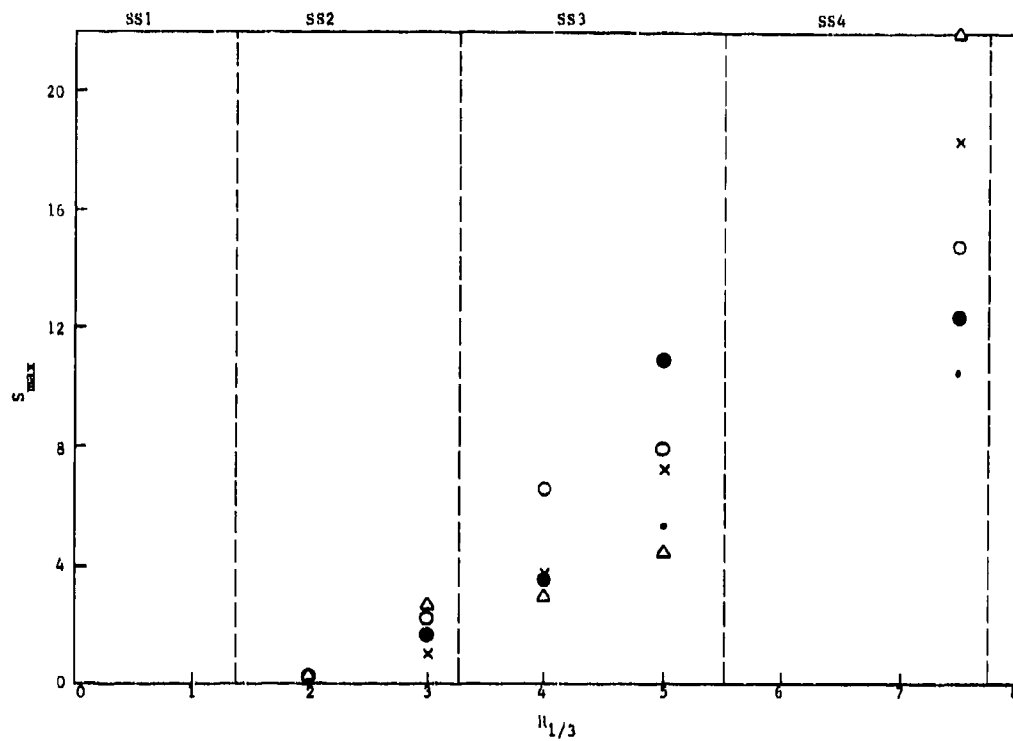

Figure 13. Maximum load displacement amplitude in random seas as a
function of line handling rate ($H_{1/3}$ = 5.0 ft).

215

Figure 14.   Maximum load displacement amplitude in random seas as a
function of seastate (line rate = 79 fpm).

REFERENCES

1. H. S. Zwibel, "Motion of Freely Suspended Loads Due to Horizontal Ship Motion in Random Head Seas," NCEL Technical Note N-1187, October 1971. (See also: The Shock and Vibration Bulletin, January 1972, pp. 235-245)

2. J. S. Bendat and A. G. Piersol, Random Data: Analysis and Measurement Procedures, Wiley-Interscience, New York, 1971.

3. M. Shinozuka and C. M. Jan, "Simulation of Multivariate and Multidimensional Processes II," Columbia University, Department of Civil Engineering and Engineering Mechanics, Technical Report No. 12, April 1971.

4. J. E. Goldberg, J. C. Bogdanoff and D. R. Sharpe, "The Response of Simple Nonlinear Systems to a Random Disturbance of the Earthquake Type," Seismological Society of America Bulletin, Vol. 54, No. 1, pp. 263-276, Feb. 1964.

NOMENCLATURE

A = Constant appearing in Pierson-Moskowitz sea spectrum (= $0.0081g^2$).

a = Wave amplitude.

β = Constant appearing in Pierson-Moskowitz sea spectrum (= $33.56/H_{1/3}^2$).

g = Acceleration of gravity.

$H_{1/3}$ = Significant wave height.

$L(t)$ = Length of lifting line.

RAO = Response amplitude operator.

$S(\omega)$ = Power spectral density function for the horizontal boom tip motion.

S_{max} = Maximum load amplitude per load cycle.

$S_s(\omega)$ = Pierson-Moskowitz sea spectrum.

SS = Seastate

t = Time

$X_s(t)$ = Horizontal position of boom.

$\theta(t)$ = Angle of lifting line with respect to the vertical.

0_n = Randomly chosen phase of the nth wave.

ω = Frequency (radians/sec).

CRITERIA DEVELOPMENT OF JK-1 AND JK-2

CARGO RESTRAINT SYSTEMS (U)

Robert Kennedy
U.S. Army Transportation Engineering Agency
Military Traffic Management and Terminal Service
Newport News, Virginia 23606

Military Traffic Management and Terminal Service (MTMTS) prepared a series of transportability test procedures designed to improve the value of test data for transportability criteria development. For the last several years, portions of the procedures have been used by military and commercial test organizations.

U.S. Army Materiel Command, Ammunition Center, Savanna, Illinois, has applied the MTMTS test procedures to an extensive transportability test program with ammunition in MILVAN containers equipped with JK-1 and JK-2 cargo restraint systems. Transportability testing included shock and vibration tests for rail, highway, and water transportation and terminal handling. The experience has provided a complete trial of the procedures for the surface intermodal tests series. Test results have produced the needed criteria information as dynamic failure loads, margins of safety, and shock and vibration data.

BACKGROUND

The U.S. Army Transportation Engineering Agency (USATEA) prepared transportability test procedures for rail, highway, air, and terminal handling. For the most part, these procedures duplicated both in intention and techniques long-standing documented test practice. The procedures differed in format from existing documents in that they were more specific and perhaps even more elementary as regards test apparatus; test reporting; facilities; and criteria for yield, failure, and margin of safety.

The biggest difference between USATEA test procedures and existing documentation is the classification of transportability tests into three categories. Method A was used to denote proof tests, or those tests required to certify that a transportation system and/or component can or cannot sustain a preestablished loading for a specified time or sequence. Method A tests are of little value for developing criteria, but proof tests are necessary for obtaining regulatory approval for some production items.

Method B tests are transportability tests conducted with full instrumentation and with test input loading increased incrementally to the point of structural yield then to the point of failure of a principal component. Method B tests are the workhorse of criteria development. By developing stresses, strains, deflections, and other measured data throughout the entire range of loadings and by developing the distribution of shocks and vibrations through the structure, effects of underloads, overloads, and the mechanical interrelation of the components can be developed. Method B tests also encourage specimen improvement during tests. A failed component may be repaired and strengthened and the input load increased to measure failure of additional components of criteria interest.

Transportability test procedures include a category, Method C, for instrumented in-service tests. The intention here is to standardize basic measurement and reporting procedures so that shock and vibration results from isolated in-service tests will be useful

219

for a comprehensive study. Criteria development from actual shipments has been hampered by lack of descriptive field notes and an incomplete description of instrumentation calibration and performance. Method C test procedures will improve in-service test results for criteria purposes by producing more uniformity in field notes and documentation.

In order to restra'n ammunition and other dense cargos in containers for intermodal shipments, restraint systems were designed by adding to existing restraints for rail, water, and highway modes to accommodate regulatory requirements for all applicable modes. Wood and mechanical bracing used successfully for years in rail was adapted for container application. Vertical restraint required by the U.S. Coast Guard was added to the rail restraint by applying more wood beams and columns. The vertical restraint structure needed additional strength beyond that required for ship environment to resist the more severe highway vertical shocks. The resulting restraint designs either in the all-lumber or the combined lumber-mechanical configurations produced inefficiencies in time and costs. These limitations are most obvious in military transportation where rapid unloading is essential.

All current restraint systems are attached partially to the container sides. For railcar and ship restraints, this form of attachment is satisfactory because the railcar sides and ship bulkheads have ample strength. Restraint attachment to container sides . . cumbersome due to the low rigidity and strength to support concentrated loads in any location. By attaching restraint members to the container sides, options are few for rapid unloading with minimum handling equipment, which is a priority military consideration. In order to unload cargo rapidly or selectively directly from a container with a rough terrain forklift, large side doors, removable container sides, or completely open flat rack configurations are needed. With cargo restraint attachments located in an area required for handling access, side or selective unloading is impractical because the restraint attachment blocks the access needed for personnel and equipment to free the cargo.

Military Traffic Management and Terminal Service (MTMTS) recognized the need for a cargo restraint system that would permit rapid container unloading with minimum materials handling equipment. The JK-1 and JK-2 cargo restraint system is one not dependent on sides or doors for restraint attachments. Preliminary engineering showed that the MTMTS

system had functional advantages over commercial systems in strength, weight, lumber conservation, and simplicity.

The MTMTS cargo restraint system was designed specifically for intermodal transportation: rail, water, and highway and terminal handling. Static and dynamic forces consequent to the transportation en ironments were analyzed, and a structure was designed that would withstand most efficiently the magnitude and direction of the most severe combination of environmental loadings. The JK-1 and JK-2 designs are structurally simple to facilitate reasonably accurate calculation of internal forces, stresses, and strengths with a minimum of mechanical assumptions. Perhaps most important is that the system is incremental. The number of restrain' components required can be from none for extremely light cargo to a sufficient number to withstand the forces resulting from the heaviest cargo permissible with the most severe transportation-induced shock and vibration loads. Storage and weight penalties for unused components are minimal. Also, only the minimum number of components need be used to produce the desired margin of safety, which conserves cargo stuffing costs and time.

The pursuit of transportability test procedures and an MTMTS cargo restraint system were conducted concurrently. It was recognized that the two projects should be brought together. The restraint system needed comprehensive transportability tests; the test procedures needed a complete trial; and shock and vibration criteria for ammunition containers based on measured data were needed. MTMTS equipped two MILVAN containers with the JK-1 and JK-2 cargo restraint systems. U.S. Army Materiel Command (USAMC) Ammunition Center, Savanna, Illinois, was assigned the task of conducting complete instrumented transportability tests. The primary task was to develop shock and vibration data for criteria for MILVAN containers with the MTMTS cargo restraint system. Transportability test procedures were followed for all testing, analysis, and reporting.

RESULTS

The transportability tests were divided into six tasks, each conducted, analyzed, and reported separately.

Task 1. Highway, In-Service, Method C.

Task 2. Laboratory, Method B.

220

Task 3. Rail, Method B.

Task 4. Highway, Method B.

Task 5. Terminal Handling, Method B.

Task 6. Rail, Highway, Terminal Handling, Method A.

Two MILVAN containers, one equipped with a JK-1 restraint and the other equipped with a JK-2 restraint, were delivered to Aberdeen Proving Ground, Aberdeen, Maryland, where the highway in-service tests originated. The cargo for the containers equipped with the JK-1 was simulated 105-mm boxed ammunition. Fig. 1 shows the MILVAN container and cargo at the completion of the trip in Savanna, Illinois. Fig. 2 shows the other container equipped with

the JK-2 system with inert loaded 155-mm single loading projectiles.

Both systems use aluminum extended floor rail bolted to the container floor beams. The JK-1 uses six floor rails; and the JK-2, four rails, as seen in the photographs. The principal difference between the JK-1 and JK-2 is the method of lateral restraint. The JK-1 uses adjustable arms affixed to the floor chocks; the JK-2 uses strapping for lateral support. The JK-1 is quicker to secure cargo but is heavier and requires more floor rails to reach cargo at all locations on the container floor. The JK-2 is less expensive to fabricate and weighs less, but it requires lateral straps that are more difficult to fasten than are the adjustable arms. Both systems were tested to provide more data
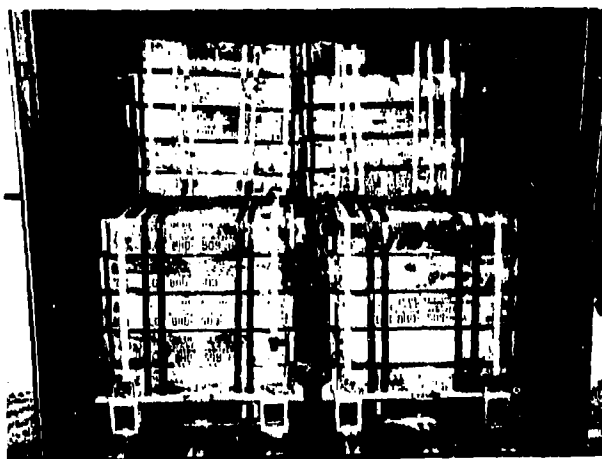

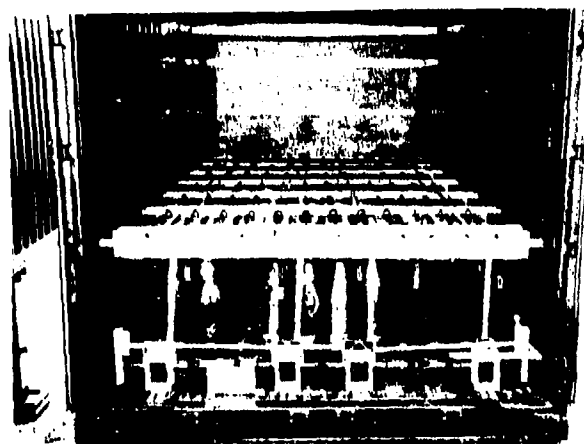Fig. 1 - 105-mm ammunition boxes in MILVAN container with JK-1 cargo restraint

Fig. 2 - 155-mm ammunition in MILVAN container with JK-2 cargo restraint

221

to aid in selection of systems for particular applications.

Task 1

For Task 1, highway in-service tests, containers were loaded to the maximum weight limit of legal allowable axle loads for the states en route. For the JK-1 system, the gross weight of the cargo and container was 40,095 pounds, and 42,094 pounds for the JK-2 system. Both containers were instrumented with continuous recording mechanical accelerometers located on the floor of the container at the door end. Both containers were transported separately on a MILVAN chassis in the 20-foot double-axle configuration with a commercial tractor and driver. Maximum peak accelerations recorded during the trip were 2.1g's (0.080 second) vertical; 1.2g's (0.080 second) lateral; and 0.5g (0.100 second) longitudinal. The acceleration amplitudes were generally lower than previously recorded by USATEA during similar in-service tests. The reduction in shock amplitude could be partially due to the JK-1 and JK-2's tight restraint preventing relative motion between the container chassis mass and the cargo mass. No conclusions as regards shock attenuation merits of restraints are intended because of the wide differences in test arrangement, such as the 35-foot container versus the 20-foot container, from Shreveport, Louisiana, to Concord, California; versus from Aberdeen, Maryland, to Savanna, Illinois; commercial chassis versus MILVAN chassis; and prototype test restraint versus production commercial restraint. The only similarities were the cargos' 155-mm and 105-mm ammunition and the instrumentation type and location.

Task 2

Task 2, laboratory tests, were run on two-high pallet loads of 155-mm unitized and 105-mm boxed and unitized inert ammunition. Task 2 tests were intended basically to experiment with two-high stacks to develop the best strapping and unitizing configuration prior to full container load testing. Throughout Task 2 tests, the hold-down straps were instrumented and the dynamic strap forces measured. Also, accelerometers were used to control and measure input forces.

Vibration tests were conducted by subjecting both the 155-mm and 105-mm ammunition to a vertical sine input of 1-inch double amplitude at 3, 4, and 5 cycles per second. The rigid hold-down produced more working of the 105-mm box nailed joints than normally seen when the boxes are not restrained in the vertical direction. The vibration tests showed that strap tension can be maintained throughout the tested vibration and that the limiting structure is the 105-mm wooden box package. The restrained 155-mm load withstood the test sequence without incident.

Fig. 3 shows the test arrangement for the shock portion of Task 2. An inclined impact tester was used to generate the longitudinal input shock. The test specimen consisted of a portion of container floor with floor rails affixed, JK-1 and JK-2 floor chocks, and metal banding. The banding was instrumented to measure both the pretension force and the superimposed dynamic forces consequent to impact.

Fig. 3 - Two-high pallet of 105-mm ammunition boxes with JK-1 restraint during incline impact test

Due to the flexibility of this type of test, many restraint configurations were tested. Criteria developed from this test were that strap pretension should be from 1,200 to 1,500 pounds to prevent zero tension at any time with dynamic loadings. Also, the chocks should be fastened to the floor rail with a torque of 80 to 100 pounds per foot. The test restraint configuration was two straps over the cargo with an additional "figure 8" unitizing strap.

The laboratory test proved quite successful because failure loads could be developed, and specimen losses due to failure were minimal due to their small size and cost. The development sequence started tests with the smallest estimated required restraint structure, and components were added or adjustments made during the test to obtain the best arrangement. This approach is practical with Task 2 tests due to the ease of changing the test specimen and retesting the restraint configurations with a single pallet stack.

Task 3

Rail impact tests, Task 3, were conducted as a failure test. Impact velocities were increased in 1-m.p.h. increments from 3 m.p.h. to the point where the test specimen could withstand no further increase in impact loading. The test specimen or test car was an 85-foot trailer on a flatcar loaded with two MILVAN chassis and containers, which, in turn, were fully loaded, one with 105-mm boxed simulated ammunition and the other with 155-mm inert loaded projectiles. The MILVAN container-chassis combination weighed 49,430 pounds with the 105-mm ammunition, and the other container-chassis weighed 50,350 pounds. The

loaded rail weight of the test car was 171,780 pounds. Impacts were affected by accelerating a fully loaded 70-ton hopper, 220,000 pounds, into the instrumented test car, which, before the impact, was standing alone with the brakes free.

Instrumentation consisted of a strain gage dynamometer coupler to measure the impact force and strain gage dynamometer tiedown straps to measure the impact forces in the restraint system. Unbonded strain gage accelerometers were also used at various locations to measure triaxial accelerations.

Strain gage data and visual observations detected substantial yield at 8-m.p.h. impact velocity, or 1,050,000 pounds coupler force. Inspection after the 12-m.p.h. impact showed that all major system components, the railcar, the chassis, the container, the wooden boxes, and the restraint system had gone beyond their yield strength to demonstrate a well-balanced system design. Fig. 4 shows the 155-mm pallet knocked out of the container by the 12-m.p.h. impact but still secured to the container floor by unitizing straps. Proof tests run on a similar test specimen show the coupler force to be under 300,000 pounds at 10 m.p.h., whereas Method B tests produced coupler forces 5 times greater, or 1,500,000 pounds at 10 m.p.h. The severity increase is due to the increase in kinetic energy consequent to a much heavier hammer car (210,000 pounds versus 170,000 pounds) combined with working the cushions to their least efficient force and travel range. At these extreme coupler forces, over 1,000,000, the cushions in the railcar and the cushions in the hitches have used up all usable travel and are substantially solid.
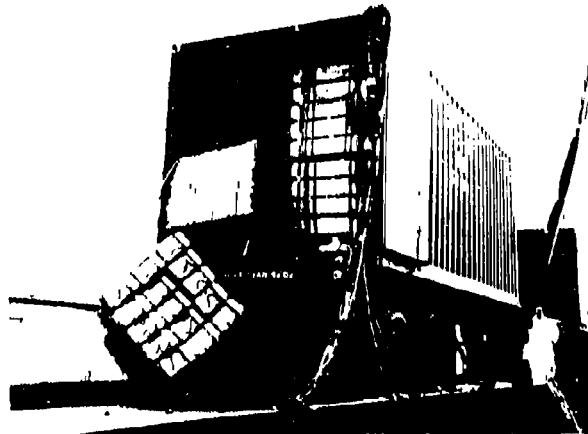

Fig. 4 - Test specimen after 12 m.p.h. impact (note how unitizing strap captured cargo)

The rail tests were conducted with several bundling and unitizing configurations for development purposes. The test results generated several restraint system improvements as an improved T-bolt, chock, base plate, and chock bearing. The restraint system was continually improved throughout testing, and the final restraint design was of equal or better strength than the other structural components in the system as regards resistance to rail impact loads. A balanced, efficient, and optimum design for the restraint system was achieved, and this met the goal of a Method B failure test.

Task 4

Task 4 was conducted by towing the same MILVAN container loads of ammunition, 155-mm and 105-mm, mounted on a MILVAN chassis over test courses. Tiedown straps were instrumented to measure pretension and dynamic forces. The washboard course consisted of 300 feet of gravel surface with transverse railroad rails spaced 26 inches apart. This test surface produced a severe resonant condition on the test specimen. Some lateral movements and some damage were found on the 105-mm ammunition boxes. The strapping configuration differed from any tried in the laboratory during preceding tests and was found by this test to be unsuccessful. Force and acceleration criteria data were developed from the washboard test. For this dynamic loading, the initial strap forces were substantially unrelated to the box bearing failure and consequent cargo slippage.

In order to obtain American Association of Railroads (AAR) approval for ammunition use, the system must withstand the rigors of the USAMC Hazard Course. This course consists

of transverse alternately spaced railroad ties projecting 6 inches above the road surface spaced at 10-foot intervals for 50 feet. Task 4 included several test runs over the Hazard Course. No box failures or slippages were detected even with the pallet loads using the unsuccessful banding arrangement. Strap tension (combined static and dynamic forces) ranged from 1,600 to 2,000 pounds, which is considered satisfactory and serves as a check on Task 2 criteria of 1,200 to 1,500 pounds pretensioning.

The most important observation from the highway tests is that vertical road resonance shock inputs are a most severe loading for the nailed joints of the wood packaging. If no vertical restraint is utilized, as with many current restraint systems, the packages merely bounce free and do not respond to the resonant input to develop high vertical cargo stresses. The current 105-mm boxes withstand this severe load with proper vertical restraint configurations and are satisfactory for restraint for intermodal shipment.

Task 5

Task 5, terminal handling tests, consisted primarily of tilt and drop tests. Instrumentation was active during these tests to measure both strap forces and pertinent accelerations. The JK-1 restraint with 105-mm boxed ammunition was selected for terminal handling tests as shown in Fig. 5. These specimen components were selected to try the rigid chock arm of the JK-1 in the tilt test and to see how the nailed box joints from the 105-mm arrangement hold up for the shock test.
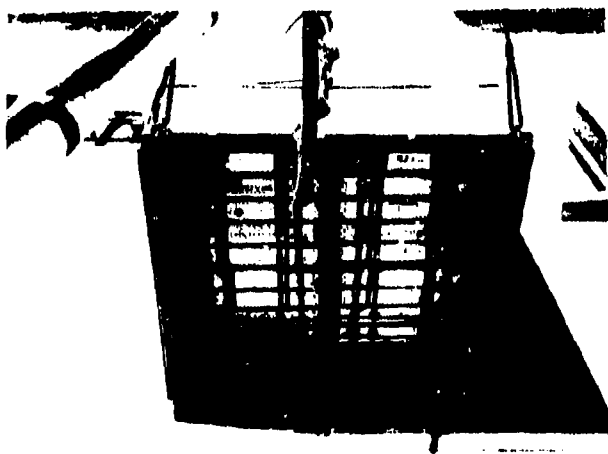

Fig. 5 - Test specimen during materials handling tests

The tilt test consisted of tilting the container 80 degrees with the vertical as shown in Fig. 6. The tilt angle is set to produce lateral forces on the cargo of comparable severity to a 50-degree ship roll plus dynamic or vertical forces consequent to the ship motion. During the tilt test the cargo remained in position and did not close the clearance between the boxes and the container wall. The measured strap forces added a maximum of 1,400 pounds during the 80-degree tilt, which is minor compared to the strap tension increases due to rail impact loadings.

Container edge drops were conducted, and the only system failure was floor beam deformation, as shown in Fig. 7. The main purpose of this failure test was to determine the dynamic load or drop height at which the container could still function without interfering with a continuous container operation at terminals. The test consisted of container edge drops from 2 inches to 24 inches in 2-inch increments.

Maximum strap tension increase at 24-inch edge drop was 1,500 pounds, which is a measure of the rebound load. The maximum vertical acceleration recorded on the container floor during the 24-inch drop was 22g's at 24 milliseconds. The system failures were seen by yielding of the container floor beams. Both the measured permanent yield and the accelerometers indicated a yield of the system at a 9-inch drop and continued accumulating yield to a 24-inch drop. After all drop testing, the packaging, restraint, and container were all intact, and the maximum floor beam yield was 1/2 inch.
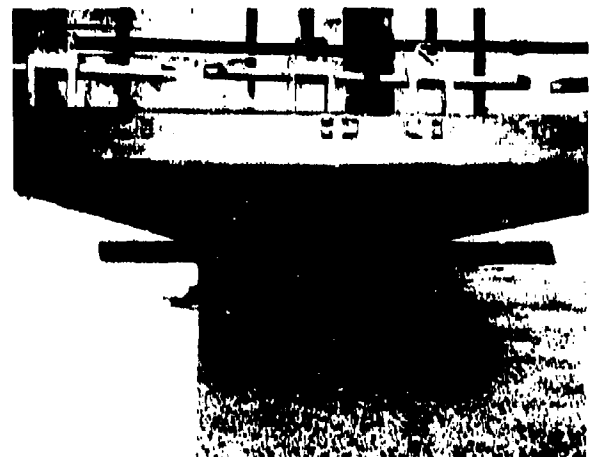

Fig. 6 - Tilt test

Fig. 7 - MILVAN floor beam deformation consequent to edge drop tests

225

It was concluded that after all the drop tests, the system could still function and not interfere with continuous handling as the containers could be reconnected to a MILVAN chassis without difficulty. The floor beam deformation caused by a severe handling drop will not damage adjacent containers or jam the container in the ship cell guides.

Task 6

Task 6, rail, highway, and terminal handling, all Method A proof tests, was conducted to obtain AAR and Coast Guard approval for use of the restraint system for ammunition shipments. Test arrangement for the rail portion is shown in Fig. 8. The rail sequence is rail impacts of 4, 6, and 8 m.p.h. and an 8-m.p.h. reverse impact. Even though the system components were subjected to greater impact forces than required for regulatory approval in previous tests, the first proof test detected new failures in the packages. This test showed the importance of aligning the cargo pallets with the container floor rails to maintain stack shear, strap tension, and exclude undesirable eccentric loading on the packages. The restraint system MILVAN combination passed the highway and tilt proof tests.

CONCLUSIONS

This program has demonstrated the value of failure tests as described in USATEA test procedures. Failure tests establish the reserve, one-time strength of a system that is so important in military transportation where the trend is toward minimum storage and holding and high-speed supply. Also, failure tests

identify many weak system components that can be improved to be more in line with other components to develop an improved mechanical system. Perhaps most important is the opportunity to establish a margin of safety for transportation system components based on actual tests so that structurally marginal components are known and that effects of overloads can be better estimated.

This first complete trial of the test procedures has shown that the goals of an interchangeable and a reproducible data base can be met. The strain gage instrumentation produced measurements that were directly usable for further mechanical and dynamic analysis. Force, stress, strain, and failure data developed on separate components agreed closely with similar data obtained from complete system tests.

Transportability criteria development has been hampered by basic variations in test report format, testing, instrumentation, and analyses. Even though the tests procedures are general, the procedures have produced data from the restraint tests that are of sufficient consistence in format and data presentation to develop transportability criteria. The resulting data are both reproducible and interchangeable with other data where the test procedures were followed.

USATEA plans to continue this program by developing and publishing criteria for restraining cargo with the JK-1 and JK-3 (improved JK-2) cargo restraint system for rail, highway, water, and terminal handling modes and intermodal shipments. Also, comprehensive cost effective studies are scheduled to compare all approved restraint systems as regards

Fig. 8 - Test arrangement for AAR and Coast Guard approval tests

aggregated costs over the system life cycle.
These cost factors will be developed from
actual military shipments by using the test
restraint systems in MILVAN containers to
secure the same cargo with the same origin
and destination points at the same time. This
should minimize undesired cost and time errors
during study.